Industrially-safe, Nitrogen-buffered Graphene CVD and its Application in Sensing Devices

Johannes Gausden

A thesis presented for the degree of

Doctor of Philosophy

Electrical and Electronic Engineering

Newcastle University

United Kingdom

January 2020

Abstract

Graphene is a two-dimensional carbon material, which has been suggested for use within many next-generation electronic applications due to its outstanding electronic and mechanical properties. Copper-catalysed chemical vapour deposition (Cu-CVD) is currently the most promising method for upscaling graphene production. However, there are safety and cost aspects which have not yet been fully explored and which are desirable to have in place prior to moving graphene production from batch- to industrial-scale production.

This thesis presents research aimed at the development of Cu-CVD graphene growth recipes, using processes which mitigate against explosive risk and reduce cost via the dilution of precursor species within nitrogen, rather than the almost universally used argon. Process development is presented for graphene growth within a nitrogen-buffered atmosphere, which demonstrates that graphene growth follows the same trends with nitrogen as is observed within argon and also provides a guideline for others wishing to develop their own graphene CVD processes.

Investigation of graphene films grown within nitrogen-buffered and argon-buffered atmospheres via Raman Spectroscopy, X-ray Photoelectron Spectroscopy and Time-of-Flight Secondary Ion Spectroscopy are presented, demonstrating that atomic nitrogen does not become incorporated within the graphene film when CVD is carried out within an N_2 atmosphere, within spectroscopically detectable limits. The use of nitrogen, rather than argon, within CVD opens possibilities for significant cost reduction, particularly within mass-production which is likely to require high volumes of process gases.

The electronic properties of the CVD graphene is explored via analysis of graphene field effect transistor (GFET) where it is shown that graphene grown via nitrogen-buffered CVD and argon-buffered CVD is indistinguishable. GFETs are used as the basis for gas-sensing devices, operating on a basis of resistance change due to charge-transfer. Decoration of GFETs with catalytically active nanoparticles to improve device sensitivity is explored, but quality variation of graphene layers is shown to be a limiting factor.

To my fiancé Lucy,

thank you for your love and support

Acknowledgements

First and foremost, I extend my heartfelt gratitude to my primary supervisor, Dr. Toby Hallam. His guidance, encouragement and support, both within my academic life and in a more pastoral role has been appreciated beyond measure. The inquisitive mode of research he encouraged me to follow has made the past couple of years a joy and I feel I have learnt all the more for it.

I must also sincerely thank Dr. Alton Horsfall for the initial offer of my PhD position and for providing the initial materials and energy for my project, along with much map- and orienteering-based banter.

I would also like to thank my secondary supervisor, Dr. Noel Healy, who has provided a calming voice in my more panicked moments and has offered me enriching opportunities outside of Newcastle University, for which I am deeply grateful.

An extremely honourable mention must be given to Dr. Daniel Naylor, who has operated as a complementary voice to Dr. Hallam. Dr. Naylor has both helped me find perspective when the workload has seemed unmanageable and offered a helpful theoretical mind when my hand-wavey practical models required clarification. In a similar vein I would like to thank Dr Jon Goss for his eclectic and level headed conversations.

I must also deeply thank Professor Anthony O'Neill, who has employed me within a research role before the submission of my thesis. His belief in my ability and understanding of the stressful dual workload these past few months has been greatly appreciated.

A huge thank you must be extended to Dr. Enrique Escobedo-Cousin, Dr. Konstantin Vasilevskiy and Mrs. Rachel Savidis, who all invested significant time training me to use the fabrication and characterisation equipment vital for my research. Dr. Escobedo-Cousin and Dr. Vasilevskiy must be especially thanked for their hours of assistance getting vital equipment back up and running. Without their insight and guidance, I would not have the understanding of equipment set-up, repair and operation that I do today.

I would also like to thank, in no particular order, Dr. Hua-Khee Chan, Professor Nick Wright, Dr. Srinivas Ganti, Luke Bradley, James Beattie and Amy Peters for their discussions regarding my research. Without such discussions, ideas rarely grow.

I would also like to thank all my colleagues and friends within the ETM department and particularly, but in no particular order, Mr. James Beattie, Mr. Ryan Siddall, Ms. Amy Peters, Dr. Chloe Peaker and Ms. Claire Meara for their camaraderie and friendship throughout my PhD. A special mention must be given to Mr. Luke Bradley, who has been an erstwhile friend and confidant, particularly in times of great stress.

I also extend my sincere gratitude to my collaborators at Universität der Bundeswehr, München, and Trinity College, Dublin. Especially, I would like to thank Dr. Kangho "Kay" Lee, who spent many, many hours trying to make my gas sensors sense and for whom I have a huge amount of gratitude.

I also wish to acknowledge the Newcastle University SAgE DTA scholarship scheme, which has supported me financially throughout my PhD.

I am deeply grateful toward my fiancé, Lucy Imber, who has been patient, kind, understanding and supportive throughout the ups and downs of my PhD; I am aware of the many sacrifices she has made and I am deeply grateful. I would also like to thank my mother, father and brother who have been supportive, encouraging and understanding throughout my PhD and have offered advice based upon their own experiences. Finally, I must thank my future in-laws, who have repeatedly gone out of their way to help and support both Lucy and myself.

Contents

List of Figures

List of Tables

Chapter 1

Introduction

1.1 Motivation

Materials science continually contributes new materials which lead to unexpected technological progression. The discovery of graphene in 2004 [1] opened a new area of material research – that of 2D materials [2, 3] – and since its isolation, has been one of the most studied materials of the past decade and a half [4–6]. Graphene's exceptional electronic properties had been predicted [7–9] before demonstration within a real system [1, 10], but it is the combination of multiple outstanding material properties such as high strength [11, 12], flexibility [13–18], thermal conductivity [19, 20], optical transparency [13, 21–24] and ultrahigh specific surface area [25, 26] which lead to an explosion of research into the use of graphene in applications which are not accessible with conventional semiconductors or metals.

Graphene has already been applied in proof-of-concept applications as a potential material for use within transparent conductive electrodes [13, 23], flexible electronics [13, 16–18], spintronics [27–29], optoelectronics [30–32], sensors [33–40] and adaptive thermal camouflage [41], to name but a few. However, the future of graphene-based technology hinges on successfully overcoming the fundamental challenge of graphene mass-production, whilst retaining its exceptional material properties.

The easiest way to isolate graphene is via micro-mechanical exfoliation from bulk graphite using Scotch tape, as demonstrated by Novoselov and Geim in their seminal paper [1]. However, whilst samples obtained via exfoliation are ideal for exploring fundamental solid state physics, due to high crystallinity and low carbon vacancy defect density [42, 43], sample production via exfoliation is non-deterministic and non-scalable and thus other

options must be explored to bring graphene to the mass market. Of the scalable methods for the production of graphene, such as Si sublimation from SiC [44–49] and liquid phase exfoliation [50–54], chemical vapour deposition (CVD) has been adopted as the most common method for the synthesis of high-quality large-area monolayer graphene [55, 56]. The term 'high-quality' is somewhat subjective; within graphene research the phrase refers to graphene films with few defects, which may take the form of sp^2 bonding defects, elemental impurities, contaminating adsorbates, graphene domain boundaries, wrinkles and cracks. Additionally, large area graphene films should be continuous and uniformly monolayer to ensure device homogeneity within wafer-scale device fabrication [56–58].

Most graphene CVD now follows the protocol introduced by Li et al. which uses copper as the catalytic growth substrate for graphene growth from gaseous hydrocarbon precursors [59]. The use of copper is advantageous when compared with the use of other transition metal catalyst films or foils, as its low carbon solubility [60, 61] makes homogeneous monolayer growth more likely [62]. Recent advancements in copper-catalysed CVD have provided methods for tailoring graphene nucleation density and domain area [63–71], domain shape [64, 67, 70, 72, 73] and domain growth rate [70, 74–76] which has ultimately lead to the CVD growth of single crystal domains up to an inch across [77] – an increase in domain area of about 8 orders of magnitude over exfoliated graphene samples, which are typically tens of microns across.

However, graphene CVD synthesis still requires process optimisation for the shift from laboratory scale to industrial scale production. CVD graphene is poly-crystalline in nature which degrades the quality of the CVD grown graphene films and thus the reduction of CVD graphene poly-crystallinity is one of the key focusses within current CVD graphene research [63–71, 74–77]. As domain boundaries are a major source of charge carrier scattering resulting in reduced charge carrier mobility [78–82] within CVD grown graphene, the density of domain boundaries, and thus graphene domains should be reduced. Reduced graphene domain density naturally requires increased graphene domain area to achieve a continuous graphene film and thus protocols for increasing graphene domain areas are of great value. However, most of the current research is conducted at the laboratory scale with results focussed on the growth of isolated ultra-large graphene domains, without demonstrating production of continuous graphene films [71, 83, 84], which is a basic requirement for the use of graphene within an industrial setting [58]. Therefore protocols for the development of continuous graphene with enlarged domain area are of importance to the field of graphene research and the shift from laboratory to industrial

scale growth. Additionally, because of system-to-system variations, the identification, rationalisation and explanation of generalised growth optimisation pathways will be of greater value to industry than the specific recipes often described within graphene CVD research.

Graphene CVD growth is also inherently unsafe, as both the graphene hydrocarbon precursor and hydrogen, which is required to protect and modulate the graphene growth, are explosive. This is of concern for copper-catalysed graphene CVD as process temperatures typically exceed 1000 °C, increasing the risk of explosion in the event of a process gas leak. However, this risk can be mitigated by the dilution of explosive process gases within an inert buffering gas. Argon is typically used within research into safe graphene CVD [58], because it is a noble gas and is thus chemically inert under the process conditions used within graphene CVD. However, the dilution of precursor gases means that large gas flow rates are required to achieve graphene growth [85] which represents a large expense when translated to industrial scale growth. Nitrogen is the logical gas to explore as a replacement for argon to reduce process cost within graphene CVD, due to its abundance and the strength of the N≡N triple bond within N_2 [86–88]. However, until now, no conclusive investigation into the non-inclusion of nitrogen within the graphene lattice during nitrogen-buffered graphene CVD was available. The opportunity to use nitrogen instead of argon to grow viable graphene will be of great value to industrial graphene growth.

Industrial safety and the wider public concern with increased levels of greenhouse and toxic gasses, such as NO_2, nicely ties together the motivation for use of large scale CVD graphene within gas sensing devices. The atomic thinness of graphene and the low density of states within pristine graphene [1, 10], coupled with a large charge carrier mobility in excess of 1000 $cm^2V^{-1}s^{-1}$ even within poorly processed devices [89], means that graphene should be an ideal candidate for forming the basis of next generation high-sensitivity gas sensors [39, 90–94]. However, graphene based gas sensors are known to have issues regarding base line drift and device saturation [95–97]. Graphene-particle composite sensors have been demonstrated to improve device sensitivity and stability [98–101] whilst operating at lower temperatures than traditional metal-oxide based gas sensing devices [102, 103]. The reduced power consumption required by such architecture allows for much more widely spread placement of sensing devices.

One issue however, has been the ability to marry graphene with a stable material of lower work function than graphene ($\sim$ 4.35 eV [104]) for increased sensitivity towards reducing gas species, due to the inherent tendency for low work function materials to

oxidise. Materials with lower work function than graphene are required for increased sensitivity towards reducing agents, as electron transport from the decorating material to the graphene channel is necessary to modulate the graphene channel resistance. This necessitates a heterojunction to be formed between graphene and a lower work function material. W_5O_{14}, which is a novel sub-oxidative state of WO_3, is found to be both stable within an ambient environment and have a work function lower than that of pristine graphene [104, 105], and thus provides an interesting avenue for such device exploration.

1.2 Thesis structure

This thesis documents experimental work on the development and characterisation of nitrogen-buffered, industrially safe graphene CVD for future industrial scale-up. The electronic and gas sensing capabilities of the fabricated graphene are also explored.

Chapter 2 presents the properties of graphene and introduces the current foremost techniques for the production of graphene. The factors affecting the quality of CVD graphene synthesis are discussed as well as current issues pertinent to graphene mass production. Graphene doping via both atomic substitution and charge transfer from adsorbates is reviewed alongside graphene doping metrology methods.

Chapter 3 summarises the main experimental techniques used throughout this research. The setup and operation of the graphene CVD reactor is detailed. The protocol for graphene transfer from its growth foil to arbitrary target substrates is introduced, alongside the methods used for graphene device fabrication. The characterisation techniques used for graphene material analysis are introduced alongside the theory behind said techniques.

Chapter 4 introduces the hot plate method as a rapid and low cost technique for CVD graphene growth analysis. Using the hot plate method, step wise optimisation of graphene CVD growth is demonstrated for graphene grown within industrially safe conditions, using H_2 and CH_4 diluted below their lower explosive limits within N_2. Growth of high-quality, continuous monolayer graphene films is demonstrated with individual domain diameters in excess of 200 µm.

Chapter 5 demonstrates that N_2 is a suitable replacement for Ar within CH_4-based hot-wall graphene CVD. Spectroscopic investigations via Raman spectroscopy, X-Ray

photoelectron spectroscopy and time-of-flight secondary-ion mass-spectroscopy show that the chemical composition of graphene grown within N_2 and Ar atmospheres are indistinguishable of each other within detectable limits.

Chapter 6 presents behaviour characteristics measured from graphene field effect transistors (GFETs) fabricated throughout this research. The repeatability of GFET behaviour is demonstrated to indicate that the fabricated GFETs are suitable to use as the basis for gas sensing devices. Gas sensing data is then presented, and the cleanliness of the post-transfer graphene film is identified as a critical parameter for successful device operation. Finally, operational gas sensors are decorated with W_5O_{14} in a bid to improve device sensitivity and the interaction between W_5O_{14} and graphene is explored.

Chapter 7 concludes this thesis by summarising the results and findings. An overview of the values and limitations of this work is presented alongside an outlook for future work.

Chapter 2

Background

2.1 Graphene Properties

Graphene is a two-dimensional (2D) allotrope of carbon, wherein carbon atoms are arranged into a flat hexagonal lattice, with a carbon atom at the vertex of each hexagon, as shown in Figure 2.1. It is the building block for many other pure carbon allotropes with different dimensionalities, such as fullerenes (0D), carbon nanotubes (1D) and graphite (3D), illustrated in Figure 2.2. All of these allotropes are sp^2 hybridised carbon, which means that each carbon is bonded to three adjacent neighbouring carbons. These forms of bonding leads to generally flexible structures with interesting electronic properties, arising from the formation of π and $\pi*$ bonds between carbon atoms [106]. Graphene has garnered significant interest since its first isolation in 2004 by Novoselov and Geim [1], due to its exceptional mechanical, thermal, optical and electronic properties.

2.1.1 Atomic Structure of Graphene

The unit cell of graphene is comprised of two geometrically discrete carbon atoms, which form the basis of the graphene sub-lattices A and B [106], depicted in Figure 2.1. The two lattice unit vectors are then written as:

$$a_1 = \frac{a_{C-C}}{2}(3, \sqrt{3}); a_2 = \frac{a_{C-C}}{2}(3, -\sqrt{3}) \tag{2.1}$$

where $a_{C-C} = 0.142$ nm, the sp^2 carbon-carbon bond length [106]. The lattice constant is calculated to be 2.41Å [106]. Graphene's reciprocal lattice vectors are then described

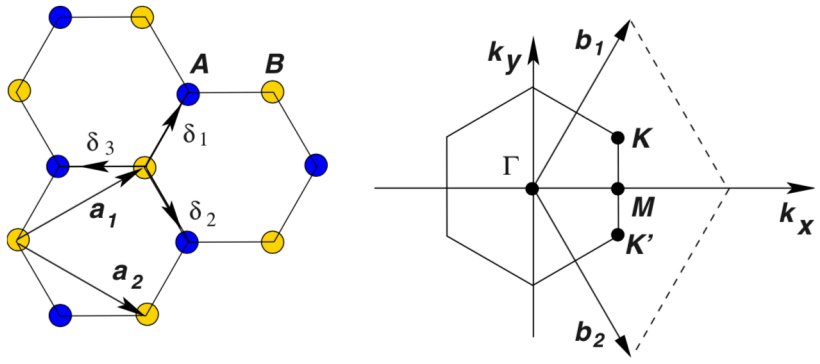

Figure 2.1: Graphene's honeycomb lattice and its Brillouin zone. Left: lattice structure of graphene, made out of two interpenetrating triangular lattices. a1 and a2 are the lattice unit vectors and δ_i i=1,2,3 are the nearest-neighbour vectors. Right: the corresponding Brillouin zone. Dirac cones are located at the K and K' points. Taken from Neto et al. [106].

by [106]:

$$b_1 = \frac{2\pi}{3a}\frac{1}{\sqrt{3}}; b_2 = \frac{2\pi}{3a}\frac{-1}{\sqrt{3}} \tag{2.2}$$

Particularly import for the physics of graphene are the Dirac points, K and K', located at the corners of the graphene Brilloun zone (BZ). The importance of the K and K' points should become clear shortly and their positions in $\underline{k}$ space are given by:

$$K = \left(\frac{2\pi}{3a}, \frac{2\pi}{3\sqrt{3}a}\right), K' = \left(\frac{2\pi}{3a}, -\frac{2\pi}{3\sqrt{3}a}\right) \tag{2.3}$$

2.1.2 Ideal Electronic Properties of Graphene

The properties of a material are closely related to its electron band structure. The electronic properties of graphene can be determined via a tight-binding approximation method [106]. To achieve this, the wavefunction of an electron is expanded, subject to the periodic crystal potential as a linear combination of the electron's orbit (LCAO) around each lattice atom. As graphene's lattice consists of two sub-lattices, A and B, the electron's wave function is written as:

$$\Psi = C_A\Psi^A + C_B\Psi^B \tag{2.4}$$

where Ψ^A and Ψ^B are the linear combinations of the electron's orbits around atoms A and B respectively. The coefficients C_A and C_B are determined from the time inde-

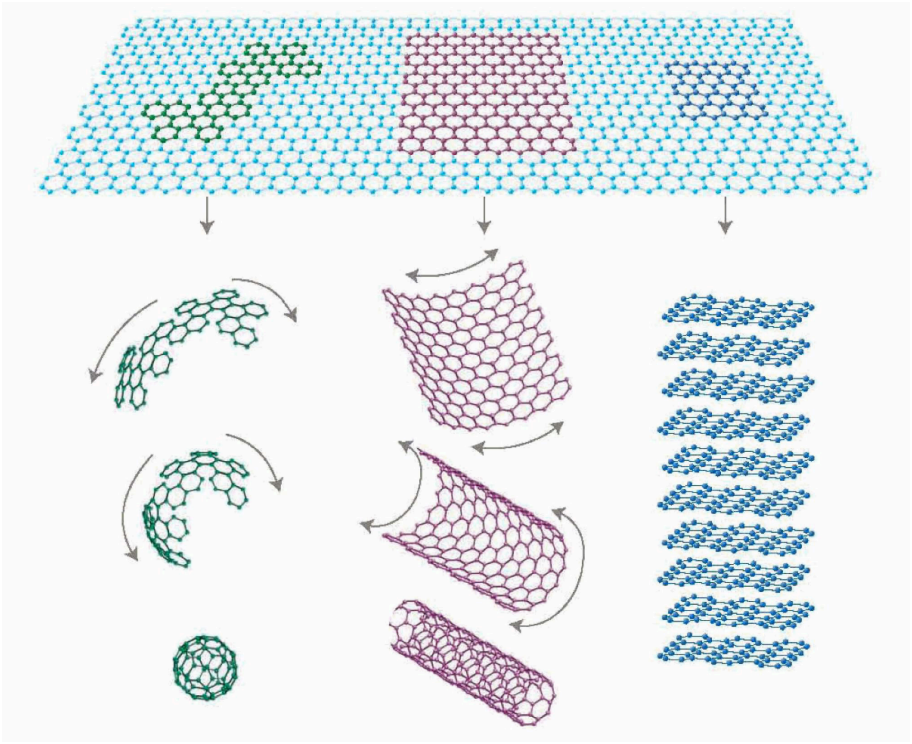

Figure 2.2: Ball and stick representations of differently dimensioned sp^2 carbon allotropes which can be considered to be based upon graphene. Taken from reference [106].

pendant Scrödinger equation, $H\Psi = E\Psi$, where H is the Hamiltonian and E is the energy eigenvalue. In the tight binding approximation, the contributions from atoms beyond the second-nearest neighbour atoms are ignored. The energy bands of graphene are given by:

$$E_{\pm}(\underline{k}) = \pm t\sqrt{3 + f(\underline{k})} - t'f(\underline{k}) \tag{2.5}$$

where

$$f(\underline{k}) = 2cos(\sqrt{3}k_y a) + 4cos\left(\frac{\sqrt{3}}{2}k_y a\right) cos\left(\frac{3}{2}k_x a\right) \tag{2.6}$$

Use of a plus sign within Equation 2.5 denotes the upper (π^*) band and likewise a minus sign denotes the lower (π) band [7, 106]. Also within Equation 2.5, t ($\approx$ 2.7 eV) and t' refer to the nearest and next-nearest neighbour hopping energies respectively, which refer to electron hopping between A/B sublattices and A/A or B/B sublattices respectively [9, 106]. The real value of t' is not well known, but ab initio calculations find $0.02t < t' < 0.2t$ depending on the tight- binding parametrisation [9]. If t' is set to 0, then the E-k spectrum is found to be symmetric around zero energy. The energy dispersion close to the Dirac points, K and K', can then be approximated as a linear relationship with

relation to momentum, $\underline{k}$, relative to the Dirac points:

$$E_{\pm}(\underline{k}) \approx \pm \nu_F \left|k\right| + O\left[\left(\frac{|k|}{K}\right)^2\right] \tag{2.7}$$

where ν_F is the Fermi velocity $\approx c/300$ and c is the speed of light within a vacuum. Thus, in the case of graphene, the Fermi velocity does not change close to the K and K' points with respect to energy or momentum, leading to a linear relationship, $E = \hbar ck$, illustrated in Figure 2.3, which resembles that of a photon and is why the K and K' points are known as Dirac points.

The linear dispersion around the Dirac points implies that charge carriers act as massless particles near the Dirac points. This explains the large mobilities of up to 250,000 $\text{cm}^2(\text{Vs})^{-1}$ observed within suspended, high-quality graphene [107]. Whilst massless charge carriers might be expected to move at c, the observed finite charge carrier mobility within graphene is attributed to charge carrier scattering due to phonons, defects and a non-zero concentration of charge carriers.

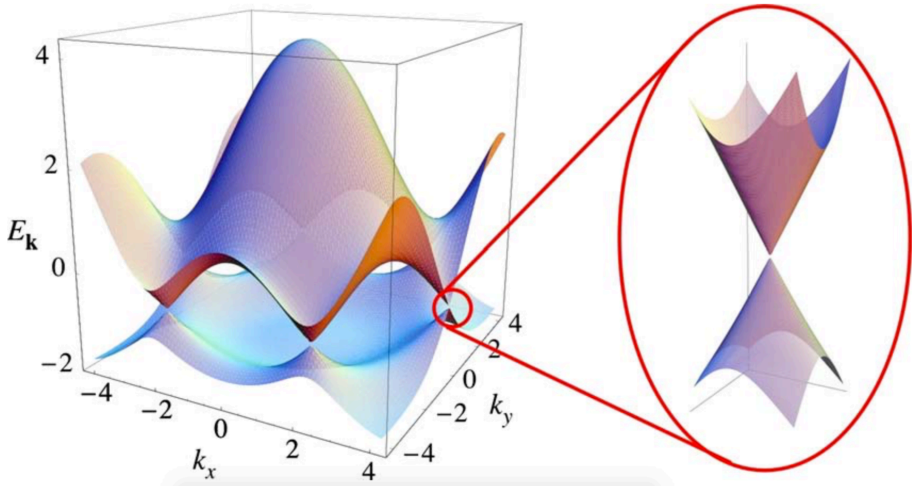

Figure 2.3: Electronic dispersion in the graphene honeycomb lattice. Left: energy spectrum in units of t for finite values of t and t', with t=2.7 eV and t'=0.2t. Right: zoom in of the energy bands close to one of the Dirac points. Taken from Neto et al. [106].

The zero band gap within graphene also means that it is possible to continuously tune between electrons and holes by applying an external electrical field. Figure 2.4 displays how the Fermi energy, E_F can be shifted away from the Dirac point such that electrons (holes) become the majority charge carriers with application of positive (negative) gate potential [108].

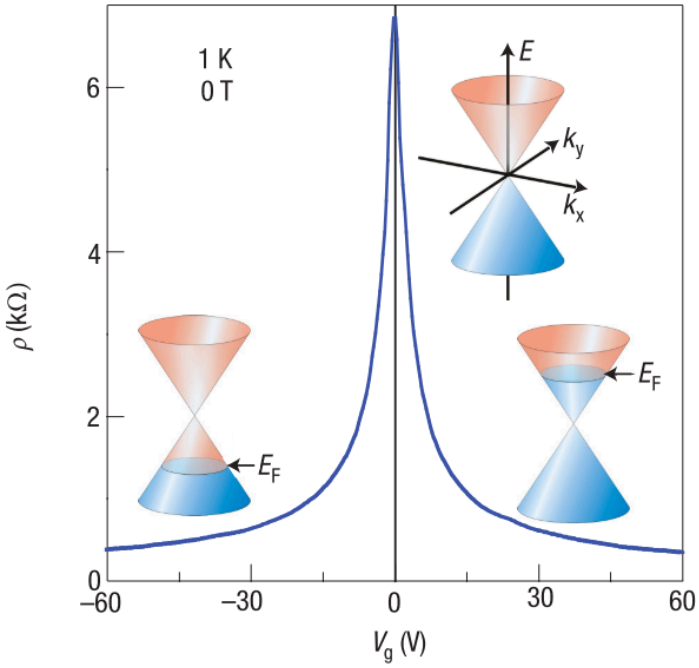

Figure 2.4: Diagram displaying the effect of tuning the graphene fermi-level using an external electric field. Taken from Novoselov and Geim [108].

2.1.3 Material Properties of Graphene

Beyond its superlative electronic properties, graphene also possesses other exceptional material properties. For instance, it possesses the greatest known Young's modulus with a value of E = 1 TPa within an intrinsic, defect free sheet [109]. This is due to the sp^2 covalent bonding within the hexagonal carbon lattice. Coupled with a fracture strength of $\sim$ 130 GPa [109], graphene is highly flexible; a property which sparked interest in the use of graphene as a component within flexible electronics [13, 110–114]. Additionally, graphene has been found to be an effective component in polymers for the improvement of their mechanical properties [115, 116] and has already been applied in this way within a number of commercial applications, from aviation components to fell-running trainers.

Graphene is also an excellent thermal conductor, which is mainly due to phonon transport within graphene [20]. The low electron carrier densities within intrinsic graphene mean that the electronic contribution to the thermal conductivity of graphene must be low and thus graphene's thermal conductivity must be predominantly phonon-based [20]. The thermal conductivity of suspended graphene was measured by Balandin et al, to be 3000 - 5000 $Wm^{-1}K^{-1}$ [19]. Whilst this value decreases when graphene is brought in contact with other materials, for example SiO_2, its thermal conductivity of 600 $Wm^{-1}k^{-1}$ [20] is still almost double that of copper (398 $Wm^{-1}K^{-1}$) [117] which is known as a highly efficient

thermal conductor. The reduction in thermal conductivity when not suspended is due to phonon interactions between the graphene sheet and adjacent material [20]. Because graphene's thermal conductivity remains impressively high, it has been considered as an optimum candidate for cooling nanostructured devices [19, 20].

Due to its atomic thinness, graphene is highly transparent across visible wavelengths, with absorbance of only 2.7% for monolayer graphene films [13, 114, 118, 119]. Transparent, conductive materials are likely to become ever more important as the use of technology such as touch screens and solar cells increases. The current leading material, indium-tin-oxide (ITO), is unlikely to remain commercially viable for much longer due to its scarcity. ITO is also a brittle, crystalline material which when stressed, may fracture, irreversibly dropping the conductivity by several orders of magnitude and limiting the use of ITO in emerging applications that require some flexibility [23, 120]. Graphene is an ideal candidate to fulfil such roles, but only if industrial-scale synthesis can be realised.

2.2 Graphene Synthesis Methods

Graphene was first isolated and had its electronic properties measured by Novoselov and Geim in 2004 [1]. This breakthrough success was achieved via micro-mechanical exfoliation (MME) of graphite and for their work, Novoselov and Geim were awarded the Nobel prize in physics in 2010 for "groundbreaking experiments regarding the two-dimensional material graphene". Although MME produces graphene of high quality, with few lattice defects, the method is laborious, non-deterministic and non-scalable. Hence, shortly after the first isolation of graphene, methods for large scale graphene production began to be explored. Figure 2.5 illustrates the most commonly used methods for graphene production, with Figures 2.5 a) and b) representing the leading top-down synthesis methods of MME and liquid phase exfoliation and Figures 2.5 c) and d) representing the bottom-up methods of CVD and epitaxial growth on SiC via Si sublimation. The advantages and disadvantages of these methods are discussed in the following sections.

Due to such large interest in graphene, significant effort has been invested in large-scale graphene production methods. Consequently, the cost per unit area of graphene has decreased by multiple orders of magnitude, from £100s for a single 10 μm $\times$ 10μm flake, to $\sim$ £60 cm^{-2} since 2004 [122]. Figure 2.6 displays world graphene production, from 2013 to 2017. Within just a four year period, total world production of graphene nanoflakes and graphene oxides increased almost four-fold from 722 tonnes per year to

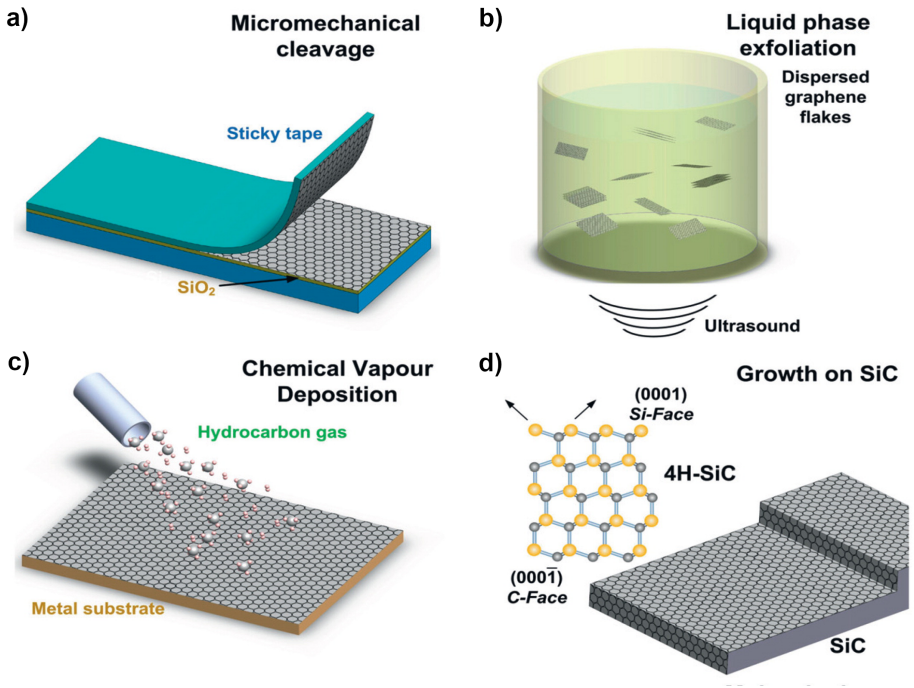

Figure 2.5: Cartoon illustrations of the four dominant methods for graphene production; a) Micro-mechanical cleavage; b) liquid phase exfoliation; c) chemical vapour deposition; d)Si sublimation from SiC. Adapted from Bonaccorso et al. [121].

2829 tonnes per year [56]. In addition, CVD graphene production appears to have reached maturity, at least with regards to area grown. Total world output jumped by between 17- and 18-fold within just two years, between 2015 and 2017, from 210×10^3 m^2 per year to 3700×10^3 m^2 [56]. The huge recent increase in m^2 production of graphene means that methods to reduce production costs should now be highly relevant.

2.2.1 Top-down Synthesis

Top-down synthesis describes processes wherein bulk material is used as the starting point from which the final nano-scale material is extracted. MME and liquid phase exfoliation (LPE) are the current leading top-down synthesis methods within graphene research.

Micro-Mechanical Exfoliation

MME, or the "Scotch Tape method", refers to the peeling of layers from a layered material, such as graphite. To achieve the production of thin films, repeated peeling of material from a bulk crystal is carried out with adhesive tape, before a thinned out area of material is pressed onto the target substrate in the hope that monolayer material adheres to the substrate and can then be used within experiments. This was the method used by Novoselov and Geim to isolate their first graphene films [1], but it is a method which

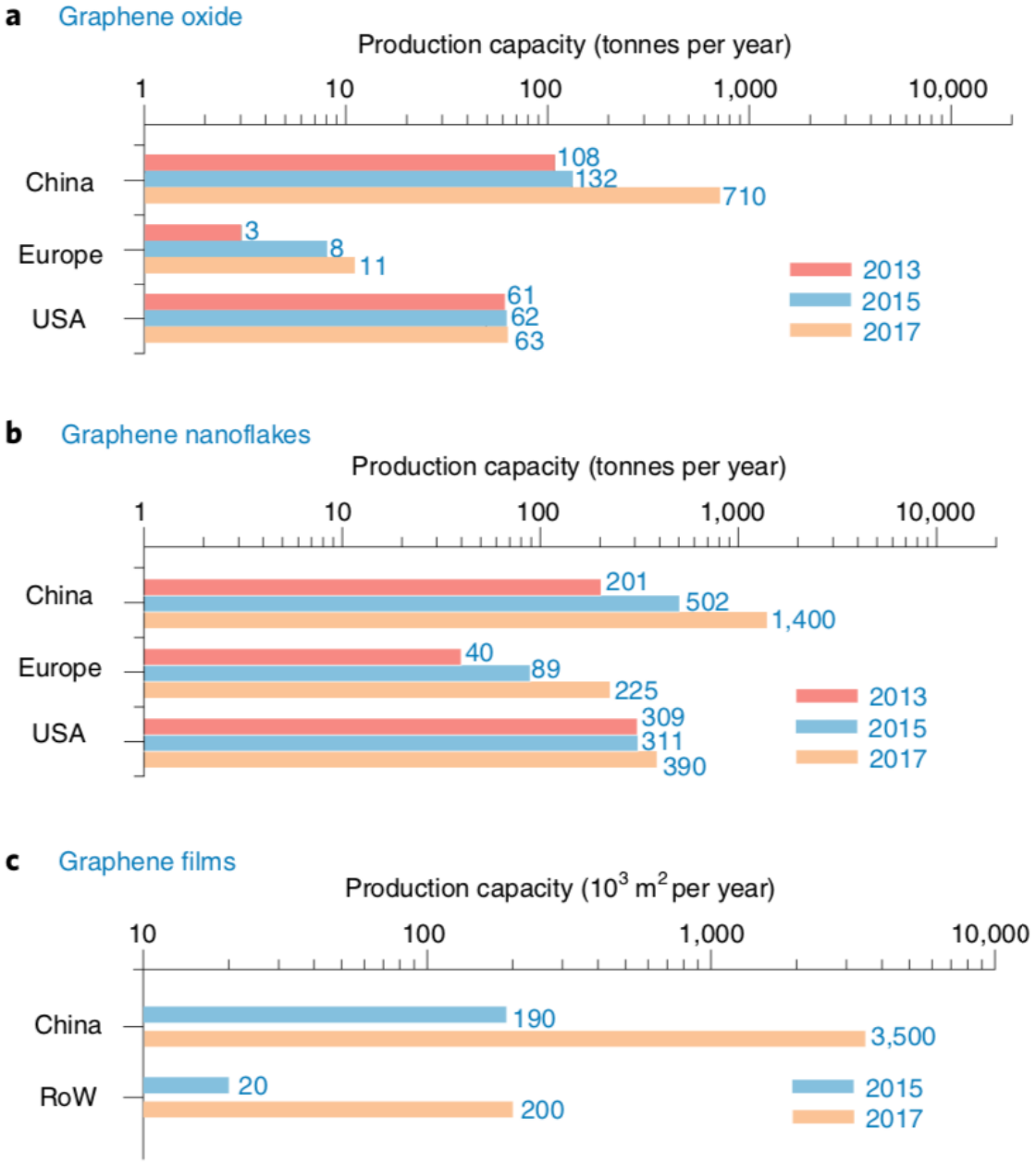

Figure 2.6: Production capacity of commercial graphene products. Annual production capacities of GO (a), graphene nano-flakes (b) and graphene films (c) in different countries and years. RoW represents the rest of world compared to China. Note that the production capacity of SuperC Technology is reported to be over 10,000 tonnes per year. Adapted from Lin et al. [56].

has been known of since at least the 1960s [123]. As graphene produced via MME comes from bulk graphite which has typically low defect densities [124], samples prepared in this way are of very high quality and are used within experiments exploring fundamental physics. However, MME is a low-throughput technique and is of little use outside of the laboratory setting. This is because MME is non-deterministic and flakes of many different thicknesses are produced during preparation. Single layer flakes are typically found

amongst regions of many multi-layer flakes and generally have areas limited to the order of a few 100 µm^2 [125, 126]. Methods such as pre-straining the top few graphene layers to weaken inter-layer bonding have been demonstrated as an option for minor improvement of the technique [125], but regardless, MME remains limited to use within research laboratories when very high quality samples are required.

Liquid Phase Exfoliation

LPE is a solution-based method for the production of large volumes of 2D materials. Rather than separating 2D flakes from the bulk material via peeling, the bulk layered material is placed into a suitable liquid, such as water or a polar solvent, and is agitated to separate the material layers [127]. Due to its inherent scalability, LPE has attracted significant attention, but LPE of graphene and subsequent device fabrication still suffers from a couple of issues: firstly, graphite does not easily form a stable dispersion because of the large interfacial tension between graphene sheets and the majority of supernatants [128]. Secondly, 2D material flakes prepared via LPE are typically sub μm in diameter [127, 128].

The resulting devices created by casting from the prepared graphene suspensions lose many of the exemplary material properties expected of graphene due to junction resistances between the deposited graphene flakes [127], but the use of solution based processing unlocks exciting alternative prospects, such as fully printable and flexible electronics [127, 129]. To address the issue of stabilised graphene suspensions, many early attempts focussed on the dispersion of graphene oxide (GO) [130, 131] or functionalised graphene [132–135] as their interfacial energies more easily allow for stabilised exfoliation and suspension in liquids. However, to regain the properties of graphene, functionalised graphene has to be un-functionalised and GO has to be reduced. Though these methods have met with partial success, the resulting graphene material is always defective and is why reduced graphene oxide (rGO) and functionalised graphene are recognised as distinct materials [3].

Hernandez et al. were the first to demonstrate successful graphene dispersion directly from graphite by sonicating graphite bulk material within N-methyl-pyrrolidone (NMP) as the supernatant [50], but this approach requires the use of an environmentally unfriendly and difficult to remove solvent. Paton et al. then provided an improved method for the production of graphene suspensions from graphite through shear exfoliation of graphite (as well as other bulk 2D materials) in liquids [51]. In contrast to the sonication-based method

demonstrated by Hernandez et al., the shear exfoliation method introduced by Paton et al. allows production of suspensions in volumes of 100 L and greater. Additionally shear exfoliation was shown to work using sodium collate as a surfactant or poly-vinyl alcohol as a polymer matrix meaning that NMP could be removed from the process. A continuation of this process was demonstrated by the Varrla et al. at Trinity College, Dublin, who used a kitchen blender and household detergent to create aqueous suspensions of defect free graphene platelets [136].

2.2.2 Bottom-up Synthesis

Bottom-up synthesis describe methods where small precursor materials are used to grow a film of the desired material. Within graphene research the bottom-up method is dominated by two methods – Si sublimation from SiC and chemical vapour deposition (CVD). Both of these methods are capable of creating wafer-scale graphene films, which are typically $> 95\%$ single layer graphene with areas of two to five layer graphene found at step edges for growth on the Si face of SiC [48, 137], or around growth surface defects for growth via CVD [138]. Bottom-up synthesis is generally regarded as the best option for batch- to mass-scale production of electronic-grade graphene, that is graphene with charge carrier mobilities in excess of 4000 $\mathrm{cm^2V^{-1}s^{-1}}$ [58].

Si Sublimation from SiC

One route to produce continuous, wafer-scale graphene films is via thermal decomposition of SiC. When heated above 1300 °C in vacuum, Si atoms sublime from the outermost layers of a SiC wafer, leaving behind reconstructed layers of graphitic material [46, 139]. Figure 2.7 displays a schematic representation of graphene growth on SiC and displays how a buffering layer forms below subsequent graphene layers for epitaxial growth on SiC [139]. The buffering layer is covalently bonded to the SiC bulk and does not have graphitic properties. In this way, it is possible to create wafer-scale graphene which is compatible with standard semi-conductor processing techniques.

As SiC has a layered structure, comprised of alternating layers of Si and C, wafers are terminated on one face with Si atoms (0001) and on the other with C atoms $(000\bar{1})$. Graphitic layers evolve differently on each face, depending on the terminating species. On the Si face, epitaxial graphene layers follow a stepped morphology, matching the underlying substrate. In addition to the buffer and epitaxial layers, multilayer regions

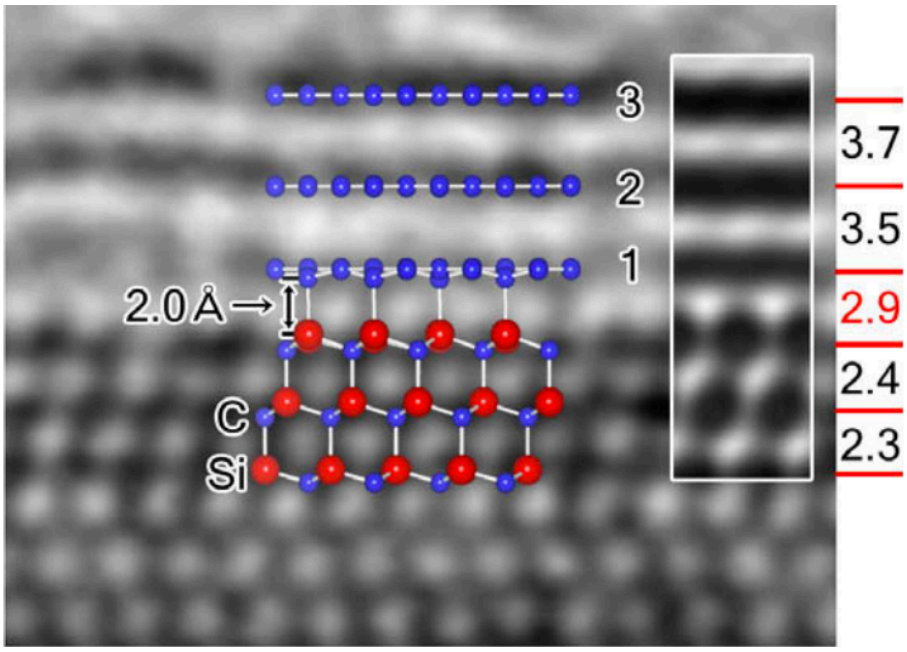

Figure 2.7: Cross sectional TEM with annotation displaying epitaxial graphene grown on SiC, with the covalently bound buffer layer. Taken from Norimatsu et al. [139].

are observed at the step edges of the substrate, as graphene growth on this face nucleates from these points and grows outwards [48]. The single layer regions grown upon the Si face may be continuous along the length of the steps up to a length of, but are limited to only a couple of μm wide due to terrace widths [44]. On the C face, graphitic layer growth remains close to atomically flat, but is polycrystalline, with graphene crystallite sizes of $\approx 1\,\mu$m [140, 141]. Finally, SiC wafers are prohibitively expensive for use as the basis for graphene growth, costing approximately $1200 for a single 6" wafer.

CVD on Transition-metal Films

CVD is the deposition of thin films via the chemical reaction of precursors at, or near, a heated surface on which the film is to be deposited [142] and is currently the foremost method for large-scale monolayer/bilayer graphene production [55, 56]. The graphene CVD process utilises thermal decomposition of hydrocarbons to provide the carbon for graphene film growth. Methane is most common hydrocarbon precursor used, because it allows the greatest control over the carbon partial pressure within the reaction chamber and thus the tightest control of graphene synthesis. However, methane-based graphene CVD requires high working temperatures of 1000 °C or greater for high quality graphene growth [143]. Investigations into the use of other precursor materials have shown promise for reducing processing temperatures (ethane [144], ethanol [145], solid sources [146]), increasing graphene film growth rates [144, 147], or creating pre-patterned graphene films

(PMMA [148]), but the resultant graphene quality is typically lower than films grown with methane at elevated temperatures. As a counter example, Chen et al. demonstrated high-quality CVD growth of graphene using ethanol as the hydrocarbon precursor, but growth was carried out at 1065 °C, indicating that elevated temperatures promote improved graphene quality [68].

Most graphene CVD uses a transition-metal foil in a dual role, as the catalyst for precursor dissociation and as the supporting surface for graphene film growth. The inclusion of a catalytic surface is necessary, particularly for methane based CVD, as it reduces the required temperature for methane dehydrogenation from 1200 °C to below 900 °C. A wide variety of metals have been investigated, with large area single crystal graphene domains, with diameters exceeding 1 mm, being achieved on Pt [149], Ir [150] and Cu [58].

Due to cost and the ease of post-graphene-growth etching of the supporting metal, Ni and Cu are the most widely investigated metals for use as the supporting foil within graphene CVD. Of these two, copper has emerged as the current favoured metal to use as a catalyst and support during graphene synthesis because the solubility of carbon within copper is atypically low for transition metals at 0.001 - 0.008% weight at 1083 °C [60, 61]. In contrast, the carbon solubility within nickel is much more typical at 0.3% weight at 1000 °C [151]. The difference in carbon solubility within copper and nickel results in different growth pathways for graphene during CVD [62, 152]. Figure 2.8 displays a schematic representation of the different graphene growth pathways for a) nickel and b) copper [62]. Because of the high carbon solubility within nickel, dissociated carbon species diffuse into the nickel first before segregating and precipitating to the surface. This results in highly polycrystalline graphene, formed from small graphene crystallites of only a few μm across, with a many multilayer regions [62, 152]. In contrast, the low solubility of carbon within copper means that carbon fragments are predominantly confined to the surface of the copper foil which leads to surface mediated graphene growth, which promotes the growth of monolayer graphene [59, 62] with domains diameters often in excess of 100 µm [70, 75, 153–155]. Additionally, graphene growth on copper is self-terminating at the point of full monolayer coverage, due to catalyst poisoning by the graphene film [59]. The interactive behaviour between carbon and copper naturally provides a low-effort route to large-scale monolayer graphene, and as homogeneous monolayer graphene is highly desirable for its electronic properties, it is easy to appreciate why copper has become the preferred metal of choice for graphene CVD. Because methane and copper are the predominantly used precursor and catalyst respectively, the rest of this section will focus

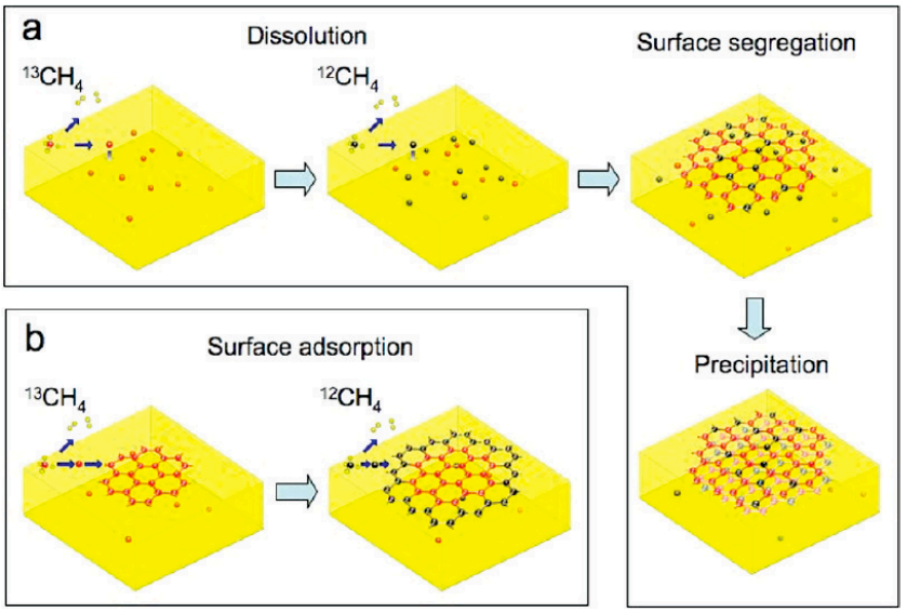

Figure 2.8: Schematic diagrams of the possible distribution of C isotopes in graphene films based on different growth mechanisms for sequential input of C isotopes. (a) Graphene with randomly mixed isotopes such as might occur from surface segregation and/ or precipitation. (b) Graphene with separated isotopes such as might occur by surface adsorption. Taken from Li et al. [62].

on methane-based, copper catalysed graphene CVD.

2.2.3 Copper Catalysed Graphene CVD

Copper catalysed CVD recipes essentially follow the protocol by Li et al. [59]. Advances in understanding of the underlying growth mechanisms mean that modified recipes are now capable of producing continuous graphene films with individual domain dimeters of 1 mm or greater [58]; a significant increase from the domain diameters of 5 - 10 μm reported within the Li paper [59]. Domain diameter is important within graphene CVD, as the electronic properties of the resultant films are closely related to the density of grain boundaries within the film [79, 81, 82, 156]. To produce a continuous graphene film whilst reducing the grain boundary density requires increased domain area, or diameter. This also requires reduced nucleation density. Therefore, much of the copper-catalysed graphene CVD research to date has focussed on maximising domain size and minimising domain density and CVD graphene quality is often referred to against these metrics.

Before discussing the parameters which can tailor graphene CVD growth behaviour, a conceptual framework is introduced within which the results can be discussed. Figure 2.9 displays a cartoon representation of graphene domain morphology and its relation to J_{flux}, which is the total influx of carbon fragments incident on a growing graphene

domain, and J_{edge} which is the relaxation diffusion rate of newly attached carbon species around the edge of a growing graphene domain. The conceptual model is primarily based upon the research of Wu et al. [157, 158], which demonstrates the evolution of graphene domain morphology as a function of H_2 partial pressure, thus varying the relationship between J_{flux} and J_{edge}. The factors influencing J_{flux} are discussed below; it is assumed that J_{edge} remains approximately constant, regardless of conditions.

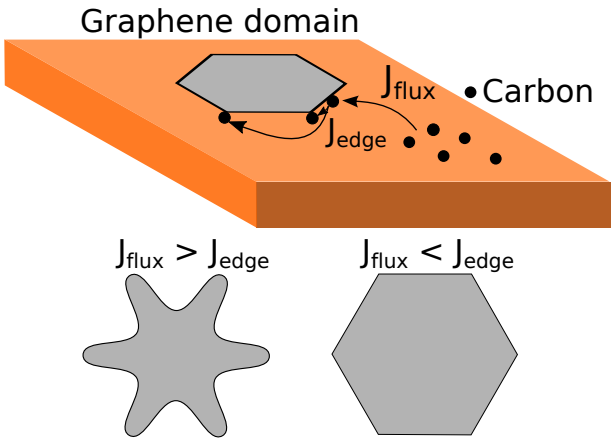

Figure 2.9: Cartoon schematic of the effect on the relationship between the rate of incident carbon fragments (J_{flux}) and relaxation rates of newly attached carbon fragments around the graphene domain edge (J_{edge}) on graphene domain morphology.

Influence of Methane Partial Pressure

Within methane-based copper-catalysed graphene CVD, the methane is used as the carbon precursor for the growth of graphene films. Increasing the methane partial pressure leads to more rapid completion of the graphene film [159], but also increases the graphene nucleation density by increasing the probability of carbon supersaturation at the copper foil surface [160]. Early production of large diameter graphene grains used reduced methane partial pressure to reduce domain density which was then followed by extended growth periods under tightly controlled conditions. Such growth is demonstrated within the research by Chen et al. [161] where a 6 hour growth was used to grow isolated graphene domains 1 mm across.

Returning to the J_{flux}/J_{edge} model, an increase in methane should increase J_{flux}, and should lead to increasingly lobed behaviour. However, as demonstrated within Chapter 4 there are limits beyond which our model framework no longer applies, and at H_2:CH_4 ratios of $\sim$ 5:1 or lower, the methane content is large enough to cause graphene to nucleate and grow so rapidly that compact but irregular domains are formed.

Influence of Hydrogen/Methane Ratio

Hydrogen was originally included to provide a protective reducing atmosphere within the reactor for the growth of the graphene film [59]. However, hydrogen has been found to have profound effects upon graphene growth and the ratio of H_2:CH_4 within the reaction space is known to have a considerable effect on the resultant domain size, density and morphology.

Increasing the partial pressure of hydrogen within the system reduces the graphene domain nucleation density [162]. The graphene domain morphology is also affected by hydrogen partial pressure [157, 163, 164], with increasing partial pressure resulting in the growth of more compact domains and reduced H_2:CH_4 creating dendritic domain morphology.

Both of these effects can be explained via the chemical equilibrium between solid graphene and gaseous CH_4 within the reaction space [157, 164], described by Equation 2.8 [164]:

$$CH_4(g) + (*) \rightleftharpoons C(ad) + 2H_2(g) \tag{2.8}$$

If more hydrogen is introduced into the system, this pushes the carbon equilibrium away from surface adsorbed carbon (graphene) and towards gaseous carbon (CH_4). In this way, both the reduction in nucleation density and the reduction in domain dendricity can be explained. Nucleation density reduction is explained by the reduction of adsorbed carbon species on the copper surface, which reduces the likelihood of carbon supersaturation and thus domain nucleation.

Domain morphology can be explained via a similar logic and returning again to the J_{flux}/J_{edge} model, increasing H_2 within the system reduces surface bound carbon. This naturally reduces J_{flux} and leads to the formation of increasingly compact domain morphology Such an effect is displayed in Figure 2.10 wherein the hydrogen partial pressure is increased from panel a) to panel l) and results in increasingly compact domain morphology [157].

Hydrogen has been described as a weak etchant towards graphene. However, the etching of graphene by hydrogen can be explained by the shifting of the equilibrium described in Equation 2.8 to the left, by the presence of superfluous hydrogen within the system, causing carbon to exist preferentially as gas (CH_4). Kraus et al. demonstrated this by growing a graphene domain and then changing the reactor atmosphere by increasing the partial pressure ratio of H_2:CH_4 ($w = p(H_2)/p(CH_4)$) such that the preferential carbon

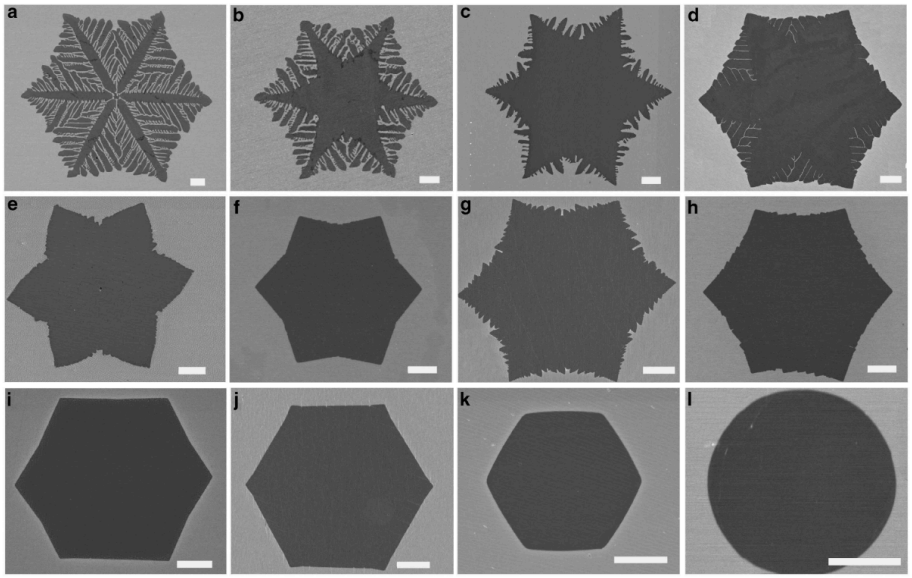

Figure 2.10: Typical SEM images of separated GFs under different conditions. All scale bars are 5mm. Taken from Wu et al. [157].

phase became gaseous CH_4. The result of their experiment is displayed in Figure 2.11, where it is clearly observed that hexagonal voids have begun to etch away from the grown graphene domain because of the shift in chemical equilibrium.

Finally, whilst the etching and inhibitive effects of hydrogen within the reaction space have been discussed above, it is worth mentioning that there is also evidence of hydrogen acting as a co-catalyst [163]. The preliminary study by Vlassiouk et al. [163], within which

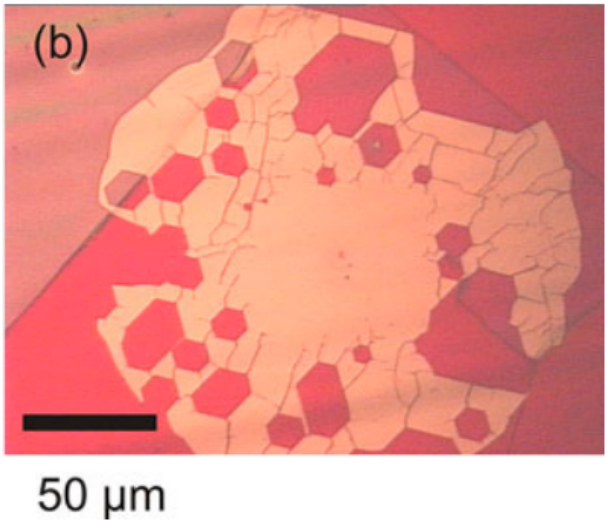

Figure 2.11: Optical image of a graphene flake after 2 hour CVD growth at $p(H_2) = 25$ mbar and $w = 1000$, where $w = p(H_2)/p(CH_4)$. Before finishing the CVD experiment the reactive atmosphere was changed and the sample was exposed to $p(H_2) = 60$ mbar at $w = 3000$ for further 30 min. As clearly seen in optical microscopy, the rim of the graphene flake turned into a circular shape and hexagonal holes were etched into the inner part of the flake, i.e. the decomposition of the previously grown graphene flake is clearly observed. Taken from Kraus et al. [164].

the initial increase in domain growth rate with increasing hydrogen content was elucidated, posited that monatomic hydrogen radicals assist the dehydrogenation of methane thus leading to the observed enhancement of graphene domain growth.

Influence of Oxygen

Tuning the partial pressures of hydrogen and methane provide a method for reducing the domain density. However, ultra-low domain densities achieved via H_2:CH_4 adjustment typically require lengthy growth periods of multiple hours which are not compatible with mass scale production [161]. The inclusion of trace amounts of oxygen at different stages within the CVD process provide further routes for reduced nucleation density and increased domain growth rate [66, 70, 154, 164, 165]. Figure 2.12 displays a schematic representation of a typical CVD growth cycle, with the different stages of ramping, anneal, growth and cooling indicated.

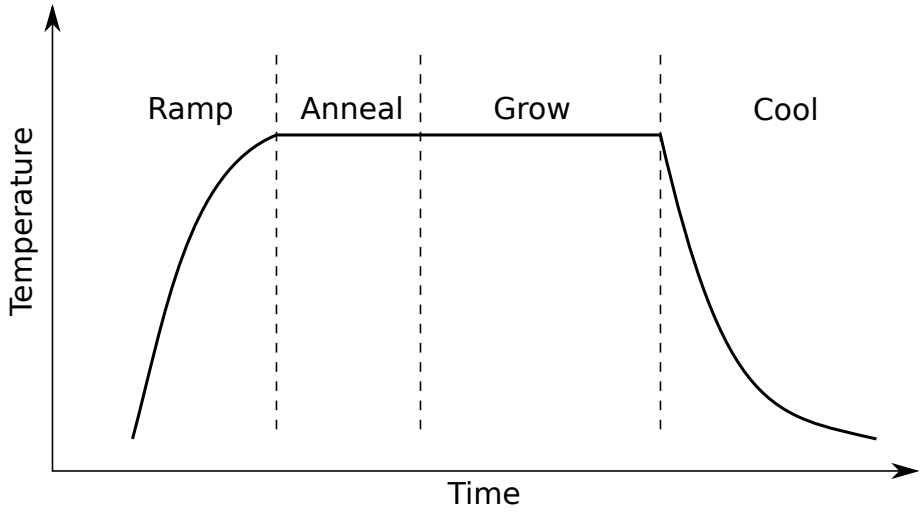

Figure 2.12: Diagramtic illustration of the temperature profile used throughout hot-wall graphene CVD process, with different stages labelled.

During the ramping and anneal stages, oxygen has the effect of removing carbon from the copper growth foils whilst forming an oxide surface on the foil [154, 164]. By removing carbon out of the foil prior to the injection of methane, it is ensured that no locations on the foil are close to carbon supersaturation, required for graphene domain nucleation, prior to methane introduction.

During the growth phase, residual oxide on the copper surface passivates nucleation sites which would otherwise promote supersaturation, due to an increase in available metal d-orbitals. Because the oxygen atoms occupy d-orbital dense regions instead of carbon, supersaturation is inhibited and graphene domain nucleation is reduced [70].

Oxidation of the copper foil surface prior to growth also increases graphene growth rate during the growth stage and domain dendricity. Using the J_{flux}/J_{edge} model, this can be explained by the increased mobility of carbon fragments on the copper surface, which is due to the removal of carbon trapping defects because of oxygen occupation of nucleation sites, which results in an increase in J_{flux}.

Buffering Gas

Many modern CVD recipes dilute methane and/or hydrogen within an inert buffering gas due to either safety concerns for the mitigation of explosions [58, 85], or to allow a reduction of precursor flow rate, typically CH_4 to provide fine control on graphene growth. Wu et al demonstrated successful growth of continuous graphene with mm-scale individual domains by diluting methane and hydrogen below their lower explosive limits (LEL) (5% and 4% respectively) within argon [58]. Dilution of explosive precursors below their LEL largely mitigates safety concerns surrounding explosive gas leaks. Indeed, with a more direct view to mass production, Zhong et al. [85] investigated roll-to-roll manufacturing of graphene using an open ended tube furnace arrangement. To avoid ambient influx through the open ends of the furnace, the reaction chamber pressure was maintained above atmospheric pressure by flowing a superfluence of buffering gas, along with the reactants, into the reaction chamber. Due to cost considerations, the buffering gas used in this instance was nitrogen, rather than the almost universally used of argon.

Within CVD graphene growth, the buffering gas should not be chemically involved in the graphene growth process. Wu et al. [157] demonstrated that the use of helium and argon produced qualitatively similar graphene growth, which suggests that the choice of buffering gas is non critical. However, the only inert gas which is cheaper than argon is nitrogen – hence the decision by Zhong et al. [85] to use nitrogen within a high flow scenario – but N_2 is not monatomic. This means that there is a risk of N_2 dissociation when a high energy environment is used and it is likely that this is the primary reason that very few groups report the use of N_2 within a graphene CVD setting. The likelihood of N_2 dissociation within a hot-wall graphene CVD set up is low however, due to the binding energy of 9.76 eV between nitrogens within N_2 [86, 88]. This assumption seems to hold, as no significant signal for nitrogen doping was observed within CVD graphene grown by the few groups to have used nitrogen as a buffering gas [85, 166], although it must be mentioned that none of these studies carried out extensive spectroscopic investigations to

confirm the presence of nitrogen within their films.

2.3 Graphene Doping

Graphene is a 0-bandgap semiconductor, meaning there is no band gap between the conduction and valence band, but also no overlap between the conduction and valence bands [2]. This is illustrated within Figure 2.13, which displays a plot of graphene's density of states (DOS). E = 0 is defined at the Dirac point, which means that the Fermi-level of pristine graphene lies exactly between the valence and conduction bands and that the DOS is infinitesimally small at the Fermi-level of pristine graphene. The touching of valence and conduction bands means that graphene is electronically flexible. By modifying the band structure of graphene through heteroatom substitution to the graphene lattice [167–170], or through the formation of nanoribbons [171], graphene can be changed to behave as a small band-gap semiconductor. Alternatively, the position of the graphene's Fermi level can be altered via charge transfer between graphene and adsorbants, to p- or n-dope the graphene channel [172, 173], as illustrated by the arrows and representative I_{ds}/V_g plots in Figure 2.13. Shifting the Fermi-level in this way changes the electronic behaviour of graphene to pseudo-metallic, increasing graphene's conductivity, due to an increase in the available states.

2.3.1 Substitutional Doping

Substitutional doping of graphene involves exchanging carbon atoms within the graphene lattice with alternative atom species. Nitrogen (n-doping) and boron (p-doping) are used as substitutional dopant atoms within graphene as they have similar atomic volumes to carbon whilst having one extra or one fewer electron respectively [174]. However, the inclusion of substitutional heteroatoms within the graphene sheet disrupts the crystal structure of intrinsic graphene, creating polar regions within the graphene sheet [175] and also, in many cases, the loss of additional carbon atoms from the graphene lattice [168]. This means that the linear dispersion around the K-point within the Brillouin zone no longer exists and therefore the graphene sheet loses many of its exceptional electronic properties.

Substitutional doping of graphene has been explored in a bid to create analogues of classical p-n field effect devices from graphene [169, 176–179], to create an electronic band

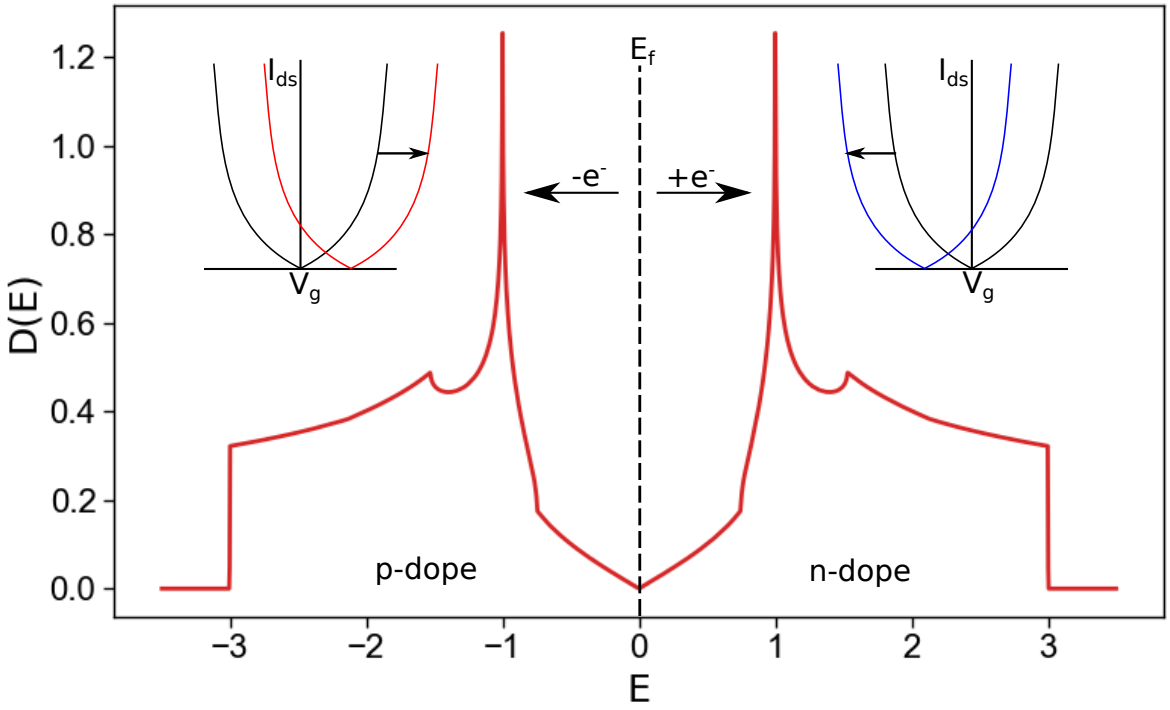

Figure 2.13: Annotated DOS diagram for graphene. Effective addition of negative charge to the graphene sheet n-dopes the graphene channel, shifting E to the right and the graphene I_{ds}/V_g curve to the left, as shown at the right hand side of the figure. Conversely, effective removal of negative charge from the graphene sheet shifts E left and the I_{ds}/V_g curve right.

gap within graphene [167, 180], to alter the electronic [176, 178, 181] and electrochemical properties of graphene [35, 182, 183] or to increase chemical sensing capabilities [35, 183, 184].

As a significant section of this thesis is concerned with unintentional inclusion of nitrogen into the graphene lattice during CVD, it is important to understand the markers associated with nitrogen-doping of the graphene lattice. Nitrogen substitution into the graphene lattice results in the addition of approximately 0.5 electrons per nitrogen to the graphene sheet [167, 185, 186], except in the case of H-free pyridinic nitrogen substitution [186]. Boron doping shares many similarities, although the electronic signature is the reverse of nitrogen doping [180].

Of more interest to this research is the investigation of nitrogen substitution into the graphene lattice via spectroscopic methods, as atmospheric p-doping of transferred CVD graphene can obscure the electronic signature of nitrogen inclusion. There are two widely used spectroscopic methods within this field which are Raman spectroscopy and X-ray photoelectron spectroscopy (XPS). Raman spectroscopy is not directly chemically sensitive, but can be used to investigate the doping, strain and carbon vacancy density

of graphene [175, 179]. As nitrogen inclusion typically results in the creation of carbon vacancies, the carbon vacancy densities can be used as an approximation of nitrogen inclusion, if calibrated against a chemically sensitive, quantitative technique such as XPS [168, 178, 179, 187]. XPS has been used extensively to study nitrogen content in intentionally N-doped graphene [168, 179, 187–189] and is able to detect the presence of nitrogen within the graphene lattice at concentrations of ~ 0.3 at% [190, 191].

2.3.2 Adsorbate Doping

Another form of graphene doping is caused by adsorbates which cause local field disruptions through charge exchange interactions. Adsorbates physisorb or chemisorb on the graphene surface, which results in partial or full charge transfer, respectively, between the graphene and the adsorbate [173].

Unintentional Dopants

In the context of CVD graphene devices, undesirable adsorbates often originate from the transfer process required to remove the graphene from its growth surface for use on a dielectric substrate [192]. Residues from the polymer support layer typically used during graphene transfer are a major source of p-doping and charge mobility reduction within graphene devices [192, 193] and as such, considerable research has been carried out to find methods for minimising or removing polymer residues. Additionally, as most transfer protocols use a wet etch to remove the growth substrate, followed by a water rinse, trapped water between the graphene film and the target substrate contribute to p-doping and charge carrier mobility reduction of the overlying graphene channel [194–197].

A number of different approaches have been investigated to combat unwanted graphene adsorbates originating from the transfer process. Annealing of graphene films within a high-vacuum or reducing environment [193] can improve the properties of transferred CVD graphene by removing adsorbates via pyrolysis or evaporation. However, Tripathi et al. recently demonstrated how the extended annealing treatments required to fully remove transfer-related adsorbates have been found to cause the graphene film to crack and tear [198].

Methods to reduce the the number of adsorbates from the transfer process have also been investigated, with many focussing on alternative polymers or supporting layers for improved support removal. For instance, both Lafkioti et al. and Hu et al. demonstrated

reduced p-doping and increased charge carrier mobility within GFET devices by treating the target substrate with hexamethyldisilazane (HMDS) prior to transfer to make the surface hydrophobic and thus reduce or eliminate trapped water underneath the graphene sheet [196, 197]. Hallam et al. demonstrated that the use of nitrocellulose, which is more easily solvated than the typical poly(methyl-methacrylate) (PMMA) [199]. More recently, Zhang et al. demonstrated graphene transfer through the use of rosin which naturally sublimes in an ambient atmosphere, thus ultimately leaving the transferred graphene clean [200]. A similar strategy was employed by Belyaeva et al. who used cyclohexane as a support layer by leveraging the difference in freezing points between water and cyclohexane to provide a liquid/solid/liquid supporting material within the etching/transfer/support removal stages [201]. This approach has the advantage of allowing the strain within the graphene sheet to relax prior to transfer but requires very tightly controlled temperatures to succeed. Paraffin has also been demonstrated as an effective transfer support by Leong et al., due to the ability of paraffin's thermal expansion to remove wrinkles within the graphene prior to transport and the fact that paraffin is a short chain alkane which does not strongly interact with graphene, thus resulting in flat, largely residue-free transfer [202].

Intentional Dopants

Beyond undesired adsorbates, the creation of hybrid graphene/nanoparticle structures provides a route towards tailoring GFET-based device properties. Many different graphene/particle systems have been explored with most based upon decoration of the graphene sheet with metal or metal-oxide nanoparticles.

For example, Lee et al. found that the deposition of Ag (Au) nanoparticles on graphene induced n- (p-)doping of the underlying graphene sheet [203], whilst in a contradictory study, Huh et al. reported that the application of Au nanoparticles produced n-doping of the graphene channel [204]. A first principles study by Khomyakov et al., suggested that the doping of the graphene sheet by a physisorbed metal such as Cu, Au or Ag is related not only to the work function of the metal but also the separation between the graphene and metal and may provide an explanation for this discrepancy, although it must be noted that within this work, Au was found to only act as a p-dopant towards graphene [173, 205]. Figure 2.14 displays Khomyakov's results on the alteration of the graphene Fermi level by physisorbed metals at separations of the graphene monolayer

van-der-Waals thickness of 3.3 Åand at a long-range separation of 5 Å [173]. Within this plot, the work function of graphene covered metal is denoted by W and W_G refers to the work function of freely standing graphene [173]. It is interesting to note that even though the work functions of Ag and Cu are greater than the surface chemical potential of graphene, direct contact between graphene and Cu or Ag should result in n-doping of the graphene sheet.

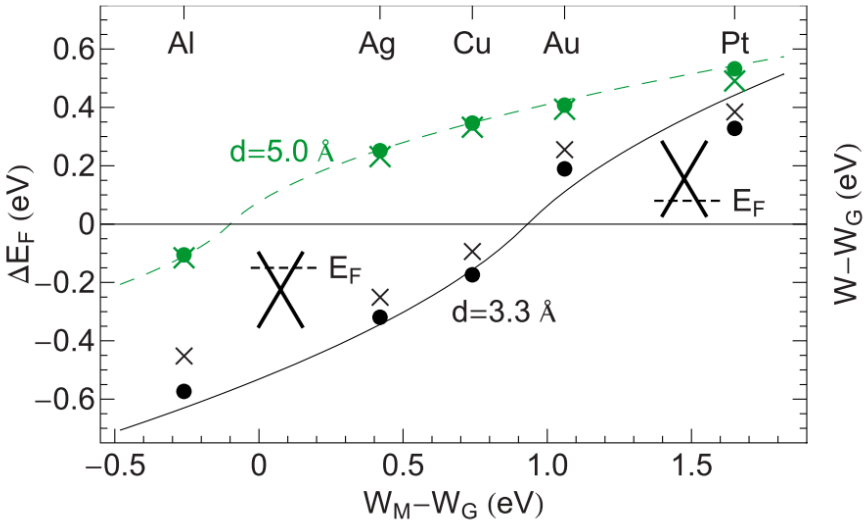

Figure 2.14: Calculated Fermi energy shift with respect to the conical point, ΔE_F (dots), and W - W_G (crosses) as a function of the clean metal-graphene work-function difference W_M - W_G. W denotes the work function of graphene-covered metal. The lower (black) and the upper (green/gray) points are for the equilibrium (d $\sim$ 3.3 Å) and large (d = 5.0 Å) graphene-metal-surface separations, respectively. The insets illustrate the position of the Fermi level with respect to the conical point. The units and increments on the RH axis are the same as those displayed on the LH axis. Taken from Khomyakov et al. [173].

Graphene-nanoparticle systems have also been explored using a wide variety of non-metal particles. Meyer et al. demonstrated efficient charge injection/extraction into OLED devices using a MO_3/graphene double layer [206], wherein MO_3 was found to p-dope the graphene layer. Z. Zhang et al. demonstrated the use of SnO_2 nanoparticles [207], whilst D. Zhang et al. demonstrated the use of ZnO nanoparticles [208] to create GFET-based gas sensors sensitised towards H_2 and CH_4 respectively. In fact gas sensors based on graphene/metal oxide nanoparticle hybrid devices are an active area of research, with Singh et al., Kodu et al. and Song et al. demonstrating ppm detection of CO and NH_3, NH_3 and propanal respectively [37, 209, 210]. In addition, semiconductor nanoparticles [98, 211, 212], poly-oxy-metallates(POMs) [213] and 2D materials such as MoS_2 or graphene oxide [40, 214] have been applied within hybrid graphene-particle architecture, with all efforts aimed at increasing the chemical sensitivity of the underlying graphene

architecture.

2.4 Gas Sensing

Because of the atomic thinness, high specific surface area, low charge carrier density and low electronic noise of graphene [33, 39, 215], it should be an exceptional material for chemical or gas sensing [216, 217]. Typically graphene based sensors are based upon FET architecture [39, 217], as displayed in Figure 2.15. If prepared correctly, small changes in charge carrier concentration within the graphene sheet, resulting from charge transfer interactions between the analyte and the graphene sheet, can produce appreciable resistance changes of graphene devices [218]. In exceptional circumstances, it is possible to detect the adsorption and desorption of single molecules using a pristine graphene device as demonstrated by Schedin et al. [33], although it must be mentioned that to achieve this detection a Hall device geometry was used, which would be impractical for most applications. As well as extreme sensitivity, one of the major appeals of graphene-based sensors is the reduced device power consumption, because graphene-based devices can operate at lower temperatures [219] than the 200 °C – 500 °C operating temperature range required by metal-oxide gas sensors [217].

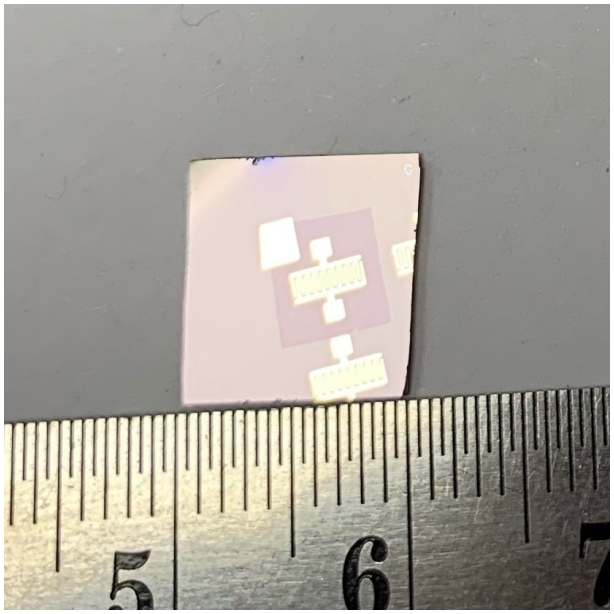

Figure 2.15: Image of a typical interdigitated GFET on 80nm SiO_2, used as the basis for graphene-based gas sensing device architecture. The contacts are Au evaporated through a shadow mask over pre-transferred graphene.

The detection of gases by graphene-based devices is mainly through observation of conductance changes upon the adsorption of analyte species. However, due to the low

density of defects and therefore low density of chemically active sites within the graphene basal plane, species adsorbed on graphene interact through physisorption, rather than chemisorption. Leenaerts et al. demonstrated, through DFT simulations, that even polar molecules, such as NO_2, which strongly physisorb to graphene, only charge exchange the equivalent of $0.1e$ per NO_2 molecule [172]. Because of the small exchange interaction between graphene and physisorbed species, the cleanliness of the graphene used within gas sensors has a significant effect on device sensitivity. Figure 2.16 displays results recorded by Guay et al., which demonstrate the effect of poly-(methyl-methacrylate) (PMMA) residue density on the response and reproducibility of graphene based gas sensing [218]. Reduction of PMMA residue density on the graphene sensor surface, achieved first via acetone rinse and subsequently by sample baking for extended periods shows marked improvement not only to device sensitivity, but also to device baseline recovery which is extremely important for successfully reproducible gas sensing behaviour.

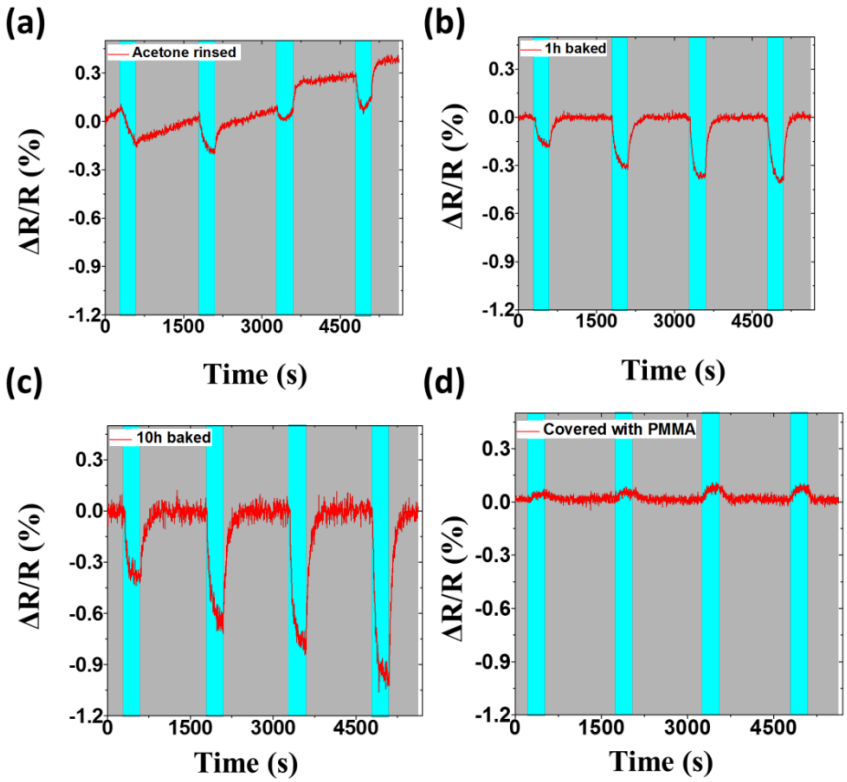

Figure 2.16: Evolution of resistance as a function of time for graphene sensors that have had the following surface treatments (a) rinsing in acetone (b) baking in forming gas for 1h (c) baking in forming gas for 10h. (d) Graphene sensor covered with 60 nm PMMA. The sensors were exposed to concentrations of 1400, 2730, 4000, and 5200 ppm, respectively in this order. Note that a baseline was subtracted from the data for clarity. Image taken from Ref [218].

Chemisorption on the other hand results in the charge exchange of $1e$ either from or to

the chemisorbed specie, due to the ionic or covalent nature of chemisorption. One route, which is garnering much interest is the improvement of the sensitivity and selectivity of CVD graphene based sensors through the use of catalytic particles to create hybrid graphene/particle systems [36, 40, 93, 94, 98, 208–210]. The basic principle is to leverage the increased interaction strength of chemisorption, using an appropriately selected metal or metal oxide nanoparticle, whilst providing a highly conductive transport layer for charge transport with the underlying graphene film.

A number of graphene/nanomaterial hybrids have been demonstrated for increased sensitivity towards both oxidising and reducing analytes; a number of examples are given below. NO_2 detection at 10 ppm was demonstrated at room temperature by Dimicoli-Salazar et al. through the use of Ge quantum dots deposited onto a CVD graphene [98]. Even greater sensitivity to NO_2 was achieved by Hong et al., who reported sub ppm detection of NO_2 over a wide temperature range of 25 °C to 200 °C through the use of MoS_2 decorated CVD graphene [40]. Detection of NH_3 at a concentration of 58 ppm at room temperature was demonstrated by Gautam et al. via gold-decorated CVD graphene [36], whereas Kodu et al. showed further improved detection of NH_3 at a concentration of 0.1 ppm through the use of V_2O_5 on graphene [209]. Zhang et al. used ZnO/rGO hybrid sensors to achieve CH_4 sensitivity of 100 ppm at an operating temperature of 190 °C [208], and although not gas sensing, Salvo et al demonstrated pH sensing within an aqueous environment through the use of undecorated graphene chemisistors [94]. Further examples of NO_2 detection [37, 92, 101, 111], NH_3 detection [37, 111], H_2 detection [113, 207, 220], CH_4 detection [221], CO detection [37] and solvent detection [222], demonstrate that graphene-particle hybrid systems have significant potential for next generation gas-sensing devices, whilst the hither-to scatter-gun approach within this nascent research field suggests that methodical studies of different graphene-particle systems would be of significant merit.

Chapter 3

Methods

3.1 Fabrication

3.1.1 CVD

Graphene is grown throughout this project within a hot-wall CVD reactor. The distinction of reactor heating method is of importance to results presented within Chapter 5, as the presence of a heating element within the reactor chamber may lead to N_2 dissociation and consequently graphene film doping. There are two classes of reactor which use heating elements to provide energy to the reactor space and are known as hot-wall (HWR) and cold-wall reactors(CWR). HWRs use a heating element external to the reaction space to provide temperature control, whereas CWRs employ an internal element to provide local heating to a specific area within the reactor. As only a small area requires heating within CWRs, CWR reactor design tends to be more compact. Heating and cooling of the reaction area can also be achieved much more quickly within CWRs than within HWRs as the thermal mass of the heating unit is reduced. However, the large thermal gradient between the heated area and the cold walls of the reactor can lead to inhomogeneous heating near the reaction surface. The reduced volume of the reactor space also often leads to turbulent gas flow, which again causes reaction heterogeneity across the reaction area [223]. Both of these effects are detrimental for homogenous graphene growth. Whilst heating within HWRs requires more energy, the HWR design provides stable, homogeneous heating throughout the reaction zone and the long tubular shape ensures approximately laminar gas flow throughout the reaction zone [223, 224]. This is important for reproducibility of results. The reproducibility of furnace behaviour means that hot wall tube reactors are widely employed within the field of graphene CVD research

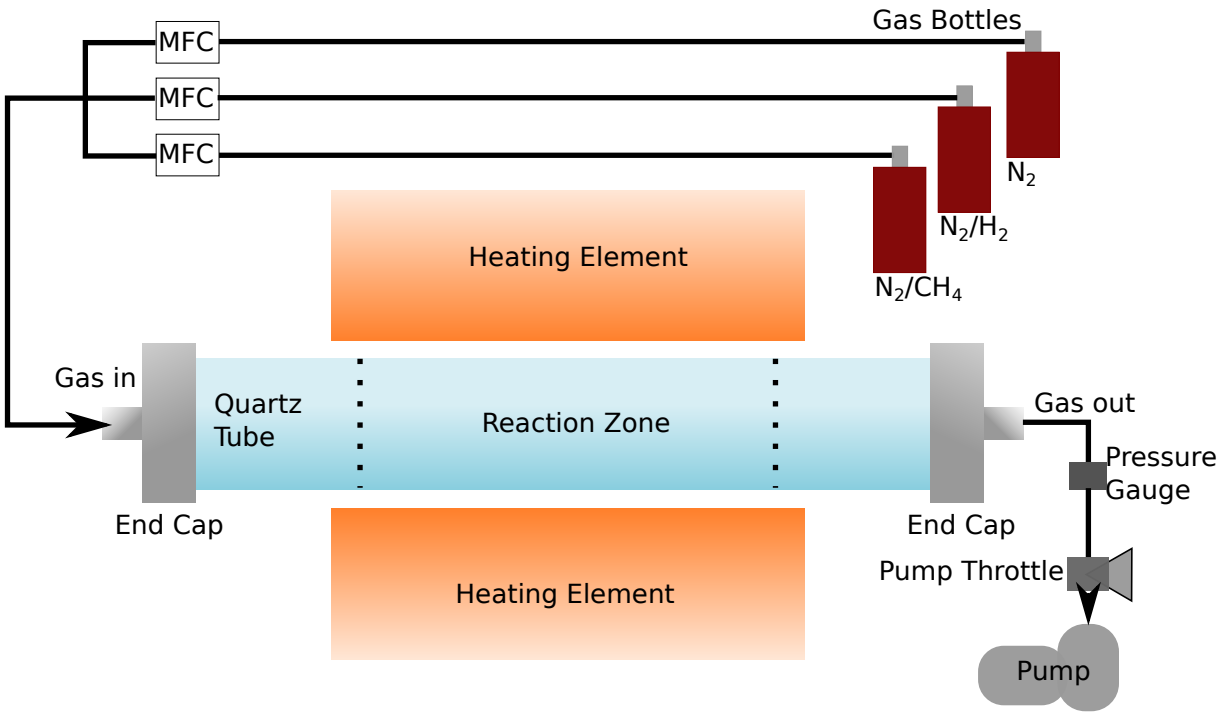

Figure 3.1: A schematic representation of the tube CVD reactor used within this work.

[58, 63, 64, 68, 85, 152, 225] and is why a HWR is chosen for the research presented within this thesis.

A schematic representation of the CVD reactor and its control systems are displayed in Figure 3.1. The reactor space is a quartz tube which is ~ 2 m in length from end-cap to end-cap, with an internal diameter of 50mm and an outer diameter of 54mm, which is fed through the middle of a Carbolite 3-zone tube furnace. The Carbolite furnace, placed at the middle of the quartz tube length is 750 mm long with an external diameter of 350 mm, and has an internal bore of 60 mm. The end zones of the Carbolite furnace are controlled by a pair of Eurotherm 2132 temperature controllers. These are slaved to the central zone which is controlled by a Eurotherm 3216 temperature controller. As the reaction space must be isolated from the ambient atmosphere, end-caps were designed to adapt between the quartz reactor tube and KF fittings. A nitrile O-ring is compressed between the end-cap body, a back "collar" and the quartz tube to create a seal. These joins have been measured to have a leak rate of less than 1.38×10^{-3} mbar.L.s^{-1} for the system used within this research. Gas flow from each bottle into the reactor is regulated a by MKS G-series mass-flow-controller (MFC) with analog control input on each gas line. Within standard operation, three gas lines are used. The MFCs used for the research presented within this thesis have flow rates of 1000 standard cubic centimetres per minute (sccm) on the nitrogen and nitrogen/hydrogen line and 200 sccm on the nitrogen/methane line. These

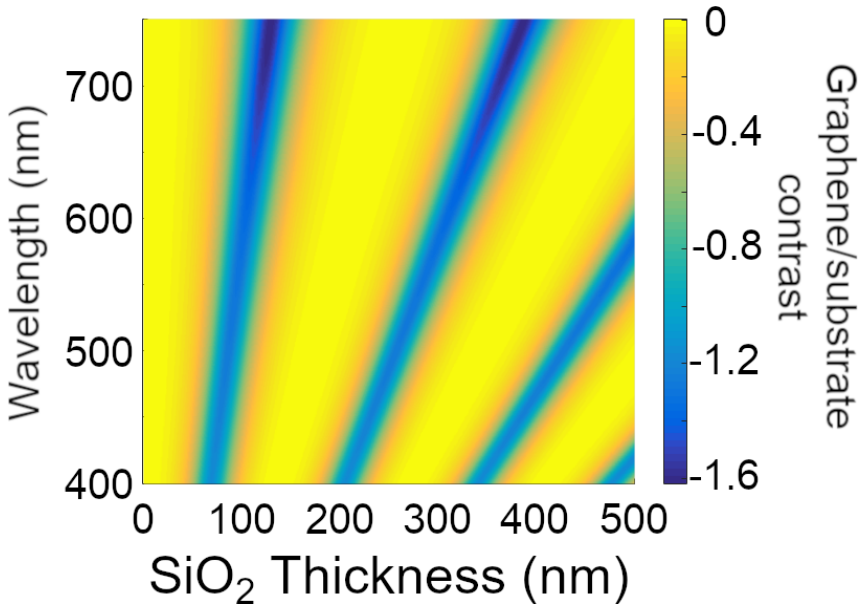

Figure 3.2: Colour map of graphene/substrate contrast for graphene placed on top of SiO_2 capped Si as a function of illuminating wavelength and SiO_2 thickness.

flow rates were selected to provide the widest possible operating window, whilst following flow rates reported by various groups within the literature [58, 63, 64, 68, 85, 152, 225]. In general, large graphene domains (domain diameter in excess of 100 µm) are achieved with high hydrogen:methane ratios, and so MFCs were selected to provide the option of tuning the hydrogen:methane ratio from 1:20 through to 250:1.

3.1.2 Polymer Assisted Graphene Transfer

Within this research, graphene is grown on copper foil. In order to investigate the graphene's properties, it is best to separate the graphene from its metal growth substrate and place it on a suitable insulating substrate.

The insulating substrate used most frequently throughout the research presented here is thermally grown SiO_2 on Si, with SiO_2 thicknesses of 85 ± 5 nm or 295 ± 10 nm as these provide the optimum optical contrast for a single layer of graphene placed on top of the bare substrate [21]. Figure 3.2 displays a colour map of the optical contrast between a single layer of graphene and the underlying SiO_2 on Si substrate as a function of oxide thickness and incident wavelength. It is seen that, for wavelengths between 500 nm and 550 nm, which correspond to green light and the human eye's region of greatest sensitivity [21], that greatest contrast between the overlaying graphene and the underlying substrate are at 80 nm and 285 nm. These "magic" oxide thicknesses also provide positive interference for light-based characterisation techniques, such as Raman spectroscopy [226].

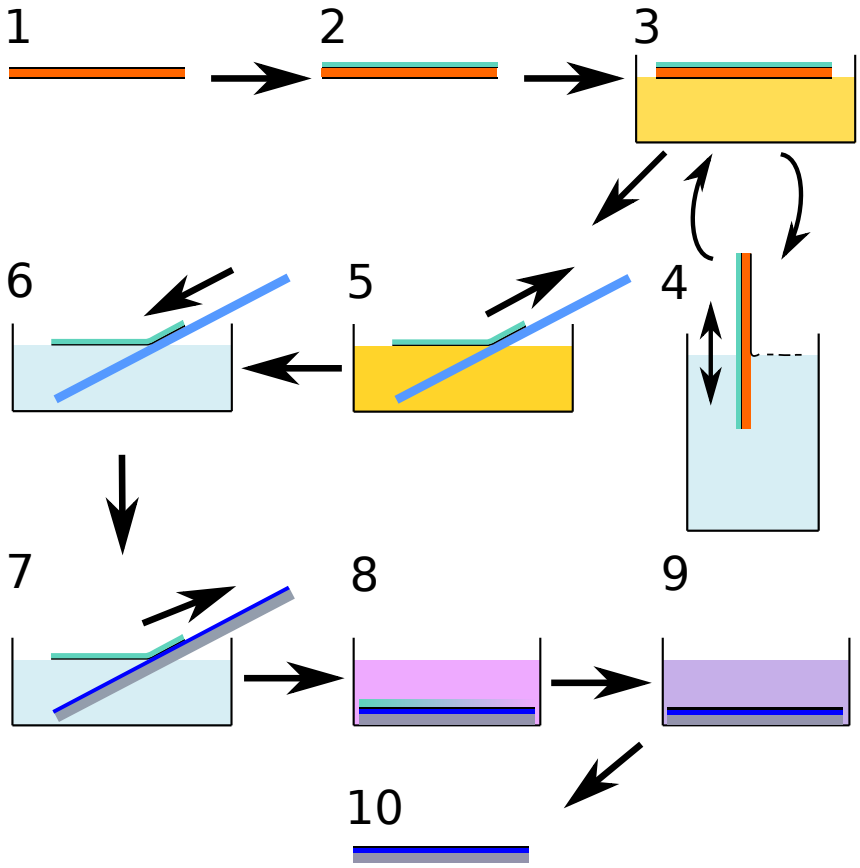

Figure 3.3: Schematic representation of wet graphene transfer from the copper growth foil to a SiO_2/Si substrate.

To transfer the graphene from the copper growth substrate to useful substrates for electrical and material characterisation, a polymer assisted transfer method is employed. It is necessary to use such a procedure because a monolayer of graphene is only one atom thick and, even with its exceptional mechanical properties [11], it is incredibly fragile to handle. By applying a polymer layer to graphene prior to removing it from its copper growth substrate, the graphene is supported and protected from damage enough for gentle handling. The polymer assisted transfer of graphene was first reported by Li et al. [62], wherein they employed PMMA as the supporting layer during graphene transfer, which has, since then, remained the prototypical polymer used for graphene transfer.

A 2014 paper by Hallam et al. [199] found that nitrocellulose resulted fewer contaminating residues on the transferred graphene surface due to easier solvation. Therefore, nitrocellulose was used as the supporting polymer layer for all work presented within this thesis, unless otherwise specified.

The polymer assisted transfer method is displayed schematically within Figure 3.3 and is described stepwise below:

1. Graphene on copper foil is obtained following CVD. It is important to note that

graphene is grown on both sides of the copper foil.

2. A 200 nm layer of nitrocellulose (NC) is spin cast from a 2% solution in ethyl acetate (Sigma Aldrich, item number 09817) via spin coating at 700 rpm for 15 s followed by 2000 rpm for 45 s, onto the desired side of the graphene/copper/graphene stack.

3. The graphene/copper/graphene/NC stack is floated, NC side up on a copper etching solution of 0.5 M ammonium persulphate (APS). APS is used instead of $FeCl_3$ as it leads to fewer residues on the graphene after transfer [199, 227].

4. To remove graphene grown on the reverse side of the foil without damaging the target graphene layer, the foil/graphene/NC stack is gently handled and the reverse side is either repeatedly dipped through the meniscus of a fresh beaker deionised (DI) water, or rinsed under a flowing DI water tap, until the foil becomes too thin to handle. Reverse side graphene removal is carried out every 2 minutes, starting 5 minutes after the etch is initiated. It is important to remove the reverse side graphene, because otherwise it detaches, scrolls up and sticks underneath the desired graphene film, degrading the quality of the transfer.

5. Once the copper has been completely removed by the APS, the graphene/NC stack is gently 'dredged' from the etchant solution with a clean microscope slide

6. The graphene/NC is gentle re-floated off of the slide onto a fresh beaker of DI water to rinse etchant residues from the graphene. The graphene is transferred in a similar manner to fresh DI water at least three times.

7. After rinsing on deionised water, the graphene/NC stack is similarly dredged onto the target substrate and is then allowed to dry overnight.

8. Following air drying, the substrate/graphene/NC is placed within a dish of acetone, to dissolve the supporting polymer layer for at least 2 hours.

9. The substrate/graphene is then taken from the dish of acetone and placed into a dish of isopropyl alcohol for 5 minutes.

10. Finally, the substrate/graphene is removed from the isopropyl alcohol and blow dried with a compressed air gun.

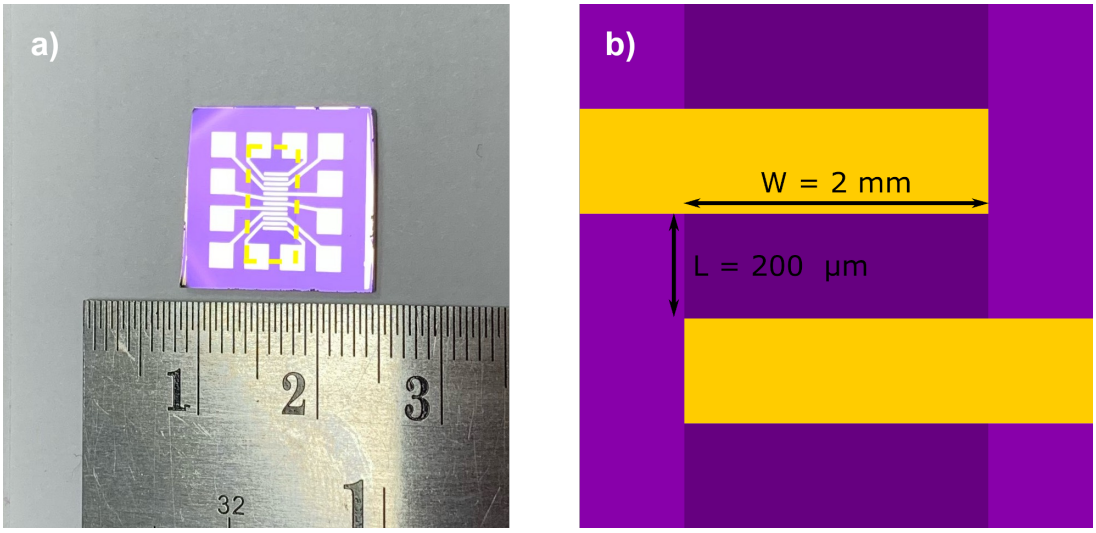

Figure 3.4: a)Image of a typical GFET fabricated within this work, with Cr/Au contacts on a Si chip capped with 300 nm SiO_2. The transferred graphene film is outlined by the yellow dashed line for increased clarity. b) cartoon schematic of the GFET channel dimensions, which is the same for all devices analysed within this work.

3.1.3 GFET Fabrication

Graphene devices studied within this research are based on graphene field effect devices (GFETs). Figure 3.4 displays an image of a typical GFET chip fabricated during this project. GFETs were fabricated by transferring CVD graphene over electrodes which were pre-patterned onto 300 nm thermally grown SiO_2 on degenerately p-doped Si wafers. The underlying Si wafer resistivity is within the range of 1 - 10 Ω cm, which allows the underlying Si substrate to be used as a global back gate during experiments. Transferring graphene onto pre-deposited electrodes was found to be more effective for batch processing GFETs and provided a greater yield ($\sim$ 60%) than evaporating electrodes through a shadow mask onto pre-transferred graphene films ($\sim$ 5%). The reason for this is not clear and further investigation would be required to understand why this is the case.

Positive photolithography with AZ5214 photoresist was used to define the electrodes by exposing photoresist to UV light through the same shadow mask used during thermal evaporation. E-beam evaporation is then used to deposit electrodes using 10 nm chromium and 40 nm gold. Chromium is used as an adhesion layer for the gold, which is used as the capping layer and contact metal as it resists corrosion and is known to reliably provide low contact resistance to graphene [228]. For these reasons, gold is used as the contact metal to graphene throughout much of the literature. A schematic of the process steps for electrode deposition is displayed in Figure 3.5 with step numbers corresponding to the description below:

1. Use a clean, dry wafer.

2. Spin on photoresist (AZ5214e) at 4000 rpm for 60s to create a layer of photoresist $\sim 1.2\,\mu m$ thick. This should be followed by a soft-bake at 90 °C for 10 minutes.

3. Place shadow mask over the substrate/photoresist stack. The mask should be as close to contact across the substrate as possible to minimise feature loss due to diffraction.

4. Expose the photoresist to UV light through the mask for 12 s. The UV light breaks bonds within the photoresist, making it more soluble.

5. Use photoresist developer (Microchem AZ 326 MIF Developer) to dissolve the UV exposed regions of photoresist. Pattern development typically takes $\sim$ 30 s.

6. Using a BOC-Edwards e-beam evaporator, deposit a 10 nm Cr/ 40 nm Au metal stack across the entire substrate. Metal film thicknesses are determined by a quartz crystal balance within the evaporation chamber.

7. Dissolve the remaining photoresist in a high-vapour pressure solvent such as NMP or DMF. This will "lift off" metal overlaying photoresist, leaving behind only the desired electrode pattern.

8. Pre-prepared copper/graphene/NC is then cut to the same size as the channel area across the electrodes and is transferred via the method described in Section 3.1.2 to create a chip with 11 GFET devices.

3.2 Analysis

3.2.1 Raman Spectroscopy

Raman spectroscopy is a non-destructive material analysis technique, which provides information on the crystalline or molecular nature of the material under interrogation. Material information is provided via the energy shifts of photons re-emitted from the sample when under intense monochromatic illumination, conventionally expressed in wavenumbers (cm^{-1}), which are referenced to the illuminating light source.

These energy shifts occur because of light-matter interactions between the illuminating photons and phonon modes within the illuminated material. Such photon energy shifting

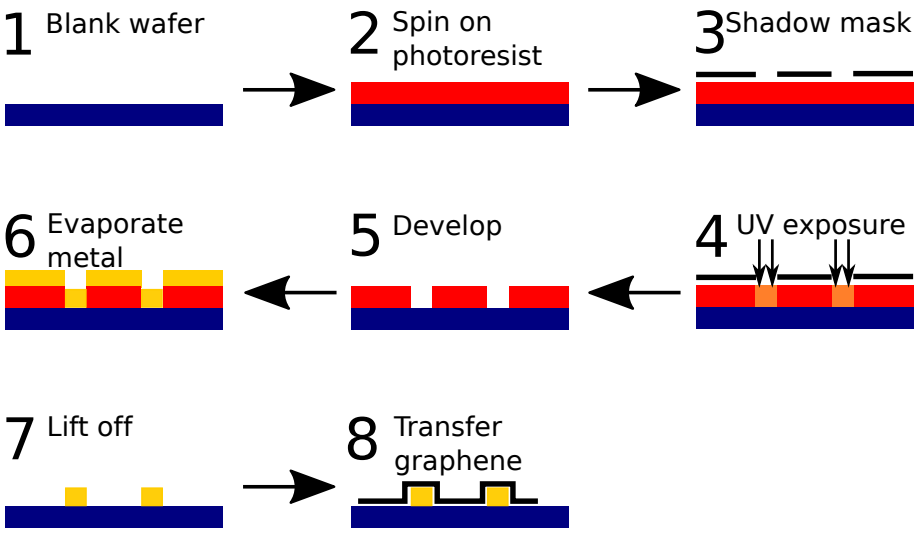

Figure 3.5: Schematic representation of photolithography, metallisation lift off and graphene transfer to create GFETs.

is known as Stokes scattering and is an example of inelastic light scattering, wherein the energy of a photon is changed during the photon-matter interaction. Figure 3.6 displays a schematic representation of Rayleigh (elastic) and Stokes and anti-Stokes (inelastic) scattering. As displayed within Figure 3.6, Rayleigh scattered photons are re-emitted (represented by the down arrow) at the same energy as they were absorbed (represented by the up arrow). However, Stokes (anti-Stokes) scattered photons are re-emitted at lower (higher) energy than their original energy upon absorption. This occurs, because for a small fraction of absorbed photons, interaction between the photon and the absorbing material leads to photon-phonon interaction, which results in the photon losing (gaining) energy to (from) the phonon and resulting in a Stokes (anti-Stokes) energy shift of the re-emitted photon. A high intensity light source is required for illumination, because only a small fraction of photons ($\sim 10^{-5}$) will be Stokes shifted [229]. It is also important to use monochromatic light so as to be able to filter out the illuminating frequency, as Stokes shifted signals are much less intense than the signals from Rayleigh scattered light. Finally, the spectral linewidth of the illuminating source sets a limit on the spectral resolution of the measured Raman spectra [230]. Thus, the illuminating source should have the narrowest practicable spectral linewidth. For these reasons, lasers are typically used as the illuminating source.

Raman spectroscopy has been used extensively for the characterisation of carbon based nanomaterials [231], and since the isolation of graphene, Raman spectroscopy has proved to be an invaluable tool for rapid, non-destructive graphene characterisation. In fact, Raman techniques are particularly powerful when applied to graphene, because the ab-

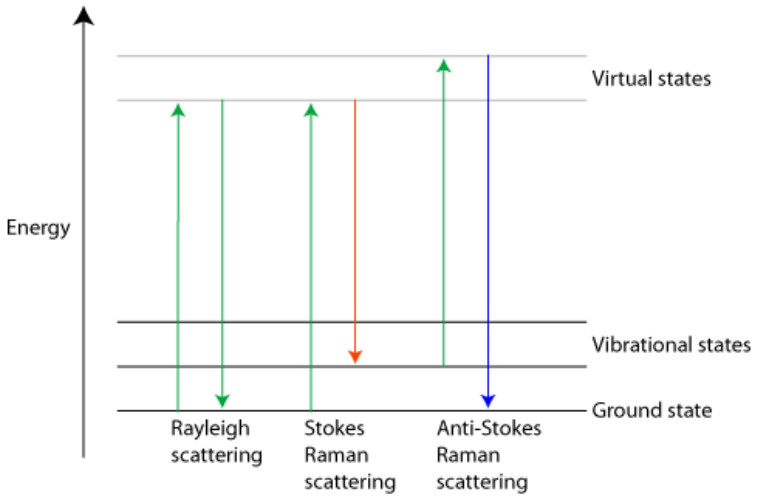

Figure 3.6: Schematic representation of Rayleigh and Stokes and anti-Stokes scattering through light-matter interaction. The decrease (increase) in energy of (anti-) Stokes scattered light is due to losing (gaining) energy from (to) a phonon, or vibrational state, within the matter.

sence of a band-gap makes all wavelengths of incident radiation resonant and therefore the Raman spectrum of graphene contains information about both atomic structure and electronic properties [231]. Additionally, the atomic thickness of graphene means that the entire thickness of the graphene sheet under illumination is measured – a condition which holds at least until to the generally accepted limit for "graphene" of 10 layers [232].

Raman spectroscopy has been shown to be a powerful tool for investigating the quality, doping and strain of graphene which is usually determined via the study of only three or four major peaks common to sp^2 hybridised carbon networks [233–235], which remain well defined even until the graphene film is severely damaged. The quality of graphene is generally considered to be based upon a measure of the carbon vacancy defect density within the graphene sheet under investigation [231, 236–243].

Figure 3.7 displays the Raman spectra obtained from a) pristine, and b) defective graphene sheets. Raman spectra from pristine graphene only show two major peaks – G and 2D. The G peak is related to the shearing mode between adjacent carbon planes within the graphene lattice, as illustrated above the G peak in Figure 3.7 a). The 2D peak is the first overtone of the D peak, which is discussed in more detail below. Unlike the D peak, which requires a defect centre to become momentum allowed, the 2D peak is a photon-double-phonon interaction involving two phonons of equal magnitude but opposite direction, and as such is momentum allowed without the presence of defects [232].

Figure 3.8 displays a schematic diagram of the photon-phonon interactions for the

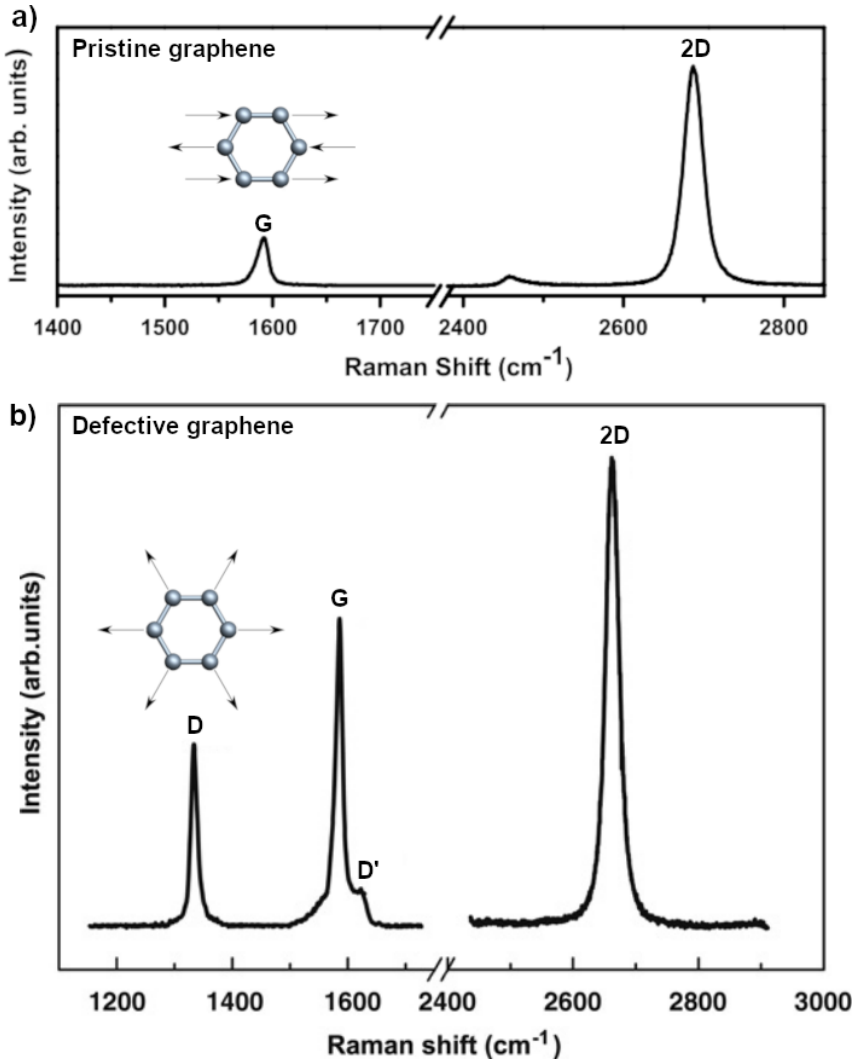

Figure 3.7: Comparative spectra taken from pristine and defective graphene, showing the characteristic D, G, 2D and D' Raman peaks. Images taken from Malard et al.[242].

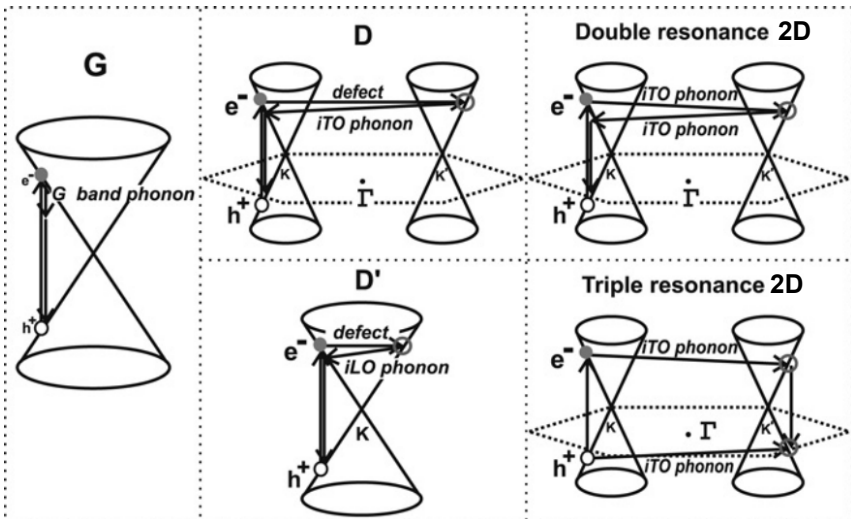

Figure 3.8: Schematic representation of the photon-phonon interactions responsible for the most common spectral peaks within Raman spectroscopy. Taken from reference [242].

most commonly discussed graphene Raman peaks – the G, D, 2D and D' [242]. Turning the discussion to the D and D' peaks, Figure 3.8 displays the requirement for the presence a defect to activate the D and D' peaks, which are particularly important to the work presented within Section 5. The D mode is related to the carbon ring breathing mode which is displayed above the D peak within Figure 3.7 b). Both the D and D' modes are due to double resonance effects, but relate to inter- and intra-valley interactions respectively [232]. Most importantly, a defect must be present to allow the D and D' modes to become Raman-active and as such they can be used as a measure of carbon vacancy densities within the graphene sheet [236, 239–242]. By plotting the positions, intensities, widths and asymmetries of the D, G, 2D and D', a wealth of information becomes available regarding the defect density, strain, doping and number of layers of the graphene sheet under investigation [231, 236–243].

As modern Raman spectrometers are capable of recording a single spectrum within 1 s, Raman spectrum maps with 256 pixels × 256 pixels across areas of 100 µm × 100 µm can easily be recorded which allows detailed analysis of the quality and homogeneity of graphene films. It should be mentioned that, in general, Raman spectroscopy is not capable of measuring chemical composition. To address this, Raman spectroscopy is often paired with chemically sensitive techniques such as XPS or TOF SIMS [191].

Within this thesis, high resolution Raman spectra were recorded using a Horiba Jobin yvon HR800 UV fitted with a Symphony Solo liquid nitrogen cooled detector. A 100x objective lens was used, with an excitation wavelength (λ) of 514.5 nm, laser spot size of 0.70 μm and an incident laser power of 4 mW at room temperature. Spectra were

recorded as the average of two measurements per spectral window with an acquisition time per measurement of 5 s, unless otherwise stated. Large area Raman spectrum maps were carried out at CRANN, Trinity College Dublin, using a WITec alpha 300 R.

3.2.2 Atomic Force Microscopy

Since its first demonstration in 1986 [244], the atomic force microscope (AFM) has been one of the foremost tools for the characterisation of nano materials. AFM uses a sharp tip mounted at the end of a cantilever which is brought into close proximity to, and rastered across, a sample surface to produce a map of surface information. In its most basic usage, the information returned will simply be the surface topography, but modern AFMs are capable of mapping information on the mechanical, electrical, electronic, magnetic and thermal properties of a sample. The working mechanisms of AFM topography measurements as well as Kelvin Probe Force Microscopy (KPFM) – a method which measures the surface work function on the nano scale are described in detail later in this section.

As the tip is scanned across the sample surface, atomic forces between the tip and sample surface lead to deflection of the AFM cantilever. Because the tip/cantilever mass is small and AFM cantilever force constants are small (typically < 42 N/m), it is possible to resolve sub-angstrom height profiles in ideal operating conditions and on the angstrom scale even within an ambient environment [244]. When the tip-sample distance is very short, such as when the AFM is operated in contact mode, the tip-sample forces are repulsive, due to electrostatic repulsion between the tip atoms and the surface atoms [244]. If relatively larger separations are used, such as in non-contact mode, the tip-sample force becomes attractive due to long range van-der-Waals forces. Figure 3.9 displays how the tip-sample force varies with tip-sample separation and marks the force regimes within which contact and non-contact modes are operated.

The deflection of the cantilever is measured by reflecting a laser off of the back of the cantilever and measuring the change in position of the reflected laser spot on a position sensitive photodiode (PSPD). The change in laser spot position on the PSPD is fed back through the AFM controllers to maintain a constant separation or force between tip and surface. Figure 3.10 provides a schematic representation of the AFM operation to measure sample topography in non-contact mode, although contact mode operation is conceptually similar. AFM tips and cantilevers are typically made of silicon and have a tip radius of curvature of ~ 10 nm [246], which allows resolution of features as small as ~ 20 nm across,

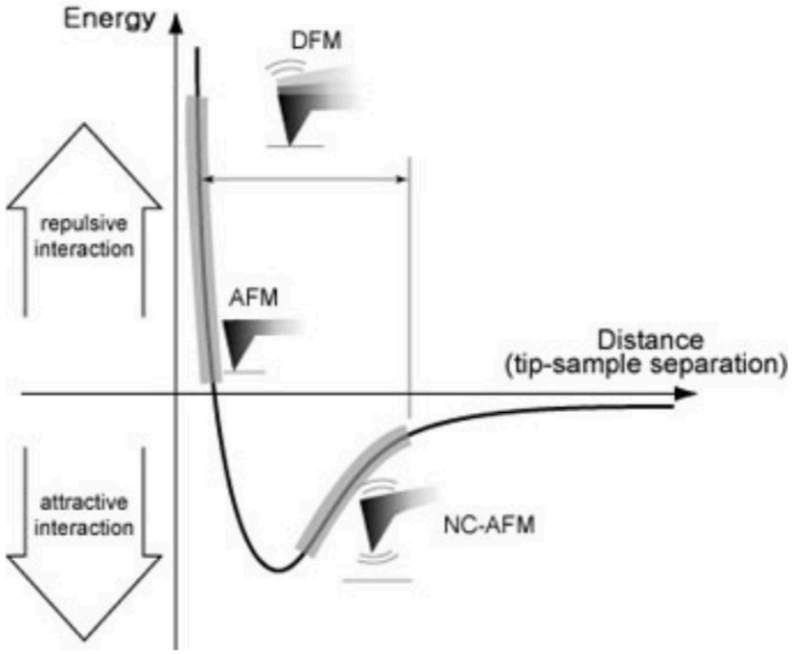

Figure 3.9: Relationship between the tip-sample force and separation; taken from reference [245].

if using a fresh tip.

The Park Systems XE-150 AFM used within this research uses two separate piezoelectric stages to separately control the x-y motion of the sample and the z-motion of the scanning tip. The separation of these stages allows relatively large scan areas, with scan side lengths of up to 100 µm and with a maximum z-range of 12 µm. However, whilst it is possible for the AFM to manage multi-micron vertical steps, feature details begin to be lost even for sharp features with heights in excess of a few 10s of nm due to tip-sample convolution and finite system feedback response.

AFM data presented within this thesis was obtained with a Park Systems XE-150 AFM, unless otherwise stated. The XE-150 was used with different modes to provide topographic and beyond-topographic information about the our graphene samples. Common AFM operation modes and the modes used within this research are discussed below.

AFM Topography Modes

There are three main AFM modes for topographical measurements – contact, non-contact and tapping – upon which all other methods are based. We discuss the two topographical scan modes available – contact and non-contact – with the Park XE-150 below.

Contact mode: This mode measures surface topography via cantilever deflection caused by the electrostatic repulsive forces between tip and sample. Within contact mode, the tip

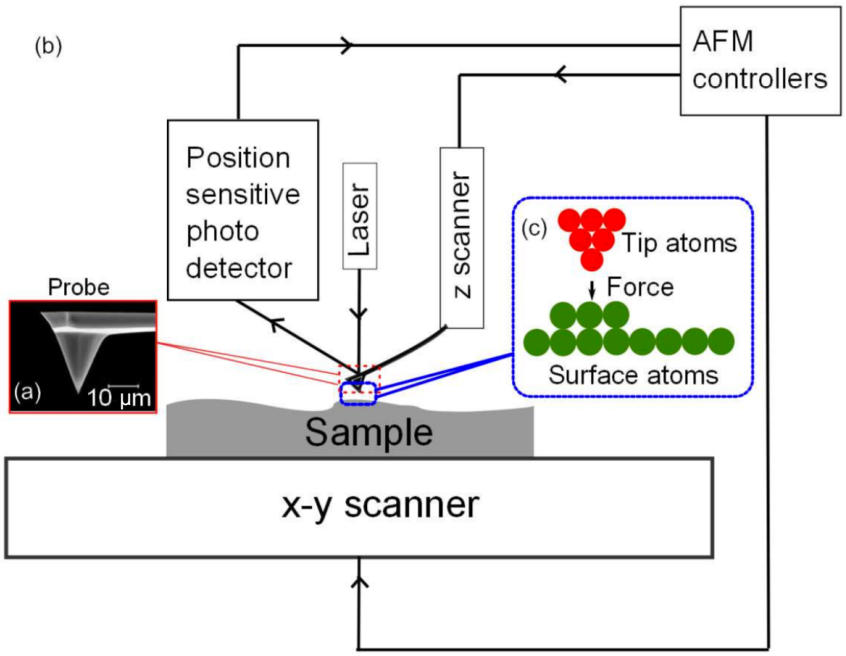

Figure 3.10: (a) shows the scanning electron microscopy image of CDT-NCHR AFM tip, (b) displays a schematic representation of Park Systems XE 150 AFM setup and (c) the attractive force experienced between tip and the sample surface when operated in non contact mode; taken from reference [245].

makes contact with the sample surface and the force between the tip and sample surface is kept constant by the AFM feedback hardware. Changes in sample height cause the cantilever to bend and thus the laser spot to change position on the PSPD. The feedback from the PSPD is used to ensure that a constant force is applied between tip and sample surface and to build up a topographic map of the sample. Soft cantilevers with low spring constants, typically around 2 N/m should be used within this mode to avoid excessive damage to both tip and sample. Contact mode is the easiest way to achieve very fine z-resolution, but this comes with the cost of potential damage to the tip or sample surface, and a high likelihood of tip contamination. Because contact mode drags the tip across the sample surface it is unsuitable for use with soft samples as it is likely to cause sample damage and tip contamination.

Non-contact mode: Within non-contact mode, the tip is held away from the sample surface by the AFM, at a separation at which the attractive van-der-Waals (vdW) forces are the dominant force between sample and tip. Within this regime however, the forces between tip and sample are very low, and it is therefore not possible to directly measure the sample surface through the deflection of the cantilever position. Instead, the cantilever is vibrated at a frequency just above its resonant frequency, typically between 100 kHz and 400 kHz, with an amplitude of a few nm. When scanning with the cantilever vibration

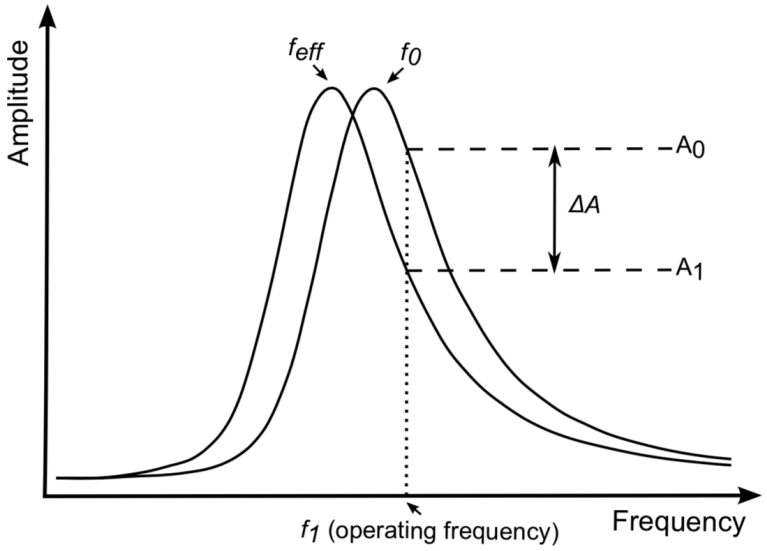

Figure 3.11: Illustration of the shift in the non contact AFM tip resonance curve due to tip-surface interactions; taken from reference [245].

set at or near to its resonant frequency, the attractive vdW forces cause a shift in the cantilever's spring constant from its intrinsic spring constant(k_0). The shifted spring constant is called the effective spring constant (k_{eff}), and is described by Equation 3.1:

$$k_{eff} = k_0 - F' \tag{3.1}$$

where F' is $\delta F/\delta$, or the force gradient. Accordingly, the closer the tip comes to the sample surface, the greater the force acting upon the tip and the greater the difference between k_0 and k_{eff}. The effective spring constant is then related to the effective cantilever resonant frequency via Equation 3.2:

$$f_{eff} = \sqrt{\frac{k_{eff}}{m}} \tag{3.2}$$

where f_{eff} and m are the effective frequency and the mass of the tip/cantilever system respectively. Therefore, if the AFM is set up such that the operating frequency, f_1, is set at a frequency just higher than the natural resonant frequency of the tip, f_0, small changes to k_{eff} and f_{eff}, caused by changes to the tip-sample forces, due to changes in tip-sample separation, lead to a large change in cantilever amplitude at the selected frequency, f_1. This effect is displayed in Figure 3.11, where f_0 represents the cantilever's natural resonant frequency and f_{eff} represents the modified resonant frequency resulting from reduced tip-sample distance. Because the f_{eff} resonance curve has shifted leftwards – that is, the resonant frequency of the tip is now lower – a large change in tip amplitude, ΔA is measured at the preselected frequency, f_1. Therefore, the change in amplitude, ΔA,

at f_1 provides an indirect, but highly sensitive measurement of topographical variation. Changes in f_1 are monitored by the z-scanner feedback loop which is used to maintain a constant tip-sample distance to map the sample surface without the tip making physical contact. Non-contact mode therefore preserves both tip and sample condition and is much less prone to tip contamination than contact mode. It is particularly useful for imaging soft or delicate sample surfaces which would otherwise be excessively damaged or lead to tip contamination upon contact. The majority of AFM data presented within this thesis has been captured via non-contact mode.

KPFM

Kelvin prove force microscopy (KPFM) is a technique based on non-contact AFM, which measures the contact potential difference (CPD) between a conductive AFM tip and the sample surface [247]. CPD is defined as:

$$V_{CPD} = \frac{\phi_{tip} - \phi_{sample}}{-e} \tag{3.3}$$

where ϕ_{tip} and ϕ_{sample} are the work functions of the tip and sample respectively, and e is the charge of an electron.

When the AFM tip is brought close to the sample surface, the difference between the tip and sample Fermi energy levels creates an electric force between sample and tip. A feedback loop nullifies this force by applying an external bias to the sample or tip (V_{DC}), with the same magnitude as the V_{CPD}. Therefore, the surface work function, or electron potential for non metals, can be calculated if ϕ_{tip} is known.

By driving the AFM tip with an AC voltage (V_{AC}), at a frequency distinct from the mechanical driving frequency (f_1), plus a DC voltage (V_{DC}), KPFM measures the work function of the sample. V_{AC} generates oscillating electrical forces between the AFM tip and the sample surface, whilst V_{DC} is applied to nullify the oscillating electrical forces that originated from the CPD between tip and sample surface.

The electrostatic force (F_{es}) between the AFM tip and sample is given by:

$$F_{es}(z) = -\frac{1}{2}\delta V^2 \frac{dC(z)}{dz} \tag{3.4}$$

where z is the direction normal to the sample surface, ΔV is the potential difference between V_{CPD} and the voltage applied to the AFM tip, and dC/dz is the gradient of the

capacitance between tip and sample surface. When $V_{AC}sin(\omega t)$+V_{DC} is applied to the AFM tip, the voltage difference ΔV will be:

$$\delta V = V_{tip} \pm V_{CPD} = (V_{DC} \pm V_{CPD}) + V_{AC}sin(\omega t) \tag{3.5}$$

Note that the $\pm$ sign depends whether the bias (V_{DC}) is applied to the sample (+) or the tip (-). In the case of the Park Systems XE 150, the sign will be - as V_{DC} is applied to the scanning tip. Substituting Eq. 3.5 in Eq. 3.4 gives the expression of the electrostatic force applied to the AFM tip:

$$F_{es}(z,t) = -\frac{1}{2}\frac{\delta C(z)}{\delta z}\left[(V_{DC} \pm V_{CPD}) + V_{AC}sin(\omega t)\right]^2 \tag{3.6}$$

which can then be divided into three parts:

$$F_{DC} = -\frac{\delta C(z)}{\delta z}\left[\frac{1}{2}(V_{DC} \pm V_{CPD})^2\right] \tag{3.7}$$

$$F_{\omega} = -\frac{\delta C(z)}{\delta z}(V_{DC} \pm V_{CPD})V_{AC} \cdot sin(\omega t) \tag{3.8}$$

$$F_{2\omega} = \frac{\delta C(z)}{\delta z}\frac{1}{4}V_{AC}^2\left[cos(2\omega t) - 1\right] \tag{3.9}$$

F_{DC} results in a static deflection of the AFM tip and F_{ω}, with frequency ω (Eq 3.8) is then used to measure V_{CPD}. $F_{2\omega}$ can be used for capacitance microscopy, but is not relevant to this research.

When electrostatic forces are applied to the tip by V_{AC} and V_{DC}, additional oscillating components are superimposed upon the mechanical oscillation of the AFM tip. To avoid crosstalk between the AFM topography measurements and KPFM measurements, it is necessary to choose ω of V_{AC} such that the frequency of V_{AC} is both far away from the driving frequency for topographic measurements and neither the frequency of V_{AC} or the mechanical oscillation are overtones of each other.

A lock-in amplifier is employed to measure V_{CPD}, by extracting the electrical force component with frequency ω, which is a function of V_{CPD} and V_{AC}. The output signal of the lock-in amplifier is then directly proportional to the difference between V_{CPD} and V_{DC} and thus V_{CPD} can be measured by applying V_{DC} to the AFM tip, such that the output signal of the lock-in amplifier is nullified and F_{ω} equals zero. Subsequently, the value of V_{DC} is acquired at each point on the sample surface and a map of the surface

work function or surface potential is created [247].

The surface potential maps created by KPFM are used within this research to explore how charge transfer occurs between graphene and an overlaid nano/micro particle, with a view on how that impacts the gas-sensing properties of the overall GFET/particle system.

3.2.3 TOF-SIMS

Time-of-flight secondary-ion-mass-spectroscopy (TOF-SIMS) is a highly chemically sensitive surface analysis technique, which is capable of providing detailed information on the chemical composition of investigated samples. The basic principle of SIMS is to use heavy primary ions to ablate a sample surface and measure the mass of the ejected secondary ions.

Unlike other SIMS techniques, TOF-SIMS pulses the primary ion source, which has been excited and filtered to ensure that the primary ions all have the same mass. As the primary ions all have the same mass, they will all reach the sample surface at the same time which then means that the secondary ions, or ion clusters, are all emitted from the sample surface at the same time. The secondary ions are then accelerated by an electric field up a flight tube towards a detector. As the secondary species are all ejected at the same time, but have different rates of acceleration, the arrival time of the secondary species at the instrument's detector can be correlated with the specie's mass. It is possible, via TOF-SIMS, to resolve mass differences of 0.01 atomic mass unit and therefore distinguish between fragments which have nominally identical atomic masses, due to mass differences which arise from atomic binding [248, 249].

TOF-SIMS is used within this research because, even within non ideal conditions, atomic species can be detected at concentrations on the order of 0.01 atomic % (at%) [191]. However, although TOF-SIMS provides quantitative analysis, it is necessary to pair the technique with other quantitative methods, particularly in the case of the research presented within this thesis because of the commonality of C/N/O fragments which are the primary elements of interest within this study.

In the case of this research, XPS and Raman spectroscopy were used as the supporting quantitative methods alongside TOF-SIMS for the analysis of chemical and defect composition within graphene films. TOF-SIMS still plays a vital role due to its capability to probe for the presence of chemical species in much smaller concentrations than XPS and because Raman is only defect sensitive within graphene Raman analysis. TOF-SIMS

data presented within this thesis was obtained at the Universität der Bundeswehr, Munich, with a Physical Electronics TOF-SIMS system, using Ga+ ions as the primary ion source and a 30 kV acceleration beam and measurement areas of 400 µm × 400 µm.

3.2.4 X-Ray Photoelectron Spectroscopy

X-Ray Photoelectron Spectroscopy (XPS) is a surface analysis technique which returns information on the chemical composition and chemical configuration the sample surface. XPS measurements are based on the photoelectric effect, which is achieved by using monochromatic x-rays to excite electrons sufficiently to escape from core atomic levels within the sample [250]. The energies of emitted photoelectrons are measured and a spectrum of intensity as a function of energy is created. The energy of emitted photoelectrons are related to their original binding states by Equation 3.10:

$$h\nu = E_k + E_B + \phi \tag{3.10}$$

where $h\nu$ is the energy of the incident x rays, E_k is the kinetic energy of the photoelectron, E_B is the binding energy of the photoelectron's original energy level and ϕ is the work function of the sample. As photoelectrons have a short mean free path (λ) within solids of $\sim$ 4 nm [251], photoelectrons generated deeper within a sample cannot escape.

Therefore, XPS is limited to surface analysis of samples. This is advantageous for the study of graphene and other 2D materials, as XPS spectra reveals information of the entire material's depth, in direct contrast to that of bulk material analysis.

Ultrahigh vacuum ($\sim 10^{-9}$ millibar) is used in XPS spectrometers due to the short mean free paths of generated photoelectrons and is required to ensure that photoelectrons reach the detector without losing energy.

XPS provides stoichiometric analysis of a material's composition, through the comparison of emission intensities for different elements. It is possible to detect chemicals within a material at parts per thousand [191] with XPS, although this is dependent on material surface roughness [252] and the chemical matrix within which the chemical species is sited [253]. Whilst XPS does not have the sensitivity of TOF SIMS or Raman spectroscopy, it provides another quantitative method for probing the chemical composition of thin films. XPS is therefore utilised as a complementary method alongside TOF-SIMS and Raman spectroscopy (non-specific defect density measurement) for the analysis of graphene film composition within this research.

XPS data presented within this thesis was taken at the Universität der Bundeswehr, Munich, with a PHI VersaProbe III, using a micro-focused monochromated Al K-alpha source (1486.6 eV). Measurements were conducted with a spot size of 100 microns and a pass energy of 26 eV using PHI SmartSoft VersaProbe software.

3.2.5 Electronic characterisation

To use GFETs as functional devices, their behaviour and performance need to be known. Electronic characterisation provides a measure of the quality of the transferred graphene sheet which can be determined by extracting the field effect mobility (μ_{FE}) and the doping of the graphene channel within GFET devices. Within this research, the gradual channel approximation (GCA) [254] is used to characterise GFET behaviour. The GCA is selected as an appropriate method, as it is widely used within the field of 2D materials research [1, 255–259] and thus provides a direct comparison of the devices fabricated throughout this research with those reported within the literature.

A Cascade probing station, in conjunction with a Keithley 4200A parameter analyser is used to record I_{ds}/V_g sweeps from the fabricated GFETs. This equipment is used because it provides a large dynamic range for recording channel current, from nA to mA.

Figure 3.12 displays a typical I_{ds}/V_g sweep, or transfer curve, taken from a GFET fabricated during this research, which displays the typical 'V' shape expected from graphene [1, 10, 194]. The 'V' shape indicates that graphene is a bipolar conductor, with holes (electrons) being the majority charge carriers to the left (right) of the conduction minimum [194]. The value of V_g at the minimum point of the transfer curve corresponds to the charge neutrality point (CNP) for the graphene device, denoted by V_{CNP}. By calculating the capacitive value of the dielectric layer, an estimate for the doping density of the graphene channel can be extracted, using Equation 3.11 [194]:

$$n_0 = \frac{V_{CNP} \cdot C_{ox}}{q} \tag{3.11}$$

where n_0 is the residual doping density of the graphene channel, expressed as n per cm^2, C_{ox} is the capacitance of the dielectric layer (SiO_2) per cm^2 and q is the unsigned electronic charge. As q is used, a positive (negative) value for n_0 indicates that the graphene channel is p-doped (n-doped).

It is also possible to extract charge carrier mobility from GFET transfer curves. Within this research, charge carrier mobility is extracted through the use of the gradual channel

approximation (GCA), which begins with the well known expression for source-drain current, given in Equation 3.12 [260]:

$$I_{ds} = \frac{W}{L}\mu_{FE}C_{ox}\left((V_g - V_t)V_{ds} - \frac{V_{ds}^2}{2}\right) \tag{3.12}$$

where I_{ds} is the drain-source current, L and W are channel length and width respectively, C_{ox} is the capacitance of the dielectric layer (SiO_2) per cm^2, μ_{FE} is the field effect mobility, V_g and V_t are the gate and threshold voltages respectively and V_{ds} is the source-drain bias. By differentiating Equation 3.12 with respect to V_g, an expression for transconductance ($g_m = \frac{\delta I_{ds}}{\delta V_g}$) independent of V_t is achieved, as displayed in Equation 3.13:

$$\frac{\delta I_{ds}}{\delta V_g} = g_m = \frac{W}{L}\mu_{FE} \cdot C_{ox} \cdot V_{ds} \tag{3.13}$$

which can then be rearranged for g_m to provide Equation 3.14:

$$\mu_{FE} = \frac{L}{W} \cdot \frac{g_m}{C_{ox} \cdot V_{ds}} \tag{3.14}$$

The field effect mobility is then extracted graphically by first plotting the transconductance, g_m, of the GFET against V_g, as shown in Figure 3.13 The values of g_m at the inflection points of the g_m/V_g plot are then substituted into Equation 3.14 to return values for μ_{FE}. Each up/down I_{ds}/V_g sweep therefore provides two values for the electron

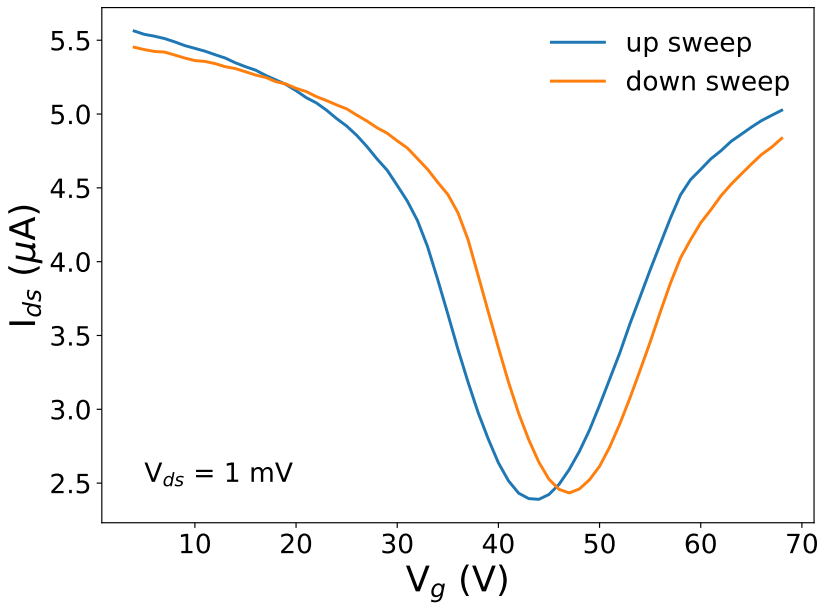

Figure 3.12: A characteristic transfer curve obtained from a GFET fabricated within this project.

and hole mobility, with both up sweep and down sweep values extracted as standard procedure.

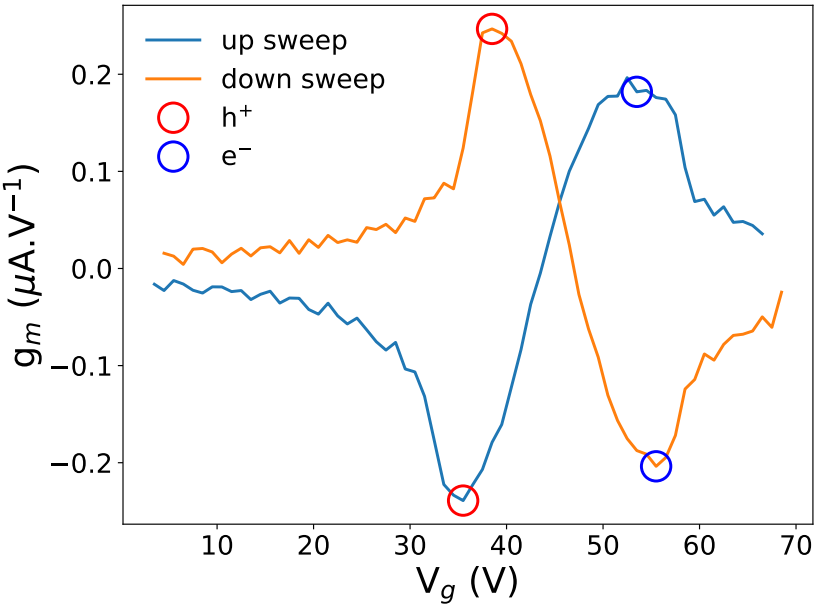

Figure 3.13: The transconductance curve obtained by numerically differentiating the transfer curve displayed in Figure 3.12. The g_m values to be substituted into Equation 3.14 are highlighted by red (blue) circles for hole (electron) g_m values.

The gradual channel approximation provides a simple, FET-compatible method for extracting important metrics relating to GFET operation and quality of graphene transfer, but rests upon a number of assumptions [254]. These assumptions are:

1. The electric field between gate and source is much greater than the electric field between source and drain.

2. The device under measurement is not saturated, and that therefore the potential gradient is constant between source and drain contacts.

3. Conduction takes place only within a thin (2D) channel.

4. Charge accumulation underneath channel contacts is neglected.

Assumptions 1-3 make the gradual channel approximation particularly suitable for application to GFETs, as graphene is 2D in nature, cannot be saturated due to a continuous density of states [1, 10] and the oxide thickness means that V_g must be swept over a range which is orders of magnitude greater than the applied V_{ds} of 1 mV to observe significant modulation, as displayed on the x-axis in Figure 3.12.

The GCA does have limitations however, and is known to underestimate charge carrier mobility in devices as it does not take contact resistance [260], or changes in μ with respect to V_g [261, pp. 500-501], into account. However, a threshold voltage is required to calculate a meaningful effective charge carrier mobility (μ_{eff}) instead of μ_{EF}, and as the current within GFETs is typically only modulated by a factor of 2-5, threshold voltage is not a meaningful concept within this work. The GCA is also widely used by researchers who have not, or can not, acquire hall carrier mobility measurements [194, 255, 262–265], meaning that the use of the GCA provides a direct comparison for devices fabricated within this research against devices reported within the literature. We therefore conclude that the GCA provides a suitable method for charge carrier mobility extraction from three-terminal graphene-based devices.

Chapter 4

Chemical Vapour Deposition of Graphene Using Industrially Safe Conditions

This chapter introduces chemical vapour deposition (CVD) of graphene and the instrumentation used within this project to achieve CVD growth of graphene. The "hot plate" technique is introduced as a rapid method for assessing post growth graphene coverage on copper foil. Optimisation results are presented for graphene recipes aimed towards full coverage of the catalytic foil with graphene combined with increased domain area and reduced graphene domain density.

For graphene to move beyond being a laboratory curiosity, methods for mass production must be developed. Various techniques for wafer-scale production of graphene have been demonstrated, such as silicon sublimation from silicon carbide [44–46, 137, 141], solution-based processing of graphene or graphene oxide suspensions [51–54] and chemical vapour deposition (CVD) [85, 157, 159, 160, 266].

Of these, CVD has become the foremost method for the production of electronic-grade graphene, as it is possible to produce high-quality, single-layer graphene with a total graphene film area limited only by the size of foil growth substrate used during CVD [58], but whilst commercial production of graphene via CVD is now possible [267], it is far from optimised. Process safety and cost reduction are two areas which are only now beginning to receive attention within the graphene literature [58, 85, 268], as much of the research to date has been examining the fundamental behaviours of graphene CVD growth [75, 157, 159, 160, 269, 270] and the graphene CVD recipes presented within this

chapter aim to address both of these issues.

To increase process safety, the explosive precursor gases, hydrogen and methane, are diluted below their lower explosive limits (LELs) of 4% and 5% respectively within a buffering gas [58, 85]. However, diluted precursor gases must be flowed into the reaction space at much greater volumes when compared with the used of pure precursor mixtures to achieve the required precursor partial pressures for graphene growth reactions to take place [85]. The use of large total gas flow rates results in the rapid consumption of the buffering gas, which is then a major cost concern when considering commercial-scale growth. As discussed previously, argon is predominantly used as the buffering gas because it is chemically inert, which means it should not interact with the growing graphene film. However, the cost of flowing sufficient argon for graphene production within industrial settings is likely to become prohibitively large.

A cheaper alternative to argon is nitrogen, as it makes up $\sim 80\%$ of Earth's atmosphere, rather than $< 1\%$ for argon. Nitrogen, whilst existing as a diatomic molecule, is also inert within most conditions, due to the triple bond between nitrogen atoms within a di-nitrogen molecule [86–88]. Therefore, replacing argon with nitrogen when using high gas flow processes to produce graphene provides a simple step for cost reduction. The increase of gas flow rate also necessarily increases the pressure within the reaction chamber above the millibar range typically reported within literature, if similar precursor pressures are to be maintained within the reactor [59, 271, 272].

The work presented within this chapter demonstrates the successful development of growth recipes for graphene grown under an a-typical 10 - 100 millibar pressure regime within a nitrogen, rather than an argon, atmosphere. In addition, as the main focus of this chapter is the development of graphene CVD recipes using low cost techniques, the "hot plate technique" is introduced and verified as a simple and cheap, yet effective method, for the characterisation of CVD graphene growth on copper foils.

4.1 Graphene CVD Optimisation

CVD graphene growth on copper is possible under a wide variety of process conditions, but not all recipes will grow graphene of equal quality [164]. Ideally, graphene grown via CVD would nucleate from a single nucleus and grow into a monocrystalline film. However, in general, graphene domain nucleation is a continuous process leading to multiple domains nucleating, which grow and stitch together to create a large continuous sheet of

polycrystalline graphene [225, 273]. The presence of domain boundaries and rotational domain misalignment degrades electronic and mechanical properties [273].

As a route to film improvement, domain boundary density should be reduced, hence domain nucleation density (ρ_D) must be reduced, which in turn means that domain area must increase to achieve full coverage. It has been observed that increased temperature [70, 274], increased H_2:CH_4 ratio [58, 162], reduced Cu foil surface roughness [275, 276] and a non-reducing pre-growth atmosphere [63, 70, 74] all contribute towards achieving large domain area, low domain density CVD graphene.

Within this chapter, the optimisation of graphene CVD is explored, with the primary aim of providing continuous graphene coverage on the copper growth foil whilst also minimising domain density. Copper is used as the catalytic growth foil because of the low solubility of carbon within copper – a trait which is atypical of transition metals [277] – which means the reaction is dominated by surface interactions and monolayer graphene growth is favoured [62]. To ensure that processing remains industrially safe, both methane and hydrogen are supplied as 2% balance within an inert buffering gas, below their lower explosive limits of 5% and 4% respectively [58, 278].

Growth optimisation is carried out in a step-wise fashion, starting with foil pretreatment, followed by temperature, H_2:CH_4 ratio, trace oxygen inclusion and finally a revisit to H_2:CH_4 ratio. Temperature is chosen as the first in-growth parameter to study as it interacts weakly with the other parameters of interest. H_2:CH_4 was chosen as the next parameter for investigation as it has been widely reported to have a significant effect on graphene nucleation and growth. Trace oxygen inclusion was then studied following a number of publications in 2016 which brought the idea to our attention [66, 75, 154, 165] Finally, H_2:CH_4 was revisited following some unexpected results from the inclusion of trace oxygen.

4.1.1 Hot Plate Method for Graphene Nucleation and Growth Analysis

Graphene grown on copper is invisible to the naked eye, normally requiring complex equipment to inspect without further processing. Instead, within this section, the hot plate method (HPM) is introduced as a low-cost technique for rapid assessment of graphene growth behaviour. Unlike common techniques for graphene analysis such as Raman spectroscopy and transmission electron microscopy (TEM) which require instruments which

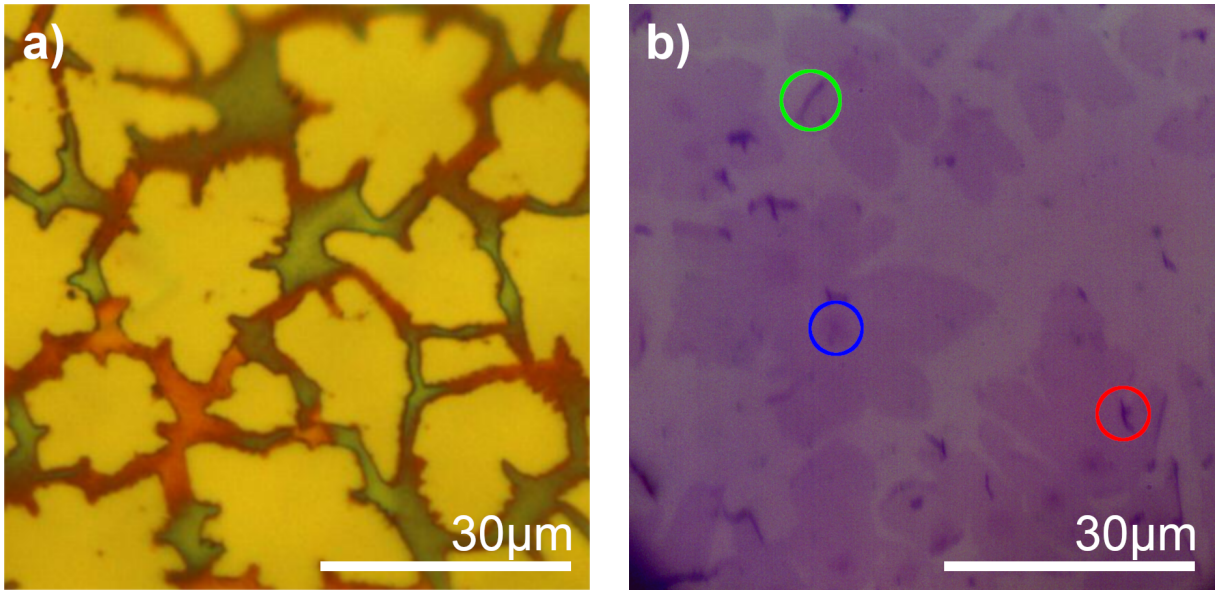

Figure 4.1: Images displaying graphene visualised on, a), growth foil via the oxidation of uncovered Cu, and, b), the corresponding image of transferred graphene on 300nm SiO_2.

typically cost £100,000s or £1,000,000s respectively, the HPM requires only a hot plate ($\sim$ £200) and a microscope. It also allows analysis of foil areas, depending on the size of graphene domain grown during CVD, on the cm^2 scale.

Figure 4.1 displays micrographs of graphene domains visualised, a), on oxidised foil and, b), after transfer to 300nm SiO_2 on Si from the same sample. Graphene domains correspond to the yellow regions in Figure 4.1 a) and the darker regions in Figure 4.1 b). To produce the colour contrast viewed in Figure 4.1 a), the Cu foil is heated on a hot plate after graphene growth at 120 °C for 5 minutes. As graphene acts as an oxygen-impermeable barrier, the Cu underneath graphene does not oxidise whilst the uncovered Cu foil will oxidise [68, 279].

To verify the validity of the HPM, partially grown graphene is transferred from foil to SiO_2 capped Si using the polymer-assisted transfer method, which is described in detail within Chapter 3. Transfer of the graphene from the foil to SiO_2 is necessary as it is difficult to decouple the properties of graphene from its native growth substrate for analysis. 300nm SiO_2 is used as the capping layer, because it renders thin graphene layers visible due to thin film interference effects and the contrast between an imaged graphene flake and the adjacent bare SiO_2 substrate can be used to estimate the graphene layer thickness [21]. As an example of thickness identification, the area of increased contrast highlighted by the blue ring in Figure 4.1 b) indicates a region of double-layered graphene which, given its location at the centre of the graphene domain, is likely situated at the nucleation site for the graphene domain [275, 280].

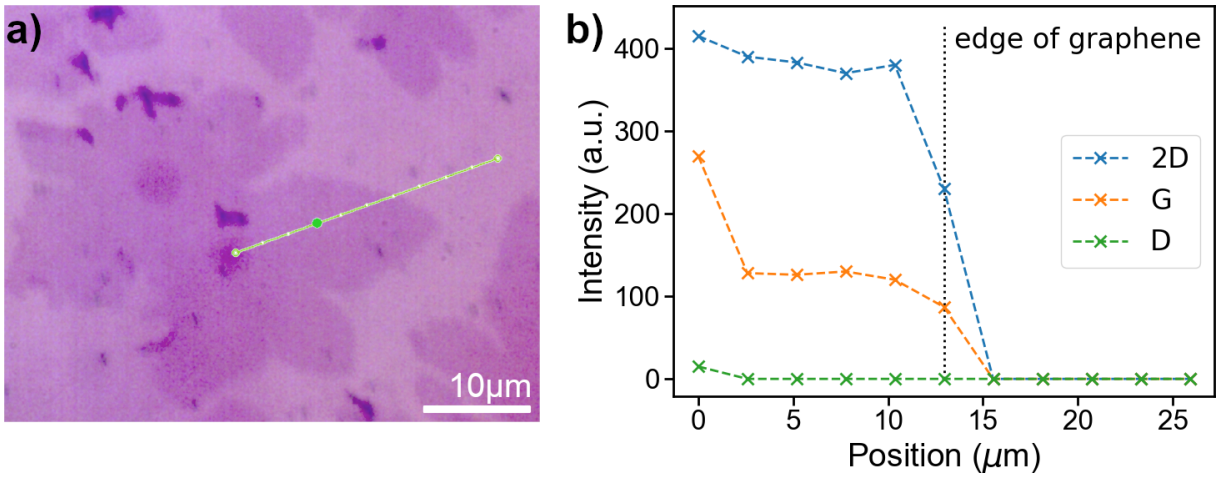

Figure 4.2: a) Micrograph of graphene domain transferred to 300nm SiO_2on Si with the path and points of the Raman line map indicated by the green line and green dots respectively.

It is observed that the domain size and morphology is comparable for graphene imaged on oxidised foil and on SiO_2. Images were not taken from the same growth area before and after transfer, because of the homogeneity of growth behaviour across the foil and difficulty of retaining feature orientation throughout the transfer process. Both images display lobed domains, with diameters of approximately 30 µm and lobe lengths of between 5 µm and 10 µm. The inter-domain separation is also similar. As graphene morphology should be preserved during polymer-assisted transfer, as reported by Reina et al. [281], it is therefore reasonable to conclude that the yellow regions observed on post-growth oxidised foils are representative of graphene coverage on the copper foil and that the HPM is an acceptable technique for rapid, low cost analysis of graphene growth behaviour.

Raman spectroscopy is used to verify that the domains observed on SiO_2 are graphene, by recording a map of Raman spectra across a lobe of the graphene domain displayed in Figure 4.2 a). Raman spectroscopy provides a powerful, non destructive method for analysing graphene quality, but becomes time consuming when large areas of material must be analysed, and is discussed in detail in Chapters 3 and 5. Figure 4.2 b) displays a plot of the D, G and 2D peak intensities as a function of position extracted from the obtained Raman spectrum linemap. The D peak requires the graphene lattice symmetry to be broken to become Raman-active, and as such can be used as a measure of defect density within the graphene lattice [236, 240, 282]. Here, we see that the 2D peak intensity remains approximately constant, regardless of graphene layer number, as shown by the multi-layer region at the centre of the domain, and subsequently the 2D/G ratio is often used as an indication of whether graphene is single- or multi-layer [226]. The plot in

Figure 4.2 b) shows that the defect density is below the detection limit of the Raman spectrometer settings used across the graphene domain, except for at the domain centre where the multi-layer nucleus is observed. The increase in D intensity is explained by the presence of non-zig-zag edges at the adlayer domain edges [283], which are Raman active due to the presence of incomplete six-fold carbon rings [236, 240, 282]. The homogeneity of the D/G ratio indicates that our CVD graphene is largely defect free within the graphene domain.

Because the graphene domain edge is not necessarily Raman D-peak active, the HPM is a better tool for quantifying domain boundary density, as the lack of a D-peak at the graphene domain edge displays that domain boundaries may not necessarily be identified via Raman spectroscopy. The HPM also allows rapid assessment of entire images with areas on the mm^2 scale, whereas assessment via Raman mapping would require lengthy measurement times and analysis periods to achieve a similar outcome. In addition, whilst it was necessary to complete at least one transfer of graphene to SiO_2 to confirm that the HPM is suitable for graphene visualisation, the polymer assisted transfer method introduces undesired residues and damage to the graphene film, highlighted by the red and green rings respectively in figure 4.1 b). The introduction of these features during transfer can obfuscate graphene domain details, hindering the analysis of growth behaviour. Greater colour contrast is also generally observed between graphene and oxidised copper, than graphene on SiO_2 and SiO_2, which makes it easier to extract graphene coverage data from images of graphene on oxidised copper, particularly when inhomogeneous lighting across high-magnification microscope images is taken into account. Analysing graphene coverage on the copper foil also removes a process step, allowing for better process flow and more rapid growth behaviour analysis.

Parameter Extraction

To characterise variations in growth behaviour under different conditions using the HPM, graphene growth is deliberately terminated before adjacent graphene domains stitch together to accurately determine ρ_D and domain size at each parameter stop. At least 5 images are collected from across each oxidised foil in order to capture growth behaviour variation across the catalytic Cu surface. Using ImageJ, the images are converted into black and white, as displayed in Figure 4.3 to analyse ρ_D and domain area. As the copper foil used within this research is polycrystaline, with crystal domains of typically a few

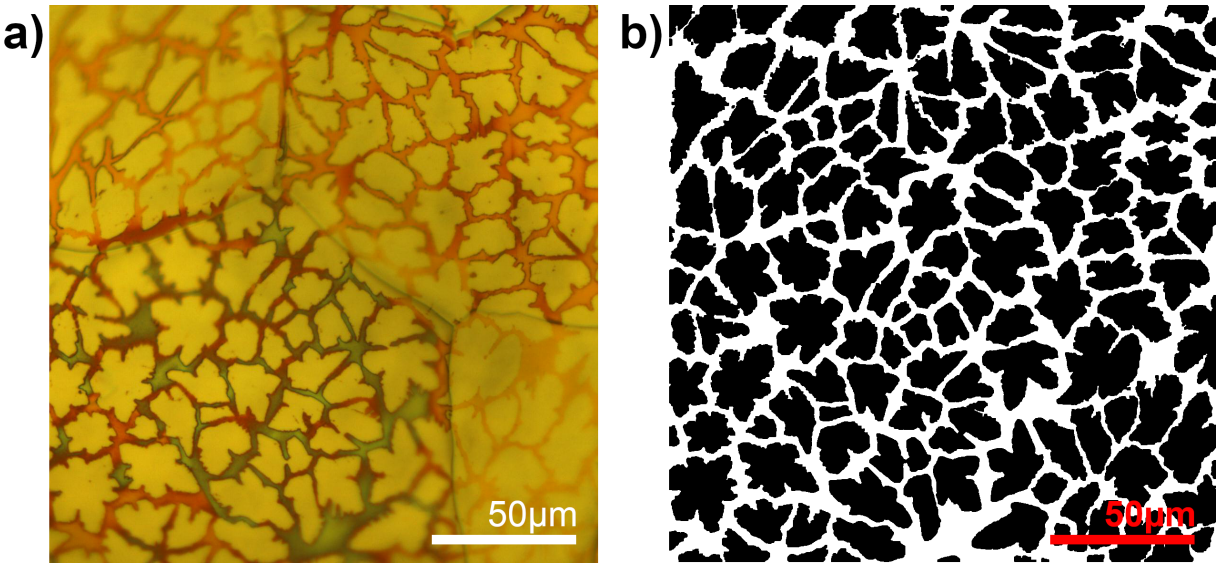

Figure 4.3: Images displaying graphene visualised on, a), growth foil via the oxidation of uncovered Cu, and, b), the same image after conversion to black and white for particle analysis with ImageJ. Blurring at the corners of image a) are due to these regions being out of focus because the foil is not perfectly flat post growth.

hundred μm across after the pre-growth annealing stage, many different crystallographic orientations of copper are present within the underlying foil. This means that the colour of the oxidised copper varies between different images and between different areas within the same image, meaning that a variety of different approaches are required to convert images to black and white for analysis. Due to the wide range of foil areas imaged throughout this chapter, a hierarchical process using ImageJ/FiJi [284] for graphene domain feature extraction was used to create the black and white image for particle analysis.

Feature retention is important for much the analysis within this chapter. Therefore, a set of increasingly manual techniques were required for satisfactory extraction of graphene coverage from the HPM images.

The most automatic method, which was most prone to feature loss, was the use of the native ImageJ colour threshold function. Colour thresholding typically worked with high magnification images, but often failed for lower magnification images because more copper grains were imaged, resulting in a wide spread of oxide colours.

If colour thresholding did not work, the image being analysed would be split into its RBG channels and a simple greyscale threshold would be applied. This method is less sensitive to copper oxide colour variances, but still struggles with shadowing caused by foil surface features such as grain boundaries.

Finally, if full image thresholding did not acceptably reproduce the cover and morphology of the imaged graphene domains, manual feature extraction was carried out through

the combined use of a colour wand and manual outlining.

Once a black and white image of the domains on the copper surface has been successfully created without significant loss of detail, ImageJ's particle analysis tool is used to extract particle data from the image. Data for the number of domains, total domain area fraction, individual domain area and individual domain perimeter are recorded from each image and analysed to provide values for graphene ρ_D, graphene domain coverage ratio, graphene domain area and graphene domain growth rate. From these extracted parameters it is then possible to quantitatively compare the quality of CVD graphene films grown under a variety of parameters, based on the ρ_D and domain area of the CVD graphene.

4.1.2 Copper Foil Polishing

When received from the supplier, the copper foils used for CVD are generally quite rough. To improve graphene growth and reduce batch-to-batch variability, electropolishing is used to reduce surface roughness and remove contaminants ingrained within the top layers of the copper foil [154, 274–276, 285]. Topological features on the copper foil surface, such as protrusions or depressions created during foil fabrication, and boundaries between copper grains within the foil, create regions with effectively reduced radius of curvature for the surface copper atoms. Because of the reduction in radius of curvature, there is an enrichment of dangling bonds from the copper surface atoms which provides increased opportunity for interaction between the copper foil and adsorbed CH_4 molecules [286, 287]. These areas of increased interaction have a greater chance of dehydrogenating adsorbed CH_4 to form CH_y, where $3 > y > 0$. As a result, the concentration of active carbon species increases around topological features, meaning that carbon supersaturation, which is required for graphene nucleation, is achieved more easily. By reducing surface roughness and therefore the density of surface features, which promote graphene domain nucleation, via electropolishing, the density of graphene domains can easily and reproducibly be reduced [154, 274–276, 288].

Copper foil is electropolished in a home-built eletrochemical cell, pictured in Figure 4.4. The vessel used as the electrochemical cell is a thin layer chromotography (TLC) tank from Sigma Aldrich (Z146226), chosen specifically as the straight side walls of the TLC tank promote an even electrical field across the cell which assists homogeneous polishing of the foil. An 85% phosphoric acid (H_3PO_4) solution is used as the electrolyte during

electrochemical polishing with two similar sheets of copper foil acting as the electrodes. The copper foils are connected to a Keithley DC source meter which provides the potential across the electrochemical cell to drive electropolishing. Material is removed from foil attached to the anode (positive terminal), polishing the foil during the process; at the same time, material is deposited on the foil connected to the cathode (negative terminal). As our electrochemical set up lacks a reference electrode, a suitable polishing potential is identified empirically by observing the potential at which bubbles appear on the Cu surface to be polished. The optimum polishing potential is set below this point to avoid significant pitting of the foil during polishing, and is found to be 2.0 V within our system.

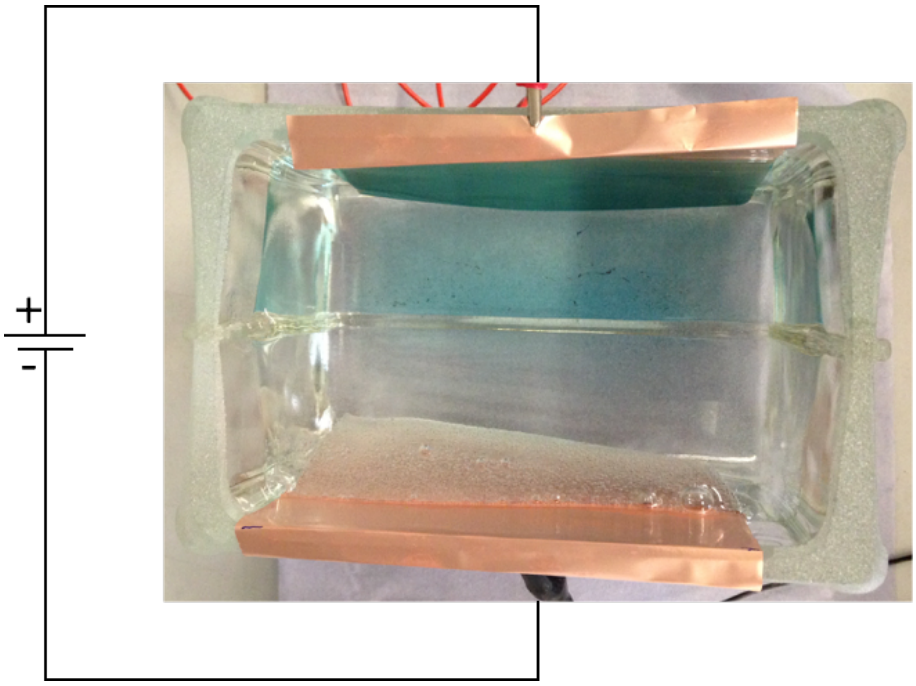

Figure 4.4: A top down view of the home-built electrochemical cell used for copper foil polishing prior to graphene CVD. The foil to be polished is connected to the anode of a DC power supply, with a second foil acting as the counter electrode.

Figure 4.5 displays AFM traces at 50 µm and 5 µm scan sizes taken from Alfa Aesar foil (part number 46365) before electropolishing (a-b) and after 10 minutes (c-d), 20 minutes (e-f) and 30 minutes (g-h) of electropolishing. Both 50 µm and 5 µm scan lengths are used to provide a more complete picture of copper surface roughness evolution. Foil RMS roughness (R_q) is observed to decrease with increasing polishing time, with the greatest reduction of roughness occurring within the first 20 minutes. A minor reduction of R_q from 5.7 nm to 5.1 nm is seen between 20 and 30 minutes polishing at the 5 µm length scale, which suggests that polishing for much longer than 30 minutes would have little effect on the copper surface. This is not unexpected, as the majority of large protrusions are likely to have been removed within 20 minutes of polishing. The 20 minute 50 µm

scan returns an anomalous increase in surface roughness when compared with the AFM data for 10 minute polished foil. The increase in roughness is explained by tip-surface tracking artefacts, seen in the bottom half of Figure 4.5 e). It is observed that if the image is cropped to remove these features, R_q reduces to 59.64 nm. The relatively large RMS values returned from the 50 µm scans are therefore attributed to long-range texturing of the copper foil, but are included to demonstrate that the foil becomes smoother at both the micro and macro scale with increased polishing time. Ultimately, the foil is found to decrease from 182.7 nm and 92.1 nm for unpolished foil to 82.4 nm and 5.16 nm for 50 µm and 5 µm scans respectively after 30 mins electropolishing at 2.0V. Finally, as electropolishing removes mass from the polished surface, extended polishing causes the foil to thin, and 30 minutes was found empirically to be the upper limit for electropolishing time, as polishing time longer than 30 minutes meant that the foil became too fragile to handle.

The images in Figure 4.5 raise an interesting question however, as to how graphene is able to grow continuously across a foil surface when, as indicated in Figure 4.5, the foil surface has much greater R_q of $\sim$ 5.6 nm, and steps and features on the order of 10 nm, than the graphene monolayer thickness of 3.3 Å even after extended electropolishing. The surprisingly high-quality of graphene grown on such comparatively rough copper can in fact be attributed to multiple factors. Graphene can be considered, mechanically, to be polymeric in nature [289], evidenced by its high flexibility [14, 113, 200], which allows graphene to grow conformally across the copper surface. Indeed, graphene domains are frequently observed to grow across even large copper surface features such as crystal boundaries [161, 162, 289–291], a behaviour which is observed throughout this research, most clearly within Figure 4.14. Additionally, throughout the heating and annealing stages, the copper grains enlarge and the copper surface becomes smoother [292], with extended (multiple hour) annealing within an H_2 environment capable of creating surfaces with sub-nm RMS roughness [293]. Finally, the growing graphene domains are found to cause the underlying copper surface to restructure into smooth steps, which is widely observed within the literature [161, 290, 293–295] and is ascribed to pinning of the copper surface features by the growing graphene [289] and oxidising defects on the copper surface [293].

Figure 4.6 a) displays an AFM image taken from a partial graphene growth still on its copper foil growth surface. The graphene was grown on electropolished copper foil using gas flow rates of 600 sccm H_2 and 200 sccm CH_4 at a growth temperature of

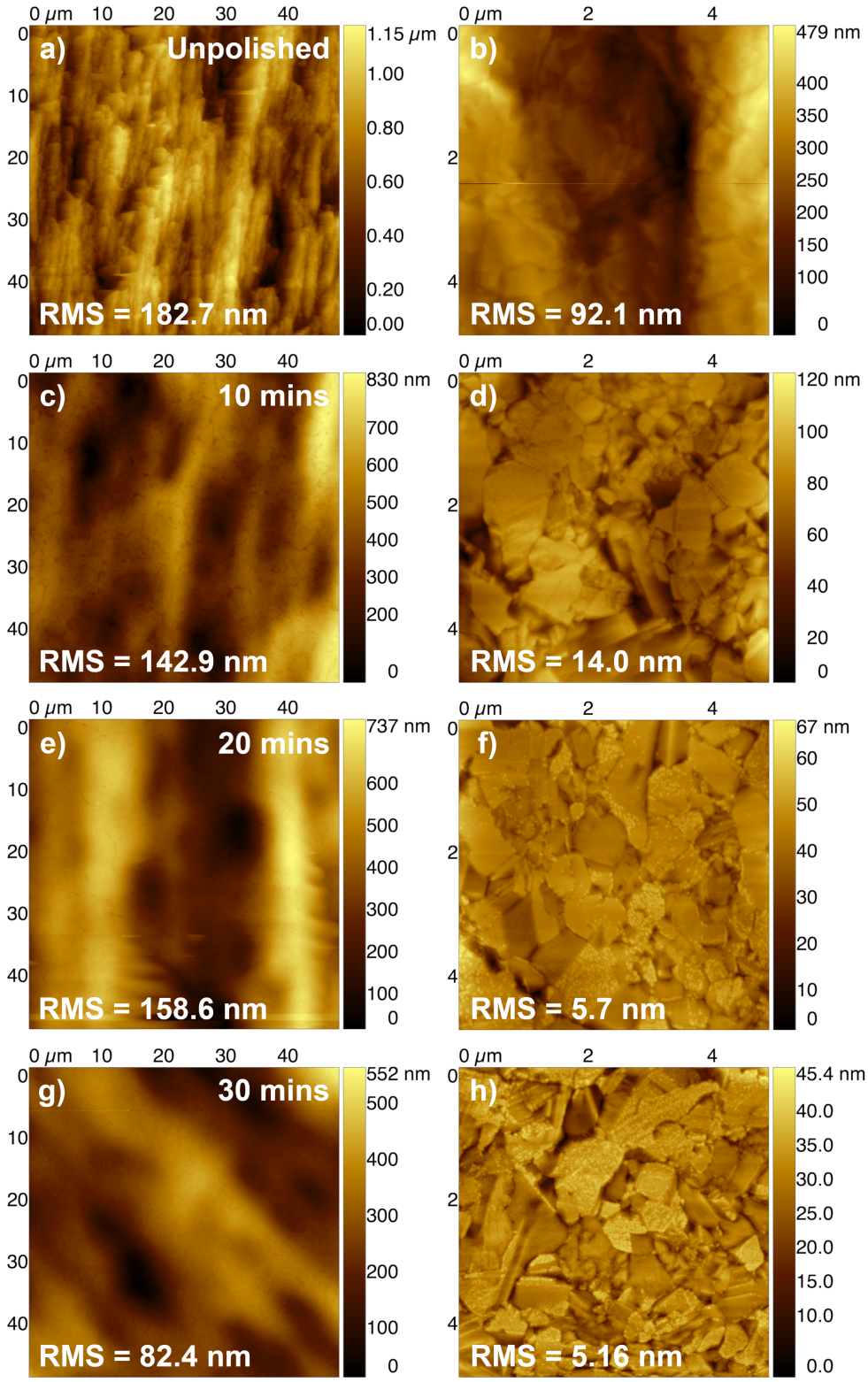

Figure 4.5: AFM images acquired from copper foil (a,b) as received; (c,d) after 10 mins polishing; (e,f) after 20 mins polishing and (g,h) after 30 mins polishing.

1050 °C and a chamber pressure of 25 mbar for 1 minute. Smooth, stepped regions are observed where the graphene has grown over the copper surface, similar to foil surface behaviour reported elsewhere within the literature [293, 295], whereas the bare copper foil shows relatively increased roughness. We attribute this increased roughness of the bare

copper foil to copper sublimation from the uncovered foil surface throughout the graphene growth process [161]. By masking the graphene covered regions within the AFM image it is possible to assess the RMS surface roughness of the bare copper foil and graphene-covered copper foil separately. R_q values are found to be 11.8 nm and 7.83 nm for bare and graphene-covered foil surfaces respectively. Whilst this appears to return a slight increase in R_q from the minimum recorded post-polishing foil R_q, these values correspond to a scan area of 20 μm $\times$ 20 μm, which is of a scale more comparable with the large area scans presented in Figure 4.5. As such these RMS values indicate a substantial reduction in surface roughness throughout graphene growth. However, the surface roughness of even the graphene-covered copper foil indicates the presence of surface features which are an order of magnitude greater than the monolayer graphene thickness. To explore this further, line profiles were extracted from across and along the terraces observed in graphene-covered copper regions, which are plotted in Figure 4.6 b). Figure 4.6 c) displays the height profile measured along a copper terrace in isolation, so that the profile features can be more clearly observed. The R_q of these lines are then calculated via Equation 4.1 [296]:

$$R_q = \left(\frac{1}{X} \Sigma \left| Z^2(x) \right| \right)^{\frac{1}{2}} \tag{4.1}$$

where X is the number of data points taken and Z(x) is the deviation of the height value at point x from the mean height value of the height profile. It is found that the R_q of the line taken across step edges (line 1) is 5.54 nm, whereas the R_q of the line taken along a step facet (line 2) is 0.39 nm. Therefore, the relatively large R_q of these graphene-covered regions to with graphene monolayer thickness, is dominated by the observed step edges. Indeed, within step facets, the surface roughness is comparable with the thickness of a graphene monolayer, which goes some way to explaining the growth of largely defect free graphene via CVD. Finally, as mentioned above, graphene can be considered to act mechanically similar to a polymer [289], which explains how it is capable of growing continuously around or across comparatively large surface step features.

To observe the effect of foil roughness on graphene nucleation behaviour, partial graphene growth is carried out by flowing 1000 sccm H_2 and 100 sccm CH_4 at a growth temperature of 1050 °C for 5 minutes. Figures 4.7 a) and b) display optical micrographs of graphene (yellow regions) grown on unpolished foil and foil prepared by electropolishing for 30 minutes respectively. Graphene domain ρ_D is observably lower and domain size is greater for graphene grown on polished foil than that for graphene grown on unpolished

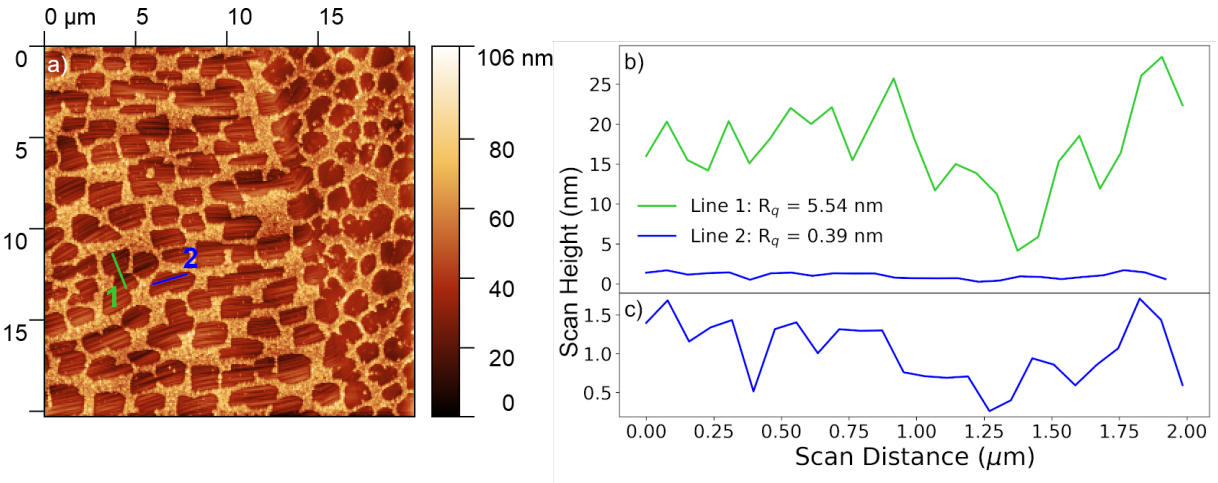

Figure 4.6: a) AFM scan of partial graphene coverage still on its growth copper foil; b) plot of line profiles extracted from the indicated lines within a); c) individual plot of line 2 to allow feature visualisation.

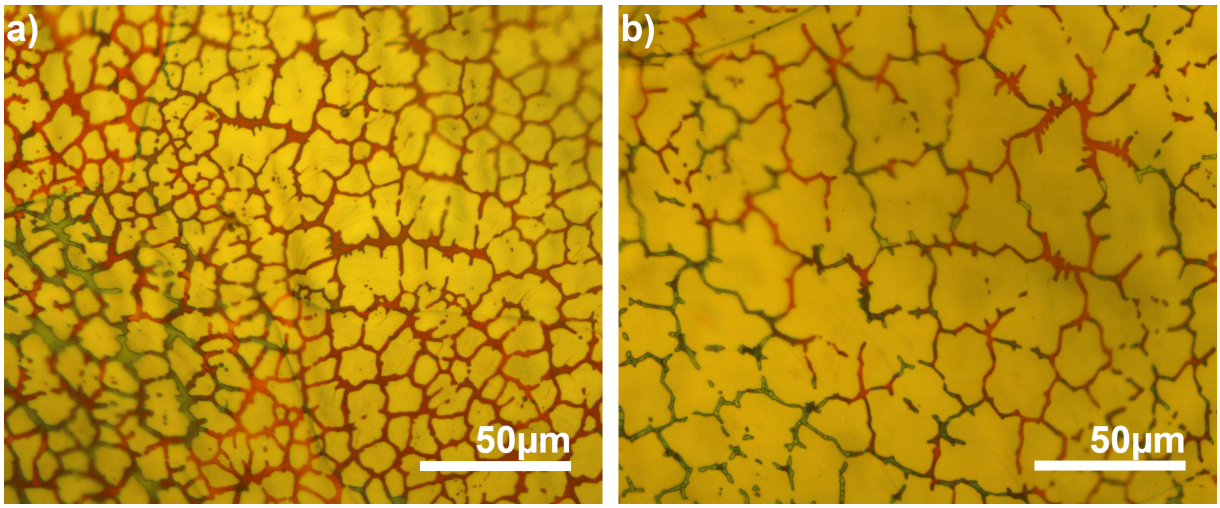

Figure 4.7: Images taken from partial graphene growths under the same condition on a) unpolished and b) 30 min polished foil.

foil. Figures 4.8 a) and b) display the mean nucleation densities and domain areas respectively, extracted from multiple micrographs taken across hot-plate tested growth foils. The extracted values show that overall mean ρ_D reduces from 13 000 mm^{-2} to 5000 mm^{-2} and that overall mean domain area increases from 30 µm^2 to 155 µm^2. The reduction of mean domain density is explained by the reduction of copper foil surface roughness, reducing nucleation sites for graphene growth. The reduction of nucleation sites increase the probability that carbon fragments are captured by a growing graphene domain rather than forming a new domain nucleus which therefore leads to lower domain density and increased domain area. As reduced foil surface roughness both reduces domain ρ_D and increases domain area for CVD, all subsequent graphene growth presented within this thesis is carried out on copper foil which has been electropolished within 85% phosphoric

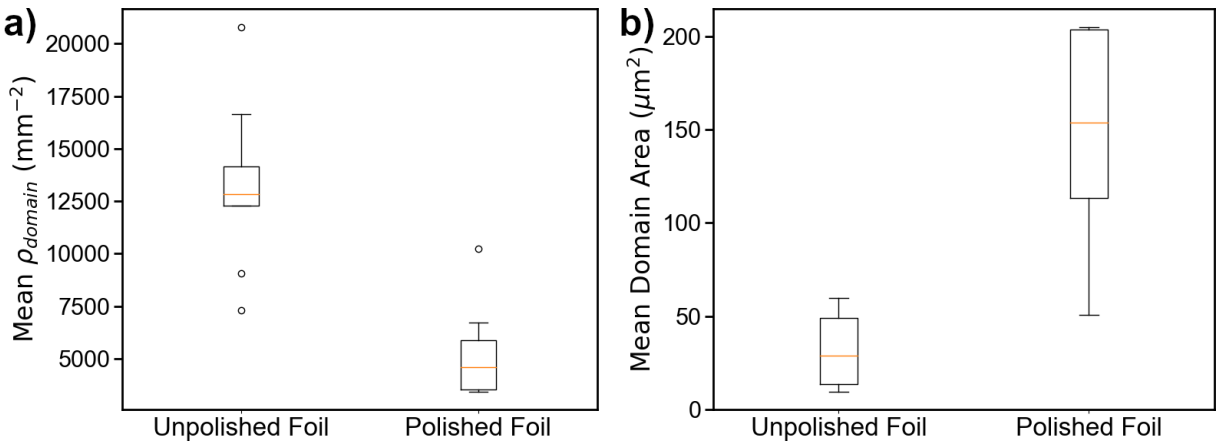

Figure 4.8: Boxplots displaying values for a) domain density and b) domain area extracted from multiple optical images of partial graphene coverage on polished and unpolished copper foil.

acid for 30 minutes at a potential of 2V.

4.1.3 Growth Temperature

Temperature, which is chosen as the the next stepwise growth optimisation is discussed within this section. Growth temperature is known to influence the nucleation and growth kinetics of graphene CVD. Increasing growth temperature should result in a), increased domain growth rate, and b), decreased domain ρ_D [83, 164, 274, 297–299].

We first discuss the effect of increased domain growth rate with increased growth temperature. For graphene domains to grow, there must be active carbon species available to join the edge of the domain. Considering CH_4 as the carbon feed-stock, gaseous CH_4 must undergo the following steps, illustrated in Figure 4.9 for the carbon to join a growing graphene domain:

1. CH_4 adsorbs onto the copper surface.

2. The copper foil catalyses the dehydrogenation of the CH_4 to create CH_y species, where $3 \geq y \geq 0$. CH_y fragments will often join together to form C_xH_y species.

3. C_xH_y species diffuse across the Cu surface.

4. The C_xH_y fragment attaches to the growing edge of the graphene domain.

All of the above steps are rate dependant upon temperature, following an Arrhenius relationship, $A = A_0 exp(-E_a/k_BT)$, where A is the successful reactions per second, A_0 is the attempt rate per second, E_a is the process activation energy, k_B is Boltzmann's

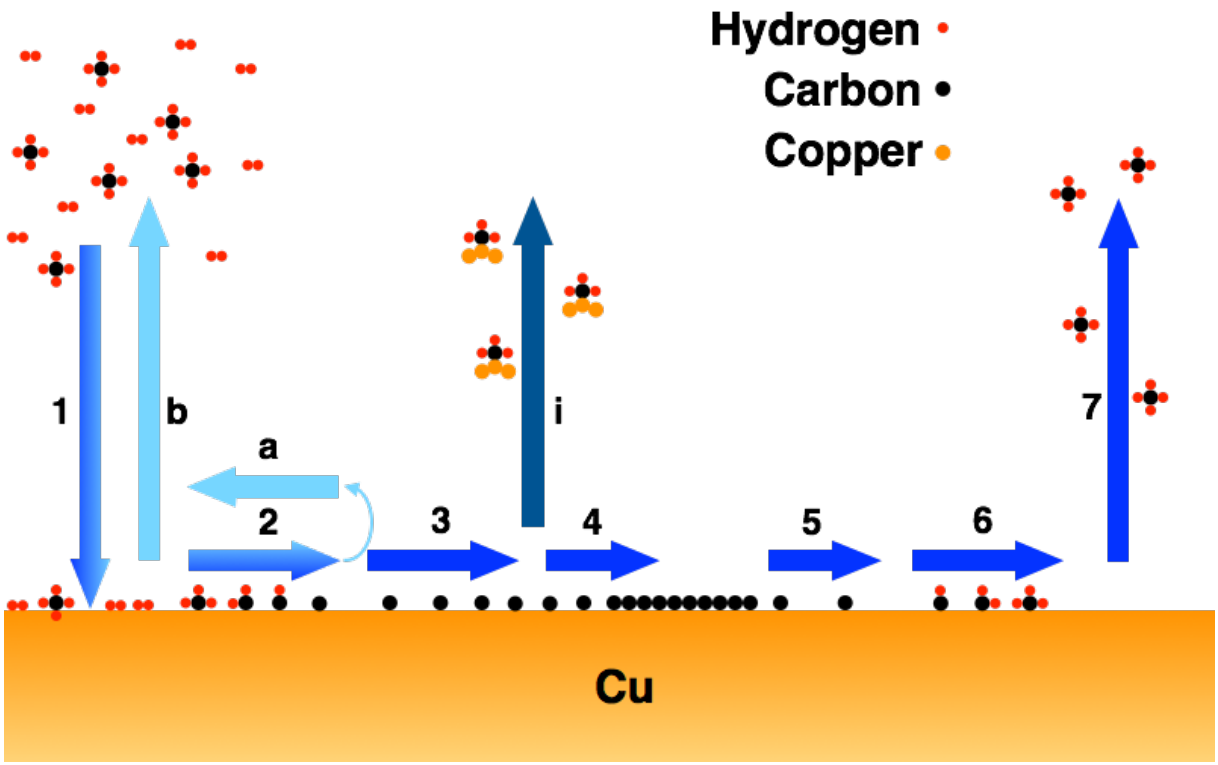

Figure 4.9: Schematic representation of the processes and interactions C-species undertake on the Cu surface during graphene CVD.

constant and T is temperature. Increased temperature results in a greater rate of reaction for each step. During graphene CVD with a sufficiently large partial pressure of CH_4, Kim et al. show that the rate limiting step – the single reaction step with the largest activation energy – is that of carbon attachment at a growing graphene edge, with $E_a = 2.6 \pm 0.5$ eV [274, 300]. If the carbon concentration is reduced significantly, then the rate limiting step may change to carbon surface diffusion [301]. Regardless of the rate limiting step, as T increases, all intermediate steps for graphene growth occur with increased frequency and therefore domain growth rate increases with increasing temperature.

Conversely, ρ_D decreases with increasing temperature. ρ_D is affected by the competition between the processes of carbon-adatom capture by existing nuclei, carbon-surface diffusion and re-evaporation of carbon-adatoms [274] (labelled processes 4, 3 and b respectively in Figure 4.9). At elevated temperatures, the number of carbon-atoms required to form a stable nucleus increases [158], increasing the probability that an adatom on the copper surface will desorb before joining or forming a stable nucleus. During graphene CVD at temperatures >870 °C, the desorption rate (process b in Figure 4.9) is significant when compered with the surface diffusion of the carbon-adatoms (process 3) [274]. The carbon-adatom lifetime and domain nucleation rate can then be considered to be desorption controlled, with increased growth temperature leading to increased adatom desorp-

tion and thus reduced ρ_D. Additionally, increased temperature results in increased copper evaporation from the foil surface (process i), which removes surface bound C-species with evaporating copper[302]. This effect will also lead to reduced ρ_D with increased temperatures at constant chamber pressure.

In this section the effect of growth temperature on graphene ρ_D and domain growth rate is investigated using the HPM. Temperature is chosen as the first parameter for investigation after foil pre-treatment, as the interpretation of the results should be largely independent of the other growth parameters. Graphene growth is carried out at temperatures between 900 °C and 1050 °C in 50 °C steps. 1050 °C is chosen as the maximum growth temperature as the melting point of copper is 1083 °C at 1 atm [303]. We use a base growth recipe using H_2 and CH_4 diluted to 2% within N_2, which are flowed into the chamber at a rates of 600 sccm and 200 sccm respectively, resulting in a growth pressure of 25 mbar. This is a combination of recipes from Hussain et al. [304] and Wu et al. [58]. To improve the economy of use of the 2% H_2/N_2 mixture, a reduced rate flow of 100sccm is used during the ramping and annealing phases prior to growth, which results in a chamber pressure of 7 mbar. This reduced flow rate is used prior to growth during all the subsequent graphene growth experiments reported within this thesis. Copper foil from Alpha Aesar, electropolished for 30 minutes at a potential of 2V, is used as the growth substrate and growth is terminated after one minute to provide partial graphene coverage of the copper foil for nucleation and growth analysis. No appreciable growth is observed within our system at growth temperatures of 900 °C or below.

The HPM images in Figure 4.10 clearly show that the graphene domains (yellow regions) increase in area with elevated growth temperature. A reduction in domain density with increasing temperature is also observed, which is most apparent between the images taken from growth temperatures of 1000 °C and 1050 °C. The domains grown at 950 °C, seen in image 4.10 (a), are compact but have not enlarged enough for detailed morphology to be observed. Domains grown at 1000 °C, Figure 4.10 (b), are considerably larger those grown at 950 °C and are compact in morphology with larger domains appearing to be irregular hexagonal in shape. The domains seen in image 4.10 (c) are yet further enlarged with widely varying morphology between flakes. As with the lower temperature growths, the domains are compact in nature but are inconsistent in morphology, although often hexagonal.

Values for the mean domain area and ρ_D after one minute of growth are plotted against temperature in Figures 4.10 (d) and (e) respectively. Mean domain area clearly increases

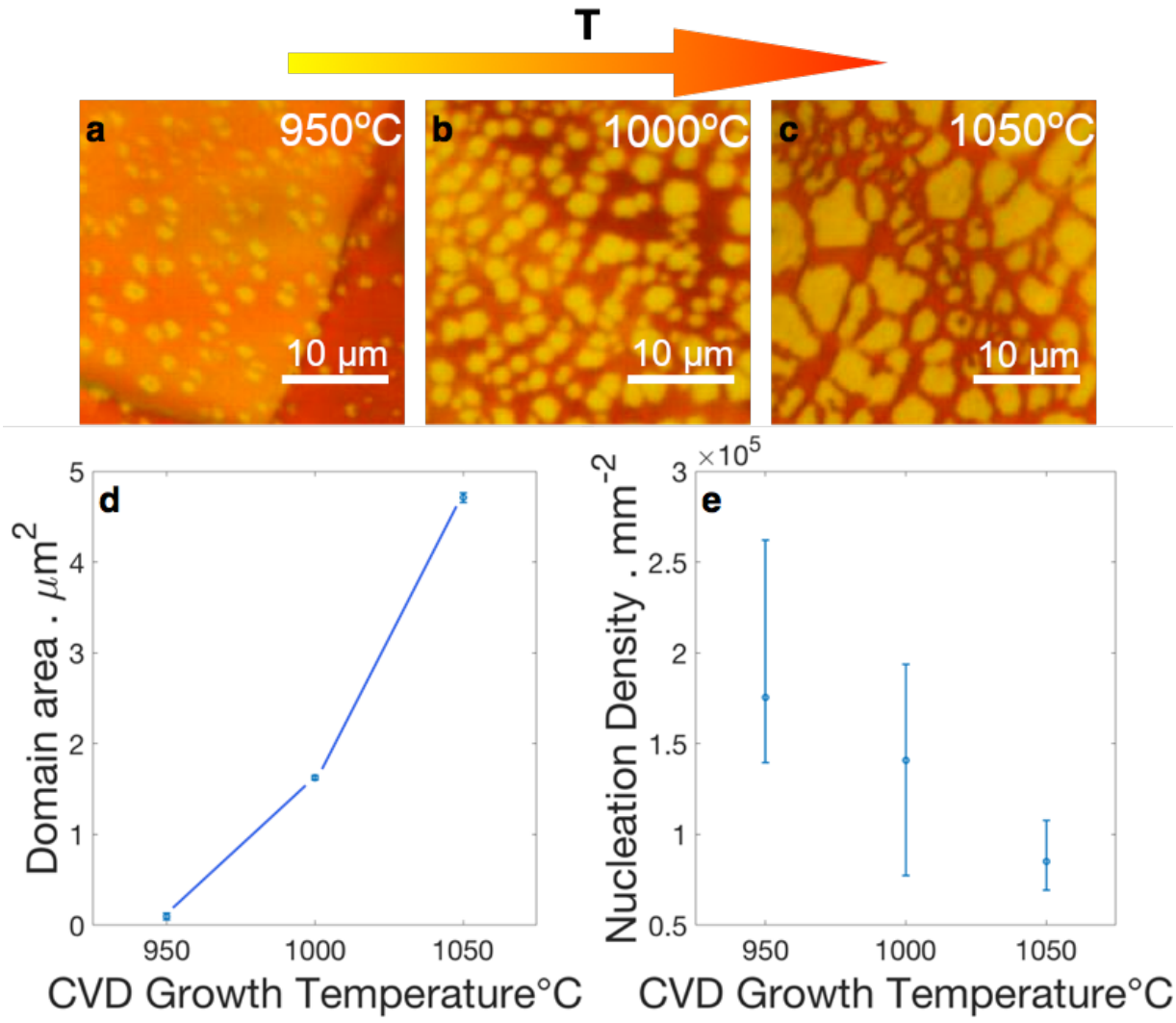

Figure 4.10: Images showing graphene growth behaviour at temperatures of 950 °C (a), 1000 °C (b) and 1050 °C (c); scale bars are 10 µm. Figure (d) displays a plot of ρ_D and graphene coverage ratio against growth temperature.

as a function of temperature, from a mean area of 0.1 µm^2 at a growth temperature of 950 °C, to 4.8 µm^2 at 1050 °C. Additionally, ρ_D displays a decreasing relationship as a function of temperature, with mean ρ_D decreasing from 2.8×10^5 cm^{-2} to 0.8×10^5 cm^{-2} when the temperature is increased from 950 °C to 1050 °C. As decreased ρ_D, increased domain area and increased domain growth rate are all desired for improved industrial CVD graphene growth, all future graphene growth reported within this work is carried out at 1050 °C, unless otherwise stated.

4.1.4 Hydrogen:Methane Ratio

Hydrogen is normally used during graphene CVD to provide a protective reducing atmosphere to avoid unwanted oxidation [163, 271, 305]. Beyond providing a protective atmosphere, the ratio of H_2:CH_4 present within the CVD chamber has a significant effect on graphene nucleation and growth behaviour [152, 157, 163, 164, 271, 302, 306, 307]. By tuning the H_2:CH_4 ratio, it is possible to control the ρ_D and domain morphology of CVD graphene [157, 163, 164, 291, 306, 307]. Within the literature, there are many different reports on the effect of growth gas mixture on graphene growth. However, the general reported trend is that increasing the ratio of hydrogen to methane reduces the ρ_D of CVD graphene on copper, but it must also be emphasised that recipes are not directly transferable between reactor systems.

It should also be understood that there are upper and lower bounds to this general trend – below a H_2:CH_4 ratio of $\sim$ 1:1, there appears to be little change in growth behaviour, whilst at very high H_2:CH_4 ratios, typically above a few 100:1, graphene becomes thermodynamically unstable and does not grow [164]. Additionally, it has been shown that H_2:CH_4 ratios for stable graphene growth are temperature dependant [164]. We therefore explore the effect of H_2:CH_4 variation on the growth of graphene films at our optimised growth temperature of 1050 °C, as identified in the previous section. Due to system limitations, neither the hydrogen or methane flow could be kept constant across all experiments; Table 4.1 summarises the parameters used during each growth. As seen in the first column of Table 4.1, H_2:CH_4 ratios of 3:1, 10:1, 100:1 and 250:1 were studied within this section. The H_2:CH_4 ratios of 10:1 and 100:1 were chosen to observe growth behaviour variation across an order of magnitude change in H_2:CH_4 ratio. The H_2:CH_4 ratio of 3:1 was retained from Section 4.1.3 as the lowest ratio setpoint, because it was considered that the use of a 1:1 H_2:CH_4 ratio, whilst providing an order of magnitude

H_2 : CH_4	H_2 flow rate . sccm	CH_4 flow rate . sccm	$P_{chamber}$. mbar	T_{grow}. minutes
3:1	600	200	25	1
10:1	1000	100	35	5
100:1	1000	10	33	15
250:1	1000	4	33	30

Table 4.1: Growth parameters used during each variation of gas mixture.

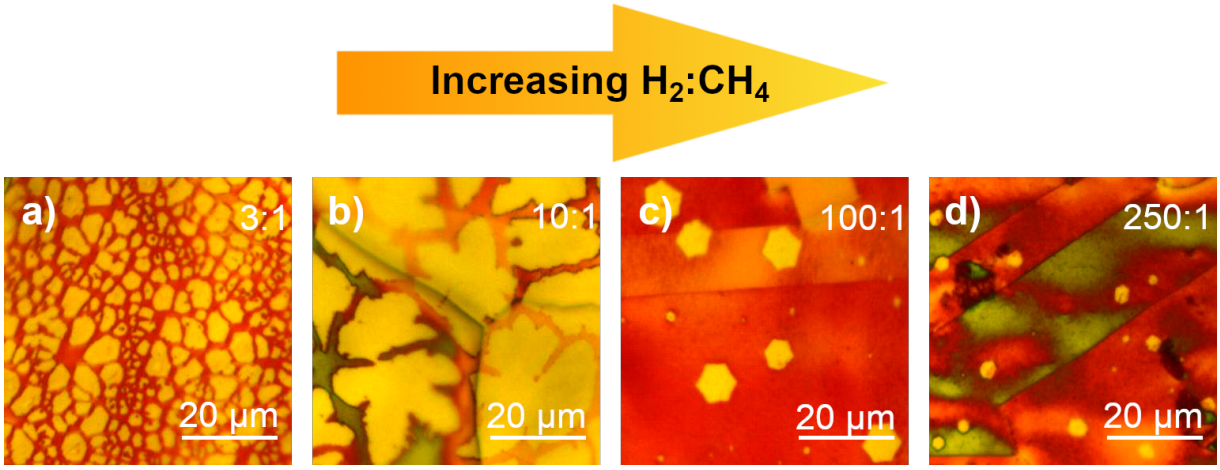

Figure 4.11: Images (a) to (d) display graphene nucleation and growth behaviour with H_2:CH_4 ratios of 3:1, 10:1, 100:1 and 250:1 respectively.

variation below 10:1, would result in too great a deviation in chamber pressure from that observed at other ratio setpoints. Finally, the H_2:CH_4 ratio of 250:1 was chosen as it represents the highest stable ratio set point available within our system. Further ratios between 10:1 and 100:1 were not studied within this section due to the revisiting of H_2:CH_4 ratios between 10:1 and 100:1 within section 4.1.6.

Figure 4.11 displays HPM micrographs for graphene grown on copper foil after visualisation with the hot plate test, and the extracted values for ρ_D and domain growth rate at each H_2:CH_4 ratio are plotted in Figure 4.12. From both Figure 4.11 and Figure 4.12, it is clear that increasing the H_2:CH_4 ratio has the desired effect of reducing ρ_D. However, there is an appreciable reduction in domain growth rate between growths carried out at 10:1 and 100:1 with the reduction of carbon availability being the dominant cause of this effect. As this section of the project is geared towards the development of industrially applicable graphene growth, 10:1 is selected as the optimum point within this optimisation stage, as it yields both reduced ρ_D and rapid domain growth rates.

It is also observed within Figure 4.11 that the growth mode of the graphene domains changes with the H_2:CH_4 ratio, in general agreement with existing literature [72, 157, 163, 291]. Ignoring the growth behaviour at 3:1 for now, because it returns poor graphene, there is a clear change in growth mode between 10:1, and 100:1 and 250:1, from lobed or

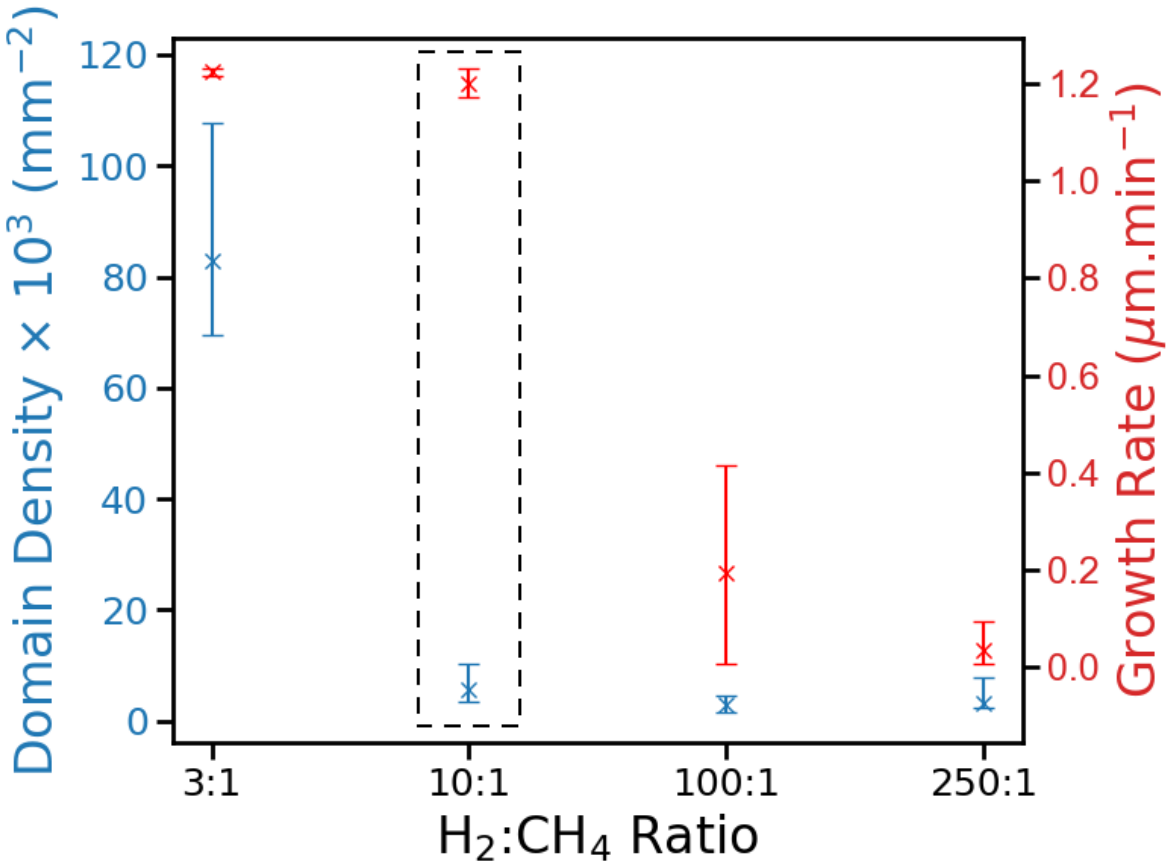

Figure 4.12: Plot displaying ρ_D (left y-axis) and domain growth rate (right y-axis) as a function of H_2:CH_4 ratio for graphene grown at 1050 °C.

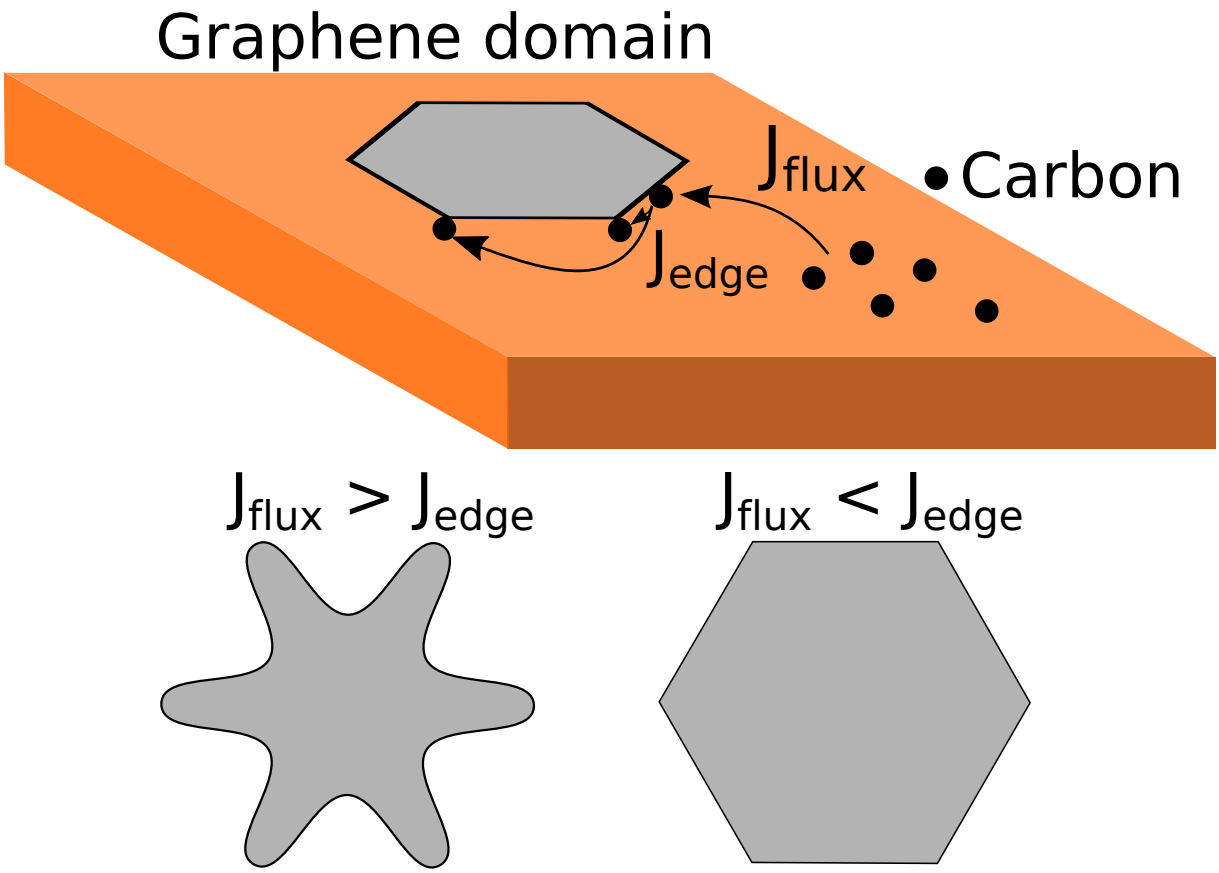

Figure 4.13: Schematic diagram of rates for incoming carbon attachment to a growing graphene domain (J_{flux}) and subsequent diffusion of the freshly joined carbon around the domain edge (J_{edge}. The lower panels provide a crude illustration of how the graphene domain growth mode differs with changing relationship between J_{flux} and J_{edge}. This is included here as a reminder of the model described within the background chapter.

dentritic, to regular compact hexagonal. By using a models from literature regarding the growth of thin epitaxial films, the shapes obtained at these different H_2:CH_4 ratios can be understood in a qualitative manner, as previously described within Chapter 2.

As displayed schematically in Figure 4.13, the relationship between the rate of adatom attachment to the graphene domain (J_{flux}, process 1) and adatom diffusion along graphene domain edges (J_{edge}, process 2) determine the final graphene domain morphology [157, 158, 291]. For example, when $J_{flux} < J_{edge}$, compact, regular hexagonal domains result, similar to those displayed in Figures 4.11 c) and d), as there is sufficient time for freshly attached carbon adatoms to diffuse around the growing carbon domain edge to energetically favourable sites before further adatoms join the growing domain and interrupt the initial adatoms relaxation [157, 291]. Conversely, if $J_{flux} > J_{edge}$, adatoms have insufficient time to relax around the graphene domain boundary and dendritic or lobed growth results, as seen in Figure 4.11 b).

Finally, the graphene growth mode observed for graphene grown within a 3:1 atmo-

sphere (Figure 4.11 a)) does not easily fit within this framework. The growth behaviour observed at 3:1 is thought to result from an abundance of active carbon – carbon from successfully fully/partially dehydrogenated CH_4 – across the entire copper surface. With such large concentrations of carbon, nucleation due to carbon supersaturation occurs rapidly and at more than an order of magnitude more locations than observed for H_2:CH_4 ratios of 10:1 or more. The high carbon concentration also means that once nucleated, graphene domains grow rapidly and with irregular morphology due to rapid, almost isotropic attachment of further carbon atoms. Because of increased ρ_D, growing domains are constrained by their neighbouring domains, necessarily resulting in small domain areas, despite rapid domain growth rate. As the irregular graphene grown at 3:1 is of undesirable quality it will not be included in the subsequent discussion.

Explaining graphene growth modes with J_{flux} and J_{edge} provides an easily digestible conceptual framework, but glosses over the many interplaying processes which are involved within these mechanisms. From the data presented in Figures 4.11 and 4.12 as well as other existing research [307], the ratio of hydrogen to methane present during CVD has a clear effect on the balance between J_{flux} and J_{edge}. Increasing the relative ratio of hydrogen within the system should reduce J_{flux} through a composite effect of many proposed mechanisms.

As hydrogen is generally accepted to be an anisotropic etchant for graphene, favouring the creation of zig-zag edges at the edge of graphene domains or etched holes [163, 308], an increase in hydrogen relative to methane can be considered to decrease J_{flux} overall. Increased presence of hydrogen within the reaction chamber, due to copper-surface occupation by atomic H, shifts the dominant surface-bound carbon species from C_2 to CH, lowering total C availability and again reducing J_{flux} [309]. The detachment barrier for freshly attached carbon species at the graphene domain edge has also been shown to be lower for CH (1.08 eV) fragments than for C_2 (2.19 eV) [309]. This leads to a reduction of carbon detachment energy from existing graphene domain edges, which increases the removal of carbon from graphene domain edges, resulting in a further reduction of J_{flux}.

Additionally increasing the partial pressure of hydrogen within the system leads to greater H-termination of graphene domain edges. Various simulation studies have demonstrated that the energy of attachment for carbon increases at H-terminated edges when compared to metal terminated edges [307, 309], and again leading to reduced J_{flux} with increased hydrogen partial pressure.

Unfortunately, there is a lack of literature regarding the rate of relaxation for carbon

atoms around the perimeter of growing graphene domains within CVD as a function of hydrogen partial pressure. However, even if making the assumption that J_{edge} remains approximately constant under all CVD conditions, the above points coupled with the data from this research should convince the reader that hydrogen plays an important role within graphene CVD, and that by selecting the appropriate H_2:CH_4 ratio, a wide range of domain nucleation densities and shapes can be selected as desired.

Finally, a comment upon the reduction of carbon concentration between growing lobes within a dendritic growth mode. As copper is required to act as a catalyst for methane dissociation [310], areas between advancing lobes experience reduced catalytic activity. This leads to a reduction in carbon available for domain growth between the advancing lobes and may result in incomplete coverage [310]. The inhomogeneous carbon concentration on the copper surface may also lead to the advancing lobe fronts capturing more carbon than the edges between lobes, increasing growth rate for the lobe edges and thus reinforcing the lobed morphology. With this in mind, whilst 10:1 has been selected as the starting point for the next stepwise optimisation, the lobed growth behaviour observed at 10:1 may mean that the growth mode results in defective areas within the completed graphene film.

4.1.5 Use of a Non-Reducing Atmosphere Pre-Growth

The previous section showed that ρ_D can be tuned by altering the ratio of H_2 and CH_4 within the reactor, but also that there is a lower ρ_D limit imposed by the equipment and gas mixtures. Recently, several studies have shown that oxidising pre-treatment of the copper substrate can effectively reduce the ρ_D of graphene domains by at least an order of magnitude [63, 66, 70, 75, 153, 165, 266, 285]. Within this section, we explore the effect of using a non-reducing pre-growth anneal to improve upon the graphene growth achieved within Section 4.1.4.

When carrying out the experiments within Section 4.1.4, a reducing atmosphere was maintained within the reaction space throughout the entire CVD process by flowing hydrogen through the reactor. Chemically, reduction is the opposite of oxidation; an atom is reduced when it receives an electron from an interaction with another atom. Conversely, the oxidation of an atom occurs when it donates an electron (or more) to an oxidising atom. Therefore, the presence of hydrogen within the reaction space prevents the copper foil from oxidising during growth and reverses the oxidation of any oxidised copper via

the reaction: $CuO + H_2 \longrightarrow Cu + H_2O$. Whilst extended hydrogen annealing of copper foils prior to CVD graphene growth has been show to reduce copper surface roughness and, consequently, ρ_D [311], hydrogen annealing has also been shown to leave carbon present within the copper foil catalyst [285]. The presence of residual carbon within the copper foil, after annealing and prior to growth, means that super-saturation of carbon on the foil surface, which is required for graphene nucleation, is reached more easily at the start of the CVD growth phase, leading to increased ρ_D [164, 285]. By avoiding the use of a reducing atmosphere during the pre-growth annealing of the copper foil, trace oxidising impurities present within either the inert feed stock gas, or from ambient leaks into the CVD reactor, have the effect of mildly oxidising the copper foil. Such a nominally inert, but mildly oxidising atmosphere is referred to within this thesis as a non-reducing atmosphere, rather than an oxidising atmosphere, to avoid connotations of intentionally added oxygen above that present from ambient system leaks and feedstock impurities.

Oxygen is a much more effective etching agent for carbon than hydrogen [274, 285] and by mildly oxidising the foil during the ramping and annealing stages prior to graphene growth, carbon is scrubbed out of the copper foil, meaning that carbon supersaturation during CVD growth results from the presence of the carbon feedstock only, and not any pre-present carbon within the copper foil [164, 285]. Oxidation of the copper foil has also been suggested to passivate nucleation points on the copper foil surface, by interacting with the areas of increased dangling bonds which would otherwise become efficient dehydrogenation sites for CH_x, where $4>x>0$ [70]. By occupying, and thus passivating, graphene nucleation sites, surface oxygen increases the likelihood that a carbon species diffusing across the foil surface will join a growing domain, rather than forming a new graphene nucleus.

To study the effect of a providing a non-reducing atmosphere throughout the ramping and annealing stages of CVD graphene growth, graphene was grown to partially cover the copper growth foil using the optimum H_2:CH_4 ratio of 10:1, as identified within Section 4.1.4. To provide graphene foil coverage suitable for analysis, graphene was grown using a growth duration of 2.5 minutes. Figure 4.14 displays microscope images of graphene domains visualised on copper growth foil after partial coverage growth preceded by a), a reducing atmosphere anneal, and b), a non-reducing atmosphere anneal. Both reducing (2% H_2/N_2) and non-reducing (N_2) atmospheres were supplied to the reactor at 100 sccm throughout the ramp and anneal stages, resulting in a pre-growth chamber pressure of 7 mbar.

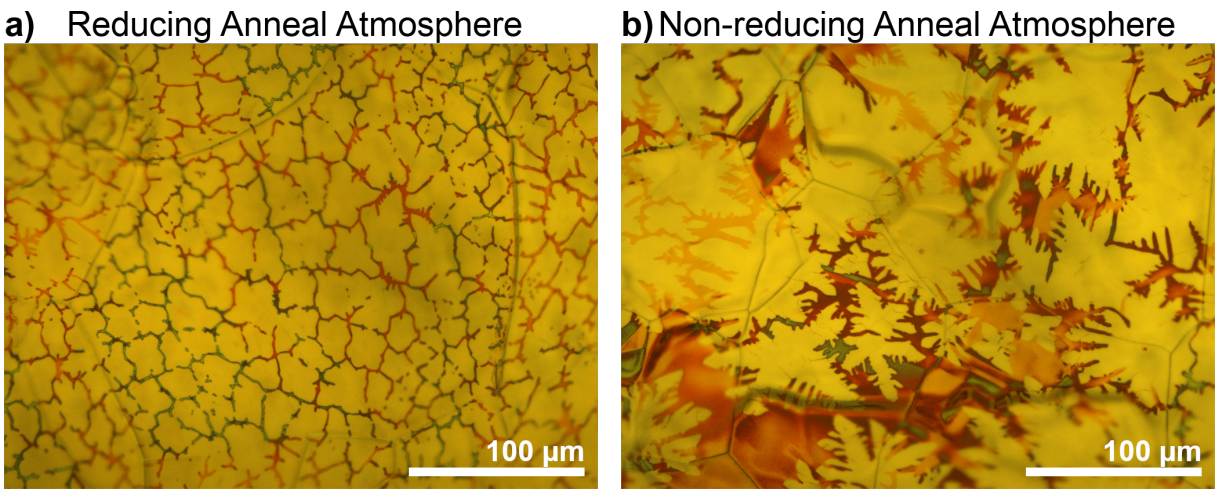

Figure 4.14: Microscope images illustrating the change in growth behaviour between using, a), a reducing atmosphere and, b), a non-reducing atmosphere throughout the ramping and annealing stages.

The graphene domains grown after a non-reducing anneal are significantly larger than those grown after a reducing anneal. The increased domain area, coupled with the reduced growth time (2.5 minutes compared with 5 minutes for non-reducing and reducing anneals respectively) means that domain growth rate is greatly increased after a non-reducing anneal. Domains grown following a non-reducing anneal are also found to be more dendritic than those grown after a reducing anneal. Both the increased growth rate, and increased dendricity are thought to originate in part from increased carbon mobility across the copper surface, as foil oxidation has neutralised carbon trapping defects [70]. This makes sense within the J_{flux}/J_{edge} model because increased surface mobility will increase J_{flux}. This effect is discussed in more detail later regarding domain dendricity.

Unlike the domain growth observed after a reducing anneal, displayed in Figure 4.14 a), where domains are all approximately the same area, the graphene grown after a non-reducing anneal, imaged in Figure 4.14 b), displays large domains alongside significantly smaller domains. Because domain growth rate should remain approximately constant throughout the majority of the duration of an incomplete coverage growth [58], the smaller domains can be assumed to have nucleated after the larger domains, illustrating that graphene nucleation is a continual process throughout the entire duration of CVD growth.

Extracted mean values for ρ_D and domain area are plotted as box and whisker plots within Figure 4.15. When a non-reducing ramp and anneal is used, ρ_D (domain area) is found to reduce (increase) by approximately one order of magnitude. The observed change of an order of magnitude in domain area and density is in agreement with similar investigations reported elsewhere in the literature [66, 76].

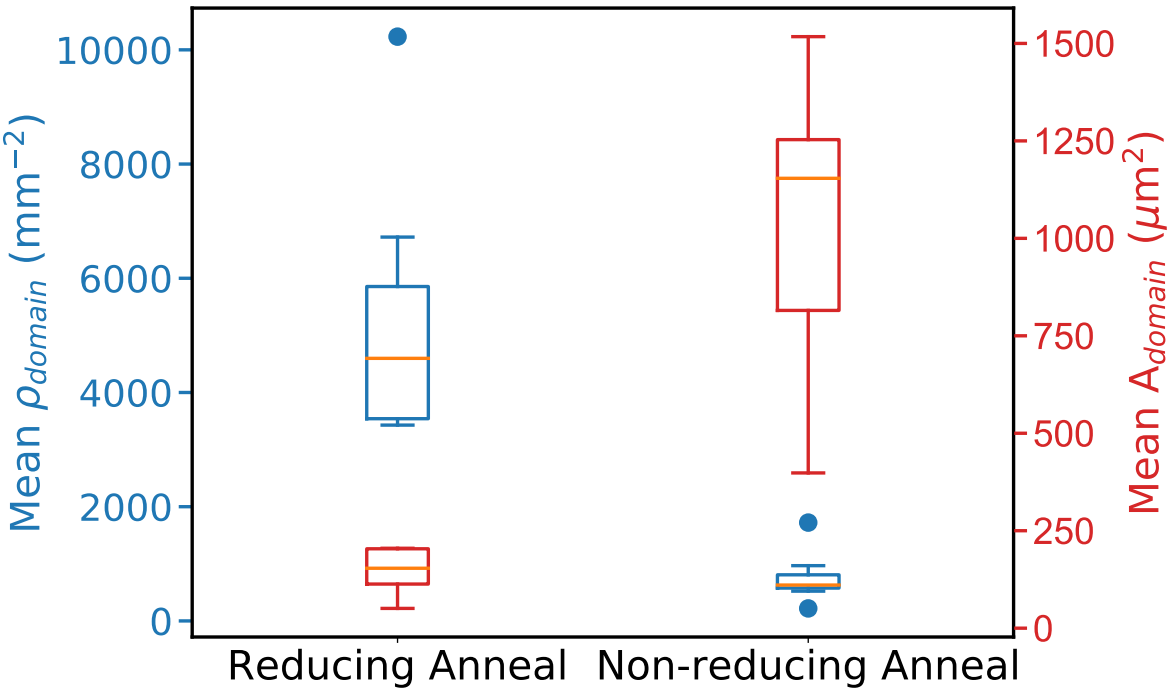

Figure 4.15: Box and whisker plots for mean nucleation densities (LH y-axis, blue) and mean domain areas (RH y-axis, red) from graphene grown within a H_2:CH_4 mixture of 10:1, following reducing and non-reducing anneal steps.

However, simple domain area and ρ_D do not provide a full picture of the graphene growth behaviour in this instance. As mentioned above, the domain growth rate of graphene grown after a non reducing anneal is greater than that of graphene grown following a reducing anneal. The domains grown after a non reducing anneal are also more dendritic in nature than those grown after a reducing anneal.

To investigate these effects, We quantify the increased domain growth rate observed after a reducing anneal. The top 1% of extracted domain area values from graphene grown after a reducing and non reducing anneal are selected for analysis, to avoid under-reporting graphene growth rate because of graphene domains seeded by secondary nucleation events. The domain areas are then divided by the growth time for each data set and the results are plotted in Figure 4.16. The growth rate is found to accelerate by almost an order of magnitude from 45 ± 17 μm^{2}minute^{-1} to 346 ± 63 μm^{2}minute^{-1}.

As stated above, the increase in growth rate after a non-reducing anneal means that the oxidation of the copper surface is increasing J_{flux} by either assisting surface methane decomposition, increasing the surface diffusion rate of surface-bound carbon species, or creating a composite of these two effects. As mentioned above, foil oxidation has the effect of increasing surface bound carbon mobility by passivating surface features that would otherwise act as carbon traps [70]. Additionally, DFT studies have calculated that

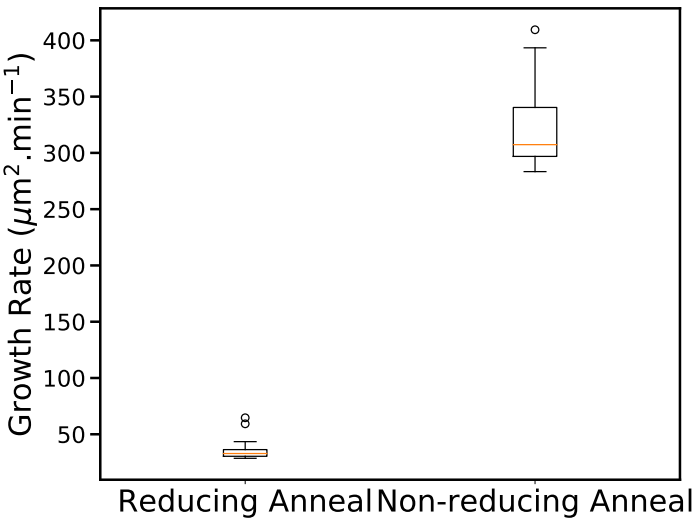

Figure 4.16: Box and whisker plot of mean domain growth rates for graphene grown after a reducing and non-reducing anneal step.

the energy barrier for methane dehydrogenation reduces on an oxidised copper surface in comparison to pristine copper and that CH_x is more stable on copper oxide than on pristine copper surfaces [312]. The increased stability of surface bound CH_x means that generated CH_x fragments have a greater probability of joining other CH_x fragments or growing domains than desorbing from the copper surface, in comparison to CH_x species on a pristine copper surface. Also, because nucleation points are passivated by surface-bound oxygen, surface bound CH_x fragments have increase probability on an oxidised copper surface of joining a growing domain rather than nucleating a new graphene domain. When considered through the lens of commercial graphene growth, increased domain growth rate after a non-reducing anneal is a positive result, as it means shorter process times are required to create graphene of increased quality.

We now consider the increased dendricity of the graphene grown after a non-reducing anneal in more detail. Because graphene grown at a H_2:CH_4 ratio of 10:1 after a non-reducing anneal displays such pronounced lobes, the issue of graphene growing between two advancing lobes is no longer trivial. Graphene lattice mismatches may arise from inter-lobe stitching across imperfectly flat growth surfaces, and as lobed domains have greater perimeter per domain area, the total area of imperfect inter-domain graphene will be increased. The more dendritic the resultant domains are, the lower the quality the final graphene sheet will be, for a complete sheet of graphene composed of similarly sized domains.

Therefore a new metric is required to compare the dendricity of the graphene domains

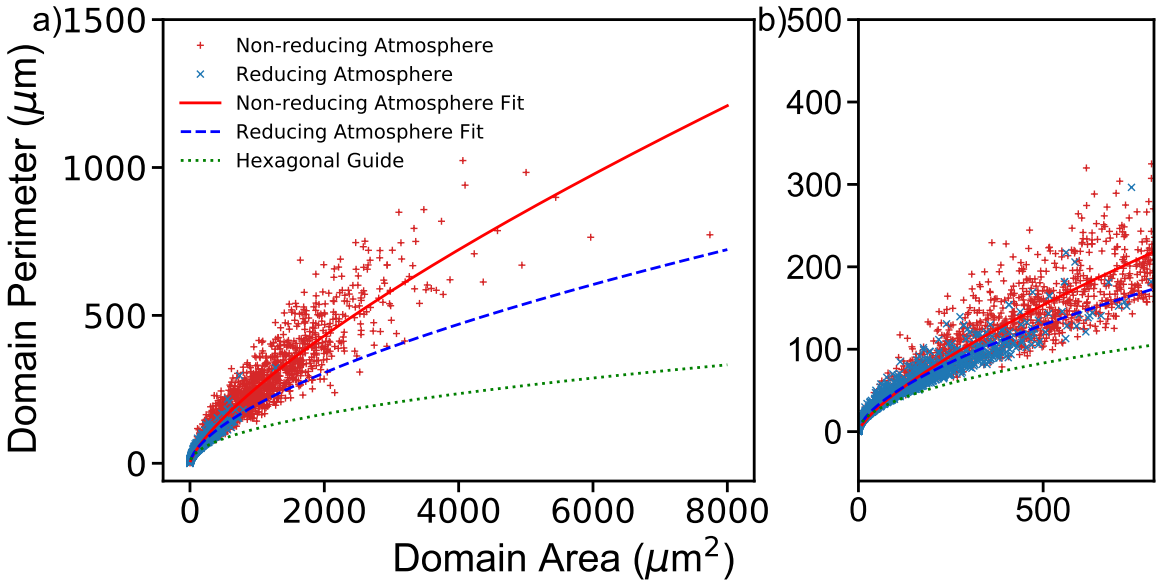

Figure 4.17: a) Domain perimeter plotted against domain area for graphene grown after reducing and non-reducing anneal stages; b) provides a magnified plot from panel a), highlighting the region where reducing and non-reducing areas are comparable.

and we suggest a simplified fractal analysis method based upon the relationship between graphene domain perimeter and area. As perimeter scales $\propto$ r and area scales $\propto$ r^2, it is not possible to quantify this analysis via a simple ratio. Instead, by plotting domain perimeter against domain area, domain dendricity behaviour for different recipes can be compared by comparing the locations of the perimeter/area curves on a perimeter/area plot and fitting the plotted points with a power law model, given in Equation 4.2:

$$P = a \cdot \ A^n \tag{4.2}$$

where A and P are the domain areas and perimeters respectively, a is a scaling factor and n is the fitted exponent. The more dendritic the growth mode of the graphene analysed, the larger the exponent, n, will be.

Figure 4.17 displays such a plot for graphene grown after reducing and non reducing anneals. A trace for regular hexagon perimeter/area is included as a guide for analysis because the arrangement of carbon atoms within a graphene lattice means that a regular hexagon is the optimum domain shape. The curves in Figure 4.17 show that graphene grown after a non-reducing anneal is more dendritic than graphene grown with a similar recipe after a reducing anneal, with fitted exponentials of 0.74 and 0.62 respectively. The increased dendricity is another indicator that J_{flux} is greater after a non-reducing anneal is greater than J_{flux} for domains after a reducing anneal, as if the assumption is held

H_2 : CH_4	H_2 flow rate . sccm	CH_4 flow rate . sccm	$P_{chamber}$. hPa	T_{grow}. minutes
50:1	1000	20	33	15
75:1	975	13	32	15
100:1	1000	10	33	15

Table 4.2: Growth parameters used within each variation of gas mixture following a non-reducing anneal period.

that carbons relax at similar rates around the edges of growing domains, an increase in dendricity is an indication of increased carbon impingement on the domain.

Within this subsection, it is shown that the use of a non-reducing annealing atmosphere reduces (increases) the domain density (area) by approximately one order of magnitude, and also increases the areal growth rate of graphene by a factor of ∼8. However, the morphology of the graphene domains is found to be less compact, which has been attributed to increased rate of attachment of carbon onto growing domains. Because domain growth rate is increased by the use of a non-reducing anneal prior to CVD, and increasing the H_2:CH_4 ratio should give lower domain density and domain dendricity, further optimisation is explored within the next section, via increasing the H_2:CH_4 ratio after the use of a non-reducing anneal.

4.1.6 H_2:CH_4 Following Non-Reducing Anneal

Because the growth rate of graphene domains grown following a non reducing anneal is greatly accelerated, H_2:CH_4 is revisited to further optimise the graphene growth. Graphene is grown within H_2:CH_4 ratios of 50:1, 75:1 and 100:1 following a non-reducing anneal; the growth parameters used within these experiments are displayed within Table 4.2.

Representative optical micrographs of the resulting graphene domains grown within atmospheres of H_2:CH_4 ratios of 50:1, 75:1 and 100:1 are displayed in Figures 4.18 a), b) and c) respectively. As the H_2:CH_4 ratio increases, foil coverage decreases, which holds for the step from 50:1 to 75:1 and 75:1 and 100:1. This is expected, as the growth time was consistent across all experiments and the reduced carbon partial pressure leads to reduced growth rates due to scarcity of graphene precursor. If only the larger domains within Figure 4.18 b) are considered, it is seen that across all H_2:CH_4 ratios, the graphene domains all possess similar six-fold morphology and upon cursory inspection, similar levels of dentricity.

However, there is an appreciable appearance of second generation domains within

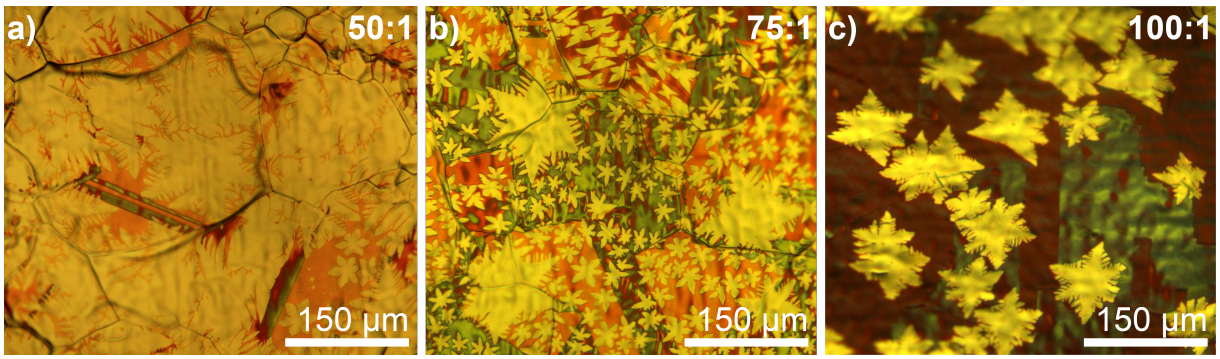

Figure 4.18: Optical micrographs of graphene domains on copper foil. Graphene domains were grown with H_2:CH_4 ratios of a) 50:1, b) 75:1 and c) 100:1.

Figure 4.18 b) which is representative of all images acquired at this H_2:CH_4 ratio. Second generation domains are defined here as domains with domain area of less than $\frac{1}{4}$ of the largest domain area grown under the same conditions. These second-generation domains appear because the presence of hydrogen within the reactor during growth gradually reduces the foil surface, which was oxidised during the annealing step. As the surface is reduced, it becomes favourable for increased density nucleation of graphene, as discussed in the previous section. Eventually, it becomes possible for many domains to nucleate rapidly, leading to a proliferation of second generation domains.

This effect is not observed for graphene grown within H_2:CH_4 mixtures of 50:1 and 100:1. Within the case of graphene grown under a H_2:CH_4 ratio of 50:1, we surmise that the first generation domains grow too quickly to allow the formation of significant numbers of second generation domains at the point that the foil surface becomes reduced. The explanation for the lack of graphene grown at 100:1 is the same as graphene grown following a reducing anneal. Whilst the reduction of the foil surface still occurs, the partial pressure of CH_4 within the chamber is insufficient to quickly nucleate further domains at the point of surface reduction, meaning that no secondary nuclei are observed.

It should be mentioned that it is possible to observe some second generation domains within Figure 4.18 a), within the bottom right corner. This is significant, as these second generation domains have appeared within a sizeable open area between first generation domains which demonstrates how the presence of existing domains prevents the nucleation of further generations through domain-edge carbon capture, as discussed within Section 4.1.4. Interestingly, the diameter and morphology of the second-generation domains are similar between 50:1 and 75:1, indicating that foil surface reduction and resulting secondary nucleation events occurred at a similar point within both experiments. This is not unexpected as the H_2 partial pressure was similar within both experiments.

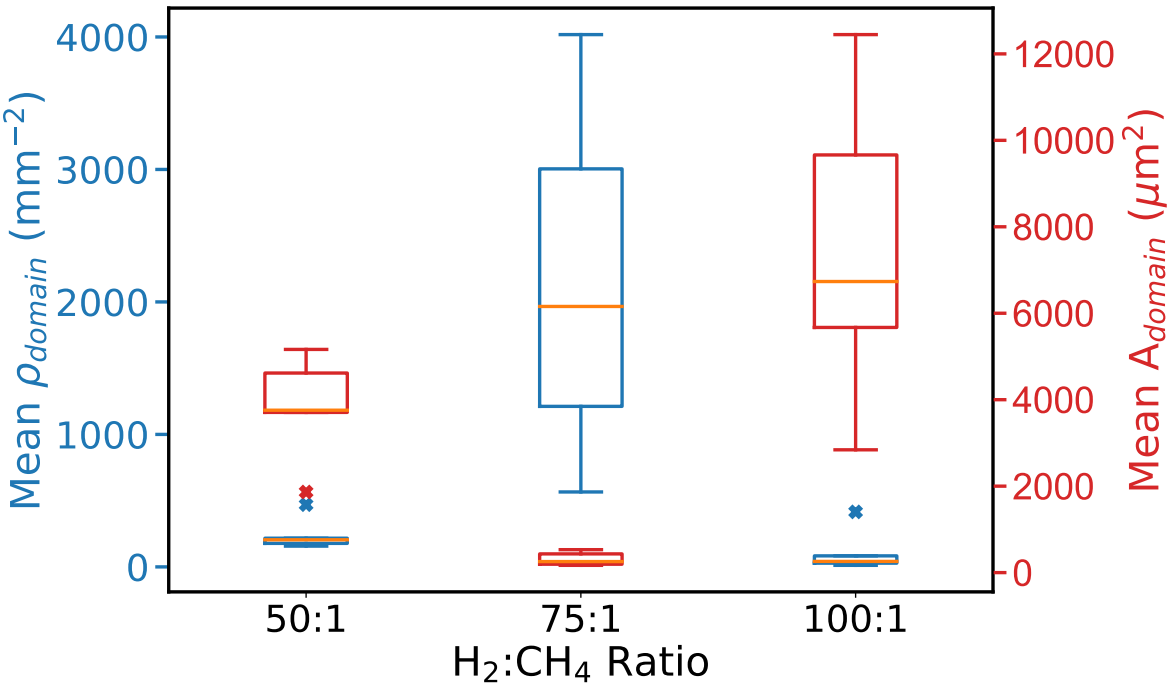

Figure 4.19: Box and whisker plots of domain densities (LH y-axis) and mean domain areas (RH y-axis) as a function of H_2:CH_4 ratio following a non-reducing anneal step.

ρ_D and domain area as a function of H_2:CH_4 ratios of 50:1, 75:1 and 100:1, following a non-reducing anneal, are now discussed. Figure 4.19 displays a box and whisker plot of nucleation densities and mean domain areas as a function of H_2:CH_4 ratio, plotted against the left- and right-hand y-axes respectively. The nucleation densities for graphene grown at H_2:CH_4 ratios of 50:1 and 100:1 are similar, with nucleation densities of 204 mm^{-2} and 41 mm^{-2} respectively. The variance of nucleation densities across these foils is found to be low, at $\pm \leq 50$ mm^{-2} for both H_2:CH_4 ratios, excluding outlying maximum points at 470 mm^{-2} and 415 mm^{-2}. These large outlier points relate to the upstream end of the growth foils, where the highest carbon concentration is found across the foil surface [279, 302], resulting in increased nucleation rates and densities.

The ρ_D for graphene grown at 75:1 is found to be much greater, with a median ρ_D of 1966 mm^{-2}. This increased ρ_D is coupled with a large variance of nucleation densities between sample images of between 565 mm^{-2} and 4018 mm^{-2}, with an interquartile range for ρ_D for graphene grown at 75:1 ranges from 1212 mm^{-2} to 3005 mm^{-2}. The increased domain ρ_D and wide variance of nucleation densities for graphene grown in a 75:1 atmosphere means that this mixture is inappropriate for CVD growth of high-quality graphene, because homogeneity of growth behaviour is important for reproducibility of ultimate devices.

Looking now at the mean domain areas from the growths carried out in H_2:CH_4 mixtures of 50:1, 75:1 and 100:1, it is clear that the growth carried out within a H_2:CH_4 mixture of 75:1 resulted in a lower mean domain area than graphene grown in H_2:CH_4 mixtures of 50:1 or 100:1. The median of mean areas for graphene domains grown at 75:1 is 255 μm^2 with an interquartile range between 194 μm^2 and 433 μm^2. This is a lower median mean area than for graphene grown at a H_2:CH_4 ratio of 10:1 and is due to the majority of nucleated domains resulting from the second-generation domain nucleation. Whilst this method fails to capture the presence of larger domain areas within the graphene grown at 75:1, it provides a useful indication of the high density of domain boundaries which would result within graphene grown within a 75:1 mixture.

Considering graphene grown within H_2:CH_4 ratios of 50:1 and 100:1, it is observed that the mean domain area grown within a 100:1 mixture is larger than that of graphene grown within a 50:1 mixture, with median of mean areas of 3757 μm^2 and 6734 μm^2 for 50:1 and 100:1 respectively. This is an unexpected result, as the growth time was the same within both 50:1 and 100:1 experiments, but the carbon partial pressure within the 100:1 mixture was half that of the 50:1 mixture. A reduction in carbon partial pressure would be expected to yield reduced graphene growth rates, but this is not found to be the case. This is because the metrics presented within Figure 4.19 do not provide a complete picture of the growth behaviour.

Figure 4.20 displays a plot of mean graphene foil coverage for graphene grown within H_2:CH_4 mixtures of 50:1, 75:1 and 100:1 following a non-reducing anneal step. The foil coverage reduces linearly between H_2:CH_4 ratios of 50:1 to 100:1, from 81% to 23%. Deviations of $\sim$ 7% from the mean value are observed for the 50:1 and 100:1 growths which suggest that graphene growth behaviour under these conditions is reasonably homogeneous, whereas the 75:1 growth displays much greater deviation of $\sim$ 20%. The large range of foil coverage within the 75:1 growth is attributed to the behaviour of the second-generation domain nucleation and growth and is a further reason why this growth recipe is the least optimal recipe of those investigated within this section. The difference of 58% foil coverage between the 50:1 and the 100:1 is pertinent to the point raised above regarding mean domain area. As the ρ_D is a slightly greater for graphene grown within a 50:1 mixture, mean domain area is restricted by adjacent growing domains.

Furthermore, as Figure 4.20 displays, graphene grown within a H_2:CH_4 mixture of 100:1 has covered less than 30% of the foil after 15 minutes growth. Because domain nucleation is an on-going process throughout graphene CVD growth the ρ_D for graphene

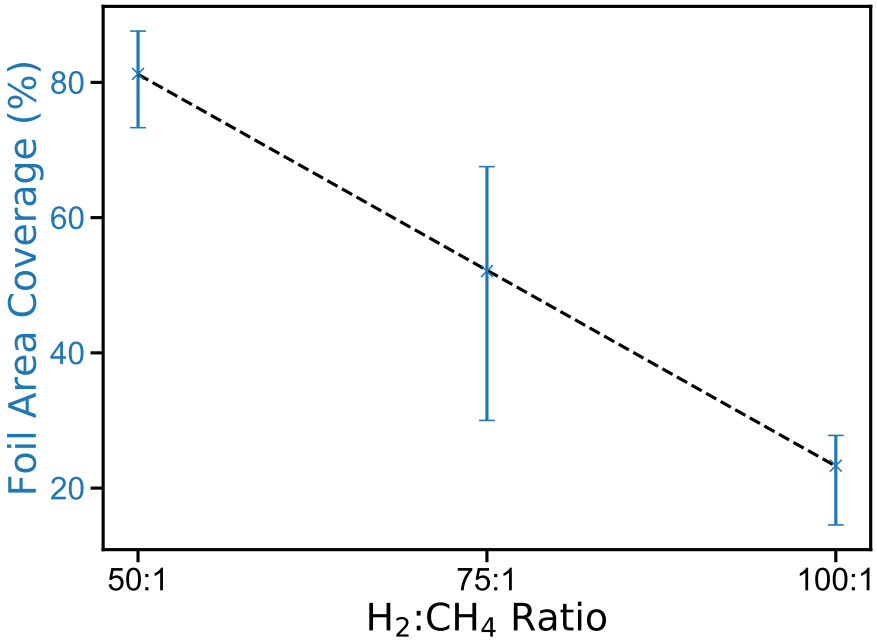

Figure 4.20: Plot displaying the foil area coverage of graphene after a 15 minute growth period following a non-reducing anneal step within H_2:CH_4 mixtures of 50:1, 75:1 and 100:1. The fitted trend displays a linear relationship to the methane partial pressure within the system.

grown within a H_2:CH_4 mixture of 100:1 is certain to increase. Additionally, as the copper foil surface is also being reduced throughout the process, the nucleation of many smaller domains becomes increasingly likely the longer the process continues. Because foil coverage rate is low within a 100:1 mixture, extended growth times, on the order of one hour, would be required to achieve full foil coverage and because this work is aimed towards optimising graphene growth for mass production, extended growth times are undesirable. However, graphene grown within a mixture of 50:1 is close to full coverage at approximately 81% foil coverage, and it is reasonable to assume that the domain density will remain constant until full foil coverage is achieved, due to the fact that new carbon fragments are more likely to be captured by existing domains, rather than nucleating new domains.

To provide a full set of metrics from this recipe optimisation step, Figure 4.21 displays a plot of domain perimeter against domain area, with fitted guides, to investigate the dendricity of graphene grown within H_2:CH_4 mixtures of 50:1 and 100:1 alongside data from first-generation domains grown within a H_2:CH_4 mixture of 75:1. A power law model is fitted to the plotted data as before and the n values for 50:1, 75:1 and 100:1 are found to be 0.94, 0.62 and 0.61 respectively. The n-values given above, coupled with Figure 4.21 clearly displays how dendricity reduces as H_2:CH_4 ratio increases. This is explained

by a reduction in carbon partial pressure as H_2:CH_4 ratio increases, which leads to a reduced J_{flux} and allows carbon fragments newly attached to a growing domain to more fully relax around the perimeter. However, graphene grown at 50:1 was found to have an n value greater than than graphene grown at 10:1, at 0.94 and 0.74 respectively. This is attributed to decreased ρ_D within the 50:1 growth, compared to the 10:1 growth, resulting in an increase in the surface carbon mean free path, providing increased effective mobility and thus increased J_{flux}.

Although graphene grown within a H_2:CH_4 mixture of 50:1 performs less well on this metric than the other recipes investigated within this section, graphene growth using a mixture of H_2:CH_4 at a ratio of 50:1 provides the optimum point for mean domain area coupled with rapid growth within the system used during this research. It is worth mentioning that although full coverage graphene has been achieved with domain diameters of over 1 mm [70, 75, 288], required growth times were greater than an hour. It should also be mentioned that this data suggests that the use of further reduced methane partial pressures should drive graphene domain growth closer to regular hexagonal morphology. However, whilst this may be preferable for the quality of individual domains, it may compromise too far on growth rate and foil coverage to be practical.

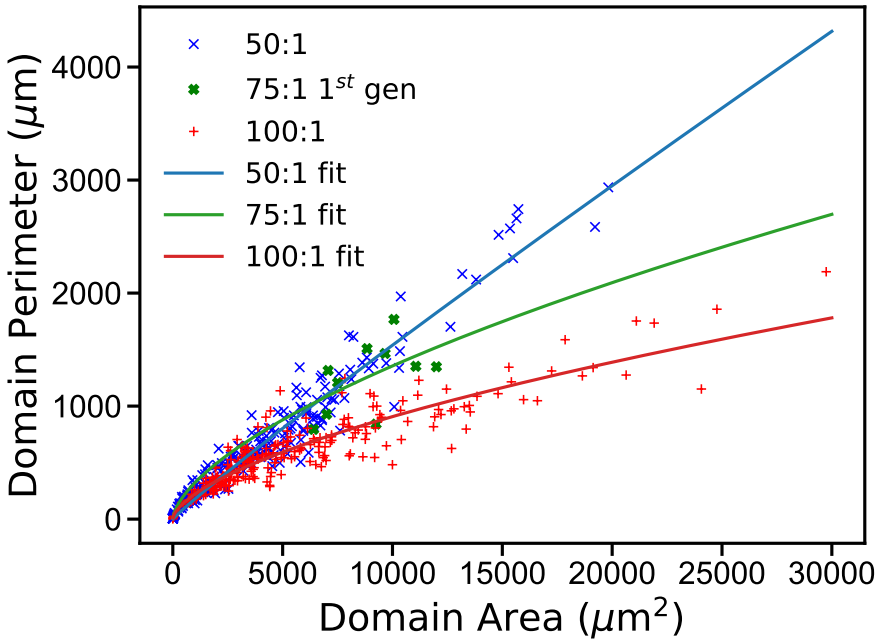

Figure 4.21: Plot of domain perimeter against domain area for graphene grown within H_2:CH_4 ratios of 50:1, 75:1 and 100:1.

Finally, having specified an optimised recipe for graphene growth within the system used throughout this research, as growth within a H_2:CH_4 mixture of 50:1 following a

non-reducing anneal, full coverage graphene was grown and transferred onto SiO_2 for characterisation. Figure 4.22 displays a micrograph taken from the foil with full graphene coverage following the HPM prior to graphene transfer. No areas with colour contrast are observed, as expected for full graphene coverage, due to the protective nature of the overlying graphene against copper foil oxidation [279]. The underlying copper foil crystal structure is easily observed with the crystal edges shown by the heavy black lines within the image. It can be seen that the copper foil grains are now hundreds of microns in diameter due to copper grain enlargement throughout the annealing and growth steps. The texturing of the copper foil surface, shown within this image as lighter troughs surrounding darker dimples, is an artefact of foil flattening between a stack of clean room wipes – the texture of the clean room wipe is transferred to the foil when pressed upon, but is found to keep the graphene film intact. Importantly, no colour contrast is observed at the copper grain boundaries, which indicates that graphene grows continuously across even large surface features. The continuous nature of the graphene film is corroborated by the homogeneous colour of the transferred graphene film on 80 nm SiO_2 on Si, as displayed in Figure 4.23 a), which indicates an unbroken transferred graphene film.

Figure 4.22: Optical micrograph of full coverage graphene on copper foil following the HPM.

Figure 4.23 a) displays a representative image of full-coverage graphene grown at 50:1 after transfer to Si capped with 80 nm SiO_2. Wrinkles and tears, which are typical of

large area graphene transfer, are visible within the image, corresponding to the darker, thread-like features and small areas of increased brightness respectively whilst no multi-layer regions are observed. This demonstrates homogeneous, monolayer graphene growth, which is desirable for graphene electronics. A characteristic Raman spectrum from the transferred graphene is displayed in Figure 4.23 b). No D peak is visible near 1350 cm^{-1}, indicating low carbon vacancy defect density within the graphene sheet. Both Figures 4.23 a) and b) demonstrate the high quality graphene grown using the optimised recipe. Figure 4.23 c) and d) show non-contact AFM scans of the transferred graphene surface. Alongside the folding typical of transferred CVD graphene, a high density of residues can be seen on the graphene surface. These most likely originate from the transfer process and indicate that transfer protocols require improvement. However, no tearing of graphene or gaps within the coverage are visible, indicating the growth of a continuous graphene layer.

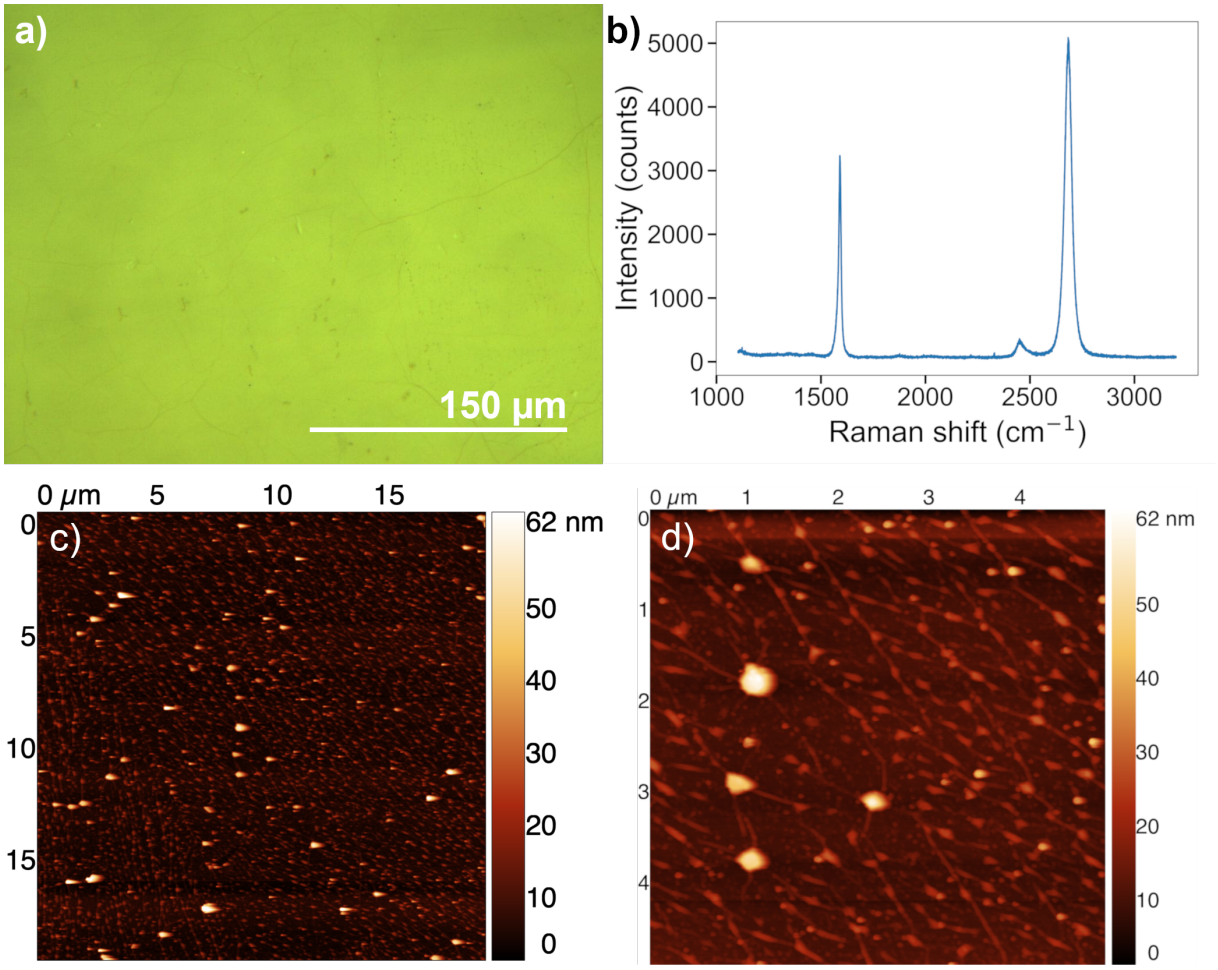

Figure 4.23: a) Optical micrograph of full coverage graphene grown within a H_2:CH_4 mixture of 50:1 transferred onto Si capped with 80 nm SiO_2; b) Raman spectrum obtained from transferred graphene; c) and d) AFM images of transferred graphene topography taken with 20 μm and 5 μm scan side lengths respectively.

4.2 Conclusion

Within this chapter, the optimisation of CVD graphene growth using hydrogen and methane diluted within nitrogen to below their lower explosive limits has been investigated. A step-wise method for the optimisation of CVD graphene growth has been presented for the equipment used within this research and provides a logical set of experiments to follow for other groups who are trying to improve the quality of their graphene CVD. Additionally, the hot-plate method, which provides a rapid, low-cost method for the visualisation of graphene domains grown on copper foil is introduced and shown to be a suitable method for graphene growth analysis without the need for expensive equipment. The successful rapid growth via industrially safe CVD of continuous graphene comprised of domains with diameters of $\sim 200\,\mu m$ has been demonstrated. This research should provide a valuable way forward for the industrial scale growth of graphene via CVD.

In addition, a simple method for measuring graphene dendricity, which is an important metric for the growth of graphene with minimal domain boundary defects has been demonstrated. A simple conceptual framework, explained via the relationship between J_{flux} and J_{edge}, has also been introduced, which should be helpful for researchers trying to optimise their own recipe by providing a simplified description of graphene growth aggregate behaviour. Finally, the recipes demonstrated throughout this chapter on the way to graphene optimisation provide indicative recipe settings for a wide range of graphene domain morphologies and densities, which may be of use for the production of 'de-tuned' graphene for applications requiring enhanced chemical or catalytic capabilities.

Chapter 5

Nitrogen as a Suitable Replacement for Argon within Hot-Wall Methane-Based Graphene Chemical Vapour Deposition

Work within this chapter published under the same title within PSS(b)
doi: 10.1002/pssb.201900240

Within this chapter we investigate replacing Ar with N_2 as the buffering gas during CVD growth. The practice of buffering CVD precursor gases with an inert gas has been used by many groups as a method to increase the total system pressure [85, 163, 313, 314], to provide a very low methane flow rate [163, 314, 315], or to dilute explosive gases below their lower explosive limit (LEL) [58, 85]. Argon is used almost ubiquitously as the inert gas within these roles because it is a monatomic Nobel gas, which means it remains chemically inert under the conditions commonly used during CVD.

As described in the previous chapter, both methane and hydrogen are critical to the CVD process. However, as argon plays no chemical role within graphene CVD, the possibility to replace argon with a cheaper alternative should be an attractive prospect when shifting from lab production to commercial synthesis. Due to its abundance, nitrogen is both environmentally and monetarily cheaper than argon, and represents the only inert gas which may provide such cost reductions.

5.1 Possible Issues Arising from the use of Nitrogen

To explore the suitability of nitrogen as a buffering gas within graphene CVD, the potential issues arising from nitrogen use should first be considered. Nitrogen exists as a diatomic molecule and there is a risk that N_2 might dissociate during CVD. Dissociated nitrogen would be able to substitute into the graphene film, as shown schematically in Figure 5.1, causing doping and disruption to the lattice. However, the N≡N bond is one of the strongest bonds known, requiring 5.19 eV to convert N≡N to H-N=N-H [88] and 9.76 eV to fully dissociate to N_2 to atomic nitrogen [87]. The large bond strength means that the probability of N_2 dissociation during CVD is vanishingly small, suggesting that nitrogen substitution into the graphene lattice is unlikely. Additionally, and importantly, copper does not act as an efficient catalyst for the dissociation of N_2 [316].

As the dissociation of N_2 into N radicals capable of graphene-lattice incorporation is unlikely, it is expected that Cu catalysed graphene grown via CVD using N_2 as the buffer gas will produce graphene indistinguishable from graphene grown via Ar buffered CVD. Recently, a small number of groups have reported the growth of graphene using N_2 as the inert buffering gas [85, 166, 317]. The Raman data published from all these studies report small I_D/I_G ratios from their graphene samples, suggesting a low defect density within the graphene sheet [236, 241, 242, 318, 319]. In addition, G. Zhong et al. reported a charge carrier Hall mobility of 5270 - 6040 $cm^2\ V^{-1}\ s^{-1}$ for their graphene transferred to SiO_2 on Si which also suggests high quality, defect free graphene [85]. However, as none of these groups studied the inclusion of nitrogen into the graphene lattice in detail, it can not be taken as a foregone conclusion that the use of nitrogen as a buffering gas during graphene CVD does not lead to nitrogen inclusion within the graphene lattice.

As stated above, N-doping of the graphene lattice via the dissociation of N≡N is the major concern within this work. Previous theoretical and experimental studies on deliberately N-doped graphene have identified the following general positions that N-heteroatoms occupy within the graphene lattice [176, 179, 187, 320], illustrated in Figure 5.1:

- Pyridinic N atoms preserve the form of the 6-membered ring it is part of, but causes vacancy defects within the adjacent carbon rings.
- Pyrrolic N atoms both reduce their host carbon rings to 5-membered rings and introduce vacancy defects within adjacent carbon rings.

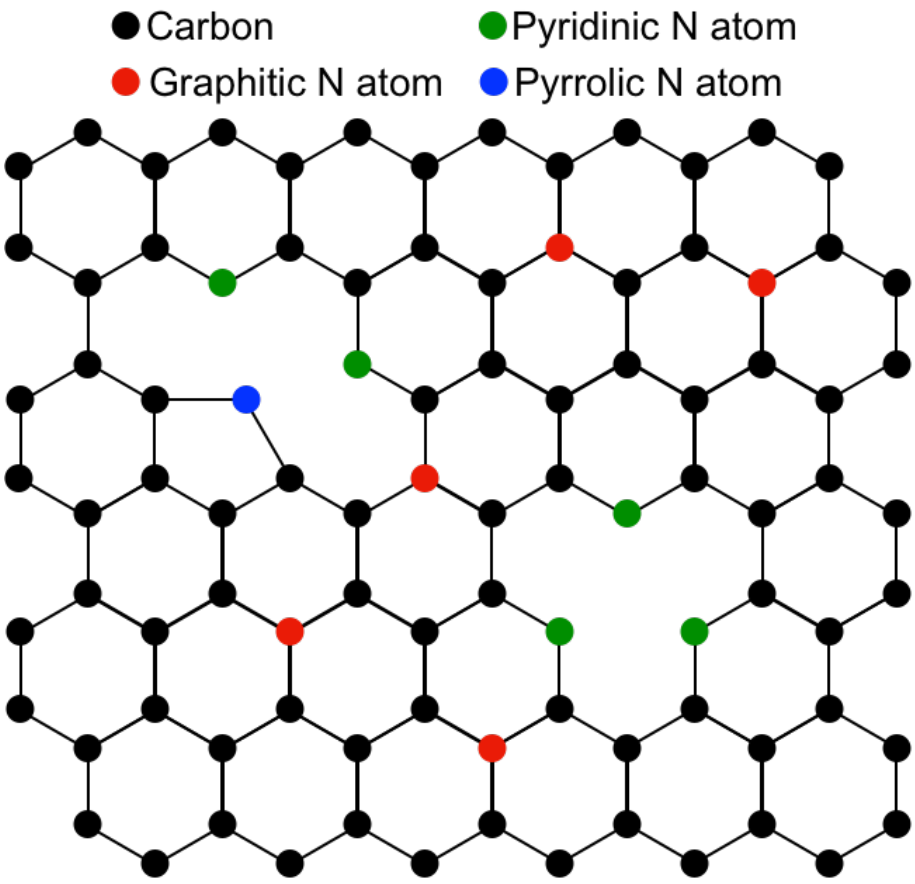

Figure 5.1: Configuration of substitutional pyridinic-, pyrrolic- and graphitic-N within the graphene lattice.

- Graphitic N atoms preserve the form of the graphene lattice. However, the difference in atomic mass and the addition of an electron introduce perturbations to the phonon dispersion within the graphene lattice.

5.2 Comparison of N_2 and Ar buffered samples

To ascertain whether N_2 is a suitable buffering gas within copper catalysed graphene CVD, samples are fabricated within Ar and N_2 atmospheres using our recipe for full coverage monolayer graphene, discussed in Chapter 4. Multiple chemically sensitive spectroscopic techniques are then employed to probe the graphene for N-related signals. The techniques used within this section, in descending order of sensitivity to the presence of atomic nitrogen within the graphene lattice are: Raman Spectroscopy, Time-of-Flight Secondary Ion Mass Spectroscopy (TOF-SIMS), and X-Ray Photon Spectroscopy (XPS).

After graphene is grown on the copper foil, multiple samples from both regimes are transferred to Si substrates capped with 300 nm or 80nm SiO_2. Graphene is also studied on the copper foil via XPS and TOF-SIMS to avoid false nitrogen signals which may

originate from contamination introduced during the transfer process.

5.2.1 Raman Spectroscopy

Background

Raman spectroscopy is a powerful non-destructive tool for graphene characterisation. A Raman spectrum acquired from defective graphene, grown during this project, which is selected so that an example of the D peak may be clearly observed, is displayed in Figure 5.2. The three major peaks used for Raman spectroscopic characterisation of graphene are highlighted and are discussed below:

- The 2D peak is useful for analysing the number of graphene layers present [232] and the strain and doping of the graphene sheet [238, 321] but is not of significance within the following section.

- The D peak is associated with the breathing mode of the carbon rings within the graphene lattice. The D peak is a single-phonon Raman mode and is momentum disallowed within pristine graphene. The presence of defects within the graphene lattice break the crystal symmetry allowing the D mode to become active [240, 241].

- The G peak is related to the shearing mode of adjacent rows of carbon atoms within the plane of the graphene lattice. The G peak intensity is related to the number of lattice rings illuminated by the laser and is not significantly altered by the presence of defects within the graphene lattice within the range of defect densities explored within this research [240, 241].

Within highly damaged samples, there may also be a smaller subsidiary peak present on the high-wavenumber side of the G peak which is referred to as the D' peak. As the relative G peak intensity remains constant before the appearance of the D' peak, it provides a useful normalisation tool for Raman spectroscopic analysis of graphene. The intensity ratio of the D peak to the G peak can then be used to measure the point defect density of graphene [231, 236, 240, 241, 243, 318] via Equation 5.1 [240], where n_D is the carbon vacancy density within the graphene lattice per cm^2, λ_L is the wavelength, in nm, of the illuminating laser light used and I_D and I_G are the relative intensities of the D and G peaks respectively. Equation 5.1 is a culmination of theoretical and empirical work carried out by Lucchese et al. [241], based upon the Raman active area of carbon vacancies

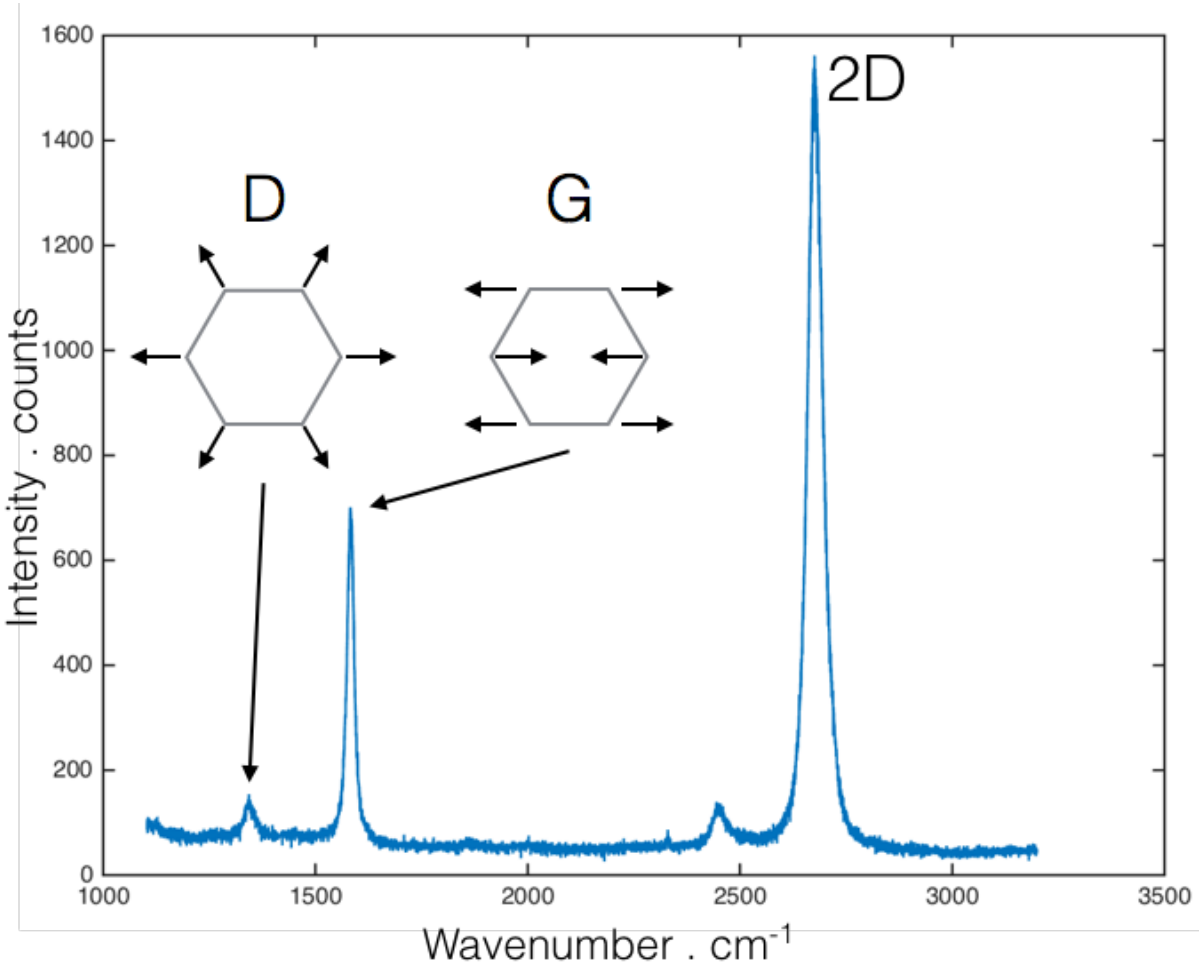

Figure 5.2: Raman spectrum of defective graphene grown during this research. The D/G ratio suggests a defect density of $\sim 2.57 \times 10^{10}\,\mathrm{cm}^{-2}$.

within a graphene sheet, which was then developed further empirically by Cancado et al. [240]. Using this equation, the Raman spectrum in Figure 5.2, acquired using a laser of wavelength 514.5 nm, relates to a graphene sheet with a carbon vacancy defect density of $2.57 \times 10^{10}\,\mathrm{cm}^{-2}$.

$$n_D = \frac{1.8 \pm 0.5 \times 10^{22}}{\lambda_L^4} . \left(\frac{I_D}{I_G}\right) \tag{5.1}$$

Equation 5.1 refers specifically to the density of defects formed by the removal of single carbon atom from the graphene lattice. As both pyridinic and pyrrolic nitrogen substitutional positions also create carbon vacancy defects within the graphene lattice, it is reasonable to assume that these substitutional positions are at least as Raman active as simple carbon vacancies within the lattice. Previous studies show however, that graphitic nitrogen defects are less Raman active than carbon vacancy defects within the graphene lattice [167, 187]. We therefore extrapolate an empirical relationship, defined in Equation 5.2, between graphitic nitrogen density per cm^2 (n_N) and the $\mathrm{I}_D/\mathrm{I}_G$ ratio from Raman spectra published by Guo et al. for graphene sheets doped with purely graphitic nitrogen

substitution [167]. The data from Guo et al. is used as it provides the most consistent Raman spectral trend we could find within the literature, based on graphitic nitrogen substitution density within graphene.

$$n_N = \left(\frac{I_D}{I_G} + 0.9542\right) \times 10^{13} \tag{5.2}$$

To assess nitrogen inclusion within the graphene matrix, the minimum resolvable nitrogen inclusion must be considered, based on a minimum resolvable I_D/I_G ratio. The minimum detectable limit is defined as the peak-to-peak amplitude of the background signal divided by the G peak prominence. Figure 5.3 illustrates the effect of increasing spectrum acquisition time on the minimum resolvable I_D/I_G ratio, wherein Raman spectra are acquired from graphene samples grown within this research, at a H_2:CH_4 ratio of 50:1 following a non-reducing anneal, with a Horiba Jobin yvon LabRam 800HR coupled with a Symphony Solo detector and a grating of 2400 cm^{-1}. It is found that increased acquisition time results in increased defect sensitivity due to a decreased minimum I_D/I_G ratio. However, as each spectrum is captured across five spectral windows, the use of longer acquisition times result in significantly increased spectrum capture time, as annotated within Figures 5.3 a) - d). A 5 s acquisition time was found to provide the optimum balance between defect sensitivity and spectrum acquisition time.

Raman Spectroscopy of Argon and Nitrogen Buffered Graphene

Figure 5.4 a) displays characteristic Raman spectra taken from argon and nitrogen buffered graphene after transfer to Si capped with 80 nm SiO_2using the optimum Raman spectrometer settings discussed above. Both the G and the 2D peaks are clearly visible and the I_{2D}/I_G ratio of 2, coupled with the single Lorentzian curve fit of the 2D peak indicate monolayer graphene [243]. Figure 5.4 b) displays a magnified view of the D peak region and it is observed that no D peak is clearly resolvable above the noise limit of the system within either spectrum. Taking the peak-to-peak noise amplitude, a minimum resolvable carbon vacancy defect density of 2.23×10^9 cm^{-2} is calculated. A corresponding minimum graphitic nitrogen density of 9.73×10^{12} cm^{-2} or 0.26 at.% is found, using our relationship extrapolated from Guo et al [167]. The reduced Raman sensitivity to graphitic substitutional nitrogen atoms is expected as the hexagonal atomic arrangement is retained within this configuration.

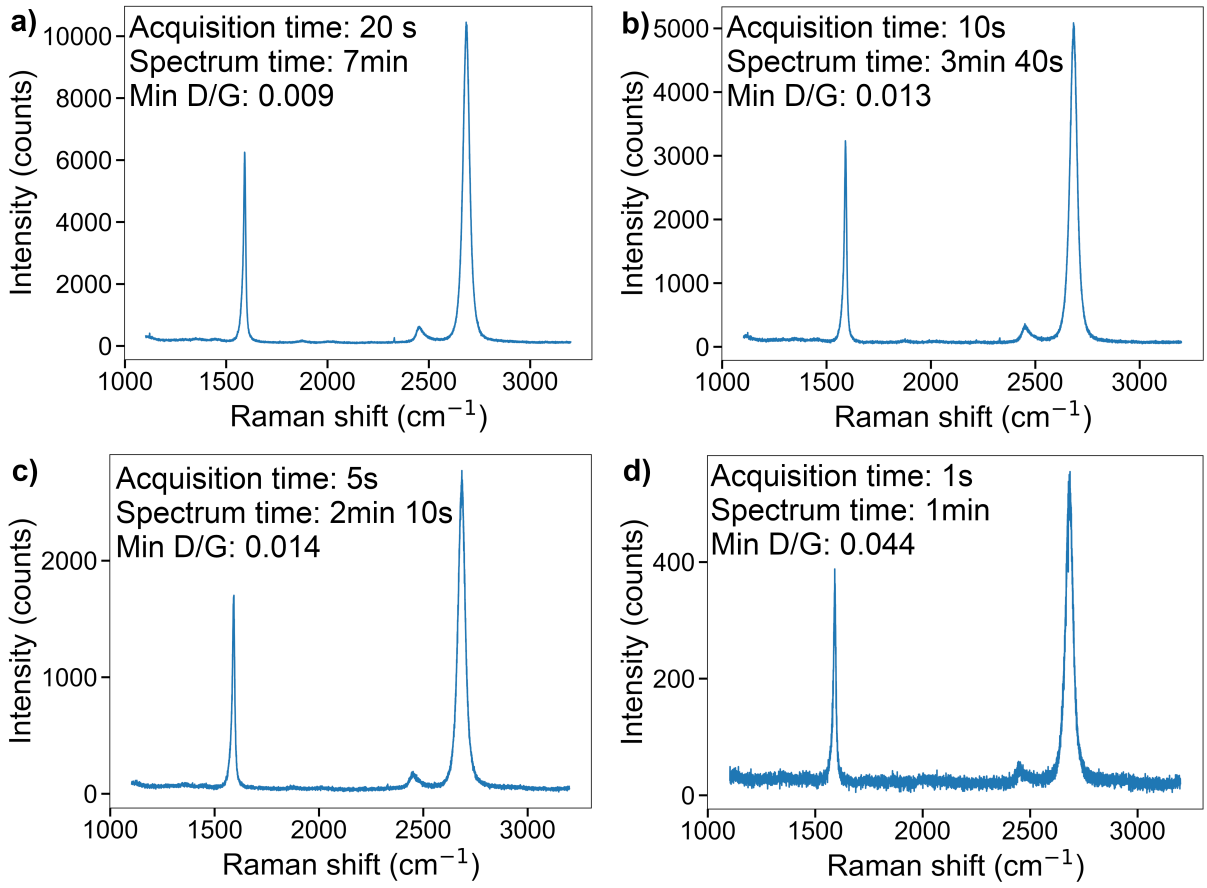

Figure 5.3: Raman spectra acquired from graphene grown during this research at a H_2:CH_4ratio of 50:1 following a non-reducing anneal. The spectral window acquisition times decrease from a) to d) providing an increase in the minimum resolvable I_D/I_G ratio.

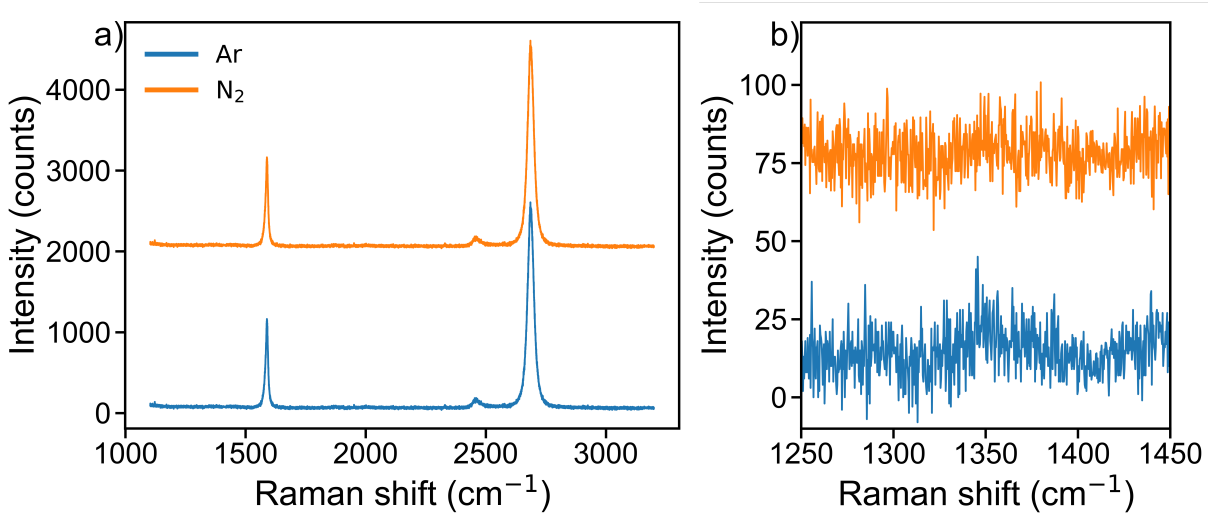

Figure 5.4: a) Raman spectra taken from argon-buffered graphene and nitrogen-buffered graphene; b) magnified view of the D-peak region.

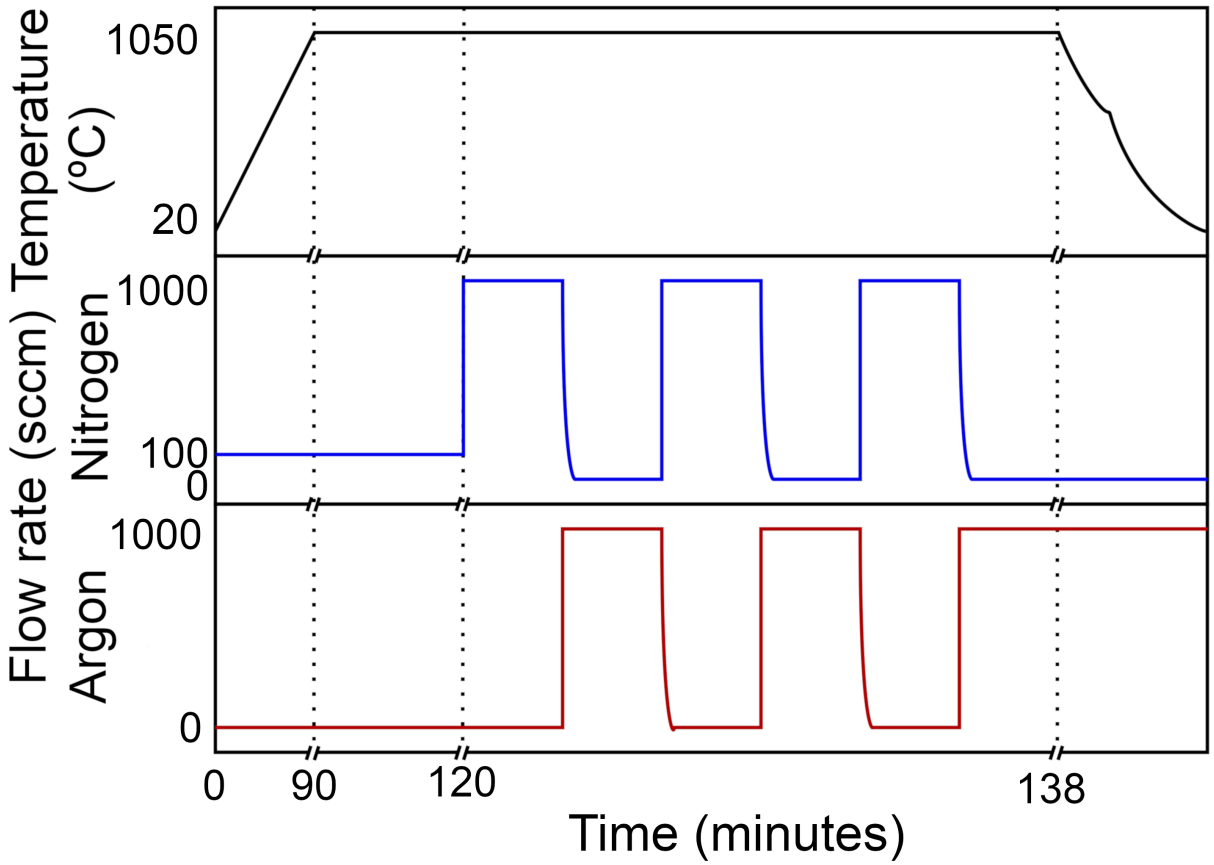

Figure 5.5: Schematic representation of the gas and temperature profiles used to grow domains within alternating nitrogen and argon atmospheres.

Raman spectroscopy of Nitrogen/Argon Phased Growth

In order to eliminate variations in Raman signal between samples introduced during the process of transferring graphene to Si/SiO_2, large isolated graphene domains were grown using a 50:1 H_2:CH_4 recipe, as introduced in Chapter 4, which was periodically switched between nitrogen- and argon-buffered atmospheres to produce domains with concentrically banded regions grown under a nitrogen or argon atmosphere[62]. The gas mixture used during growth is displayed schematically in Figure 5.5. The time required to exchange the buffering gas environment within the CVD chamber was found to be 20 s and the duration of each gas phase within a cycle was 3 minutes. The length of the evacuation time in relation to the length of time of each phase means that regions which are only nitrogen or argon buffered should dominate within the graphene film.

Following the growth of isolated domains approximately 300 µm across, radial line scans are recorded using a Horiba Jobin yvon Raman LabRam HR800 spectroscope. Figure 5.6 displays a microscope image of one such domain with lines 1-4 indicating the paths of the radial line scans. Magnified images of the line scan paths are displayed in Figure 5.7 a), c), e) and g). The plots displayed in Figure 5.7 b), d), f) and h) show the

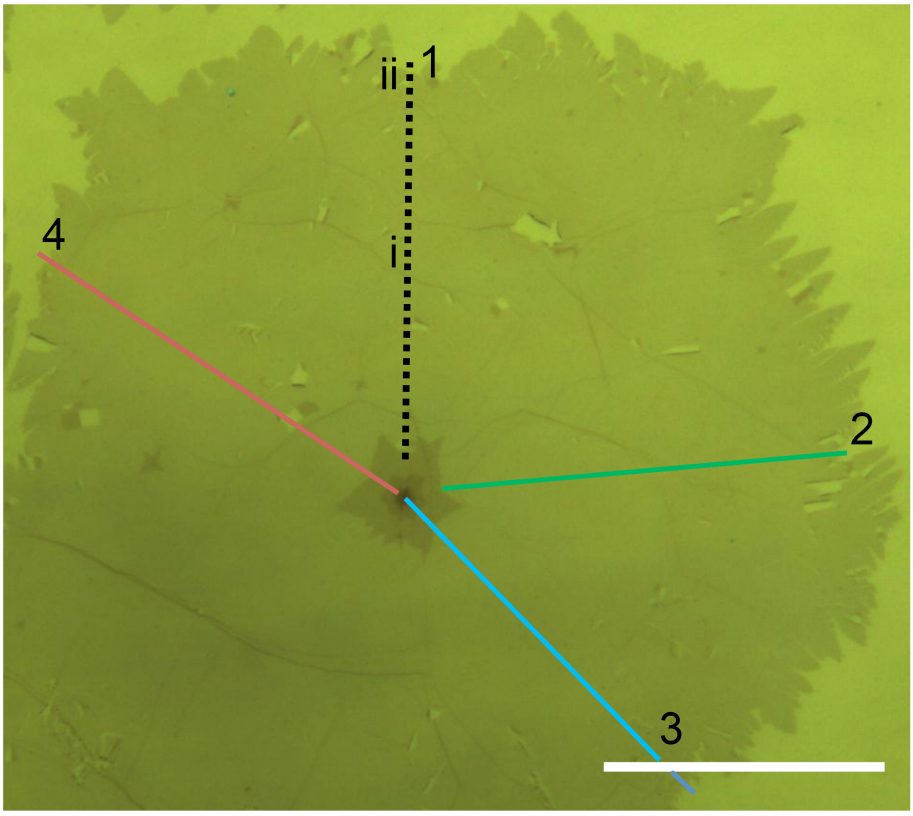

Figure 5.6: Optical micrograph of a graphene domain grown under periodically switched nitrogen and argon atmosphere. Lines 1-4 indicate the paths taken by the radial line scans. The scale bar represents 100 µm.

corresponding I_D/I_G ratios extracted for each point along the line scans. The grey/blue regions at the bottom of each plot indicates a conservative minimum resolvable I_D/I_G ratio of 0.018. Data points indicated within the grey/blue regions represent automatically extracted I_D/I_G ratios which lie below the conservative minimum detection limit for the Raman spectrometer. Two prominent features above the minimum detection limit are observed in Figure 5.7 b), marked i and ii on Figures 5.6 and 5.7 a). The feature at i can be identified as a large fold in the graphene flake. Folds such as this are known to produce an increase in the D-peak signal, because of the graphene sheet breaking crystal symmetry due to a small radius of curvature [199]. The second large peak correlates with the edge of the graphene flake and is due to the presence of non zig-zag flake edges which are also known to be D-mode active [283]. The increase in I_D/I_G ratio close to the 0 µm position can be ascribed to the edges of the multilayer graphene found at the centre of the flake which are also not purely zig zag. Due to the graphene transfer process, folds and tears are present within all analysed flakes. Increases in the I_D/I_G ratio are universally observed at these features and at the middle and edge of flakes of every flake measured, as shown in Figures 5.7 c) - h). Importantly, the periodicity of the I_D/I_G ratio increases

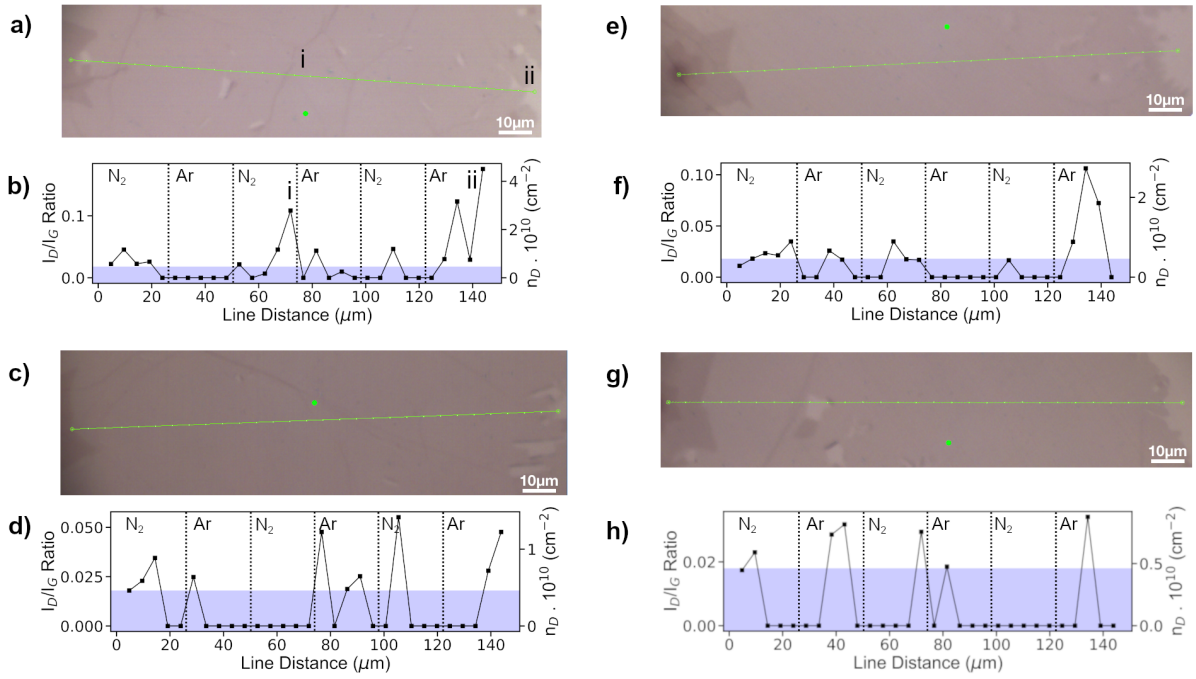

Figure 5.7: Magnified images of linescans 1-4 indicated in Figure 5.6, a, c, e and g respectively and the associated I_D/I_G plots b, d, f and h respectively.

do not match that of the carrier-gas variations introduced during growth as demarcated by the dashed lines and labels in Figures 5.7 b), d), f) and h). The lack of corresponding periodicity within Figures 5.7 b), d), f) and h) and the correlation of large increases in the I_D/I_G ratio to macroscopic defects is further confirmation that nitrogen has not been incorporated into the graphene during growth, within the sensitivity of our spectrometer.

The demarcated regions are considered to be the best possible approximation for the expected nitrogen- and argon-buffered regions. This approximation is based on the assumption that the analysed graphene domains grew at a linear rate with respect to radius throughout the entire growth period, rather than a growth rate that was linear with respect to area, and is thought to be valid for the following reasons:

1. Carbon-domain edge-attachment, rather than carbon-surface diffusion, was the rate limiting step, evidenced by the 'feathered' graphene domain edges [157]. Graphene domain morphology based on growth rate limiting steps is discussed in more detail in Section 4.1.4.

2. At the point of growth termination, graphene foil area coverage was $< 80\%$, meaning that:

   (a) sufficient copper foil surface was still available to catalyse CH_4 decomposition to maintain growth rates [58, 62, 164] and

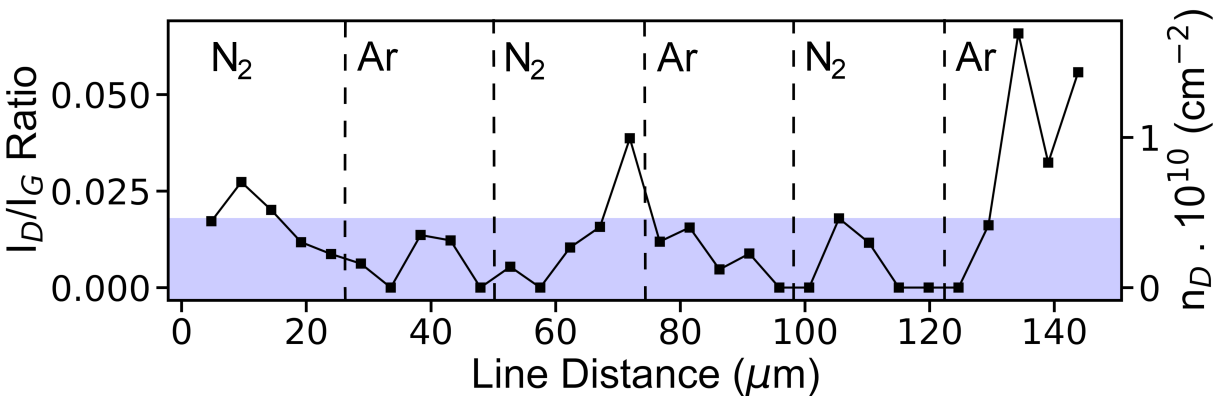

Figure 5.8: Averaged radial linescan values from the graphene domain displayed in Figure 5.6.

(b) inter-domain growth competition had not begun, meaning growth rates were maintained throughout [58, 164, 322].

Indeed, the linear radial growth rate has been demonstrated experimentally by Li et al. [323] and Srinivasan et al. [322], via the use of similar protocols, within which ^{12}C and ^{13}C were alternated between throughout the graphene growth period. As the location of the Raman peaks from graphene grown with ^{13}C are downshifted with respect to graphene grown with ^{12}C [62, 322, 323], the resulting maps of Raman peak locations displays a clear radially linear growth rate [322, 323].

To reduce the impact of local features on the Raman linescans, Figure 5.8 displays the mean I_D/I_G value from all the radial line scans obtained from the graphene domain. Apart from the two spikes in I_D/I_G signal, which are an artifact of the features labelled as i and ii in Figures 5.7 a) and b), the mean I_D/I_G ratio remains below the minimum detection limit across all line scans. It is important to emphasise again that increases in I_D/I_G ratios show no relation to the gas switching periodicity, indicated by the dashed lines and labels within Figure 5.8.

To further confirm the absence of banded I_D/I_G increases, micro-Raman mapping was carried out on graphene domains grown under switched nitrogen and argon atmospheres. The micro-Raman maps were recorded using a WITec alpha 300 R with a 532 nm excitation laser, a 20X objective lens and a spectral grating with 600 lines/mm. Maps were taken over an area of 160 um x 160 um with spectra acquired in 1 um steps in the x and y directions (i.e. 160 x 160 spectra) using an acquisition time of 0.05 s for each spectrum. Optical micrographs of graphene domains transferred onto 80 nm SiO2 on Si are displayed in Figures 5.9 a), b) and c). The corresponding Raman maps are displayed in Figures 5.9 d), e) and f). Figures 5.9 b), c), e) and f) are from the same domain, with Figures

b) and e) displaying the centre of the graphene domain and c) and f)displaying the edge of the graphene domain. This is done to show that the I_D/I_G ratio behaviour remains homogeneous throughout the entire graphene domain. Using a similar process to the one described for the data displayed in Figure 5.7, the minimum resolvable peak height from spectra obtained with the micro-Raman instrument corresponds to an I_D/I_G ratio of 0.03. This returns a minimum detection limit of 7.71 x 10^9 cm^{-2} for point defects, or 9.84 x 10^{12} cm^{-2} for graphitic nitrogen. As explained previously, the substitution of nitrogen into the graphene lattice during nitrogen-buffered CVD would be expected to result in increased D-peak intensity. The lack of observable banding within both domains further indicates that nitrogen is not present in the graphene sheet within the detection limit of the micro-Raman instrument.

5.2.2 XPS

As Raman spectroscopy does not return explicit chemical information about hetero-atoms or defects within the graphene lattice X-ray photoelectron spectroscopy (XPS) was employed for its chemical sensitivity, as another method to probe graphene grown under argon and nitrogen atmospheres for the presence of nitrogen within the film. XPS data was acquired with a PHI VersaProbe III, using a micro-focussed monochromated Al K-alpha source (1486.6 eV) and dual-beam charge neutralisation. Measurements were conducted with a spot size of 100 microns and a pass energy of 26 eV using PHI SmartSoft VersaProbe software. Core-level spectra were acquired around the N1s and C1s binding energies. These binding energies were chosen as the presence of nitrogen is most likely to be observable within these energy envelopes, either due to the presence of nitrogen or due to carbon-nitrogen bonding. Figure 5.10 displays the N1s core-level spectra obtained from nitrogen-buffered and argon-buffered graphene on the copper growth foil (as-grown) and after PMMA-mediated transfer to SiO2. The N1s spectra are corrected with a linear fit before plotting and visual inspection reveals no resolvable features within the spectra taken from graphene transferred to SiO2 or from the as-grown nitrogen-buffered graphene. A small peak is observed within the spectrum taken from the as-grown argon-buffered graphene – as no nitrogen is expected within this sample this is an unexpected feature and more investigation is required to understand this result. However, the height of the peak observed is approximately the minimum resolvable height in relation to the peak-to-peak amplitude of the background noise, which allows a minimum detection limit

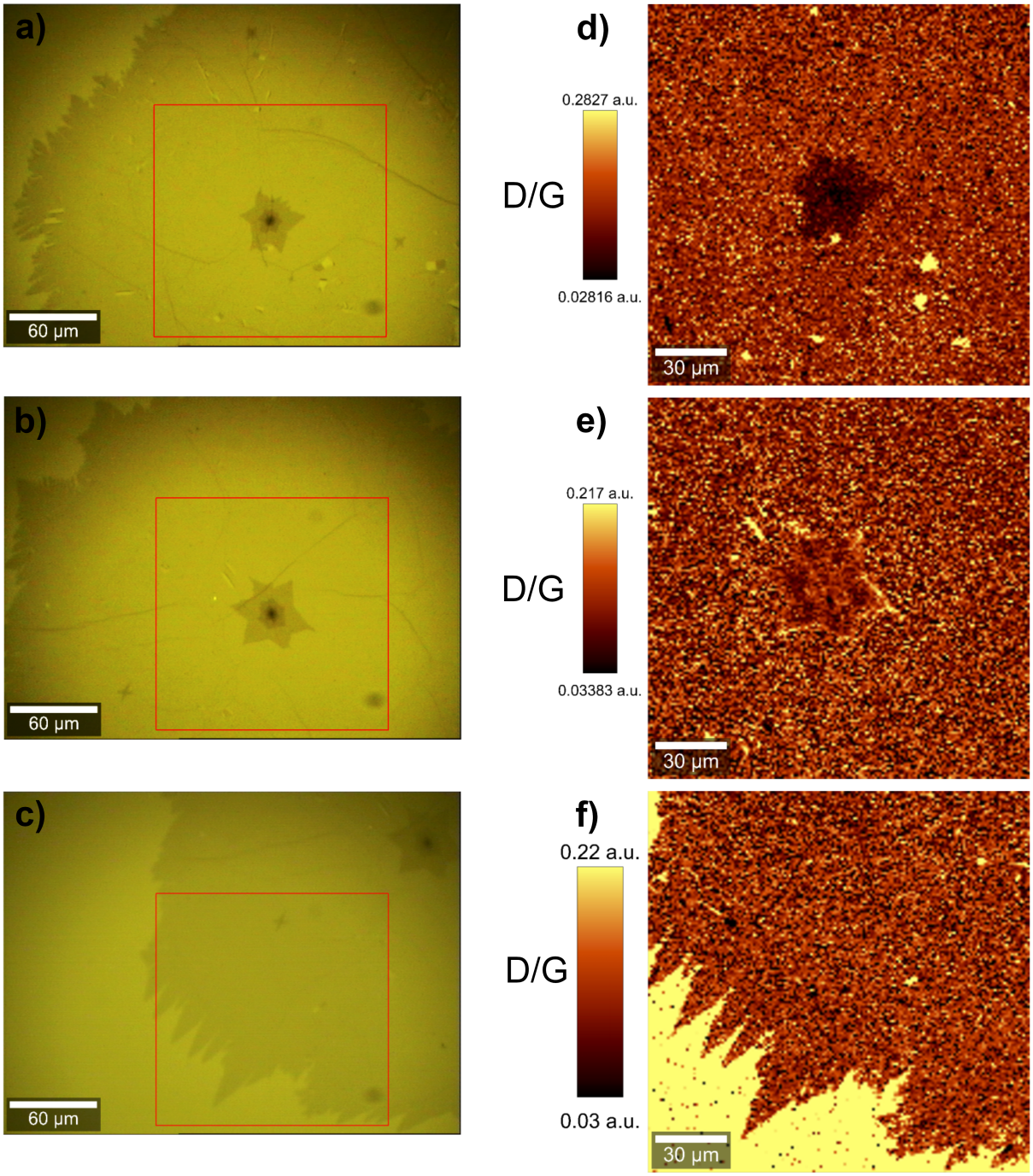

Figure 5.9: Optical micrographs of graphene domains transferred to 80nm SiO_2on Si,a), b) and c) and the corresponding micro-Raman maps d), e) and f). Images b) and c) and maps e) and f) are from the same domain but display the centre and the edge of the domain respectively.

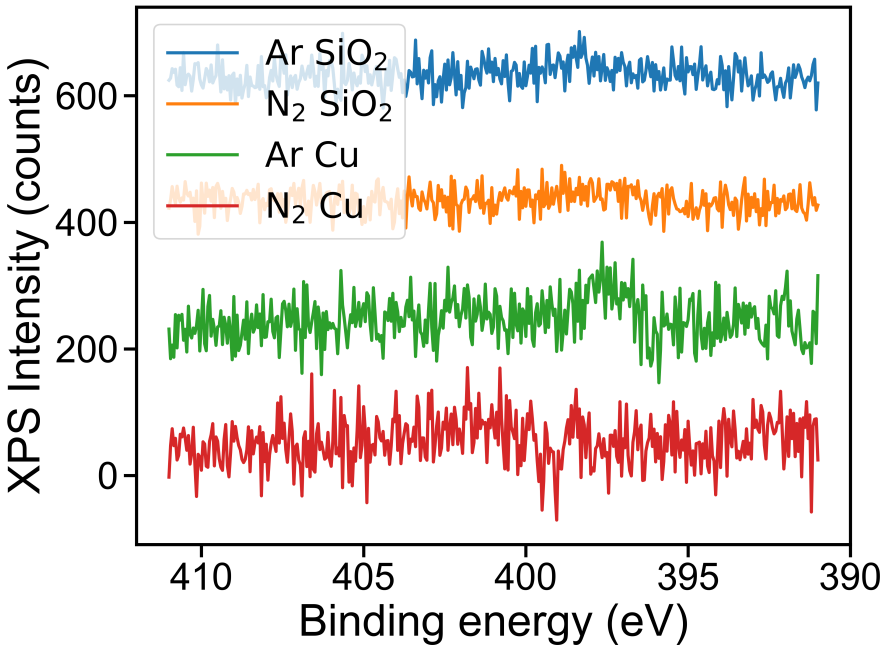

Figure 5.10: N1s core-level XPS spectra obtained from nitrogen-buffered and argon-buffered graphene on the copper growth foil (as-grown) and after PMMA-mediated transfer to SiO2.

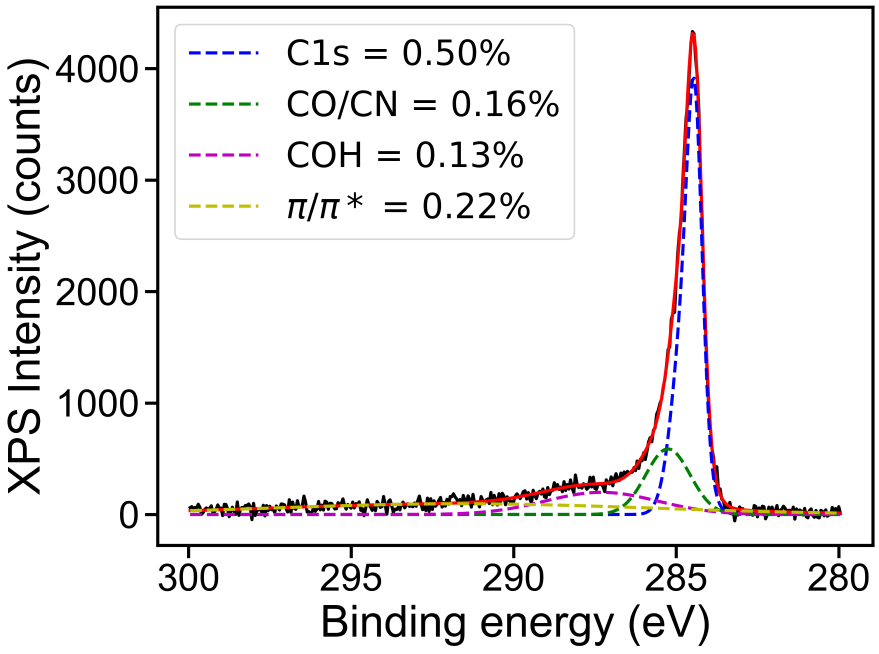

Figure 5.11: C1s core-level XPS spectrum recorded from argon-buffered graphene on the copper growth foil.

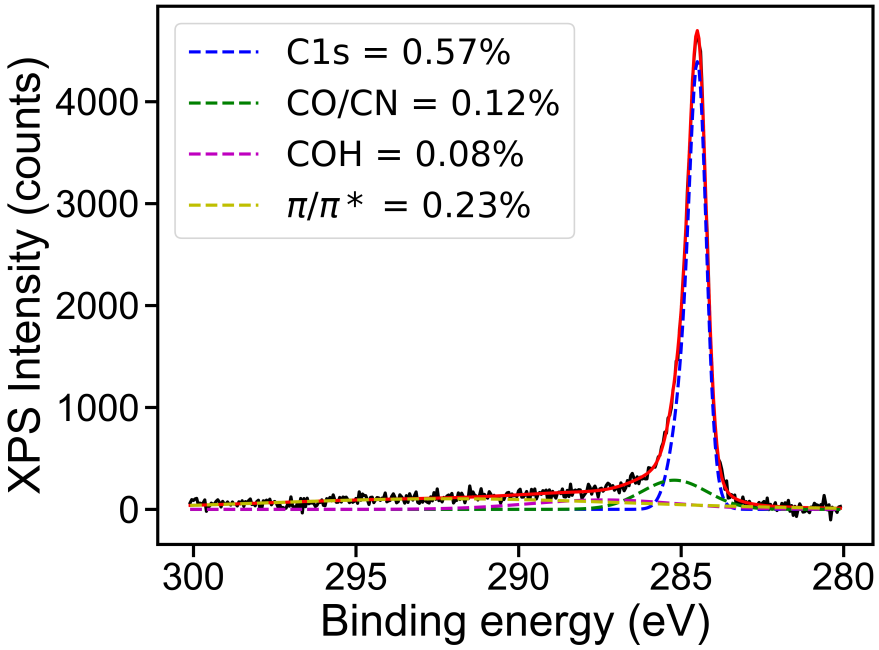

Figure 5.12: C1s core-level XPS spectrum recorded from nitrogen-buffered graphene on the copper growth foil.

for nitrogen to be calculated. By extracting the areas of the resolvable N1s peak within the Ar graphene on foil spectrum and the total area of the fit for the C1s peak acquired from the as-grown argon-buffered graphene, displayed in Figure 5.11, after application of the relevant sensitivity factors for nitrogen and carbon [253] the minimum detection limit for nitrogen within graphene on copper is found to be 0.84 ± 0.28 at.%. This is greater than quoted values for minimum detectable nitrogen content within carbon [190] and can be ascribed to the increased peak-to-peak amplitude of the background signal due to scattering caused by the roughness of the copper foil [252]. As the surface roughness of the graphene transferred to SiO2 is much reduced, the peak-to-peak amplitude of the background signal is reduced by a factor of 2.5 and thus the minimum detectable N1s signal allows a minimum nitrogen detection limit of 0.34 ± 0.14 at.%, which is in good agreement with values quoted elsewhere[190].

Figures 5.11 and 5.12 display the C1s spectra for as-grown argon- and nitrogen-buffered graphene respectively. Both spectra are well fitted by 3 Gaussian peaks at 285.3 eV, 287.3 eV and 291.6 eV in addition to the sp^2 peak centred at 284.5 eV. We assign these peaks to C-C, C-H or C-N bonding, C-O-H or C-O-C bonding and C=O bonding respectively [187]. As nitrogen is not expected within the argon-buffered graphene, we ascribe the peak at 285.3 eV within Figure 5.11 to C-C or C-H bonding. The area of the peak at 285.3 eV is larger in Figure 5.11, obtained from argon-buffered graphene, than in the XPS spectrum

from the nitrogen-buffered graphene, displayed in Figure 5.12. If taken in conjunction with the N1s data, it is possible to conclude that the nitrogen concentration within nitrogen-buffered graphene lies below the detection limit of 0.35 at.% for the X-ray photoelectron spectrometer within the settings used. There are no observed increases in nitrogen-related XPS signals within the graphene grown under a nitrogen-buffered atmosphere. The C1s core-level spectra are not presented for graphene transferred to SiO2 on Si because XPS signals from polymer residues containing C-C and C-O groups would obscure the relevant energy envelope for exploring the presence of C-N bonding.

5.2.3 TOF-SIMS

TOF-SIMS was used to as a further probe to study the elemental composition of graphene on copper and after polymer-assisted transfer to SiO_2. Surface measurements were taken with a PhiNano TOF II spectrometer using a Ga+ primary ion gun (30 keV; current: 3 nA), bunched mode and negative ion polarity. After data acquisition, spectra were normalised by the total spectrum count number. Figure 5.13 displays the count fractions of the relevant nitrogen bearing species (CN and CNO) recorded. The CN and CNO count fractions are more than five times greater within the data recorded from the nitrogen-buffered graphene on copper than the argon-buffered graphene on copper. As mentioned previously, it is thought that nitrogen-bearing species dissolve into the copper foil during growth. The TOF-SIMS data for both as-grown samples display a clear peak at the mass/charge value for copper of m/z = 62.93, demonstrating sputtering of the copper foil below the graphene during data acquisition. The count fractions of CN and CNO within the spectra acquired from argon-buffered and nitrogen-buffered graphene on $SiO_2$are comparable. The count fractions for both species are slightly smaller within the nitrogen-buffered graphene than the argon-buffered graphene, but are still easily resolvable within the count fraction detection limit of $(5.09 \pm 3.58) \times 10^{-5}$ for the spectrometer and measurement parameters. No copper signal is observed within either spectrum indicating that the increased nitrogen signal originated from the copper foil rather than the graphene. The TOF-SIMS data does not indicate that nitrogen substitutes into the graphene lattice during nitrogen buffered graphene growth within copper-catalysed methane-based hot-wall CVD.

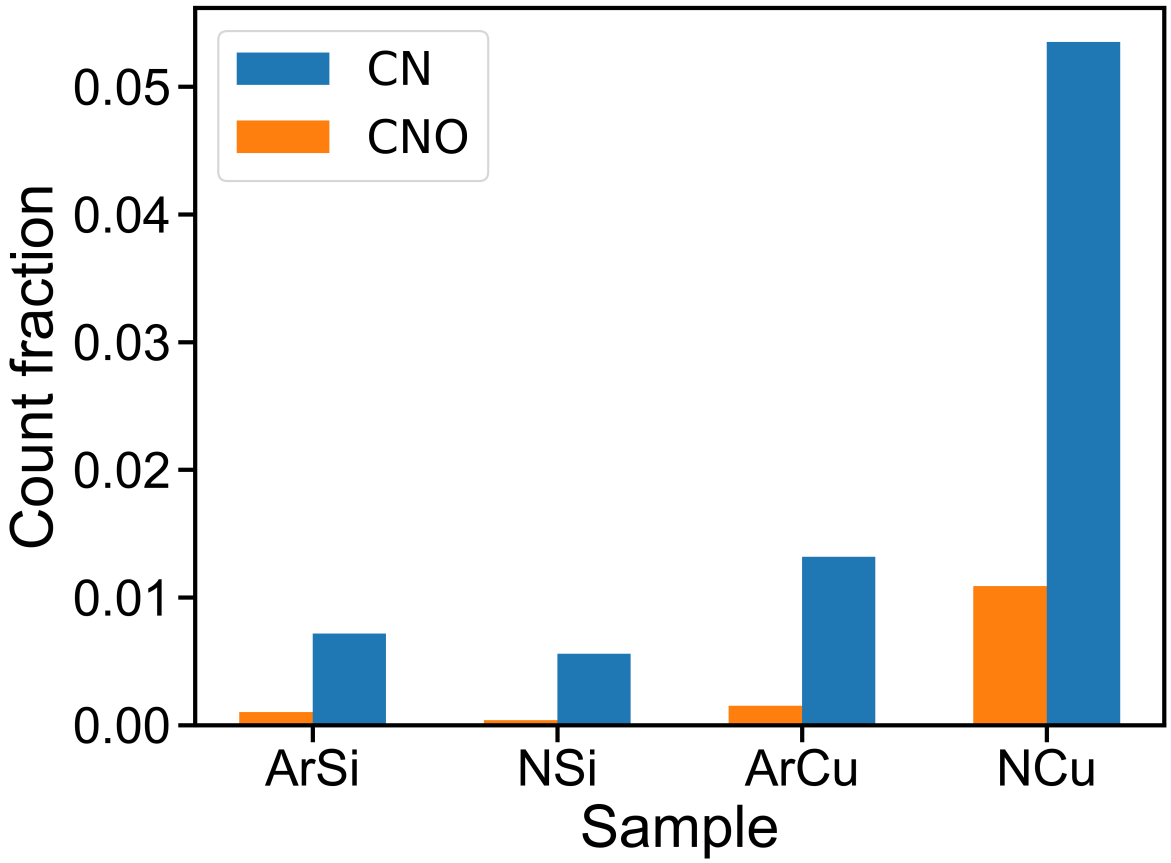

Figure 5.13: TOF-SIMS measurement count fractions of CN and CNO molecular fragments, recorded from nitrogen- and argon-buffered graphene, after transfer to SiO_2 and from graphene left on the copper growth foil.

5.2.4 Electronic Characterisation

Finally, electronic characterisation of GFETs can provide an indication of substitutional nitrogen within the graphene lattice, due to n-doping effects from substitutional nitrogen atoms. It is possible to measure the residual doping of the graphene channel by recording the location of the GFET transfer curve minimum, or charge neutrality point (CNP), denoted by V_{CNP}. Recall from Chapter 3.2.5, that the CNP location can be equated to residual doping via $n_0 = V_{CNP} \cdot C_{ox}/q$, where n_0 is the residual channel doping density per cm^2, C_{ox} is the oxide capacitance per cm^2 (11.505 nF cm^{-2} for 300 nm SiO_2) and q is the unsigned elementary electronic charge.

Figure 5.14 displays characteristic transfer curves taken from GFETs fabricated using N-graphene (N-GFET) and Ar-graphene (Ar-GFET). Both the N-GFET V_{CNP} and Ar-GFET V_{CNP} are found to lie at 40 V, which corresponds to a residual p-doping density of 2.87×10^{12} cm^{-2}. Uncertainties of -0.5 V for both Ar- and N-GFETs, and +0.5 V and +1.0 V for Ar- and N-GFETs have been applied to the CNP, resulting in residual doping densities confidence intervals of $\pm$ 3×10^{10} cm^{-2} for the Ar-GFET, and - 3×10^{10} and + 6×10^{10} cm^{-2} for the N-GFET. As the residual doping densities of both the Ar- and N-graphene channels are found to be similar and within the same V_g interval, it is possible to state that n-doping of the N-GFET graphene channel due to nitrogen inclusion within the graphene lattice is not detectable within the sensitivity of this experiment or above the p-doping effect of transfer residues. An increased uncertainty interval was applied to the positive side of CNP of the N-GFET transfer curve, due to the reduced gradient observed within the n-conducting region of the N-GFET. The reduced gradient of the N-GFET transfer curve may be due to an increased density of polarisable oxygen-bearing groups, such as water, adjacent to the graphene channel [194, 196, 324, 325] – the increased density of which are likely an artefact of the N-GFET having been fabricated approximately a year earlier within the project. However, more research would be required to confirm the exact source of this behaviour. Additionally, the inclusion of nitrogen within the graphene lattice would be expected to significantly reduce the charge carrier mobility within the N-GFET [187], but the electron (hole) mobilities were found, via the gradual channel approximation (see Chapter 3.2.5), to be 1700 cm^2 V^{-1} s^{-1} (1300 cm^2 V^{-1} s^{-1}) and 970 cm^2 V^{-1} s^{-1} (1300 cm^2 V^{-1} s^{-1}) for Ar-graphene and N-graphene respectively; both well within the expected mobility value range for GFETs fabricated during this research. Finally, the channel doping densities extracted from Figure 5.14, suggest that graphitic-N

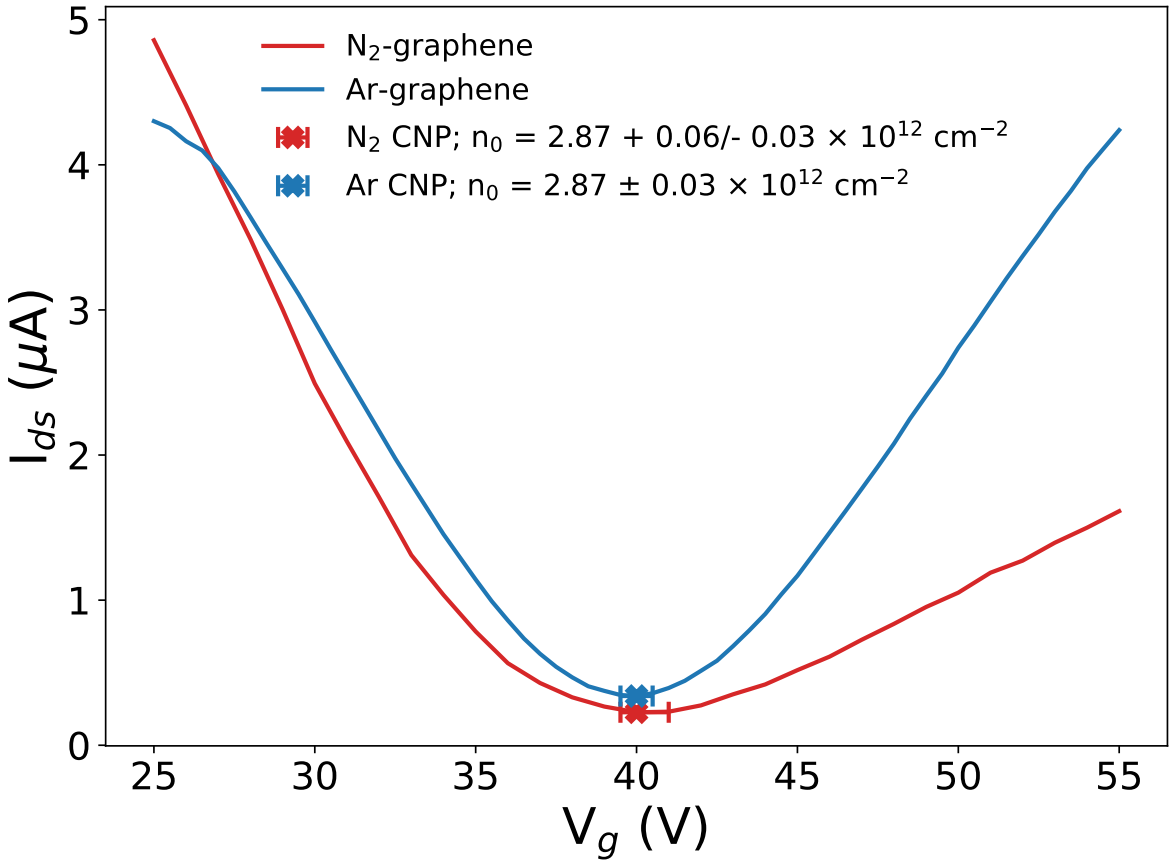

Figure 5.14: GFET transfer curves taken from Ar- and N-GFETs, showing that the CNP lies within a similar range for both Ar- and N-GFETs, suggesting that nitrogen does not substitute into the graphene lattice during nitrogen-buffered graphene CVD.

substitution cannot be present within the graphene lattice at levels similar to the minimum spectroscopic detection limit of $\sim 10^{13}$ cm^{-2}, as assuming that each nitrogen donates 0.5 e$^-$ to the graphene sheet [167, 185, 186], the N-GFET CNP would have to lie at $V_g \approx$ -20 V. Only graphitic substitutional nitrogen is considered here, as both pyridinic and pyrrolic substitutional nitrogen are assumed to be detectable, via Raman spectroscopy, at densities of 2.23×10^9 cm^{-2}. This would correspond to a negligible CNP shift of $\sim$ 0.1 V in comparison to both the CNP shift and range of CNP shifts observed within this research, as presented in more detail within Chapter 6.

5.2.5 Conclusion

The suitability of using nitrogen as a cheaper buffering alternative to argon within hot-walled graphene CVD was explored by growing samples under argon-buffered, nitrogen-buffered and alternating argon- and nitrogen-buffered atmospheres. Raman spectroscopy, XPS and TOF SIMS were used to look for increased nitrogen signal within the graphene

lattice. No evidence of increased nitrogen content within the nitrogen-buffered graphene or within the nitrogen-buffered phases of the graphene grown under alternating nitrogen/argon atmosphere was observed within the detection limits of the spectroscopic techniques used. Additionally, no comparative n-doping of N-GFET channels were observed when compared electronically, via the recording of GFET transfer curves, with Ar-GFETs. We therefore conclude that nitrogen is a suitable buffering gas for use within methane-based hot-wall graphene CVD.

Chapter 6

W_5O_{14}-Graphene Hybrid Gas Sensors

Within this chapter, gas sensing devices based upon graphene field effect transistor (GFET) architecture are explored. Graphene is investigated as a gas sensing material because its unique combination of atomic thinness [1], small density of states close to the graphene charge neutrality point [1, 10] and low noise [222, 326, 327], which means that interactions between the graphene and physisorbed gaseous species should create measurable resistance responses to even small gas concentrations [33, 91, 328]. However, because the graphene basal plane has few or no chemically active sites, gas sensing interactions are due to physisorption and therefore graphene gas sensors have poor selectivity between different gaseous species [172, 329]. In addition, graphene sensors sense all adsorbates on the graphene channel, which means that residues introduced during GFET fabrication are also sensed by the graphene channel and can lead to device desensitisation [218]. To address this problem, hybrid graphene/particle sensors have been widely investigated with a view to improving graphene device sensitivity and selectivity [40, 98, 101, 208, 220].

W_5O_{14} is a sub-stoichiometric form of WO_3, which has only become reliably producible recently [330]. Last year, Yu et al. demonstrated high-sensitivity of W_5O_{14} to 1 ppm H_2S at temperatures between 150 °C and 375 °C [331], due to chemisorption reaction charge exchange. Because H_2S acts as a reducing agent, graphene/W_5O_{14} hybrid systems should display selectivity and increased sensitivity towards reducing agents, such as NH_3, through the activation of chemisorption based charge exchange between W_5O_{14} and analyte gas, followed by a change in the conductivity of the graphene channel.

This chapter is organised as follows: First, the mechanisms for gas sensing via chemisorp-

tion and physisorption are introduced. This is followed by a discussion on the choice of W_5O_{14} microparticles for graphene functionalisation and data is presented for the deposition of W_5O_{14} microparticles from suspension in ethanol. The graphene/W_5O_{14} material system is then characterised at the micro scale via KPFM of W_5O_{14} particles on graphene. Characteristic operation of GFETs used within this research is displayed, which demonstrates behaviour consistent with reported values [262–265] and is used to discuss GFETs doping effects. The macro-doping effect of W_5O_{14} on graphene is then presented via gate bias transfer curves which show the n-doping effect of W_5O_{14} on graphene. Finally, a comparison of gas sensing behaviour between non-decorated and W_5O_{14}-decorated GFETs is presented.

6.1 Sensing Mechanisms

Whilst graphene has been shown to be sensitive to both reducing and oxidising gas species [33, 91, 328], the mechanism responsible gas sensing on prisitine graphene is physisorption [328, 332]. When compared with chemisorption, the interaction between physisorbed species and the underlying material is known to be weak [332, 333]. Indeed, using density functional theory (DFT), Leenaerts et al. calculated that NH_3 weakly physisorbs on pristine graphene with an energy of physisorption of approximately 35meV [172]. Additionally, a physisorbed NH_3 molecule donates only $0.03e$ to the pristine graphene [172], which would result in negligible channel resistance changes if a devices were to be operated with direct current (DC) for resistance modulation observation.

The case is a little different for NO_2, whose lowest unoccupied molecular orbit (LUMO) hybridises more strongly with graphene due to the paramagentism of NO_2 molecules [172]. Leenaerts et al. showed that the energy of physisorption of NO_2 on pristine graphene is greater than that of NH_3 at 67meV and the charge transfer to the NO_2 LUMO results in a charge transfer of $0.1e$ from the graphene to the adsorbed NO_2 [172]. Whilst the interaction between NO_2 and graphene is greater than that of NH_3 on graphene, physisorption interactions are still considerably weaker than chemisorption interactions [332, 334]. Therefore, to increase device sensitivity towards NH_3, a suitable material for NH_3 chemisorption should be selected. As W_5O_{14} has been shown to be sensitive towards reducing gas species, with chemisorption as the sensing mechanism, we propose the use of W_5O_{14} as a decorating particle for a graphene-hybrid system.

Figure 6.1 a) displays a schematic representation of the physisorption interaction be-

tween NO_2 and NH_3 on bare pristine graphene. Figure 6.1 b) shows a schematic representation of the chemisorption interaction expected between NH_3 and W_5O_{14} on graphene, based upon the W_5O_{14} sensing results of Yu et al. [331]. The magnitude and direction of charge transfer between the adsorbed gas molecule and either graphene or W_5O_{14} on graphene is illustrated by the arrow labels and arrow directions respectively. From the arrow labels in Figure 6.1 it can be seen that the magnitude of charge transfer occurring in chemisorption is at least one order of magnitude greater than that within the physisorption interactions. The chemisorption interaction between NO_2 and W_5O_{14} is not displayed, as temperatures considerably above the operational temperatures used within this study are required to further oxidise W_5O_{14}, whereas reduction of W_5O_{14} has been demonstrated within the operational temperature range used within this study [331]. A representative schematic is displayed in Figure 6.1 c), where the highlighted green region shows the area either side of the Fermi-level of pristine graphene which is most sensitive to charge exchange. This region is most sensitive to adsorbates, because even small charge exchange will have a large effect on the location of the graphene Fermi energy. Arrows are provided as reminders of which way the Fermi-level moves upon p- or n-doping. The arrows labelled chemisorb and physisorb represent the interaction strength between graphene and a chemi/physisorbed molecule, with chemisorption having a greater effect. Note that none of the arrows in Figure 6.1 c) are to scale and are only representative of different interactions.

6.2 W_5O_{14} Particles

The success demonstrated by hybrid graphene-particle devices [40, 98, 101, 208, 220] inspired the investigation of hybrid W_5O_{14}/graphene gas sensors to improve graphene-based gas sensor device sensitivity towards NH_3. As W_5O_{14} particles have already demonstrated sensitivity toward another reducing gas, H_2S [331], coupling W_5O_{14} with an underlying graphene channel is expected to result in improved device sensitivity and response times.

W_5O_{14} is a sub-oxidation state of tungsten, which is typically found in the fully oxidised stoichiometry, WO_3 [105]. Saqib et al. showed that W_5O_{14} has distinctly different material properties to WO_3. One key difference is that WO_x changes from a semiconductor with a bandgap of between 2.5 eV - 3.2 eV when it has stoichiometry of WO_3 [335], to a metallic conductor in W_5O_{14} stoichiometry [105, 330]. Electrical resistivity also drops from approximately 10^4 Ωcm [336] for WO_3, to 25 $\mu\Omega$cm when the stoichiometry is

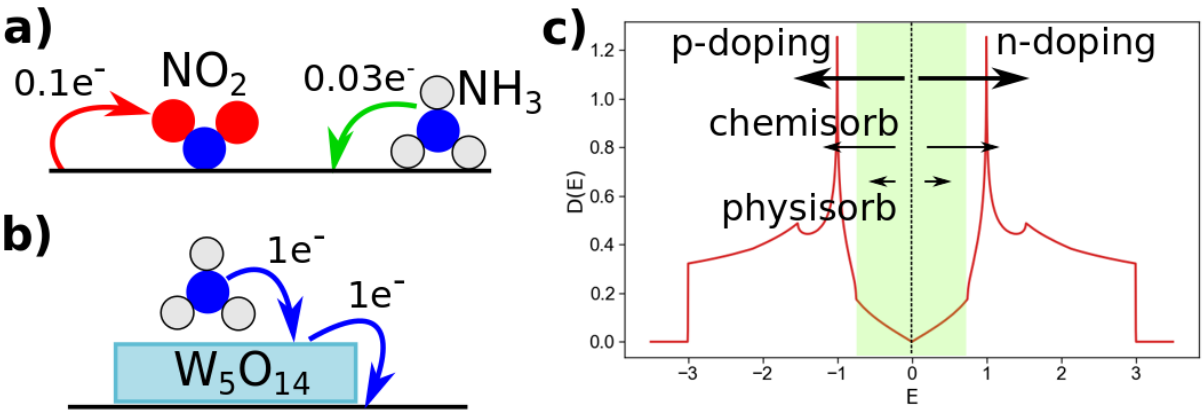

Figure 6.1: Schematic representations of, a) physisorption of NO_2 and NH_3, and b) chemisorption of NH_3, on pristine graphene. The magnitude and direction of charge transfer between gas molecule and graphene is indicated by the arrow labels and arrows respectively. c) displays a plot of the DOS in graphene. The highlighted green region shows the area either side of the Fermi-level of pristine graphene which is most sensitive to charge exchange. The size of the arrows labelled for chemisorption and physisorption represent the difference in interaction strength between graphene and a chemi/physisorbed molecule. Note that none of the arrows are to scale and are only representative of different interactions.

changes to W_5O_{14} [105, 330].

KPFM studies conducted by Saqib et al. of W_5O_{14} on freshly exfoliated highly ordered pyrrolitic graphite (HOPG) show that W_5O_{14} has a facet-dependant surface potential of 4.20 to 4.34 eV [105].

6.2.1 Deposition of WOx on Graphene

W_5O_{14} particles were supplied by the Remskar group from the Solid State Physics Department, at the Jozef Stefan Institute, Ljubljana, Slovenia. The W_5O_{14} particles were then suspended in ethanol before exploring deposition via spin-casting and drop casting were investigated.

Spin casting was found to be ineffective as the W_5O_{14} particles do not adhere strongly enough to the underlying graphene to avoid re-dispersion upon subsequent W_5O_{14} suspension application. As material being spin cast experiences a centrifugal force which is used to spread the material, re-dispersed W_5O_{14} particles are forced to the edge, and subsequently off, the target substrate. This effect prevents surface coverage of W_5O_{14} from increasing beyond that achieved within the first application ($\sim$ 2% surface coverage) and is therefore considered and unsuitable method for W_5O_{14} deposition.

Therefore drop casting was used for W_5O_{14} particle deposition as it allows W_5O_{14} surface coverage to be selected via dose application. Due to the rapid evaporation rate of

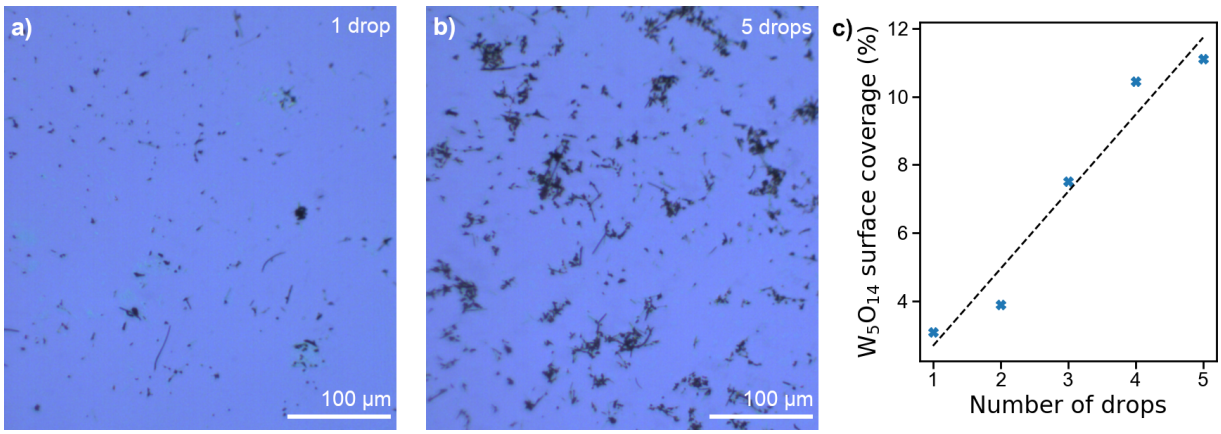

Figure 6.2: Micrograph images of W_5O_{14} microparticle density on SiO_2 substrate after a) one 50 µl drop, b) five 50 µl drops and c), plot displaying substrate surface area coverage of W_5O_{14} microparticles as a function of drops applied.

ethanol and the size of the W_5O_{14} micro particles, coffee-ring effects were not found to be a major issue. The coffee-ring effect relates to the deposition of particulate matter within a suspension in a ring-like fashion as a drop of liquid dries on a solid surface [337]. However, as displayed in Figure 6.2 b), clumping of W_5O_{14} particles begins to occur after multiple suspension applications. Although this is not an ideal outcome, device area coverage by W_5O_{14} is the more important metric and so drop casting is used as the method for W_5O_{14} deposition. Figure 6.2 displays optical micrographs of W_5O_{14} surface coverage after a), one application and b), five applications. An appreciable increase in area coverage is observed and the area coverage is found to have an approximately linear relationship with respect to the number of drop cast applications, displayed in Figure 6.2 c). This means that it is possible to tailor the W_5O_{14} particle density, or coverage, by repeated drop casting from the W_5O_{14} microparticle suspension followed by visual inspection after each drop application until the desired particle density is achieved. Optical microscopy is found to be sufficient to visualise W_5O_{14} coverage which allows for rapid coverage assessment.

6.3 KPFM W_5O_{14} on Graphene

KPFM is used to probe the electron surface potential of W_5O_{14} on transferred CVD graphene, to investigate relative material work functions thus allowing W_5O_{14}-graphene charge transfer to be predicted. The working mechanism of KPFM is describe in detail in Chaper 3. KPFM creates corresponding topographical and electron surface potential maps across areas of interest which enables the investigation of the work functions of graphene and W_5O_{14}. This, is turn, allows predictions to be formed regarding W_5O_{14}-

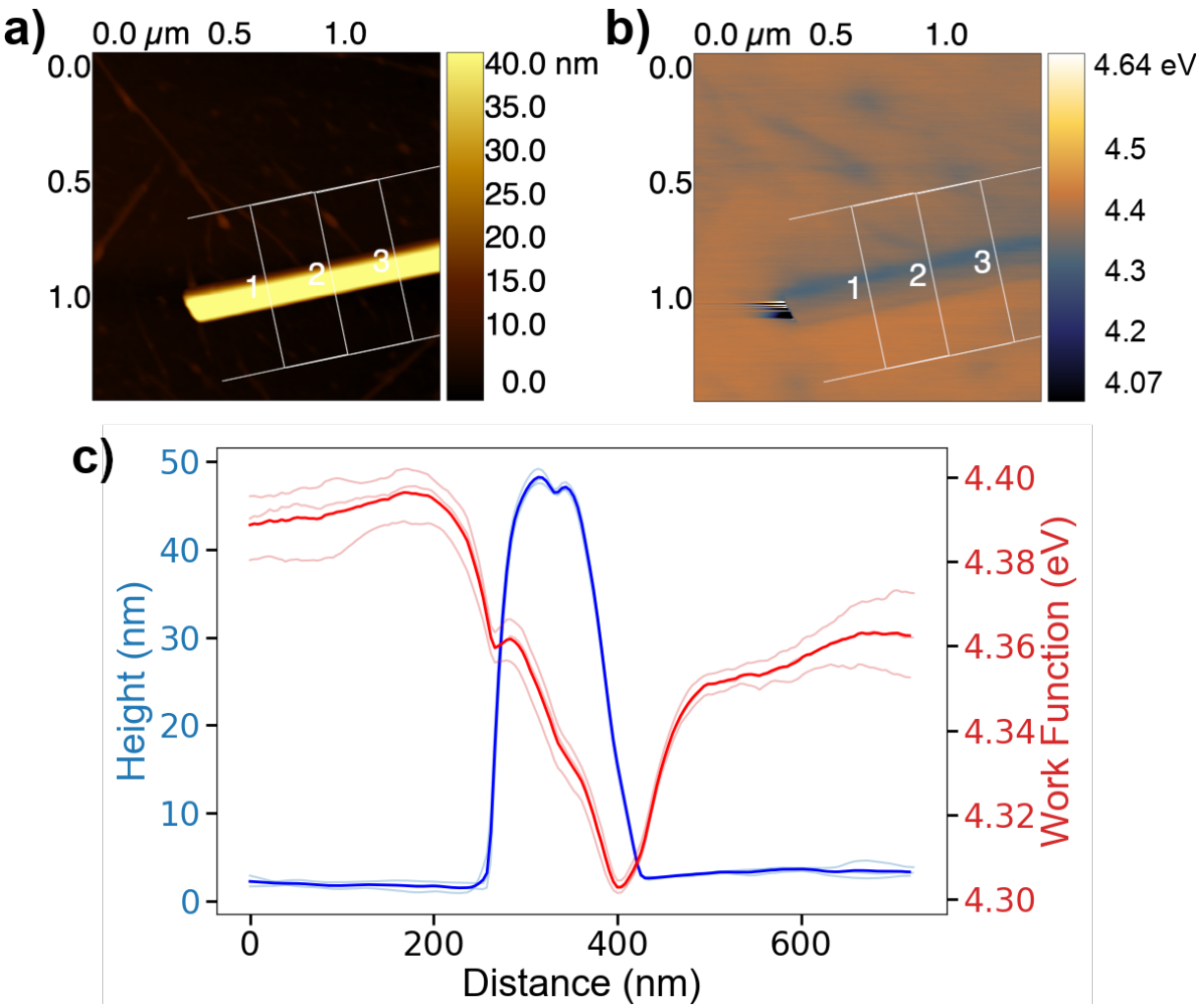

Figure 6.3: AFM maps of a W_5O_{14}-nanowire on CVD graphene. a) displays topography; b) displays the KPFM surface map; c) plot of line profiles extracted across the W_5O_{14} nanowire.

graphene charge transfer. The importance of W_5O_{14}-graphene charge transfer is discussed in more detail in Section 6.4.

Figure 6.3 displays a representative AFM/KPFM scan taken from W_5O_{14} on graphene. Before and after scanning, the work function of the AFM tip was calibrated against a thin gold film to allow the direct display of measured work functions – a), topography and b), KPFM surface maps are presented alongside c), a plot of the indicated line profiles extracted across the W_5O_{14} nanowire within a) and b). It can be seen from the KPFM measurements that the electron surface potential is reduced across the W_5O_{14} nanowire, with a work function (Φ_{WOx}) of between 50 meV to 100 meV lower than that of the surrounding graphene sheet. The difference between the graphene and W_5O_{14} work functions are greater than expected from reported values by Leenaerts et al. for pristine graphene on SiO_2 (4.35 eV) [104] and W_5O_{14} on Highly oriented pyrolytic graphite (HOPG) (4.20 eV to 4.34 eV) as measured by Saquib et al. [105]. The KPFM measurements suggest that

the Fermi-level of the graphene sheet is slightly lower, i.e. $\Phi_{graphene}$ is slightly increased, when compared to the expected value for pristine graphene. The increase in $\Phi_{graphene}$ is also evidenced by the positive shift of the CNP from $V_g = 0$ V, presented within Figure 6.5. The non-homogeneity of $\Phi_{graphene}$ across the graphene surface also shows that there is localised p-doping of the graphene sheet. This p-doping most likely originates from polymer residues introduced during the graphene transfer, as such work function puddles are common to all KPFM measurements taken throughout this research, regardless of whether the graphene sheet has been functionalised or not.

We now consider the KPFM profile of the W_5O_{14} nanowire. The stepped surface potential profile across the W_5O_{14} nanowire is observed within all KPFM scans carried out throughout this research and is in agreement with observations reported by Saquib et al. [105]. Small local decreases of Φ_{WOx} are observed in the centre of nanowire facets and are thought to be related to increased oxygen vacancy defects [105]. As Φ_{WOx} is measured to be lower than $\Phi_{graphene}$, there will be electron transfer from W_5O_{14} particles to the graphene, causing of n-doping of the graphene channel, which is discussed in more detail within Section 6.4.

6.4 GFETs and GFET Doping

6.4.1 As-fabricated GFET Characteristics

GFETs are used within this project as a platform for gas sensing devices. The fabrication process for these GFETs is described in detail within Chapter 3. Figure 6.4 displays an 11-device GFET chip fabricated on SiO_2 during this project. The contacts are defined via UV-photolithography and contacts are deposited via e-beam evaporation of 40 nm gold on 10 nm chromium, followed by photoresist lift-off, prior to CVD-graphene transfer. The graphene channel is deposited on top of the pre-patterned contacts and is outlined with a yellow dashed line within Figure 6.4 for increased clarity. GFET yield was found to increase by fabricating GFETs this way, although the reason for increased yield is currently unclear and requires further investigation to understand. Additionally, for the purposes of this research, it is desirable to have more graphene exposed to the surrounding gaseous medium as the metal contacts should not display sensitivity towards gaseous analytes due to their continuous and large density of states. Therefore, the fabricating gas sensors by patterning contacts first followed by graphene transfer is of benefit to device yield and to

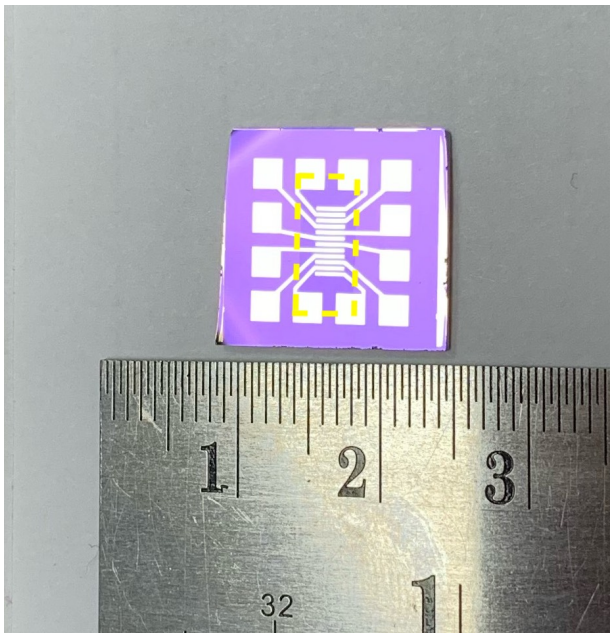

Figure 6.4: Image of a typical GFET fabricated within this work, with Cr/Au contacts on a Si chip capped with 300 nm SiO_2. The graphene channel is outlined by the yellow dashed line for increased clarity. This is a duplicate image of Figure 3.4 included as a reminder within this section.

sensor architecture.

Following fabrication, I_{ds}/V_g sweeps are performed on the GFETs to extract values for charge carrier mobility and channel doping density. Figure 6.5 displays a characteristic curve obtained from an I_{ds}/V_g sweep. The curve displays the typical 'V' shape expected from a GFET transfer curve [1, 10] and the blue and red circles indicate the locations of the charge neutrality point (CNP) for the up and down V_g sweeps respectively. As the CNP for both up and down V_g sweeps lies between + 40 V < V_g < + 50 V, the GFET is seen to be heavily p-doped [195]. P-doping is often observed for GFETs fabricated from CVD graphene transferred from the growth foil using a polymer support layer and wet etching and is caused by polymer contaminants on the graphene surface and water molecules trapped between the graphene and target substrate [195, 329, 338–341].

Graphene charge carrier mobility can be extracted from the GFET transfer curve. As discussed in Chapter 3, by taking the differential of I_{ds} with respect to V_g within the linear regions either side of the CNP, an estimate for charge carrier mobility can be found via the gradual channel approximation (GCA) [194, 255, 261] using Equation 6.1:

$$\mu = \frac{g_m \cdot L}{W \cdot V_{ds} \cdot C_{ox}} \tag{6.1}$$

where μ is charge carrier mobility; g_m is transconductance, equivalent to dI_{ds}/dV_g; V_{ds}

is the source-drain potential, which is maintained at 1 mV throughout the I_{ds}/V_g measurements presented within this chapter; C_{ox} is the capacitance of the SiO_2 layer and is calculated to be 11.505 nF for a SiO_2 capping layer of 300 nm; W and L are the channel width and length of 2 mm and 200 µm respectively. Maximum transconductance (g_m) is selected from both electron and hole regions in both the up and down I_{ds}/V_g sweeps to calculate μ, as detailed in Chapter 3. The GCA and the assumptions made when invoking it are discussed in more detail in Chapter 3, but it is generally accepted that this calculation will provide an underestimate for charge carrier mobility within the device [255, 261]. However, as the GCA is a widely used technique within graphene and 2D materials research, it is an appropriate method for comparing devices fabricated within this research with those reported within the literature. The electron (hole) mobility extracted from this transfer curve was found to be 1760 ± 100 $cm^2V^{-1}s^{-1}$ (2195 ± 35 $cm^2V^{-1}s^{-1}$), which is similar to reported mobility values extracted via the gradual channel approximation from graphene transferred onto SiO_2 [262–264] and is better than similarly large devices [265]. Measured charge carrier mobility is typically lower from devices of increased channel area as the number of channel defects increases due to the increased likelihood of channel defects. Whilst folding and tearing defect densities are independent of the CVD graphene quality, improved graphene CVD growth reduces the graphene grain boundary density and thus improves channel conductivity. The reduction of graphene domain grain boundary density is discussed in detail in Chapter 4.

Figure 6.6 displays box and whisker plots compiled from the mobilities extracted, via the GCA, from all successful GFETs fabricated throughout this research. As indicated on the x-axes of Figure 6.7, 8 GFET chips were successfully fabricated and analysed. Each GFET chip has 11 devices on it and thus, analysis from a total of 88 GFETs is presented within this section. The electron and hole mobilities are typically between 1500 - 2000 $cm^2V^{-1}s^{-1}$, which agrees with mobility values reported for similarly sized GFET devices fabricated on SiO_2 [265]. GFET devices from this research which present low mobility have significant tearing of the measured graphene channel which reduces the effective channel width and reduces charge carrier mobility through sheet edge scattering [342].

The location of the CNPs with respect to V_g (V_{CNP}) can then be used to calculate the magnitude of the residual charge transfer doping within the graphene channel via Equation 6.2, which is repeated here from Chapter 3 for convenience:

$$n_0 = \frac{V_{CNP} \cdot C_{ox}}{q} \tag{6.2}$$

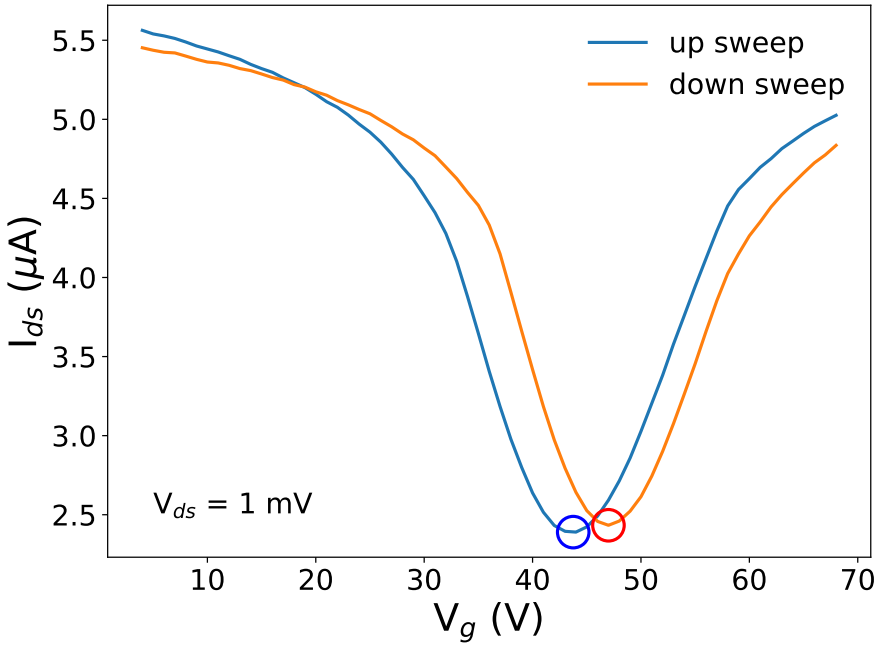

Figure 6.5: Characteristic I_{ds}/V_g sweep from GFET fabricated within this research. A fixed source-drain bias of 1 mV is used during gate sweeps. The blue and red circles highlight the CNP observed during the up and down gate sweeps respectively.

where n_0 is the residual doping density of the graphene channel, expressed as n per cm^2; C_{ox} is the capacitance of the dielectric layer (SiO_2) per cm^2 and q is the unsigned electronic charge. As q is used, a positive (negative) value for n_0 indicates that the graphene channel is p-doped (n-doped). Using Equation 6.2, the net residual charge density for the device presented in Figure 6.5 is found to be 3.16×10^{12} holes cm^{-2} and 3.37×10^{12} holes cm^{-2} for the up sweep and down sweep respectively. CNP hysteresis is observed within all samples and is predominantly ascribed to polarisable silanol groups on the SiO_2 surface and water molecules trapped between the graphene and SiO_2 substrate [194, 196, 324, 325]. Similar observations have been observed within carbon nanotube research [343, 344]. The hysteresis observed between CNP points for up and down sweeps can be used to calculate an approximate charge trap density and in the case of the device presented within Figure 6.5, the charge trap density is found to be 2.1×10^{11} cm^{-2}. The doping densities and hysteresis extracted from these devices are typical of graphene devices fabricated on SiO_2 [195].

Figure 6.7 displays plots of mean and range extracted values of, a), residual channel charge density for all GFET devices calculated from the location of the CNP measured during the up-sweep, b), residual channel charge density for all GFET devices calculated from the CNP location during the down-sweep and c), the charge trap density calculated

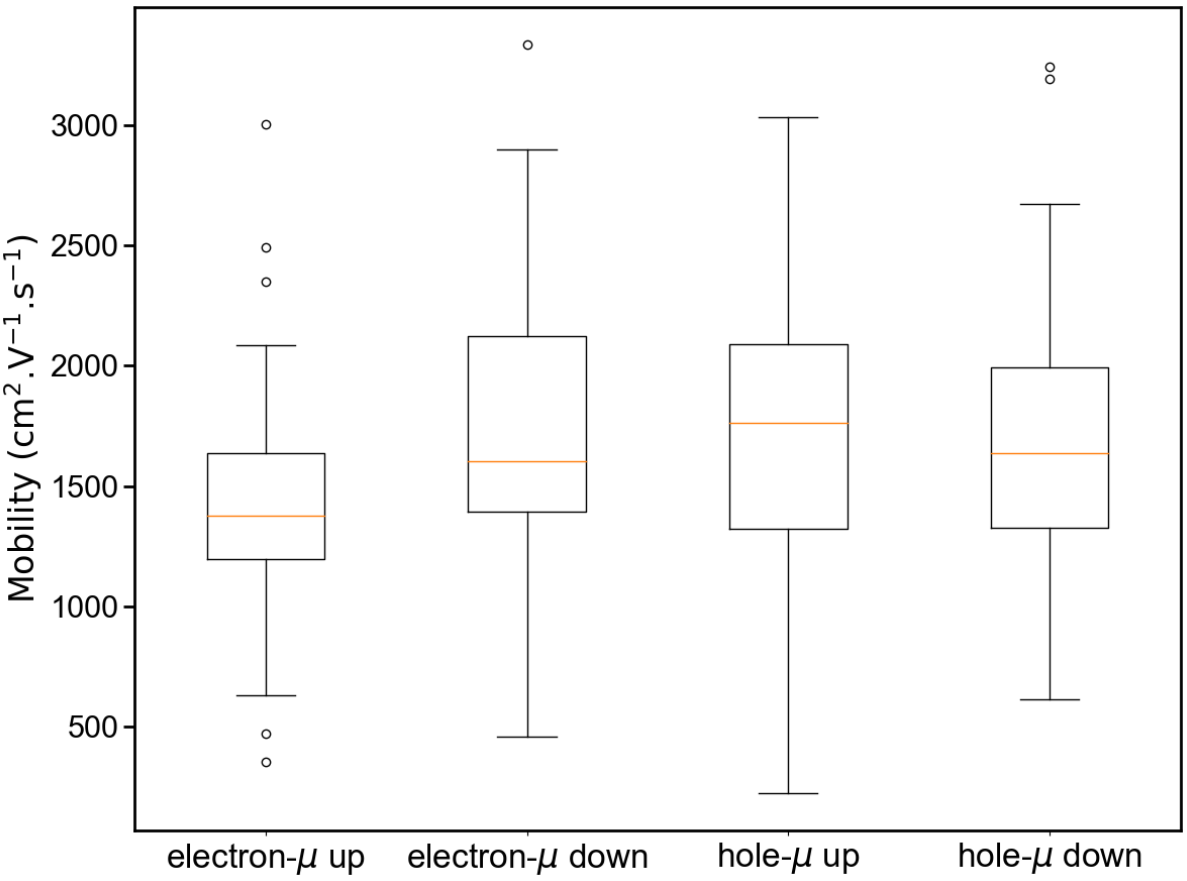

Figure 6.6: Box and whisker plot of mobilities from all GFETs fabricated throughout this research.

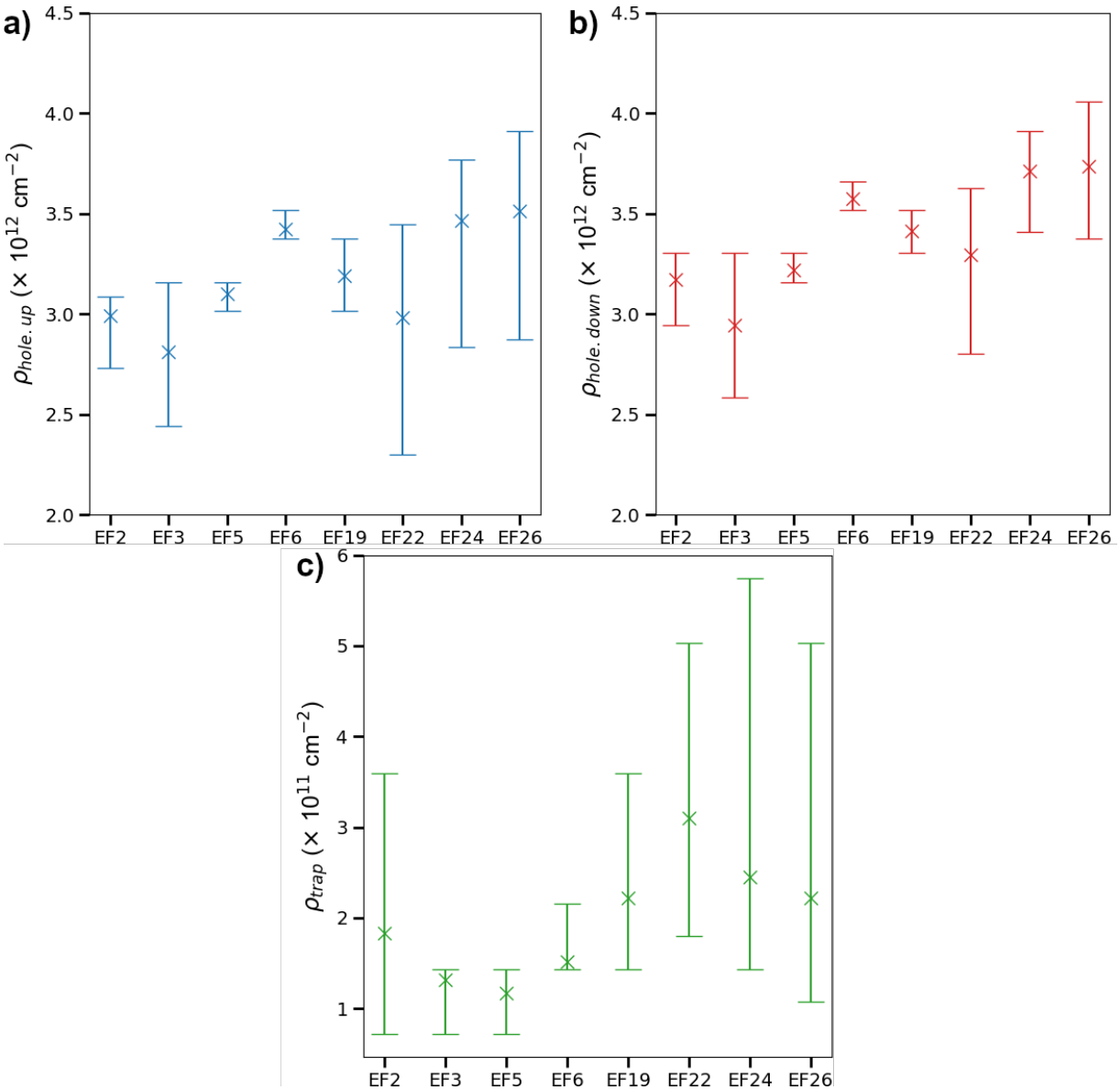

Figure 6.7: Plots of calculated residual charge densities within the graphene channel for a), up I_{ds}/V_g sweep and b), down I_{ds}/V_g sweep and c), charge trap densities calculated from CNP hysteresis.

from CNP hysteresis for all GFET devices. Devices values are plotted against their corresponding GFET chip, to illustrate GFET behaviour variation.

We see from Figure 6.7 that the spread in residual charge can be as large as 2×10^{12} holes cm^{-2} between GFETs fabricated on the same chip, but also that the mean residual charge values across all chips are within about 0.5×10^{12} holes cm^{-2}. Because the graphene transfer step is carried out by hand, and GFET chips are batch made, such a tight cluster of mean residual charge shows that the GFET fabrication technique is acceptably reproducible, as is the subsequent behaviour of the fabricated GFET devices. It is also observed that the GFET chips with large variations in residual channel charge, are also typically the chips which display large variation in charge trap densities. These variations are ascribed to the presence of polarisable species such as silanol groups and water at the graphene-SiO_2 interface [194, 196, 324, 343, 344].

Having established that as fabricated GFETs are p-doped and that W_5O_{14} particles should n-dope the transferred CVD-graphene, as shown by the KPFM data, we investigate the macro-scale effect of W_5O_{14} application to GFET via the evolution of I_{ds}/V_g curves upon successive W_5O_{14} depositions. Figure 6.8 displays the evolution of graphene channel I_{ds}/V_g sweep following multiple rounds of 0.5 ml W_5O_{14} suspension application. After each W_5O_{14} suspension application, the graphene CNP experiences a negative shift. After 9 drop cast applications the V_{CNP} has shifted from $V_g = 34.5$ V to $V_g = 0$ V. Thus, at this point the W_5O_{14} particles have donated 2.48×10^{12} electrons cm^2 to the graphene sheet. Subsequent applications are not found to cause further negative shifting of the graphene CNP (data not shown). This is because pristine graphene has a work function which is very close to that of W_5O_{14} (4.35 eV and 4.34 eV respectively), and therefore, once the Fermi-level of the graphene channel has been returned to its neutral point through electron donation from W_5O_{14}, the Fermi-levels are equal and thus there is no charge transfer from W_5O_{14} to the graphene.

The data presented in Figure 6.8 means that with the correct W_5O_{14} dosage, the aggregate charge transfer into the graphene gas sensor channels from adsorbates and W_5O_{14} particles can be tailored such that $V_g = 0$ V lies within a region of the I_{ds}/V_g sweep with maximum transconductance ($g_m = dI_{ds}/dV_g$). This should result in increased sensitivity to physisorbed gaseous analytes, as further charge transfer to or from the adsorbed gasses should result in an increased change in I_{ds}.

Figure 6.9 displays charge carrier mobilities extracted from the I_{ds}/V_g after each application. Despite the addition of material to the graphene device, which would be expected

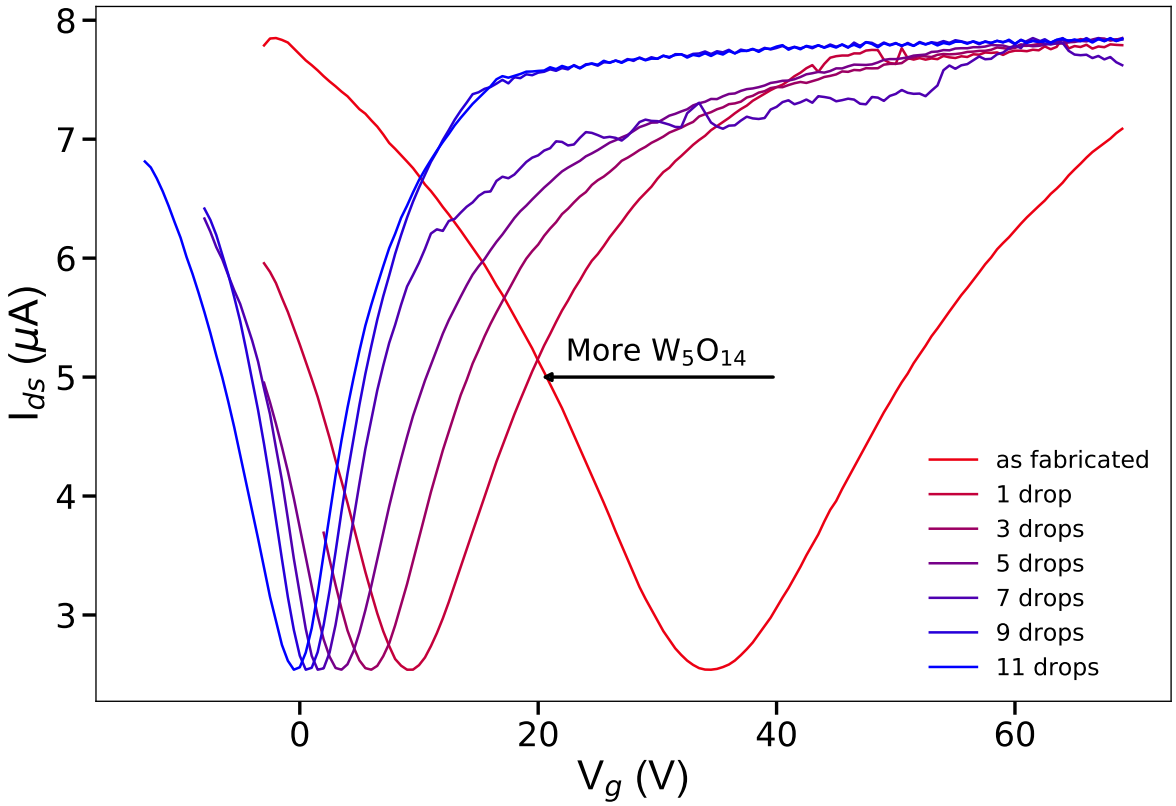

Figure 6.8: Evolution of graphene channel I_{ds}/V_g sweep following the application of multiple 0.5 ml drops of W_5O_{14} suspension.

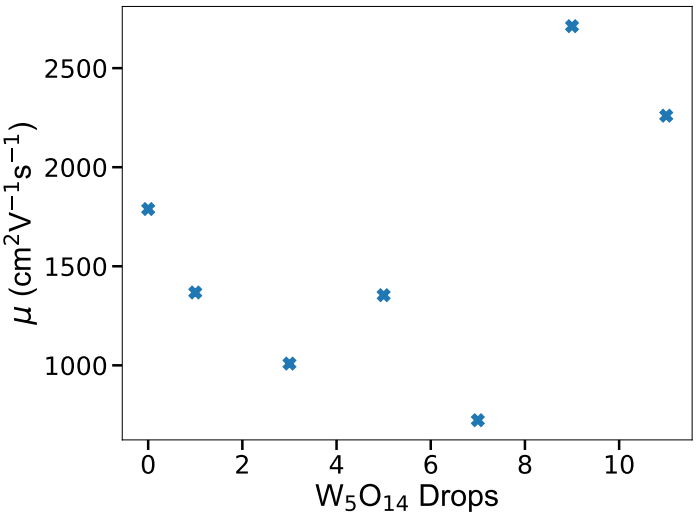

Figure 6.9: Evolution of graphene charge carrier mobilities following multiple rounds of W_5O_{14} application.

to increase charge scattering, the charge carrier mobilities remain close to their original value. The retention of device charge carrier mobility makes post-transfer doping rectification, through the application of W_5O_{14} or similar low work function particles, an attractive prospective method for restoring GFET behaviour.

6.5 Gas Sensing

6.5.1 GFET Gas Sensors

Having successfully demonstrated reproducible device behaviour across devices on the same chip, the sensing characteristics of undecorated graphene devices are investigated. Sensing tests were carried out by Dr. Kangho Lee at the Universität Der Bundeswehr, München, within a custom-made gas-sensing chamber. During measurement, the sensing chamber is maintained at 0.9 bar by continuously flowing 100 sccm N_2, which allows for immediate gas exchange during all measurements. Measurements were conducted by maintaining a potential, V_{ds} = 10mV, across device channels whilst simultaneously monitoring the channel resistance. NO_2 was then periodically pulsed into the chamber at a concentration of 1ppm while devices were monitored for corresponding resistance change.

Channel resistance is expected to change when gas species adsorb on the graphene surface through a charge transfer mechanism between gas adsorbate and graphene channel [345]. A schematic representation of the expected charge transfer between idealised graphene and an physisorbed NO_2 molecule is displayed in Figure 6.1 a). As discussed within Section 6.1, the NO_2 LUMO hybridises with the graphene electron orbitals which leads to the transfer of $0.1e$ from the graphene sheet to the NO_2. This causes a downshift of the graphene Fermi-level into the graphene's valence band, which has an effect analogous to p-doping the graphene, shifting the graphene CNP right.

To remove unwanted atmospheric adsorbates, device chips are subjected to a vacuum anneal treatment [193, 346] immediately prior to loading into the gas-sensing chamber. The vacuum anneal is carried out within a vacuum chamber at a pressure of 8×10^{-6} mbar and at a temperature of 100 °C for a period of at least one hour. Figure 6.10 displays a representative plot of device response upon exposure to 1 ppm NO_2, when operating at room temperature and 162 °C. It can be seen that no response to NO_2 is observed at room temperature, but when run at an elevated temperature of 160 °C, a response of

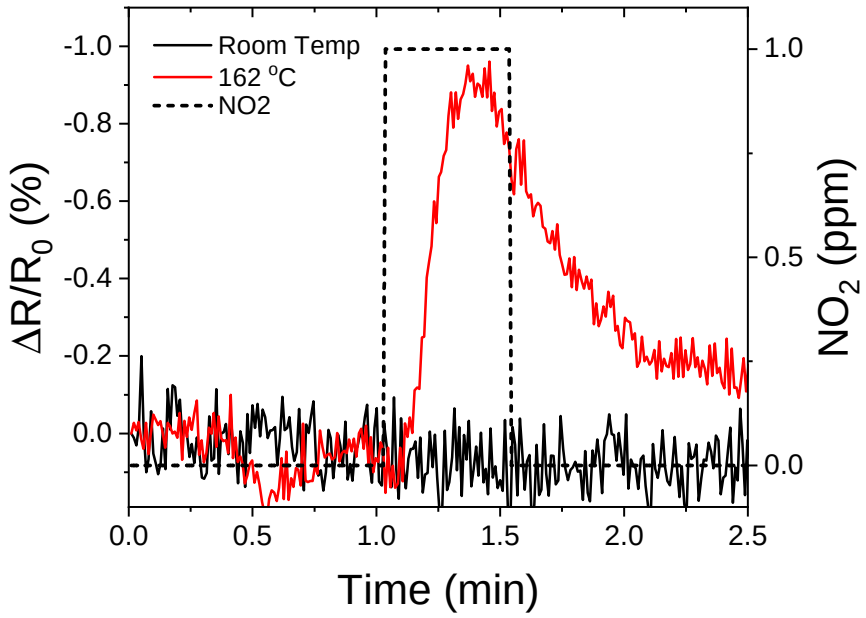

Figure 6.10: A plot displaying the sensor response upon exposure to 1 ppm NO_2 from a representative device of chip EF6.

0.9% relative resistance decrease is observed. After a period of 1 minute following NO_2 injection, channel resistance has stabilised, but at a reduced relative resistance value of -0.2%. This suggests that repeated gas exposure could lead to device saturation and is a well known issue for graphene gas sensing devices [38, 95].

6.5.2 W_5O_{14}-graphene Gas Sensors

After characterising the sensing behaviour of the graphene gas sensors upon exposure to NO_2, 0.5 ml of W_5O_{14} dispersion is applied to half of the channels on the sensor chip, as indicated in Figure 6.11.

As the transferred CVD graphene used within this research is heavily p-doped by adsorbates and the effect of the W_5O_{14} particles is to shift the graphene CNP left towards $V_g = 0$ V via electron donation, it is reasonable to suggest that W_5O_{14} decoration will increase the sensitivity of the GFET gas sensors towards physisorbed NO_2 by shifting the transfer curve such that $V_g = 0$ lies within a region on the GFET transfer curve with increased transconductance. Figure 6.12 displays a comparison of representative NO_2-sensing behaviour between bare graphene GFETs and a W_5O_{14}-decorated GFETs, pre- and post-W_5O_{14} application.

Figure 6.12 a) displays the resistance change of channel 3, a representative un-decorated GFET device, upon exposure to 1ppm NO_2 before and after channels 5-11 are decorated

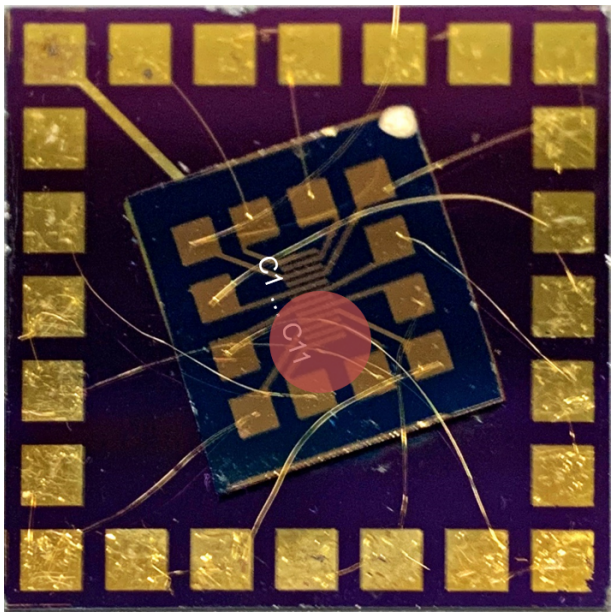

Figure 6.11: Macroscope image of chip with 11 GFET devices for use as gas sensors. The red circle demonstrates the area within which W_5O_{14} particles were deposited. Text highlights channel numbering from 1 to 11, with channel 1 at the top of the chip and channel 11 at the bottom of the chip. Channels 5-11 are W_5O_{14}-decorated on this device chip.

with W_5O_{14}. It is seen in Figure 6.12 a), that the resistance response of the representative undecorated channel reduces after decoration of W_5O_{14} onto channels 5-11. This reduced response may be due to partial saturation of the channel upon exposure to the ambient atmosphere during W_5O_{14} drop casting.

However, this trend is not observed from channel 6, which is used as the representative channel for gas sensing behaviour of W_5O_{14}-decorated channels. Figure 6.12 b) displays representative resistance response from a channel which received W_5O_{14} decoration before and after W_5O_{14} application. W_5O_{14} decorated GFETs display very slightly increased sensitivity to NO_2following W_5O_{14} application, but this is accompanied by increased device reaction time and recovery time. We explain the small increase in sensitivity to NO_2 of the W_5O_{14}-decorated devices by the leftward shift in graphene CNP due to charge transfer between W_5O_{14} and graphene [218]. Because W_5O_{14} should not provide a site for NO_2 physisorption at the temperatures used within this experiment.

Unfortunately, NH_3 was not available for gas sensing tests within the time frame of this project and so the hypothesis for improved sensitivity and selectivity of W_5O_{14}-decorated, graphene-based gas sensors could not be tested.

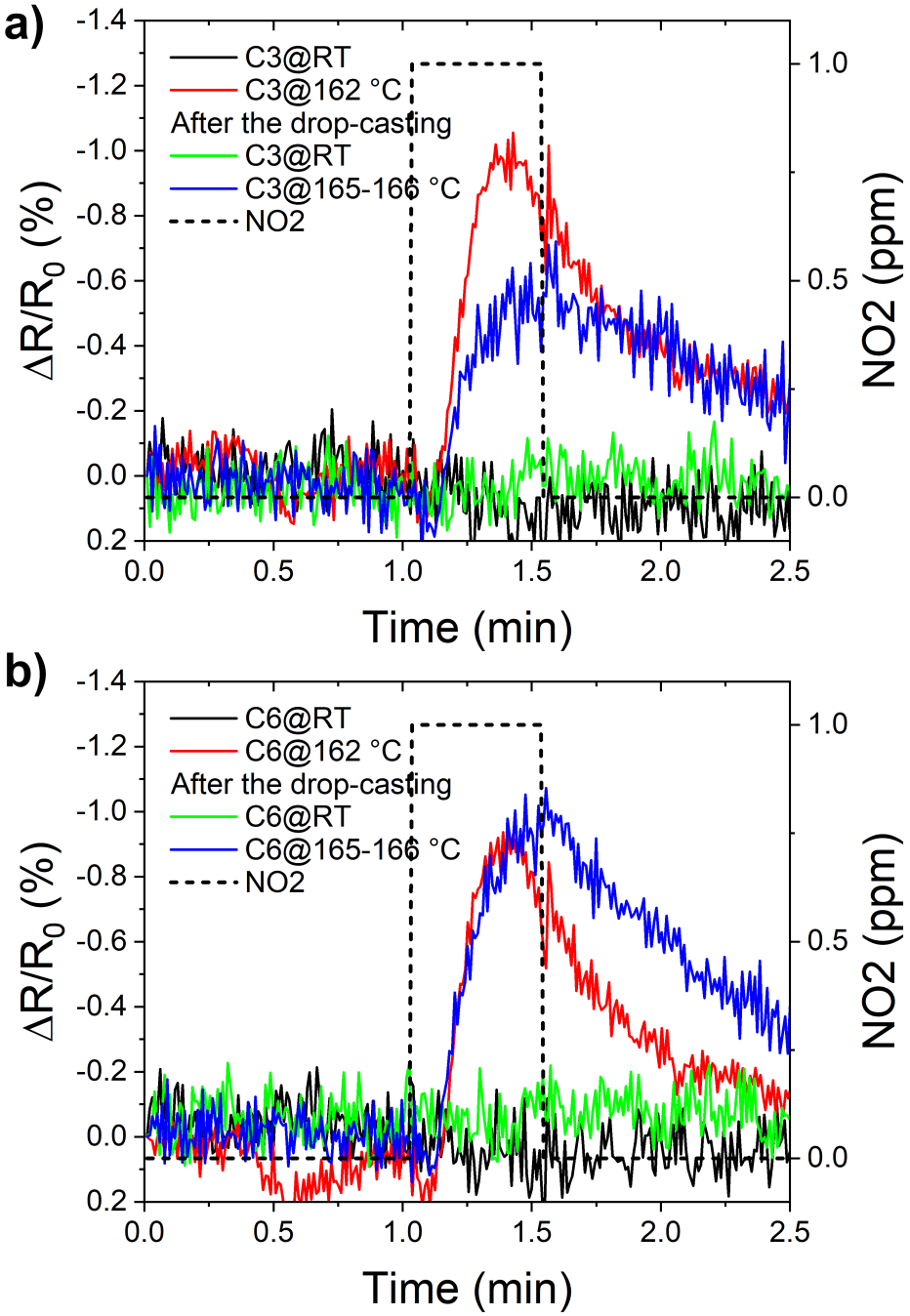

Figure 6.12: a) representative comparison of non-decorated channel resistance change upon exposure to 1ppm NO_2 pre-and post-W_5O_{14} application to other devices on the same chip; b) representative data of channel resistance response from a channel which received W_5O_{14}-decoration, upon exposure to 1ppm NO_2. The red and blue curves refer to channel resistance response before and after W_5O_{14} application respectively.

6.6 Conclusion

Within this chapter, a conceptual framework for gas-sensor operation based around the differences in graphene/adsorbate interaction depending upon whether the adsorbed gas is physisorbed or chemisorbed is introduced. W_5O_{14} is introduced as a hopeful material for increasing the sensitivity and selectivity of graphene-based gas sensors towards NH_3 and other reducing gas species. KPFM data revealed a small work function difference between transferred CVD graphene and W_5O_{14} nanowires, as well as the presence of localised work function changes within the graphene which is thought to be due to residues introduced during the polymer assisted transfer step. Despite the presence of polymer residues, the reproducible fabrication of GFETs was demonstrated with minimal variance in mean GFET behaviour. Detection of NO_2 at a concentration of 1ppm has been demonstrated using bare graphene gas sensors and the addition of W_5O_{14} was found to cause minimal improvement of device sensitivity to NO_2. The mechanism for this is though to be due to electron transfer between W_5O_{14} and graphene counter-acting p-doping adsorbates introduced during the polymer assisted transfer step. Unfortunately, NH_3 was not available within the time frame of the project and so our hypothesis regarding improved selectivity of W_5O_{14} towards reducing gas species could not be tested. We therefore conclude that graphene shows potential as a gas sensing material. In addition, graphene based gas sensors can be operated at lower temperatures than conventional metal-oxide based gas sensors. Improved graphene cleanliness would enhance device operation through a reduction of p-doping which would place $V_g = 0$ V at a location on the I_{ds}/V_g curve with increased g_m.

Chapter 7

Conclusions and outlook

The research within this thesis was intended to advance graphene CVD technology and graphene based gas sensor technology.

Regarding the advancement of graphene CVD technology, the research presented within this thesis addresses two areas which we believe will be of direct benefit to those interested in moving graphene CVD growth to industrial-scale production. Firstly, a generalised path for the optimisation of CVD graphene growth has been identified, which should be applicable to all CVD reactor systems. While the recipes presented within this thesis are not directly transferable to other CVD systems, the suggested process flow and relative process stops should allow any research group to improve the quality of their CVD graphene growth. In addition, when compared with other copper catalysed CVD optimisation recipes, further figures of merit, such dendricity, are discussed in relation to the final continuous graphene film. However, questions still exist regarding whether growth behaviour is similar within a nitrogen or argon atmosphere when the same recipe is employed. Because the suitability of nitrogen as a buffering gas within CVD graphene growth has been a major point of this thesis, a future avenue for study would be a truly comparative set of growth carried out within recipes which are identical in everything but the buffering gas.

The second advancement for mass production of graphene via CVD is the finding that the use of nitrogen as a buffering gas within hot-wall methane-based graphene CVD does not lead to the incorporation of nitrogen heteroatoms within the graphene lattice within detectable limits. This is of profound significance for the mass production of graphene, especially for systems which use open-ended roll-to-roll fabrication, because of the large process gas flow rates required to maintain positive pressure within the reactor space to

prevent ambient atmosphere ingression. Additionally, nitrogen is hugely abundant and thus relatively cheap. It is not unreasonable to suggest that large scale operations would use on-site nitrogen isolation which would further reduce costs; a tactic which would likely be impractical if argon were used instead. However, as outlined above, there would be value in assessing the commutability of argon-buffered and nitrogen-buffered recipes. Another path for research could be the inclusion of a device within the reactor system, which would allow for the deliberate dissociation of nitrogen during graphene growth, to provide a flexible system for on demand growth of pristine or nitrogen-doped graphene.

The last section of this research investigated the suitability of graphene and graphene-particle composite systems for use within gas-sensing devices. Even though the GFETs used as the basic devices within this section were shown to be heavily doped by transfer residues, sensing of NO_2 at 1ppm level was successfully demonstrated. The use of W_5O_{14} microparticles appeared to have a small positive effect on device sensitivity, although it is believed that the graphene-W_5O_{14} system should be more sensitive to NH_3 rather than NO_2. Unfortunately, due to time and equipment limitations this hypothesis was not able to be tested and is an obvious path to take for future gas sensing research. The application of W_5O_{14} particles to the graphene sheet has been demonstrated as an effective way to return the graphene charge neutrality point towards its natural 0 V_g location. Thus, the intelligent application of particle suspensions on graphene could be an interesting research area to explore to unlock various graphene device behaviours. This section of research has demonstrated that graphene transfer protocols which result in fewer surface contaminants are of the utmost importance for graphene-based gas sensing projects.

Bibliography

[1] K. S. Novoselov, A. K. Geim, S. Morozov, D. Jiang, Y. Zhang, S. V. Dubonos, I. V. Grigorieva, and A. A. Firsov, "Electric Field Effect in Atomically Thin Carbon Films," *Science*, vol. 306, no. 5696, pp. 666–669, 2004.

[2] K. S. Novoselov, A. Mishchenko, A. Carvalho, and A. H. Castro Neto, "2D materials and van der Waals heterostructures," *Science*, vol. 353, no. 6298, 2016.

[3] R. Mas-Ballesté, C. Gómez-Navarro, J. Gómez-Herrero, and F. Zamora, "2D materials: To graphene and beyond," *Nanoscale*, vol. 3, no. 1, pp. 20–30, 2011.

[4] W. Ren and H.-M. Cheng, "The global growth of graphene," *Nature Nanotechnology*, vol. 9, pp. 726–730, oct 2014.

[5] A. P. Kauling, A. T. Seefeldt, D. P. Pisoni, R. C. Pradeep, R. Bentini, R. V. Oliveira, K. S. Novoselov, and A. H. Castro Neto, "The Worldwide Graphene Flake Production," *Advanced Materials*, vol. 30, no. 44, pp. 1–6, 2018.

[6] R. Ye and J. M. Tour, "Graphene at fifteen," *ACS Nano*, vol. 13, no. 10, pp. 10872–10878, 2019.

[7] P. R. Wallace, "The Band Theory of Graphite," *Physical Review*, vol. 71, pp. 622–634, may 1947.

[8] F. Maeda, T. Takahashi, H. Ohsawa, S. Suzuki, and H. Suematsu, "Unoccupied-electronic-band structure of graphite studied by angle-resolved secondary-electron emission and inverse photoemission," *Physical Review B*, vol. 37, pp. 4482–4488, mar 1988.

[9] S. Reich, J. Maultzsch, C. Thomsen, and P. Ordejón, "Tight-binding description of graphene," *Physical Review B - Condensed Matter and Materials Physics*, vol. 66, no. 3, pp. 354121–354125, 2002.

[10] K. S. Novoselov, A. K. Geim, S. V. Morozov, D. Jiang, M. I. Katsnelson, I. V. Grigorieva, S. V. Dubonos, and A. A. Firsov, "Two-dimensional gas of massless Dirac fermions in graphene," *Nature*, vol. 438, no. 7065, pp. 197–200, 2005.

[11] L. Xiang, S. Y. Ma, F. Wang, and K. Zhang, "Nanoindentation models and Young's modulus of few-layer graphene: a molecular dynamics simulation study," *Journal of Physics D: Applied Physics*, vol. 48, p. 395305, oct 2015.

[12] D. Akinwande, C. J. Brennan, J. S. Bunch, P. Egberts, J. R. Felts, H. Gao, R. Huang, J. S. Kim, T. Li, Y. Li, K. M. Liechti, N. Lu, H. S. Park, E. J. Reed, P. Wang, B. I. Yakobson, T. Zhang, Y. W. Zhang, Y. Zhou, and Y. Zhu, "A review on mechanics and mechanical properties of 2D materials—Graphene and beyond," *Extreme Mechanics Letters*, vol. 13, pp. 42–77, 2017.

[13] K. S. Kim, Y. Zhao, H. Jang, S. Y. Lee, J. M. Kim, K. S. Kim, J. H. Ahn, P. Kim, J. Y. Choi, and B. H. Hong, "Large-scale pattern growth of graphene films for stretchable transparent electrodes," *Nature*, vol. 457, no. 7230, pp. 706–710, 2009.

[14] Y. Wang, R. Yang, Z. Shi, L. Zhang, D. Shi, E. Wang, and G. Zhang, "Super-elastic graphene ripples for flexible strain sensors," *ACS Nano*, vol. 5, no. 5, pp. 3645–3650, 2011.

[15] R. You, Y. Q. Liu, Y. L. Hao, D. D. Han, Y. L. Zhang, and Z. You, "Laser Fabrication of Graphene-Based Flexible Electronics," *Advanced Materials*, vol. 1901981, pp. 1–22, 2019.

[16] N. Petrone, I. Meric, T. Chari, K. L. Shepard, and J. Hone, "Graphene field-effect transistors for radio-frequency flexible electronics," *IEEE Journal of the Electron Devices Society*, vol. 3, no. 1, pp. 44–48, 2015.

[17] H. Jang, Y. J. Park, X. Chen, T. Das, M. S. Kim, and J. H. Ahn, "Graphene-Based Flexible and Stretchable Electronics," *Advanced Materials*, vol. 28, no. 22, pp. 4184–4202, 2016.

[18] B. J. Kim, H. Jang, S. K. Lee, B. H. Hong, J. H. Ahn, and J. H. Cho, "High-performance flexible graphene field effect transistors with ion gel gate dielectrics," *Nano Letters*, vol. 10, no. 9, pp. 3464–3466, 2010.

[19] A. A. Balandin, S. Ghosh, W. Bao, I. Calizo, D. Teweldebrhan, F. Miao, and C. N. Lau, "Superior Thermal Conductivity of Single-Layer Graphene," *Nano Letters*, vol. 8, pp. 902–907, mar 2008.

[20] E. Pop, V. Varshney, and A. K. Roy, "Thermal properties of graphene: Fundamentals and applications," *MRS Bulletin*, vol. 37, no. 12, pp. 1273–1281, 2012.

[21] P. Blake, E. W. Hill, A. H. Castro Neto, K. S. Novoselov, D. Jiang, R. Yang, T. J. Booth, and A. K. Geim, "Making graphene visible," *Applied Physics Letters*, vol. 91, no. 6, 2007.

[22] L. A. Falkovsky, "Optical properties of graphene," *Journal of Physics: Conference Series*, vol. 129, p. 012004, oct 2008.

[23] J. K. Wassei and R. B. Kaner, "Graphene, a promising transparent conductor," *Materials Today*, vol. 13, no. 3, pp. 52–59, 2010.

[24] S. Roddaro, P. Pingue, V. Piazza, V. Pellegrini, and F. Beltram, "The optical visibility of graphene: Interference colors of ultrathin graphite on SiO2," *Nano Letters*, vol. 7, no. 9, pp. 2707–2710, 2007.

[25] S. W. Cranford and M. J. Buehler, "Packing efficiency and accessible surface area of crumpled graphene," *Physical Review B*, vol. 84, p. 205451, nov 2011.

[26] X. Li, Y. Chen, Z. Cheng, L. Jia, S. Mo, and Z. Liu, "Ultrahigh specific surface area of graphene for eliminating subcooling of water," *Applied Energy*, vol. 130, pp. 824–829, oct 2014.

[27] A. Avsar, H. Ochoa, B. Ozyilmaz, and B. J. V. Wees, "Colloquium: Spintronics in graphene and other two-dimensional materials," *arXiv*, 2019.

[28] S. Li, K. V. Larionov, Z. I. Popov, T. Watanabe, K. Amemiya, S. Entani, P. V. Avramov, Y. Sakuraba, H. Naramoto, P. B. Sorokin, and S. Sakai, "Graphene/Half-Metallic Heusler Alloy: A Novel Heterostructure toward High-Performance Graphene Spintronic Devices," *Advanced Materials*, vol. 1905734, pp. 1–9, 2019.

[29] W. Han, R. K. Kawakami, M. Gmitra, and J. Fabian, "Graphene spintronics," 2014.

[30] F. Bonaccorso, Z. Sun, T. Hasan, and A. C. Ferrari, "Graphene photonics and optoelectronics," *Nature Photonics*, vol. 4, no. 9, pp. 611–622, 2010.

[31] A. Autere, H. Jussila, Y. Dai, Y. Wang, H. Lipsanen, and Z. Sun, "Nonlinear Optics with 2D Layered Materials," *Advanced Materials*, vol. 1705963, p. 1705963, mar 2018.

[32] Q. Bao, H. Zhang, B. Wang, Z. Ni, C. H. Y. X. Lim, Y. Wang, D. Y. Tang, and K. P. Loh, "Broadband graphene polarizer," *Nature Photonics*, vol. 5, no. 7, pp. 411–415, 2011.

[33] F. Schedin, A. K. Geim, S. V. Morozov, E. W. Hill, P. Blake, M. I. Katsnelson, and K. S. Novoselov, "Detection of individual gas molecules adsorbed on graphene," *Nature Materials*, vol. 6, no. 9, pp. 652–655, 2007.

[34] Y. H. Zhang, Y. B. Chen, K. G. Zhou, C. H. Liu, J. Zeng, H. L. Zhang, and Y. Peng, "Improving gas sensing properties of graphene by introducing dopants and defects: A first-principles study," *Nanotechnology*, vol. 20, no. 18, 2009.

[35] Y. Wang, Y. Shao, D. W. Matson, J. Li, and Y. Lin, "Nitrogen-Doped Graphene and Its Biosensing," *ACS nano*, vol. 4, no. 4, pp. 1790–1798, 2010.

[36] M. Gautam and A. H. Jayatissa, "Ammonia gas sensing behavior of graphene surface decorated with gold nanoparticles," *Solid-State Electronics*, vol. 78, pp. 159–165, 2012.

[37] G. Singh, A. Choudhary, D. Haranath, A. G. Joshi, N. Singh, S. Singh, and R. Pasricha, "ZnO decorated luminescent graphene as a potential gas sensor at room temperature," *Carbon*, vol. 50, no. 2, pp. 385–394, 2012.

[38] Q. He, S. Wu, Z. Yin, and H. Zhang, "Graphene-based electronic sensors," *Chemical Science*, vol. 3, no. 6, pp. 1764–1772, 2012.

[39] W. Yuan and G. Shi, "Graphene-based gas sensors," *Journal of Materials Chemistry A*, vol. 1, no. 35, p. 10078, 2013.

[40] H. S. Hong, N. H. Phuong, N. T. Huong, N. H. Nam, and N. T. Hue, "Highly sensitive and low detection limit of resistive NO2 gas sensor based on a MoS2/graphene two-dimensional heterostructures," *Applied Surface Science*, vol. 492, no. June, pp. 449–454, 2019.

[41] O. Salihoglu, H. B. Uzlu, O. Yakar, S. Aas, O. Balci, N. Kakenov, S. Balci, S. Olcum, S. Süzer, and C. Kocabas, "Graphene-Based Adaptive Thermal Camouflage," *Nano Letters*, p. acs.nanolett.8b01746, 2018.

[42] K. E. Whitener and P. E. Sheehan, "Graphene synthesis," *Diamond and Related Materials*, vol. 46, pp. 25–34, jun 2014.

[43] R. Beams, L. Gustavo Cançado, and L. Novotny, "Raman characterization of defects and dopants in graphene," *Journal of Physics Condensed Matter*, vol. 27, no. 8, 2015.

[44] C. Berger, "Electronic Confinement and Coherence in Patterned Epitaxial Graphene," *Science*, vol. 312, pp. 1191–1196, may 2006.

[45] W. A. de Heer, C. Berger, X. Wu, P. N. First, E. H. Conrad, X. Li, T. Li, M. Sprinkle, J. Hass, M. L. Sadowski, M. Potemski, and G. Martinez, "Epitaxial graphene," *Solid State Communications*, vol. 143, no. 1-2, pp. 92–100, 2007.

[46] N. Camara, G. Rius, J. R. Huntzinger, A. Tiberj, N. Mestres, P. Godignon, and J. Camassel, "Selective epitaxial growth of graphene on SiC," *Applied Physics Letters*, vol. 93, no. 12, 2008.

[47] C. Virojanadara, M. Syväjarvi, R. Yakimova, L. I. Johansson, A. A. Zakharov, and T. Balasubramanian, "Homogeneous large-area graphene layer growth on 6H-SiC(0001)," *Physical Review B*, vol. 78, p. 245403, dec 2008.

[48] W. Norimatsu and M. Kusunoki, "Formation process of graphene on SiC (0001)," *Physica E: Low-dimensional Systems and Nanostructures*, vol. 42, pp. 691–694, feb 2010.

[49] M. Beshkova, L. Hultman, and R. Yakimova, "Device applications of epitaxial graphene on silicon carbide," *Vacuum*, vol. 128, pp. 186–197, jun 2016.

[50] Y. Hernandez, V. Nicolosi, M. Lotya, F. M. Blighe, Z. Sun, S. De, I. T. McGovern, B. Holland, M. Byrne, Y. K. Gun'ko, J. J. Boland, P. Niraj, G. Duesberg, S. Krishnamurthy, R. Goodhue, J. Hutchison, V. Scardaci, A. C. Ferrari, and J. N. Coleman, "High-yield production of graphene by liquid-phase exfoliation of graphite," *Nature Nanotechnology*, vol. 3, no. 9, pp. 563–568, 2008.

[51] K. R. Paton, E. Varrla, C. Backes, R. J. Smith, U. Khan, A. O'Neill, C. Boland, M. Lotya, O. M. Istrate, P. King, T. Higgins, S. Barwich, P. May, P. Puczkarski, I. Ahmed, M. Moebius, H. Pettersson, E. Long, J. Coelho, S. E. O'Brien, E. K. McGuire, B. M. Sanchez, G. S. Duesberg, N. McEvoy, T. J. Pennycook, C. Downing, A. Crossley, V. Nicolosi, and J. N. Coleman, "Scalable production of large quantities of defect-free few-layer graphene by shear exfoliation in liquids," *Nature Materials*, vol. 13, no. 6, pp. 624–630, 2014.

[52] M. Yi and Z. Shen, "A review on mechanical exfoliation for the scalable production of graphene," *Journal of Materials Chemistry A*, vol. 3, no. 22, pp. 11700–11715, 2015.

[53] Y. Xu, H. Cao, Y. Xue, B. Li, and W. Cai, "Liquid-Phase Exfoliation of Graphene: An Overview on Exfoliation Media, Techniques, and Challenges," *Nanomaterials*, vol. 8, p. 942, nov 2018.

[54] Y. Gai, W. Wang, D. Xiao, H. Tan, M. Lin, and Y. Zhao, "Exfoliation of Graphite into Graphene by a Rotor–Stator in Supercritical CO 2 : Experiment and Simulation," *Industrial & Engineering Chemistry Research*, vol. 57, pp. 8220–8229, jun 2018.

[55] B. Deng, Z. Liu, and H. Peng, "Toward Mass Production of CVD Graphene Films," *Advanced Materials*, vol. 31, no. 9, pp. 1–25, 2019.

[56] L. Lin, H. Peng, and Z. Liu, "Synthesis challenges for graphene industry," *Nature Materials*, vol. 18, no. 6, pp. 520–524, 2019.

[57] X. Liang, B. A. Sperling, I. Calizo, G. Cheng, C. A. Hacker, Q. Zhang, Y. Obeng, K. Yan, H. Peng, Q. Li, X. Zhu, H. Yuan, A. R. Hight Walker, Z. Liu, L. M. Peng, and C. A. Richter, "Toward clean and crackless transfer of graphene," *ACS Nano*, vol. 5, no. 11, pp. 9144–9153, 2011.

[58] X. Wu, G. Zhong, L. D'Arsié, H. Sugime, S. Esconjauregui, A. W. Robertson, and J. Robertson, "Growth of Continuous Monolayer Graphene with Millimeter-sized Domains Using Industrially Safe Conditions," *Scientific Reports*, vol. 6, p. 21152, feb 2016.

[59] X. Li, W. Cai, J. An, S. Kim, J. Nah, D. Yang, R. Piner, A. Velamakanni, I. Jung, E. Tutuc, S. Banerjee, L. Colombo, and R. Ruoff, "Large area synthesis of high quality and uniform graphene films on copper foils," *Science*, vol. 324, no. 5932, pp. 1312–1314, 2009.

[60] R. B. McLellan, "The solubility of carbon in solid gold, copper, and silver," *Scripta Metallurgica*, vol. 3, pp. 389–391, jun 1969.

[61] G. A. López and E. J. Mittemeijer, "The solubility of C in solid Cu," *Scripta Materialia*, vol. 51, no. 1, pp. 1–5, 2004.

[62] X. Li, W. Cai, L. Colombo, and R. Ruoff, "Evolution of graphene growth on Ni and Cu by carbon isotope labeling," *Nano letters*, vol. 12, no. Cvd, pp. 1–15, 2009.

[63] H. Zhou, W. J. Yu, L. Liu, R. Cheng, Y. Chen, X. Huang, Y. Liu, Y. Wang, Y. Huang, and X. Duan, "Chemical vapour deposition growth of large single crystals of monolayer and bilayer graphene," *Nature Communications*, vol. 4, pp. 1–8, 2013.

[64] S. Choubak, P. L. Levesque, E. Gaufres, M. Biron, P. Desjardins, and R. Martel, "Graphene CVD: Interplay between growth and etching on morphology and stacking by hydrogen and oxidizing impurities," *Journal of Physical Chemistry C*, vol. 118, no. 37, pp. 21532–21540, 2014.

[65] S. Chaitoglou and E. Bertran, "Effect of pressure and hydrogen flow in nucleation density and morphology of graphene bidimensional crystals," *Materials Research Express*, vol. 3, no. 7, 2016.

[66] Y. P. Hsieh, Y. H. Chu, H. G. Tsai, and M. Hofmann, "Reducing the graphene grain density in three steps," *Nanotechnology*, vol. 27, no. 10, 2016.

[67] D. Geng, H. Wang, and G. Yu, "Graphene single crystals: Size and morphology engineering," *Advanced Materials*, vol. 27, no. 18, pp. 2821–2837, 2015.

[68] X. Chen, P. Zhao, R. Xiang, S. Kim, J. Cha, S. Chiashi, and S. Maruyama, "Chemical vapor deposition growth of 5 mm hexagonal single-crystal graphene from ethanol," *Carbon*, vol. 94, pp. 810–815, 2015.

[69] H. Abuhimd, "Chemical vapor deposition parameters dependent length control of hexagonal graphene," *Proceedings of the Institution of Mechanical Engineers, Part E: Journal of Process Mechanical Engineering*, vol. 231, no. 6, pp. 1187–1196, 2017.

[70] Y. Hao, M. S. Bharathi, L. Wang, Y. Liu, H. Chen, S. Nie, X. Wang, H. Chou, C. Tan, B. Fallahazad, H. Ramanarayan, C. W. Magnuson, E. Tutuc, B. I. Yakobson, K. F. McCarty, Y.-W. Zhang, P. Kim, J. Hone, L. Colombo, and R. S. Ruoff, "The Role of Surface Oxygen in the Growth of Large Single-Crystal Graphene on Copper," *Science*, vol. 342, pp. 720–723, nov 2013.

[71] D. Ding, P. Solís-Fernández, R. M. Yunus, H. Hibino, and H. Ago, "Behavior and role of superficial oxygen in Cu for the growth of large single-crystalline graphene," *Applied Surface Science*, vol. 408, pp. 142–149, 2017.

[72] E. Meca, J. Lowengrub, H. Kim, C. Mattevi, and V. B. Shenoy, "Epitaxial graphene growth and shape dynamics on copper: Phase-field modeling and experiments," *Nano Letters*, vol. 13, no. 11, pp. 5692–5697, 2013.

[73] K. Kumar and E. H. Yang, "On the growth mode of two-lobed curvilinear graphene domains at atmospheric pressure," *Scientific Reports*, vol. 3, pp. 1–7, 2013.

[74] V. Miseikis, D. Convertino, N. Mishra, M. Gemmi, T. Mashoff, S. Heun, N. Haghighian, F. Bisio, M. Canepa, V. Piazza, and C. Coletti, "Rapid CVD growth of millimetre-sized single crystal graphene using a cold-wall reactor," *2D Materials*, vol. 2, no. 1, 2015.

[75] X. Xu, Z. Zhang, L. Qiu, J. Zhuang, L. Zhang, H. Wang, C. Liao, H. Song, R. Qiao, P. Gao, Z. Hu, L. Liao, Z. Liao, D. Yu, E. Wang, F. Ding, H. Peng, and K. Liu, "Ultrafast growth of single-crystal graphene assisted by a continuous oxygen supply," *Nature Nanotechnology*, vol. 11, no. 11, pp. 930–935, 2016.

[76] S. Yin, X. Zhang, C. Xu, Y. Wang, Y. Wang, P. Li, H. Sun, M. Wang, Y. Xia, C. T. Lin, P. Zhao, and H. Wang, "Chemical vapor deposition growth of scalable monolayer polycrystalline graphene films with millimeter-sized domains," *Materials Letters*, vol. 215, pp. 259–262, 2018.

[77] T. Wu, X. Zhang, Q. Yuan, J. Xue, G. Lu, Z. Liu, H. Wang, H. Wang, F. Ding, Q. Yu, X. Xie, and M. Jiang, "Fast growth of inch-sized single-crystalline graphene from a controlled single nucleus on Cu-Ni alloys," *Nature Materials*, vol. 15, no. 1, pp. 43–47, 2016.

[78] L. A. Jauregui, H. Cao, W. Wu, Q. Yu, and Y. P. Chen, "Electronic properties of grains and grain boundaries in graphene grown by chemical vapor deposition," *Solid State Communications*, vol. 151, no. 16, pp. 1100–1104, 2011.

[79] L. Tapasztó, P. Nemes-Incze, G. Dobrik, K. Jae Yoo, C. Hwang, and L. P. Biró, "Mapping the electronic properties of individual graphene grain boundaries," *Applied Physics Letters*, vol. 100, no. 5, 2012.

[80] L. P. Biró and P. Lambin, "Grain boundaries in graphene grown by chemical vapor deposition," *New Journal of Physics*, vol. 15, 2013.

[81] H. Zhang, G. Lee, C. Gong, L. Colombo, and K. Cho, "Grain Boundary Effect on Electrical Transport Properties of Graphene," *The Journal of Physical Chemistry C*, vol. 118, no. 5, pp. 2338–2343, 2014.

[82] C. J. Páez, A. L. Pereira, J. N. Rodrigues, and N. M. Peres, "Electronic transport across linear defects in graphene," *Physical Review B - Condensed Matter and Materials Physics*, vol. 92, no. 4, 2015.

[83] S. Wang, H. Hibino, S. Suzuki, and H. Yamamoto, "Atmospheric Pressure Chemical Vapor Deposition Growth of Millimeter-Scale Single-Crystalline Graphene on the Copper Surface with a Native Oxide Layer," *Chemistry of Materials*, vol. 28, no. 14, pp. 4893–4900, 2016.

[84] J. Chen, M. Cui, G. Wu, T. Wang, J. M. Mbengue, Y. Li, and M. Li, "Fast growth of large single-crystalline graphene assisted by sequential double oxygen passivation," *Carbon*, vol. 116, pp. 133–138, 2017.

[85] G. Zhong, X. Wu, L. D'Arsie, K. B. Teo, N. L. Rupesinghe, A. Jouvray, and J. Robertson, "Growth of continuous graphene by open roll-to-roll chemical vapor deposition," *Applied Physics Letters*, vol. 109, no. 19, 2016.

[86] J. M. Hendrie, "Dissociation energy of N2," *The Journal of Chemical Physics*, vol. 22, no. 9, pp. 1503–1507, 1954.

[87] J. P. Appleton, M. Steinberg, and D. J. Liquornik, "Shock-tube study of nitrogen dissociation using vacuum-ultraviolet light absorption," *The Journal of Chemical Physics*, vol. 48, no. 2, pp. 599–608, 1968.

[88] W. T. Borden, "Why Are Addition Reactions to N 2 Thermodynamically Unfavorable?," *The Journal of Physical Chemistry A*, vol. 121, pp. 1140–1144, feb 2017.

[89] J. Y. Hwang, C. C. Kuo, L. C. Chen, and K. H. Chen, "Correlating defect density with carrier mobility in large-scaled graphene films: Raman spectral signatures for the estimation of defect density," *Nanotechnology*, vol. 21, no. 46, 2010.

[90] R. B. Kaner, B. H. Weiller, Y. Yang, M. J. Allen, V. C. Tung, and J. D. Fowler, "Practical Chemical Sensors from Chemically Derived Graphene," *ACS Nano*, vol. 3, no. 2, pp. 301–306, 2009.

[91] F. Yavari, E. Castillo, H. Gullapalli, P. M. Ajayan, and N. Koratkar, "High sensitivity detection of NO 2 and NH 3 in air using chemical vapor deposition grown graphene," *Applied Physics Letters*, vol. 100, no. 20, 2012.

[92] A. Cagliani, D. M. A. Mackenzie, L. K. Tschammer, F. Pizzocchero, K. Almdal, and P. Bøggild, "Large-area nanopatterned graphene for ultrasensitive gas sensing," *Nano Research*, vol. 7, no. 5, pp. 743–754, 2014.

[93] S. S. Varghese, S. Lonkar, K. K. Singh, S. Swaminathan, and A. Abdala, "Recent advances in graphene based gas sensors," *Sensors and Actuators, B: Chemical*, vol. 218, pp. 160–183, 2015.

[94] P. Salvo, B. Melai, N. Calisi, C. Paoletti, F. Bellagambi, A. Kirchhain, M. Trivella, R. Fuoco, and F. Di Francesco, "Graphene-based devices for measuring pH," *Sensors and Actuators B: Chemical*, vol. 256, pp. 976–991, mar 2018.

[95] M. Gautam and A. H. Jayatissa, "Gas sensing properties of graphene synthesized by chemical vapor deposition," *Materials Science and Engineering C*, vol. 31, no. 7, pp. 1405–1411, 2011.

[96] Y. Liu, J. Yu, Y. Cui, T. Hayasaka, H. Liu, X. Li, and L. Lin, "An AC sensing scheme for minimal baseline drift and fast recovery on graphene FET gas sensor," in *TRANSDUCERS 2017 - 19th International Conference on Solid-State Sensors, Actuators and Microsystems*, pp. 230–233, 2017.

[97] H. Liu, Y. Liu, Y. Chu, T. Hayasaka, N. Joshi, Y. Cui, X. Wang, Z. You, and L. Lin, "AC phase sensing of graphene FETs for chemical vapors with fast recovery and minimal baseline drift," *Sensors and Actuators B: Chemical*, vol. 263, pp. 94–102, jun 2018.

[98] L. Dong, P. Zheng, Y. Yang, M. Zhang, Z. Xue, Z. Wang, G. Liu, P. Li, K. S. Teh, Y. Su, B. Cai, G. Wang, and Z. Di, "NO 2 gas sensor based on graphene decorated with Ge quantum dots," *Nanotechnology*, vol. 30, p. 074004, feb 2019.

[99] R. A. G. Ranola, I. Concina, F. B. Sevilla, M. Ferroni, L. Sangaletti, G. Sberveglieri, and E. Comini, "Room temperature trimethylamine gas sensor based on aqueous dispersed graphene," *Proceedings of the 2015 18th AISEM Annual Conference, AISEM 2015*, pp. 1–4, 2015.

[100] J. Zhang, X. Liu, G. Neri, and N. Pinna, "Nanostructured Materials for Room-Temperature Gas Sensors," *Advanced Materials*, vol. 28, no. 5, pp. 795–831, 2016.

[101] A. Mishra, S. Basu, N. P. Shetti, and K. R. Reddy, "Metal oxide nanohybrids-based low-temperature sensors for NO 2 detection: a short review," *Journal of Materials Science: Materials in Electronics*, vol. 30, no. 9, pp. 8160–8170, 2019.

[102] H. Meixner, J. Gerblinger, U. Lampe, and M. Fleischer, "Thin-film gas sensors based on semiconducting metal oxides," *Sensors and Actuators: B. Chemical*, vol. 23, no. 2-3, pp. 119–125, 1995.

[103] A. Dey, "Semiconductor metal oxide gas sensors: A review," 2018.

[104] O. Leenaerts, B. Partoens, F. M. Peeters, A. Volodin, and C. Van Haesendonck, "The work function of few-layer graphene," *Journal of Physics Condensed Matter*, vol. 29, no. 3, 2017.

[105] M. Saqib, J. Jelenc, L. Pirker, S. D. Škapin, L. De Pietro, U. Ramsperger, A. Knápek, I. Müllerová, and M. Remškar, "Field emission properties of single crystalline W5O14 and W18O49 nanowires," *Journal of Electron Spectroscopy and Related Phenomena*, mar 2019.

[106] A. H. Castro Neto, F. Guinea, N. M. R. Peres, K. S. Novoselov, and A. K. Geim, "The electronic properties of graphene," *Reviews of Modern Physics*, vol. 81, pp. 109–162, jan 2009.

[107] K. I. Bolotin, K. J. Sikes, Z. Jiang, M. Klima, G. Fudenberg, J. Hone, P. Kim, and H. L. Stormer, "Ultrahigh electron mobility in suspended graphene," *Solid State Communications*, vol. 146, no. 9-10, pp. 351–355, 2008.

[108] A. K. GEIM and K. S. NOVOSELOV, "The rise of graphene," in *Nanoscience and Technology*, vol. 6, pp. 11–19, Co-Published with Macmillan Publishers Ltd, UK, aug 2009.

[109] C. Lee, X. Wei, J. W. Kysar, and J. Hone, "Measurement of the Elastic Properties and Intrinsic Strength of Monolayer Graphene," *Science*, vol. 321, pp. 385–388, jul 2008.

[110] C. J. An, S. J. Kim, H. O. Choi, D. W. Kim, S. W. Jang, M. L. Jin, J. M. Park, J. K. Choi, and H. T. Jung, "Ultraclean transfer of CVD-grown graphene and its application to flexible organic photovoltaic cells," *Journal of Materials Chemistry A*, vol. 2, no. 48, pp. 20474–20480, 2014.

[111] B. Cho, J. Yoon, M. G. Hahm, D.-H. Kim, A. R. Kim, Y. H. Kahng, S.-W. Park, Y.-J. Lee, S.-G. Park, J.-D. Kwon, C. S. Kim, M. Song, Y. Jeong, K.-S. Nam, and H. C. Ko, "Graphene-based gas sensor: metal decoration effect and application to a flexible device," *J. Mater. Chem. C*, vol. 2, no. 27, pp. 5280–5285, 2014.

[112] G. Eda, G. Fanchini, and M. Chhowalla, "Large-area ultrathin films of reduced graphene oxide as a transparent and flexible electronic material," *Nature Nanotechnology*, vol. 3, no. 5, pp. 270–274, 2008.

[113] M. G. Chung, D. H. Kim, D. K. Seo, T. Kim, H. U. Im, H. M. Lee, J. B. Yoo, S. H. Hong, T. J. Kang, and Y. H. Kim, "Flexible hydrogen sensors using graphene with palladium nanoparticle decoration," *Sensors and Actuators, B: Chemical*, vol. 169, no. 13382, pp. 387–392, 2012.

[114] S. Bae, H. Kim, Y. Lee, X. Xu, J. S. Park, Y. Zheng, J. Balakrishnan, T. Lei, H. Ri Kim, Y. I. Song, Y. J. Kim, K. S. Kim, B. Özyilmaz, J. H. Ahn, B. H. Hong, and S. Iijima, "Roll-to-roll production of 30-inch graphene films for transparent electrodes," *Nature Nanotechnology*, vol. 5, no. 8, pp. 574–578, 2010.

[115] J. R. Potts, D. R. Dreyer, C. W. Bielawski, and R. S. Ruoff, "Graphene-based polymer nanocomposites," 2011.

[116] R. J. Young, M. Liu, I. A. Kinloch, S. Li, X. Zhao, C. Vallés, and D. G. Papageorgiou, "The mechanics of reinforcement of polymers by graphene nanoplatelets," *Composites Science and Technology*, vol. 154, pp. 110–116, 2018.

[117] D. D. Chung, "Materials for thermal conduction," *Applied Thermal Engineering*, vol. 21, no. 16, pp. 1593–1605, 2001.

[118] J. W. Weber, V. E. Calado, and M. C. M. van de Sanden, "Optical constants of graphene measured by spectroscopic ellipsometry," *Applied Physics Letters*, vol. 97, p. 091904, aug 2010.

[119] Y. U. Jung, K. W. Park, S. T. Hur, S. W. Choi, and S. J. Kang, "High-transmittance liquid-crystal displays using graphene conducting layers," *Liquid Crystals*, vol. 41, no. 1, pp. 101–105, 2014.

[120] Z. Chen, H. Okumura, G. C. Hadjipanayis, and Q. Chen, "Microstructure refinement and magnetic property enhancement of nanocomposite Pr2Fe14B/α-Fe magnets by small substitution of M for Fe (M = Cr, Nb, Ti and Zr)," *Journal of Alloys and Compounds*, vol. 327, no. 1-2, pp. 201–205, 2001.

[121] F. Bonaccorso, A. Lombardo, T. Hasan, Z. Sun, L. Colombo, and A. C. Ferrari, "Production and processing of graphene and 2d crystals," 2012.

[122] "The Price of Graphene." `https://www.graphenea.com/pages/graphene-price{\#}.XiYQaC2cZhE`. Accessed: 2020-01-20.

[123] R. F. Frindt and A. D. Yoffe, "Physical properties of layer structures : optical properties and photoconductivity of thin crystals of molybdenum disulphide," *Proceedings of the Royal Society of London. Series A. Mathematical and Physical Sciences*, vol. 273, pp. 69–83, apr 1963.

[124] A. Arndt, D. Spoddig, P. Esquinazi, J. Barzola-Quiquia, S. Dusari, and T. Butz, "Electric carrier concentration in graphite: Dependence of electrical resistivity and magnetoresistance on defect concentration," *Physical Review B - Condensed Matter and Materials Physics*, vol. 80, no. 19, pp. 1–5, 2009.

[125] S. B. Desai, S. R. Madhvapathy, M. Amani, D. Kiriya, M. Hettick, M. Tosun, Y. Zhou, M. Dubey, J. W. Ager, D. Chrzan, and A. Javey, "Gold-Mediated Exfoliation of Ultralarge Optoelectronically-Perfect Monolayers," *Advanced Materials*, vol. 28, no. 21, pp. 4053–4058, 2016.

[126] M. C. Da Costa, H. B. Ribeiro, F. Kessler, E. A. De Souza, and G. J. Fechine, "Micromechanical exfoliation of two-Dimensional materials by a polymeric stamp," *Materials Research Express*, vol. 3, no. 2, pp. 1–6, 2016.

[127] A. G. Kelly, T. Hallam, C. Backes, A. Harvey, A. S. Esmaeily, I. Godwin, J. Coelho, V. Nicolosi, J. Lauth, A. Kulkarni, S. Kinge, L. D. Siebbeles, G. S. Duesberg, and J. N. Coleman, "All-printed thin-film transistors from networks of liquid-exfoliated nanosheets," *Science*, vol. 356, no. 6333, pp. 69–73, 2017.

[128] D. Parviz, F. Irin, S. A. Shah, S. Das, C. B. Sweeney, and M. J. Green, "Challenges in Liquid-Phase Exfoliation, Processing, and Assembly of Pristine Graphene," *Advanced Materials*, vol. 28, no. 40, pp. 8796–8818, 2016.

[129] M.-A. Fardin, "On the Rheology of Cats," *Rheology Bulletin*, vol. 83, no. 2, pp. 16–17, 2014.

[130] T. Chen, B. Zeng, J. L. Liu, J. H. Dong, X. Q. Liu, Z. Wu, X. Z. Yang, and Z. M. Li, "High throughput exfoliation of graphene oxide from expanded graphite with assistance of strong oxidant in modified Hummers method," in *Journal of Physics: Conference Series*, vol. 188, 2009.

[131] X. Zhou and Z. Liu, "A scalable, solution-phase processing route to graphene oxide and graphene ultralarge sheets," *Chemical Communications*, vol. 46, no. 15, pp. 2611–2613, 2010.

[132] M. J. McAllister, J. L. Li, D. H. Adamson, H. C. Schniepp, A. A. Abdala, J. Liu, M. Herrera-Alonso, D. L. Milius, R. Car, R. K. Prud'homme, and I. A. Aksay, "Single sheet functionalized graphene by oxidation and thermal expansion of graphite," *Chemistry of Materials*, vol. 19, no. 18, pp. 4396–4404, 2007.

[133] S. Park, J. An, R. D. Piner, I. Jung, D. Yang, A. Velamakanni, S. B. T. Nguyen, and R. S. Ruoff, "Aqueous suspension and characterization of chemically modified graphene sheets," *Chemistry of Materials*, vol. 20, no. 21, pp. 6592–6594, 2008.

[134] J. Geng and H. T. Jung, "Porphyrin functionalized graphene sheets in aqueous suspensions: From the preparation of graphene sheets to highly conductive graphene films," *Journal of Physical Chemistry C*, vol. 114, no. 18, pp. 8227–8234, 2010.

[135] N. A. Nebogatikova, I. V. Antonova, V. Y. Prinz, I. I. Kurkina, V. I. Vdovin, G. N. Aleksandrov, V. B. Timofeev, S. A. Smagulova, E. R. Zakirov, and V. G. Kesler, "Fluorinated graphene dielectric films obtained from functionalized graphene suspension: Preparation and properties," *Physical Chemistry Chemical Physics*, vol. 17, no. 20, pp. 13257–13266, 2015.

[136] E. Varrla, K. R. Paton, C. Backes, A. Harvey, R. J. Smith, J. McCauley, and J. N. Coleman, "Turbulence-assisted shear exfoliation of graphene using household detergent and a kitchen blender," *Nanoscale*, vol. 6, no. 20, pp. 11810–11819, 2014.

[137] G. M. Rutter, N. P. Guisinger, J. N. Crain, E. A. Jarvis, M. D. Stiles, T. Li, P. N. First, and J. A. Stroscio, "Imaging the interface of epitaxial graphene with silicon carbide via scanning tunneling microscopy," *Physical Review B - Condensed Matter and Materials Physics*, vol. 76, no. 23, pp. 1–6, 2007.

[138] H. Zhao, Y. C. Lin, C. H. Yeh, H. Tian, Y. C. Chen, D. Xie, Y. Yang, K. Suenaga, T. L. Ren, and P. W. Chiu, "Growth and Raman spectra of single-crystal trilayer graphene with different stacking orientations," *ACS Nano*, vol. 8, no. 10, pp. 10766–10773, 2014.

[139] W. Norimatsu and M. Kusunoki, "Transitional structures of the interface between graphene and 6H-SiC (0 0 0 1)," *Chemical Physics Letters*, vol. 468, no. 1-3, pp. 52–56, 2009.

[140] G. Prakash, M. A. Capano, M. L. Bolen, D. Zemlyanov, and R. G. Reifenberger, "AFM study of ridges in few-layer epitaxial graphene grown on the carbon-face of 4H-SiC (000$\bar{1}$)," *Carbon*, vol. 48, no. 9, pp. 2383–2393, 2010.

[141] J. L. Tedesco, G. G. Jernigan, J. C. Culbertson, J. K. Hite, Y. Yang, K. M. Daniels, R. L. Myers-Ward, C. R. Eddy, J. A. Robinson, K. A. Trumbull, M. T. Wetherington, P. M. Campbell, and D. K. Gaskill, "Morphology characterization of argon-mediated epitaxial graphene on C-face SiC," *Applied Physics Letters*, vol. 96, no. 22, 2010.

[142] N. Archer, "Chemical vapour deposition," *Physics in Technology*, vol. 10, pp. 152–161, jul 1979.

[143] S. Chaitoglou and E. Bertran, "Effect of temperature on graphene grown by chemical vapor deposition," *Journal of Materials Science*, vol. 52, no. 13, pp. 8348–8356, 2017.

[144] X. Sun, L. Lin, L. Sun, J. Zhang, D. Rui, J. Li, M. Wang, C. Tan, N. Kang, D. Wei, H. Q. Xu, H. Peng, and Z. Liu, "Low-Temperature and Rapid Growth of Large Single-Crystalline Graphene with Ethane," *Small*, vol. 1702916, p. 1702916, 2017.

[145] A. Guermoune, T. Chari, F. Popescu, S. S. Sabri, J. Guillemette, H. S. Skulason, T. Szkopek, and M. Siaj, "Chemical vapor deposition synthesis of graphene on copper with methanol, ethanol, and propanol precursors," *Carbon*, vol. 49, no. 13, pp. 4204–4210, 2011.

[146] Z. Sun, Z. Yan, J. Yao, E. Beitler, Y. Zhu, and J. M. Tour, "Growth of graphene from solid carbon sources," *Nature*, vol. 468, no. 7323, pp. 549–552, 2010.

[147] X. D. Chen, Z. Chen, W. S. Jiang, C. Zhang, J. Sun, H. Wang, W. Xin, L. Lin, M. K. Priydarshi, H. Yang, Z. B. Liu, J. G. Tian, Y. Zhang, Y. Zhang, and Z. Liu, "Fast Growth and Broad Applications of 25-Inch Uniform Graphene Glass," *Advanced Materials*, vol. 29, no. 1, pp. 1–9, 2017.

[148] W. Wu, L. A. Jauregui, Z. Su, Z. Liu, J. Bao, Y. P. Chen, and Q. Yu, "Growth of single crystal graphene arrays by locally controlling nucleation on polycrystalline Cu using chemical vapor deposition," *Advanced Materials*, vol. 23, no. 42, pp. 4898–4903, 2011.

[149] L. Gao, W. Ren, H. Xu, L. Jin, Z. Wang, T. Ma, L. P. Ma, Z. Zhang, Q. Fu, L. M. Peng, X. Bao, and H. M. Cheng, "Repeated growth and bubbling transfer of graphene with millimetre-size single-crystal grains using platinum," *Nature Communications*, vol. 3, 2012.

[150] R. Van Gastel, A. T. N'Diaye, D. Wall, J. Coraux, C. Busse, N. M. Buckanie, F. J. Meyer Zu Heringdorf, M. Horn Von Hoegen, T. Michely, and B. Poelsema, "Selecting a single orientation for millimeter sized graphene sheets," *Applied Physics Letters*, vol. 95, no. 12, pp. 2007–2010, 2009.

[151] J. J. Lander, H. E. Kern, and A. L. Beach, "Solubility and diffusion coefficient of carbon in nickel: Reaction rates of nickel-carbon alloys with barium oxide," *Journal of Applied Physics*, vol. 23, no. 12, pp. 1305–1309, 1952.

[152] M. Losurdo, M. M. Giangregorio, P. Capezzuto, and G. Bruno, "Graphene CVD growth on copper and nickel: role of hydrogen in kinetics and structure," *Physical Chemistry Chemical Physics*, vol. 13, no. 46, p. 20836, 2011.

[153] L. Gan and Z. Luo, "Turning off hydrogen to realize seeded growth of subcentimeter single-crystal graphene grains on copper," *ACS Nano*, vol. 7, no. 10, pp. 9480–9488, 2013.

[154] P. Braeuninger-Weimer, B. Brennan, A. J. Pollard, and S. Hofmann, "Understanding and Controlling Cu-Catalyzed Graphene Nucleation: The Role of Impurities, Roughness, and Oxygen Scavenging," *Chemistry of Materials*, vol. 28, no. 24, pp. 8905–8915, 2016.

[155] B. Huet and J. P. Raskin, "Role of the Cu substrate in the growth of ultra-flat crack-free highly-crystalline single-layer graphene," *Nanoscale*, vol. 10, no. 46, pp. 21898–21909, 2018.

[156] O. V. Yazyev and S. G. Louie, "Electronic transport in polycrystalline graphene," *Nature Materials*, vol. 9, no. 10, pp. 806–809, 2010.

[157] B. Wu, D. Geng, Z. Xu, Y. Guo, L. Huang, Y. Xue, J. Chen, G. Yu, and Y. Liu, "Self-organized graphene crystal patterns," *NPG Asia Materials*, vol. 5, no. 1, pp. e36–7, 2013.

[158] Z. Zhang, "Atomistic Processes in the Early Stages of Thin-Film Growth," *Science*, vol. 276, pp. 377–383, apr 1997.

[159] L. Colombo, X. Li, B. Han, C. Magnuson, W. Cai, Y. Zhu, and R. S. Ruoff, "Growth kinetics and defects of CVD graphene on Cu," in *ECS Transactions*, vol. 28, pp. 109–114, 2010.

[160] X. Li, C. W. Magnuson, A. Venugopal, J. An, J. W. Suk, B. Han, M. Borysiak, W. Cai, A. Velamakanni, Y. Zhu, L. Fu, E. M. Vogel, E. Voelkl, L. Colombo, and R. S. Ruoff, "Graphene films with large domain size by a two-step chemical vapor deposition process," *Nano Letters*, vol. 10, no. 11, pp. 4328–4334, 2010.

[161] S. Chen, H. Ji, H. Chou, Q. Li, H. Li, J. W. Suk, R. Piner, L. Liao, W. Cai, and R. S. Ruoff, "Millimeter-size single-crystal graphene by suppressing evaporative loss of Cu during low pressure chemical vapor deposition," *Advanced Materials*, vol. 25, no. 14, pp. 2062–2065, 2013.

[162] H. Zhang, Y. Zhang, B. Wang, Z. Chen, Y. Sui, Y. Zhang, C. Tang, B. Zhu, X. Xie, G. Yu, Z. Jin, and X. Liu, "Effect of hydrogen in size-limited growth of graphene by atmospheric pressure chemical vapor deposition," *Journal of Electronic Materials*, vol. 44, no. 1, pp. 79–86, 2015.

[163] I. Vlassiouk, M. Regmi, P. Fulvio, S. Dai, P. Datskos, G. Eres, and S. Smirnov, "Role of hydrogen in chemical vapor deposition growth of large single-crystal graphene," *ACS Nano*, vol. 5, no. 7, pp. 6069–6076, 2011.

[164] J. Kraus, L. Böbel, G. Zwaschka, and S. Günther, "Understanding the Reaction Kinetics to Optimize Graphene Growth on Cu by Chemical Vapor Deposition," *Annalen der Physik*, vol. 529, no. 11, pp. 1–16, 2017.

[165] N. Reckinger, X. Tang, F. Joucken, L. Lajaunie, R. Arenal, E. Dubois, B. Hackens, L. Henrard, and J. F. Colomer, "Oxidation-assisted graphene heteroepitaxy on copper foil," *Nanoscale*, vol. 8, no. 44, pp. 18751–18759, 2016.

[166] K. P. Beh, F. K. Yam, R. Abdalrheem, Y. Z. Ng, F. H. A. Suhaimi, H. S. Lim, and M. Z. Mat Jafri, "Raman Studies on Pre- and Post-Processed CVD Graphene Films Grown under Various Nitrogen Carrier Gas Flows," *Journal of Physics: Conference Series*, vol. 995, p. 012057, apr 2018.

[167] B. Guo, Q. Liu, E. Chen, H. Zhu, L. Fang, and J. R. Gong, "Controllable N-doping of graphene," *Nano Letters*, vol. 10, no. 12, pp. 4975–4980, 2010.

[168] D. Geng, S. Yang, Y. Zhang, J. Yang, J. Liu, R. Li, T. K. Sham, X. Sun, S. Ye, and S. Knights, "Nitrogen doping effects on the structure of graphene," *Applied Surface Science*, vol. 257, no. 21, pp. 9193–9198, 2011.

[169] X. Wang, G. Sun, P. Routh, D.-H. Kim, W. Huang, and P. Chen, "Heteroatom-doped graphene materials: syntheses, properties and applications," *Chem. Soc. Rev.*, vol. 43, no. 20, pp. 7067–7098, 2014.

[170] M. Rybin, A. Pereyaslavtsev, T. Vasilieva, V. Myasnikov, I. Sokolov, A. Pavlova, E. Obraztsova, A. Khomich, V. Ralchenko, and E. Obraztsova, "Efficient nitrogen doping of graphene by plasma treatment," *Carbon*, vol. 96, pp. 196–202, 2016.

[171] M. Y. Han, B. Özyilmaz, Y. Zhang, and P. Kim, "Energy band-gap engineering of graphene nanoribbons," *Physical Review Letters*, vol. 98, no. 20, pp. 1–4, 2007.

[172] O. Leenaerts, B. Partoens, and F. M. Peeters, "Adsorption of H2 O, N H3, CO, N O2, and NO on graphene: A first-principles study," *Physical Review B - Condensed Matter and Materials Physics*, vol. 77, no. 12, pp. 1–6, 2008.

[173] P. A. Khomyakov, G. Giovannetti, P. C. Rusu, G. Brocks, J. Van Den Brink, and P. J. Kelly, "First-principles study of the interaction and charge transfer between graphene and metals," *Physical Review B - Condensed Matter and Materials Physics*, vol. 79, no. 19, pp. 1–12, 2009.

[174] H. Liu, Y. Liu, and D. Zhu, "Chemical doping of graphene," *Journal of Materials Chemistry*, vol. 21, no. 10, pp. 3335–3345, 2011.

[175] J. Li, L. Lin, D. Rui, Q. Li, J. Zhang, N. Kang, Y. Zhang, H. Peng, Z. Liu, and H. Q. Xu, "Electron-Hole Symmetry Breaking in Charge Transport in Nitrogen-Doped Graphene," *ACS Nano*, vol. 11, no. 5, pp. 4641–4650, 2017.

[176] D. Wei, Y. Liu, Y. Wang, H. Zhang, L. Huang, and G. Yu, "Synthesis of N-doped graphene by chemical vapor deposition and its electrical properties.," *Nano*, vol. 9, no. 5, pp. 1752–8, 2009.

[177] B. Anand, M. Karakaya, G. Prakash, S. Siva Sankara Sai, R. Philip, P. Ayala, A. Srivastava, A. K. Sood, A. M. Rao, and R. Podila, "Dopant-configuration controlled carrier scattering in graphene," *RSC Advances*, vol. 5, no. 73, pp. 59556–59563, 2015.

[178] M. Scardamaglia, B. Aleman, M. Amati, C. Ewels, P. Pochet, N. Reckinger, J.-F. Colomer, T. Skaltsas, N. Tagmatarchis, R. Snyders, L. Gregoratti, and C. Bittencourt, "Nitrogen implantation of suspended graphene flakes: Annealing effects and selectivity of sp2 nitrogen species," *Carbon*, vol. 73, pp. 371–381, jul 2014.

[179] R. Podila, J. Chacón-Torres, J. T. Spear, T. Pichler, P. Ayala, and A. M. Rao, "Spectroscopic investigation of nitrogen doped graphene," *Applied Physics Letters*, vol. 101, no. 12, 2012.

[180] L. S. Panchakarla, K. S. Subrahmanyam, S. K. Saha, A. Govindaraj, H. R. Krishnamurthy, U. V. Waghmare, and C. N. Rao, "Synthesis, structure, and properties of boron- and nitrogen-doped graphene," *Advanced Materials*, vol. 21, no. 46, pp. 4726–4730, 2009.

[181] L. Zhao, R. He, K. T. Rim, T. Schiros, K. S. Kim, H. Zhou, C. Gutierrez, S. P. Chockalingam, C. J. Arguello, L. Palova, D. Nordlund, M. S. Hybertsen, D. R. Reichman, T. F. Heinz, P. Kim, A. Pinczuk, G. W. Flynn, and A. N. Pasupathy, "Visualizing Individual Nitrogen Dopants in Monolayer Graphene," *Science*, vol. 333, pp. 999–1003, aug 2011.

[182] Y. Shao, S. Zhang, M. H. Engelhard, G. Li, G. Shao, Y. Wang, J. Liu, I. A. Aksay, and Y. Lin, "Nitrogen-doped graphene and its electrochemical applications," *Journal of Materials Chemistry*, vol. 20, no. 35, pp. 7491–7496, 2010.

[183] Z. H. Sheng, X. Q. Zheng, J. Y. Xu, W. J. Bao, F. B. Wang, and X. H. Xia, "Electrochemical sensor based on nitrogen doped graphene: Simultaneous determination of ascorbic acid, dopamine and uric acid," *Biosensors and Bioelectronics*, vol. 34, no. 1, pp. 125–131, 2012.

[184] R. Lv, Q. Li, A. R. Botello-Méndez, T. Hayashi, B. Wang, A. Berkdemir, Q. Hao, A. L. Eléas, R. Cruz-Silva, H. R. Gutiérrez, Y. A. Kim, H. Muramatsu, J. Zhu, M. Endo, H. Terrones, J. C. Charlier, M. Pan, and M. Terrones, "Nitrogen-doped graphene: Beyond single substitution and enhanced molecular sensing," *Scientific Reports*, vol. 2, pp. 1–8, 2012.

[185] D. Usachov, O. Vilkov, A. Grüneis, D. Haberer, A. Fedorov, V. K. Adamchuk, A. B. Preobrajenski, P. Dudin, A. Barinov, M. Oehzelt, C. Laubschat, and D. V. Vyalikh, "Nitrogen-doped graphene: Efficient growth, structure, and electronic properties," *Nano Letters*, vol. 11, no. 12, pp. 5401–5407, 2011.

[186] T. Schiros, D. Nordlund, L. Pálová, D. Prezzi, L. Zhao, K. S. Kim, U. Wurstbauer, C. Gutiérrez, D. Delongchamp, C. Jaye, D. Fischer, H. Ogasawara, L. G. M. Pettersson, D. R. Reichman, P. Kim, M. S. Hybertsen, and A. N. Pasupathy, "Connecting dopant bond type with electronic structure in n-doped graphene," *Nano Letters*, vol. 12, no. 8, pp. 4025–4031, 2012.

[187] J. B. McManus, A. Hennessy, C. P. Cullen, T. Hallam, N. McEvoy, and G. S. Duesberg, "Controlling Defect and Dopant Concentrations in Graphene by Remote Plasma Treatments," *Physica Status Solidi (B) Basic Research*, vol. 254, no. 11, pp. 1–6, 2017.

[188] Y. F. Lu, S. T. Lo, J. C. Lin, W. Zhang, J. Y. Lu, F. H. Liu, C. M. Tseng, Y. H. Lee, C. T. Liang, and L. J. Li, "Nitrogen-doped graphene sheets grown by chemical vapor deposition: Synthesis and influence of nitrogen impurities on carrier transport," *ACS Nano*, vol. 7, no. 8, pp. 6522–6532, 2013.

[189] J. Lin, R. Y. Tay, H. Li, L. Jing, S. H. Tsang, A. Bolker, C. Saguy, and E. H. T. Teo, "Concentric dopant segregation in CVD-grown N-doped graphene single crystals," *Applied Surface Science*, vol. 454, no. March, pp. 121–129, 2018.

[190] A. G. Shard, "Detection limits in XPS for more than 6000 binary systems using Al and Mg Kα X-rays," *Surface and Interface Analysis*, vol. 46, no. 3, pp. 175–185, 2014.

[191] J. Gausden, R. Siris, T. Stimpel-Lindner, N. McEvoy, G. S. Duesberg, and T. Hallam, "Nitrogen as a Suitable Replacement for Argon within Methane-Based Hot-Wall Graphene Chemical Vapor Deposition," *Physica Status Solidi (B)*, vol. 1900240, p. 1900240, 2019.

[192] A. Pirkle, J. Chan, A. Venugopal, D. Hinojos, C. W. Magnuson, S. McDonnell, L. Colombo, E. M. Vogel, R. S. Ruoff, and R. M. Wallace, "The effect of chemical residues on the physical and electrical properties of chemical vapor deposited graphene transferred to SiO2," *Applied Physics Letters*, vol. 99, no. 12, pp. 2009–2012, 2011.

[193] W. Xie, L. T. Weng, K. M. Ng, C. K. Chan, and C. M. Chan, "Clean graphene surface through high temperature annealing," *Carbon*, vol. 94, pp. 740–748, 2015.

[194] P. Joshi, H. E. Romero, A. T. Neal, V. K. Toutam, and S. A. Tadigadapa, "Intrinsic doping and gate hysteresis in graphene field effect devices fabricated on SiO2 substrates," *Journal of Physics Condensed Matter*, vol. 22, no. 33, 2010.

[195] S. Goniszewski, M. Adabi, O. Shaforost, S. M. Hanham, L. Hao, and N. Klein, "Correlation of p-doping in CVD Graphene with Substrate Surface Charges," *Scientific Reports*, vol. 6, no. March, pp. 1–9, 2016.

[196] M. Lafkioti, B. Krauss, T. Lohmann, U. Zschieschang, H. Klauk, K. V. Klitzing, and J. H. Smet, "Graphene on a hydrophobic substrate: Doping reduction and hysteresis suppression under ambient conditions," *Nano Letters*, vol. 10, no. 4, pp. 1149–1153, 2010.

[197] Z. Hu, D. Prasad Sinha, J. U. Lee, and M. Liehr, "Substrate dielectric effects on graphene field effect transistors," *Journal of Applied Physics*, vol. 115, no. 19, 2014.

[198] M. Tripathi, A. Mittelberger, K. Mustonen, C. Mangler, J. Kotakoski, J. C. Meyer, and T. Susi, "Cleaning graphene: Comparing heat treatments in air and in vacuum," 2017.

[199] T. Hallam, N. C. Berner, C. Yim, and G. S. Duesberg, "Strain, Bubbles, Dirt, and Folds: A Study of Graphene Polymer-Assisted Transfer," *Advanced Materials Interfaces*, vol. 1, no. 6, pp. 1–7, 2014.

[200] Z. Zhang, J. Du, D. Zhang, H. Sun, L. Yin, L. Ma, J. Chen, D. Ma, H. M. Cheng, and W. Ren, "Rosin-enabled ultraclean and damage-free transfer of graphene for large-area flexible organic light-emitting diodes," *Nature Communications*, vol. 8, pp. 1–9, 2017.

[201] L. A. Belyaeva, W. Fu, H. Arjmandi-Tash, and G. F. Schneider, "Molecular caging of graphene with cyclohexane: Transfer and electrical transport," *ACS Central Science*, vol. 2, no. 12, pp. 904–909, 2016.

[202] W. S. Leong, H. Wang, J. Yeo, F. J. Martin-Martinez, A. Zubair, P. C. Shen, Y. Mao, T. Palacios, M. J. Buehler, J. Y. Hong, and J. Kong, "Paraffin-enabled graphene transfer," *Nature Communications*, vol. 10, no. 1, pp. 1–8, 2019.

[203] J. Lee, K. S. Novoselov, and H. S. Shin, "Interaction between Metal and Graphene: Dependence on the Layer Number of Graphene," *ACS Nano*, vol. 5, pp. 608–612, jan 2011.

[204] S. Huh, J. Park, K. S. Kim, B. H. Hong, and S. B. Kim, "Selective n-type doping of graphene by photo-patterned gold nanoparticles," *ACS Nano*, vol. 5, no. 5, pp. 3639–3644, 2011.

[205] G. Giovannetti, P. A. Khomyakov, G. Brocks, V. M. Karpan, J. Van Den Brink, and P. J. Kelly, "Doping graphene with metal contacts," *Physical Review Letters*, vol. 101, no. 2, pp. 4–7, 2008.

[206] J. Meyer, P. R. Kidambi, B. C. Bayer, C. Weijtens, A. Kuhn, A. Centeno, A. Pesquera, A. Zurutuza, J. Robertson, and S. Hofmann, "Metal oxide induced charge transfer doping and band alignment of graphene electrodes for efficient organic light emitting diodes," *Scientific Reports*, vol. 4, pp. 1–7, 2014.

[207] Z. Zhang, X. Zou, L. Xu, L. Liao, W. Liu, J. Ho, X. Xiao, C. Jiang, and J. Li, "Hydrogen gas sensor based on metal oxide nanoparticles decorated graphene transistor," *Nanoscale*, vol. 7, no. 22, pp. 10078–10084, 2015.

[208] D. Zhang, N. Yin, and B. Xia, "Facile fabrication of ZnO nanocrystalline-modified graphene hybrid nanocomposite toward methane gas sensing application," *Journal of Materials Science: Materials in Electronics*, vol. 26, no. 8, pp. 5937–5945, 2015.

[209] M. Kodu, A. Berholts, T. Kahro, J. Eriksson, R. Yakimova, T. Avarmaa, I. Renge, H. Alles, and R. Jaaniso, "Highly Sensitive NH3 Sensors Using CVD and Epitaxial Graphene Functionalised with Vanadium(V) Oxide: A Comparative Study," *Proceedings*, vol. 2, no. 13, p. 854, 2018.

[210] H. Song, L. Zhang, C. He, Y. Qu, Y. Tian, and Y. Lv, "Graphene sheets decorated with SnO2 nanoparticles: in situ synthesis and highly efficient materials for cataluminescence gas sensors," *Journal of Materials Chemistry*, vol. 21, no. 16, p. 5972, 2011.

[211] A. Di Bartolomeo, "Graphene Schottky diodes: An experimental review of the rectifying graphene/semiconductor heterojunction," *Physics Reports*, vol. 606, pp. 1–58, 2016.

[212] P. Wang, X. Li, Z. Xu, Z. Wu, S. Zhang, W. Xu, H. Zhong, H. Chen, E. Li, J. Luo, Q. Yu, and S. Lin, "Tunable graphene/indium phosphide heterostructure solar cells," *Nano Energy*, vol. 13, pp. 509–517, apr 2015.

[213] L. Huder, C. Rinfray, D. Rouchon, A. Benayad, M. Baraket, G. Izzet, F. Lipp-Bregolin, G. Lapertot, L. Dubois, A. Proust, L. Jansen, and F. Duclairoir, "Evidence for Charge Transfer at the Interface between Hybrid Phosphomolybdate and Epitaxial Graphene," *Langmuir*, vol. 32, no. 19, pp. 4774–4783, 2016.

[214] W. Li, X. Geng, Y. Guo, J. Rong, Y. Gong, L. Wu, X. Zhang, P. Li, J. Xu, G. Cheng, M. Sun, and L. Liu, "Reduced graphene oxide electrically contacted graphene sensor for highly sensitive nitric oxide detection," *ACS Nano*, vol. 5, no. 9, pp. 6955–6961, 2011.

[215] Y. Zhang, E. E. Mendez, and X. Du, "Mobility-Dependent Low-Frequency Noise in Graphene Field-Effect Transistors," *ACS Nano*, vol. 5, pp. 8124–8130, oct 2011.

[216] W. Fu, L. Jiang, E. P. van Geest, L. M. Lima, and G. F. Schneider, "Sensing at the Surface of Graphene Field-Effect Transistors," *Advanced Materials*, vol. 29, no. 6, pp. 1–25, 2017.

[217] S. Yang, C. Jiang, and S.-h. Wei, "Gas sensing in 2D materials," *Applied Physics Reviews*, vol. 4, no. 2, p. 021304, 2017.

[218] J.-M. Guay, R. Rautela, S. Scarfe, P. Lazar, S. Azimi, C. Grenapin, A. Halpin, W. Wang, L. Andrzejewski, R. Plumadore, J. Park, M. Otyepka, J.-M. Menard, and A. Luican-Mayer, "Mechanistic insight into the limiting factors of graphene-based environmental sensors," pp. 1–14, nov 2019.

[219] M. Donarelli and L. Ottaviano, "2D Materials for Gas Sensing Applications: A Review on Graphene Oxide, MoS , WS and Phosphorene," *Sensors (Basel, Switzerland)*, vol. 18, no. 11, 2018.

[220] D. T. Phan, J. S. Youn, and K. J. Jeon, "High-sensitivity and fast-response hydrogen sensor for safety application using Pt nanoparticle-decorated 3D graphene," *Renewable Energy*, vol. 144, pp. 167–171, 2019.

[221] R. Ghanbari, R. Safaiee, and M. M. Golshan, "A dispersion-corrected DFT investigation of CH 4 adsorption by silver-decorated monolayer graphene in the presence of ambient oxygen molecules," *Applied Surface Science*, vol. 457, no. February, pp. 303–314, 2018.

[222] V. K. Nagareddy, H. K. Chan, S. C. Hernández, V. D. Wheeler, R. L. Myers-Ward, L. O. Nyakiti, C. R. Eddy, S. G. Walton, J. P. Goss, N. G. Wright, D. K. Gaskill, and A. B. Horsfall, "Detection of polar chemical vapors using epitaxial graphene grown on SiC (0001)," *Applied Physics Letters*, vol. 102, no. 17, 2013.

[223] H. Arjmandi-Tash, N. Lebedev, P. M. van Deursen, J. Aarts, and G. F. Schneider, "Hybrid cold and hot-wall reaction chamber for the rapid synthesis of uniform graphene," *Carbon*, vol. 118, pp. 438–442, 2017.

[224] J. M. Kay and R. M. Nedderman, *Fluid mechanics and transfer processes*. Cambridge [Cambridgeshire]; New York, N.Y.: Cambridge University Press, 1985.

[225] X. Li, W. Cai, J. An, S. Kim, J. Nah, D. Yang, R. Piner, A. Velamakanni, I. Jung, E. Tutuc, S. K. Banerjee, L. Colombo, and R. S. Ruoff, "Large area synthesis of high-quality and uniform graphene films on copper foils," *Science*, vol. 324, no. 5932, pp. 1312–1314, 2009.

[226] Z. Ni, Y. Wang, T. Yu, and Z. Shen, "Raman spectroscopy and imaging of graphene," *Nano Research*, vol. 1, no. 4, pp. 273–291, 2008.

[227] M. Wang, E. H. Yang, R. Vajtai, J. Kono, and P. M. Ajayan, "Effects of etchants in the transfer of chemical vapor deposited graphene," *Journal of Applied Physics*, vol. 123, p. 195103, may 2018.

[228] L. A. Sordan, A. Mansouri, P. Pedrinazzi, E. Guerriero, M. Fiocco, A. Pesquera, A. Centeno, A. Zurutuza, A. Behnam, E. A. Carrion, E. Pop, and Roman, "Ultra-low contact resistance in graphene devices at the Dirac point," *2D Materials*, vol. 5, no. 2, p. 25014, 2018.

[229] R. R. Jones, D. C. Hooper, L. Zhang, D. Wolverson, and V. K. Valev, "Raman Techniques: Fundamentals and Frontiers," 2019.

[230] C. Headoffice, "Application Note: Have I selected the right laser for my Raman experiments?." `https://www.coboltlasers.com/wp-content/uploads/2018/05/Have-I-selected-the-right-laser-for-Raman-2018-03-01.pdf`. Accessed: 2020-05-07.

[231] A. C. Ferrari and D. M. Basko, "Raman spectroscopy as a versatile tool for studying the properties of graphene," *Nature Nanotechnology*, vol. 8, no. 4, pp. 235–246, 2013.

[232] A. C. Ferrari, J. C. Meyer, V. Scardaci, C. Casiraghi, M. Lazzeri, F. Mauri, S. Piscanec, D. Jiang, K. S. Novoselov, S. Roth, and A. K. Geim, "Raman spectrum of graphene and graphene layers," *Physical Review Letters*, vol. 97, no. 18, pp. 1–4, 2006.

[233] M. Popov, V. Churkin, A. Kirichenko, V. Denisov, D. Ovsyannikov, B. Kulnitskiy, I. Perezhogin, V. Aksenenkov, and V. Blank, "Raman Spectra and Bulk Modulus of Nanodiamond in a Size Interval of 2–5 nm," *Nanoscale Research Letters*, vol. 12, pp. 4–9, 2017.

[234] S. Heeg, L. Shi, T. Pichler, and L. Novotny, "Raman resonance profile of an individual confined long linear carbon chain," *Carbon*, vol. 139, pp. 581–585, 2018.

[235] A. C. Ferrari and J. Robertson, "Raman spectroscopy of amorphous, nanostructured, diamond–like carbon, and nanodiamond," *Philosophical Transactions of the Royal Society of London. Series A: Mathematical, Physical and Engineering Sciences*, vol. 362, pp. 2477–2512, nov 2004.

[236] M. S. Dresselhaus, A. Jorio, A. G. Souza Filho, and R. Saito, "Defect characterization in graphene and carbon nanotubes using Raman spectroscopy," *Philosophical Transactions of the Royal Society A: Mathematical, Physical and Engineering Sciences*, vol. 368, no. 1932, pp. 5355–5377, 2010.

[237] N. G. Kovalchuk, K. A. Nigerish, M. M. Mikhalik, N. I. Kargin, I. V. Komissarov, and S. L. Prischepa, "Possibility of Determining the Graphene Doping Level Using Raman Spectra," *Journal of Applied Spectroscopy*, vol. 84, no. 6, pp. 995–998, 2018.

[238] Z. H. Ni, T. Yu, Z. Q. Luo, Y. Y. Wang, L. Liu, C. P. Wong, J. M. Miao, W. Huang, and Z. X. Shen, "Probing Charged Impurities in Suspended Graphene Using Raman Spectroscopy," *Acs Nano*, vol. 3, no. 3, pp. 569–574, 2009.

[239] A. Eckmann, A. Felten, A. Mishchenko, L. Britnell, R. Krupke, K. S. Novoselov, and C. Casiraghi, "Probing the nature of defects in graphene by Raman spectroscopy," *Nano Letters*, vol. 12, no. 8, pp. 3925–3930, 2012.

[240] L. G. Cançado, A. Jorio, E. H. Ferreira, F. Stavale, C. A. Achete, R. B. Capaz, M. V. Moutinho, A. Lombardo, T. S. Kulmala, and A. C. Ferrari, "Quantifying defects in graphene via Raman spectroscopy at different excitation energies," *Nano Letters*, vol. 11, no. 8, pp. 3190–3196, 2011.

[241] M. M. Lucchese, F. Stavale, E. H. Ferreira, C. Vilani, M. V. Moutinho, R. B. Capaz, C. A. Achete, and A. Jorio, "Quantifying ion-induced defects and Raman relaxation length in graphene," *Carbon*, vol. 48, no. 5, pp. 1592–1597, 2010.

[242] L. M. Malard, M. A. Pimenta, G. Dresselhaus, and M. S. Dresselhaus, "Raman spectroscopy in graphene," *Physics Reports*, vol. 473, no. 5-6, pp. 51–87, 2009.

[243] A. C. Ferrari, "Raman spectroscopy of graphene and graphite: Disorder, electron-phonon coupling, doping and nonadiabatic effects," *Solid State Communications*, vol. 143, no. 1-2, pp. 47–57, 2007.

[244] G. Binnig, C. F. Quate, and C. Gerber, "Atomic Force Microscope," *Physical Review Letters*, vol. 56, pp. 930–933, mar 1986.

[245] P. Systems, *Park AFM User Manual v1.7*. Park Systems; Suwon Korea: Park Systemsl, 2004.

[246] "NuNano Scout 350." `https://www.nunano.com/store/scout-350`. Accessed: 2019-10-27.

[247] W. Melitz, J. Shen, A. C. Kummel, and S. Lee, "Kelvin probe force microscopy and its application," *Surface Science Reports*, vol. 66, no. 1, pp. 1–27, 2011.

[248] R. N. S. Sodhi, "Time-of-flight secondary ion mass spectrometry (TOF-SIMS):—versatility in chemical and imaging surface analysis," *The Analyst*, vol. 129, no. 6, pp. 483–487, 2004.

[249] S. Fearn, *An introduction to time-of-flight secondary ion mass spectrometry (ToF-SIMS) and its application to materials science*. 2015.

[250] J. F. Moulder and J. Chastain, *Handbook of X-ray Photoelectron Spectroscopy: A Reference Book of Standard Spectra for Identification and Interpretation of XPS Data*. Physical Electronics Division, Perkin-Elmer Corporation, 1992.

[251] D. Briggs, "Handbook of X-ray Photoelectron Spectroscopy C. D. Wanger, W. M. Riggs, L. E. Davis, J. F. Moulder and G. E.Muilenberg Perkin-Elmer Corp., Physical Electronics Division, Eden Prairie, Minnesota, USA, 1979. 190 pp. $195," *Surface and Interface Analysis*, vol. 3, pp. v–v, aug 1981.

[252] D. Bianchi, L. Katona, J. Brenner, G. Vorlaufer, A. Vernesa, and W. S. Werner, "Numerical approximation of AR-XPS spectra for rough surfaces considering the effect of electron shadowing," *Surface and Interface Analysis*, vol. 47, no. 1, pp. 15–21, 2015.

[253] R. J. Ward and B. J. Wood, "A comparison of experimental and theoretically derived sensitivity factors for XPS," *Surface and Interface Analysis*, vol. 18, no. 9, pp. 679–684, 1992.

[254] W. Shockley, "A Unipolar "Field-Effect" Transistor," *Proceedings of the IRE*, vol. 40, pp. 1365–1376, nov 1952.

[255] F. Crowne, "Classical Gradual-Channel Modeling of Graphene Field- Effect Transistors (FETs)," *Sensors (Peterborough, NH)*, no. August, 2010.

[256] Y. Ma, C. Shen, A. Zhang, L. Chen, Y. Liu, J. Chen, Q. Liu, Z. Li, M. R. Amer, T. Nilges, A. N. Abbas, and C. Zhou, "Black Phosphorus Field-Effect Transistors with Work Function Tunable Contacts," *ACS Nano*, vol. 11, no. 7, pp. 7126–7133, 2017.

[257] E. Ponomarev, Á. Pásztor, A. Waelchli, A. Scarfato, N. Ubrig, C. Renner, and A. F. Morpurgo, "Hole Transport in Exfoliated Monolayer MoS 2," *ACS Nano*, vol. 12, pp. 2669–2676, mar 2018.

[258] B. Chen, H. Huang, X. Ma, L. Huang, Z. Zhang, and L. M. Peng, "How good can CVD-grown monolayer graphene be?," *Nanoscale*, vol. 6, no. 24, pp. 15255–15261, 2014.

[259] M. Weis, "Gradual channel approximation models for organic field-effect transistors: The space-charge field effect," *Journal of Applied Physics*, vol. 111, no. 5, 2012.

[260] J. He, X. Zhang, Y. Wang, and R. Huang, "New method for extraction of MOSFET parameters," *IEEE Electron Device Letters*, vol. 22, no. 12, pp. 597–599, 2001.

[261] D. K. Schroder, *Semiconductor Material and Device Characterization*. New York, NY, USA: Wiley-Interscience, 2006.

[262] K. Nagashio, T. Yamashita, T. Nishimura, K. Kita, and A. Toriumi, "Electrical transport properties of graphene on SiO2 with specific surface structures," *Journal of Applied Physics*, vol. 110, no. 2, p. 024513, 2011.

[263] J. Ryu, Y. Kim, D. Won, N. Kim, J. S. Park, E. K. Lee, D. Cho, S. P. Cho, S. J. Kim, G. H. Ryu, H. A. Shin, Z. Lee, B. H. Hong, and S. Cho, "Fast synthesis of high-performance graphene films by hydrogen-free rapid thermal chemical vapor deposition," *ACS Nano*, vol. 8, no. 1, pp. 950–956, 2014.

[264] C. Wang, W. Chen, C. Han, G. Wang, B. Tang, C. Tang, Y. Wang, W. Zou, X. A. Zhang, S. Qin, S. Chang, and L. Wang, "Growth of millimeter-size single crystal graphene on Cu foils by circumfluence chemical vapor deposition," *Scientific Reports*, vol. 4, pp. 1–5, 2014.

[265] Y. REN, C. ZHU, W. CAI, H. LI, Y. HAO, Y. WU, S. CHEN, Q. WU, R. D. PINER, and R. S. RUOFF, "An Improved Method for Transferring Graphene Grown By Chemical Vapor Deposition," *Nano*, vol. 07, no. 01, p. 1150001, 2012.

[266] J. Li, D. Wang, and L.-J. Wan, "Unexpected functions of oxygen in a chemical vapor deposition atmosphere to regulate graphene growth modes," *Chem. Commun.*, vol. 51, no. 85, pp. 15486–15489, 2015.

[267] "Aixtron Graphene, https://www.graphene-info.com/aixtron, accessed 2020-01-25."

[268] Y. Feng, D. J. Trainer, H. Peng, Y. Liu, and K. Chen, "Safe growth of graphene from non-flammable gas mixtures via chemical vapor deposition," *Journal of Materials Science and Technology*, vol. 33, no. 3, pp. 285–290, 2017.

[269] K. Li, C. He, M. Jiao, Y. Wang, and Z. Wu, "A first-principles study on the role of hydrogen in early stage of graphene growth during the CH4dissociation on Cu(1 1 1) and Ni(1 1 1) surfaces," *Carbon*, vol. 74, pp. 255–265, 2014.

[270] T.-o. Terasawa and K. Saiki, "Effect of vapor-phase oxygen on chemical vapor deposition growth of graphene," *Applied Physics Express*, vol. 8, no. 3, p. 035101, 2015.

[271] P. R. Kidambi, C. Ducati, B. Dlubak, D. Gardiner, R. S. Weatherup, M. B. Martin, P. Seneor, H. Coles, and S. Hofmann, "The parameter space of graphene chemical vapor deposition on polycrystalline Cu," *Journal of Physical Chemistry C*, vol. 116, no. 42, pp. 22492–22501, 2012.

[272] B. Huet and J. P. Raskin, "Pressure-Controlled Chemical Vapor Deposition of Single-Layer Graphene with Millimeter-Size Domains on Thin Copper Film," *Chemistry of Materials*, vol. 29, no. 8, pp. 3431–3440, 2017.

[273] H. S. Song, S. L. Li, H. Miyazaki, S. Sato, K. Hayashi, A. Yamada, N. Yokoyama, and K. Tsukagoshi, "Origin of the relatively low transport mobility of graphene grown through chemical vapor deposition," *Scientific Reports*, vol. 2, pp. 1–6, 2012.

[274] H. Kim, C. Mattevi, M. R. Calvo, J. C. Oberg, L. Artiglia, S. Agnoli, C. F. Hirjibehedin, M. Chhowalla, and E. Saiz, "Activation energy paths for graphene nucleation and growth on Cu," *ACS Nano*, vol. 6, no. 4, pp. 3614–3623, 2012.

[275] Z. Luo, Y. Lu, D. W. Singer, M. E. Berck, L. A. Somers, B. R. Goldsmith, and A. T. C. Johnson, "Effect of substrate roughness and feedstock concentration on growth of wafer-scale graphene at atmospheric pressure," *Chemistry of Materials*, vol. 23, no. 6, pp. 1441–1447, 2011.

[276] G. H. Han, F. Güneş, J. J. Bae, E. S. Kim, S. J. Chae, H. J. Shin, J. Y. Choi, D. Pribat, and Y. H. Lee, "Influence of copper morphology in forming nucleation seeds for graphene growth," *Nano Letters*, vol. 11, no. 10, pp. 4144–4148, 2011.

[277] S. Esconjauregui, C. M. Whelan, and K. Maex, "The reasons why metals catalyze the nucleation and growth of carbon nanotubes and other carbon nanomorphologies," *Carbon*, vol. 47, no. 3, pp. 659–669, 2009.

[278] K. L. Cashdollar, I. A. Zlochower, G. M. Green, R. A. Thomas, and M. Hertzberg, "Flammability of methane, propane, and hydrogen gases," *Journal of Loss Prevention in the Process Industries*, vol. 13, pp. 327–340, may 2000.

[279] C. Jia, J. Jiang, L. Gan, and X. Guo, "Direct optical characterization of graphene growth and domains on growth substrates," *Scientific Reports*, vol. 2, pp. 1–6, 2012.

[280] J. D. Wood, S. W. Schmucker, A. S. Lyons, E. Pop, and J. W. Lyding, "Effects of polycrystalline Cu substrate on graphene growth by chemical vapor deposition," *Nano Letters*, vol. 11, no. 11, pp. 4547–4554, 2011.

[281] A. Reina, H. Son, L. Jiao, B. Fan, M. S. Dresselhaus, Z. F. Liu, and J. Kong, "Transferring and identification of single- and few-layer graphene on arbitrary substrates," *Journal of Physical Chemistry C*, vol. 112, no. 46, pp. 17741–17744, 2008.

[282] K.-i. Sasaki, Y. Tokura, and T. Sogawa, "The Origin of Raman D Band: Bonding and Antibonding Orbitals in Graphene," *Crystals*, vol. 3, no. 1, pp. 120–140, 2013.

[283] B. Krauss, P. Nemes-Incze, V. Skakalova, L. P. Biro, K. V. Klitzing, and J. H. Smet, "Raman scattering at pure graphene zigzag edges," *Nano Letters*, vol. 10, no. 11, pp. 4544–4548, 2010.

[284] J. Schindelin, I. Arganda-Carreras, E. Frise, V. Kaynig, M. Longair, T. Pietzsch, S. Preibisch, C. Rueden, S. Saalfeld, B. Schmid, J. Y. Tinevez, D. J. White, V. Hartenstein, K. Eliceiri, P. Tomancak, and A. Cardona, "Fiji: An open-source platform for biological-image analysis," 2012.

[285] C. W. Magnuson, X. Kong, H. Ji, C. Tan, H. Li, R. Piner, C. A. Ventrice, and R. S. Ruoff, "Copper oxide as a "self-cleaning" substrate for graphene growth," *Journal of Materials Research*, vol. 29, no. 3, pp. 403–409, 2014.

[286] T. Liang, C. Luan, H. Chen, and M. Xu, "Exploring oxygen in graphene chemical vapor deposition synthesis," *Nanoscale*, vol. 9, no. 11, pp. 3719–3735, 2017.

[287] B. Xing, X.-Y. Pang, and G.-C. Wang, "C–H bond activation of methane on clean and oxygen pre-covered metals: A systematic theoretical study," *Journal of Catalysis*, vol. 282, pp. 74–82, aug 2011.

[288] A. Mohsin, L. Liu, P. Liu, W. Deng, I. N. Ivanov, G. Li, O. E. Dyck, G. Duscher, J. R. Dunlap, K. Xiao, and G. Gu, "Synthesis of millimeter-size hexagon-shaped graphene single crystals on resolidified copper," *ACS Nano*, vol. 7, no. 10, pp. 8924–8931, 2013.

[289] N. Bartelt and K. McCarty, "Graphene growth on metal surfaces," *MRS Bulletin*, vol. 37, pp. 1158–1165, dec 2012.

[290] B. Wu, D. Geng, Y. Guo, L. Huang, Y. Xue, J. Zheng, J. Chen, G. Yu, Y. Liu, L. Jiang, and W. Hu, "Equiangular hexagon-shape-controlled synthesis of graphene on copper surface," *Advanced Materials*, vol. 23, no. 31, pp. 3522–3525, 2011.

[291] S. Das and J. Drucker, "Nucleation and growth of single layer graphene on electrodeposited Cu by cold wall chemical vapor deposition," *Nanotechnology*, vol. 28, no. 10, 2017.

[292] S. Jin, M. Huang, Y. Kwon, L. Zhang, B.-W. Li, S. Oh, J. Dong, D. Luo, M. Biswal, B. V. Cunning, P. V. Bakharev, I. Moon, W. J. Yoo, D. C. Camacho-Mojica, Y.-J. Kim, S. H. Lee, B. Wang, W. K. Seong, M. Saxena, F. Ding, H.-J. Shin, and R. S. Ruoff, "Colossal grain growth yields single-crystal metal foils by contact-free annealing," *Science*, vol. 362, no. 6418, pp. 1021–1025, 2018.

[293] A. Ibrahim, S. Akhtar, M. Atieh, R. Karnik, and T. Laoui, "Effects of annealing on copper substrate surface morphology and graphene growth by chemical vapor deposition," *Carbon*, vol. 94, pp. 369–377, 2015.

[294] X. H. Kong, H. X. Ji, R. D. Piner, H. F. Li, C. W. Magnuson, C. Tan, A. Ismach, H. Chou, and R. S. Ruoff, "Non-destructive and rapid evaluation of chemical vapor deposition graphene by dark field optical microscopy," *Applied Physics Letters*, vol. 103, no. 4, 2013.

[295] X. Wu, G. Zhong, and J. Robertson, "Nondestructive optical visualisation of graphene domains and boundaries," *Nanoscale*, vol. 8, no. 36, pp. 16427–16434, 2016.

[296] R. De, D. Albuquerque, T. Cruz, F. Yamaji, and F. Leite, "Measurement of the Nanoscale Roughness by Atomic Force Microscopy: Basic Principles and Applications," *Atomic Force Microscopy - Imaging, Measuring and Manipulating Surfaces at the Atomic Scale*, 2012.

[297] K. Celebi, M. T. Cole, J. W. Choi, F. Wyczisk, P. Legagneux, N. Rupesinghe, J. Robertson, K. B. Teo, and H. G. Park, "Evolutionary kinetics of graphene formation on copper," *Nano Letters*, vol. 13, no. 3, pp. 967–974, 2013.

[298] N. S. Safron and M. S. Arnold, "Experimentally determined model of atmospheric pressure CVD of graphene on Cu," *Journal of Materials Chemistry C*, vol. 2, no. 4, pp. 744–755, 2014.

[299] X. Li, L. Colombo, and R. S. Ruoff, "Synthesis of Graphene Films on Copper Foils by Chemical Vapor Deposition," *Advanced Materials*, pp. 6247–6252, 2016.

[300] E. Loginova, N. C. Bartelt, P. J. Feibelmarr, and K. F. McCarty, "Factors influencing graphene growth on metal surfaces," *New Journal of Physics*, vol. 11, 2009.

[301] S. Nie, J. M. Wofford, N. C. Bartelt, O. D. Dubon, and K. F. McCarty, "Origin of the mosaicity in graphene grown on Cu(111)," *Physical Review B - Condensed Matter and Materials Physics*, vol. 84, no. 15, pp. 1–7, 2011.

[302] S. Bhaviripudi, X. Jia, M. S. Dresselhaus, and J. Kong, "Role of kinetic factors in chemical vapor deposition synthesis of uniform large area graphene using copper catalyst," *Nano Letters*, vol. 10, no. 10, pp. 4128–4133, 2010.

[303] C. Shen, Y. Jia, X. Yan, W. Zhang, Y. Li, F. Qing, and X. Li, "Effects of Cu contamination on system reliability for graphene synthesis by chemical vapor deposition method," *Carbon*, vol. 127, pp. 676–680, 2018.

[304] S. Hussain, M. W. Iqbal, J. Park, M. Ahmad, J. Singh, J. Eom, and J. Jung, "Physical and electrical properties of graphene grown under different hydrogen flow in low pressure chemical vapor deposition," *Nanoscale Research Letters*, vol. 9, no. 1, pp. 1–9, 2014.

[305] S. Choubak, M. Biron, P. L. Levesque, R. Martel, and P. Desjardins, "No graphene etching in purified hydrogen," *Journal of Physical Chemistry Letters*, vol. 4, no. 7, pp. 1100–1103, 2013.

[306] W. He, D. Geng, and Z. Xu, "Pattern evolution characterizes the mechanism and efficiency of CVD graphene growth," *Carbon*, vol. 141, pp. 316–322, 2019.

[307] H. Shu, X. Chen, and F. Ding, "The edge termination controlled kinetics in graphene chemical vapor deposition growth," *Chemical Science*, vol. 5, no. 12, pp. 4639–4645, 2014.

[308] T. Niu, J. Zhang, and W. Chen, "Atomic mechanism for the growth of wafer-scale single-crystal graphene: theoretical perspective and scanning tunneling microscopy investigations," *2D Materials*, vol. 4, p. 042002, aug 2017.

[309] Z. Qiu, P. Li, Z. Li, and J. Yang, "Atomistic Simulations of Graphene Growth: From Kinetics to Mechanism," *Accounts of Chemical Research*, vol. 51, no. 3, pp. 728–735, 2018.

[310] H. Kim, E. Saiz, M. Chhowalla, and C. Mattevi, "Modeling of the self-limited growth in catalytic chemical vapor deposition of graphene," *New Journal of Physics*, vol. 15, 2013.

[311] P. Procházka, J. Mach, D. Bischoff, Z. Lišková, P. Dvořák, M. Vaňatka, P. Simonet, A. Varlet, D. Hemzal, M. Petrenec, L. Kalina, M. Bartošík, K. Ensslin, P. Varga, J. Čechal, and T. Šikola, "Ultrasmooth metallic foils for growth of high quality graphene by chemical vapor deposition," *Nanotechnology*, vol. 25, no. 18, 2014.

[312] S. Gottardi, K. Müller, L. Bignardi, J. C. Moreno-López, T. A. Pham, O. Ivashenko, M. Yablonskikh, A. Barinov, J. Björk, P. Rudolf, and M. Stöhr, "Comparing graphene growth on Cu(111) versus oxidized Cu(111)," *Nano Letters*, vol. 15, no. 2, pp. 917–922, 2015.

[313] Q. Yu, L. A. Jauregui, W. Wu, R. Colby, J. Tian, Z. Su, H. Cao, Z. Liu, D. Pandey, D. Wei, T. F. Chung, P. Peng, N. P. Guisinger, E. A. Stach, J. Bao, S. S. Pei, and Y. P. Chen, "Control and characterization of individual grains and grain boundaries in graphene grown by chemical vapour deposition," *Nature Materials*, vol. 10, no. 6, pp. 443–449, 2011.

[314] I. Vlassiouk, S. Smirnov, M. Regmi, S. P. Surwade, N. Srivastava, R. Feenstra, G. Eres, C. Parish, N. Lavrik, P. Datskos, S. Dai, and P. Fulvio, "Graphene nucleation density on copper: Fundamental role of background pressure," *Journal of Physical Chemistry C*, vol. 117, no. 37, pp. 18919–18926, 2013.

[315] N. Lisi, T. Dikonimos, F. Buonocore, M. Pittori, R. Mazzaro, R. Rizzoli, S. Marras, and A. Capasso, "Contamination-free graphene by chemical vapor deposition in quartz furnaces," *Scientific Reports*, vol. 7, p. 9927, dec 2017.

[316] A. Logadottir, T. H. Rod, J. K. Nørskov, B. Hammer, S. Dahl, and C. J. Jacobsen, "The Brønsted-Evans-Polanyi relation and the volcano plot for ammonia synthesis over transition metal catalysts," *Journal of Catalysis*, vol. 197, no. 2, pp. 229–231, 2001.

[317] M. Lavin-Lopez, J. Valverde, S. Ordoñez-Lozoya, A. Paton-Carrero, and A. Romero, "Role of inert gas in the Cvd-graphene synthesis over polycrystalline nickel foils," *Materials Chemistry and Physics*, vol. 222, pp. 173–180, 2019.

[318] F. Tuinstra and J. L. Koenig, "Raman Spectrum of Graphite," *The Journal of Chemical Physics*, vol. 53, no. 3, pp. 1126–1130, 1970.

[319] F. Banhart, J. Kotakoski, and A. V. Krasheninnikov, "Structural Defects in Graphene," *Acs Nano*, vol. 5, no. 1, pp. 26–41, 2011.

[320] C. Zhang, L. Fu, N. Liu, M. Liu, Y. Wang, and Z. Liu, "Synthesis of nitrogen-doped graphene using embedded carbon and nitrogen sources," *Advanced Materials*, vol. 23, no. 8, pp. 1020–1024, 2011.

[321] J. E. Lee, G. Ahn, J. Shim, Y. S. Lee, and S. Ryu, "Optical separation of mechanical strain from charge doping in graphene," *Nature Communications*, vol. 3, no. May, pp. 1024–1028, 2012.

[322] B. M. Srinivasan, Y. Hao, R. Hariharaputran, S. Rywkin, J. C. Hone, L. Colombo, R. S. Ruoff, and Y.-W. Zhang, "Oxygen-Promoted Chemical Vapor Deposition of Graphene on Copper: A Combined Modeling and Experimental Study," *ACS Nano*, p. acsnano.8b04460, 2018.

[323] Q. Li, H. Chou, J. H. Zhong, J. Y. Liu, A. Dolocan, J. Zhang, Y. Zhou, R. S. Ruoff, S. Chen, and W. Cai, "Growth of adlayer graphene on Cu studied by carbon isotope labeling," *Nano Letters*, vol. 13, no. 2, pp. 486–490, 2013.

[324] H. Wang, Y. Wu, C. Cong, J. Shang, and T. Yu, "Hysteresis of Electronic Transport in Graphene Transistors," *ACS Nano*, vol. 4, pp. 7221–7228, dec 2010.

[325] A. Temiryazev, A. Frolov, and M. Temiryazeva, "Atomic-force microscopy study of self-assembled atmospheric contamination on graphene and graphite surfaces," *Carbon*, vol. 143, pp. 30–37, mar 2019.

[326] A. A. Balandin, "Low-frequency 1/f noise in graphene devices," *Nature Nanotechnology*, vol. 8, no. 8, pp. 549–555, 2013.

[327] D. Kuzum, H. Takano, E. Shim, J. C. Reed, H. Juul, A. G. Richardson, J. De Vries, H. Bink, M. A. Dichter, T. H. Lucas, D. A. Coulter, E. Cubukcu, and B. Litt, "Transparent and flexible low noise graphene electrodes for simultaneous electrophysiology and neuroimaging," *Nature Communications*, vol. 5, no. May, pp. 1–10, 2014.

[328] T. O. Wehling, K. S. Novoselov, S. V. Morozov, E. E. Vdovin, M. I. Katsnelson, A. K. Geim, and A. I. Lichtenstein, "Molecular doping of graphene," *Nano Letters*, vol. 8, no. 1, pp. 173–177, 2008.

[329] T. Wehling, M. Katsnelson, and A. Lichtenstein, "Adsorbates on graphene: Impurity states and electron scattering," *Chemical Physics Letters*, vol. 476, pp. 125–134, jul 2009.

[330] M. Remškar, J. Kovac, M. Viršek, M. Mrak, A. Jesih, and A. Seabaugh, "W 5 O 14 Nanowires," *Advanced Functional Materials*, vol. 17, pp. 1974–1978, aug 2007.

[331] W. Yu, Z. Shen, F. Peng, Y. Lu, M. Ge, X. Fu, Y. Sun, X. Chen, and N. Dai, "Improving gas sensing performance by oxygen vacancies in sub-stoichiometric WO 3−x," *RSC Advances*, vol. 9, no. 14, pp. 7723–7728, 2019.

[332] J. Dai and J. Yuan, "Physisorption to chemisorption transition of NO 2 on graphene induced by the interplay of SiO 2 substrate and van der Waals forces: A first principles study," *Chemical Physics*, vol. 405, no. 2, pp. 161–166, 2012.

[333] S. M. Kozlov, F. Viñes, and A. Görling, "Bonding mechanisms of graphene on metal surfaces," *Journal of Physical Chemistry C*, vol. 116, no. 13, pp. 7360–7366, 2012.

[334] R. Long, "Understanding the electronic structures of graphene quantum dot physisorption and chemisorption onto the TiO2 (110) surface: A first-principles calculation," *ChemPhysChem*, vol. 14, no. 3, pp. 579–582, 2013.

[335] F. Wang, C. Di Valentin, and G. Pacchioni, "Electronic and Structural Properties of WO 3 : A Systematic Hybrid DFT Study," *The Journal of Physical Chemistry C*, vol. 115, pp. 8345–8353, apr 2011.

[336] T. Hirose, I. Kawano, and M. Niino, "Electrical Conductivity of Tungsten Trioxide (WO 3)," *Journal of the Physical Society of Japan*, vol. 33, pp. 272–272, jul 1972.

[337] P. J. Yunker, T. Still, M. A. Lohr, and A. G. Yodh, "Suppression of the coffee-ring effect by shape-dependent capillary interactions," *Nature*, vol. 476, no. 7360, pp. 308–311, 2011.

[338] H. Lee, K. Paeng, and I. S. Kim, "A review of doping modulation in graphene," *Synthetic Metals*, vol. 244, no. May, pp. 36–47, 2018.

[339] W. H. Lin, T. H. Chen, J. K. Chang, J. I. Taur, Y. Y. Lo, W. L. Lee, C. S. Chang, W. B. Su, and C. I. Wu, "A direct and polymer-free method for transferring graphene grown by chemical vapor deposition to any substrate," *ACS Nano*, vol. 8, no. 2, pp. 1784–1791, 2014.

[340] M. Chen, R. C. Haddon, R. Yan, and E. Bekyarova, "Advances in transferring chemical vapour deposition graphene: A review," *Materials Horizons*, vol. 4, no. 6, pp. 1054–1063, 2017.

[341] M. Lafkioti, B. Krauss, T. Lohmann, U. Zschieschang, H. Klauk, K. V. Klitzing, and J. H. Smet, "Graphene on a hydrophobic substrate: Doping reduction and hysteresis suppression under ambient conditions," *Nano Letters*, vol. 10, no. 4, pp. 1149–1153, 2010.

[342] D. M. Basko, "Boundary problems for Dirac electrons and edge-assisted Raman scattering in graphene," *Physical Review B - Condensed Matter and Materials Physics*, vol. 79, no. 20, 2009.

[343] W. Kim, A. Javey, O. Vermesh, Q. Wang, Y. Li, and H. Dai, "Hysteresis caused by water molecules in carbon nanotube field-effect transistors," *Nano Letters*, vol. 3, no. 2, pp. 193–198, 2003.

[344] S. A. McGill, S. G. Rao, P. Manandhar, P. Xiong, and S. Hong, "High-performance, hysteresis-free carbon nanotube field-effect transistors via directed assembly," *Applied Physics Letters*, vol. 89, no. 16, pp. 1–4, 2006.

[345] A. C. Crowther, A. Ghassaei, N. Jung, and L. E. Brus, "Strong charge-transfer doping of 1 to 10 layer graphene by NO 2," *ACS Nano*, vol. 6, no. 2, pp. 1865–1875, 2012.

[346] K. Kumar, Y. S. Kim, and E. H. Yang, "The influence of thermal annealing to remove polymeric residue on the electronic doping and morphological characteristics of graphene," *Carbon*, vol. 65, pp. 35–45, 2013.